Delft University of Technology - Norwegian University of Science and Technology

Operability of Offshore Wind Turbine Blade Installation with a Semi-Submersible Crane Vessel

Numerical Modelling and Dynamic Analysis of Relative Motion Between Blade Root and Hub During Single Blade Installation

Ellen Kroon

TU Delft NTNU

Operability of Offshore Wind Turbine Blade Installation with a Semi-Submersible Crane Vessel

Numerical Modelling and Dynamic Analysis of Relative Motion Between Blade Root and Hub During Single Blade Installation

by

Ellen Kroon

to obtain the degree of Master of Science at the
Delft University of Technology, and the
Norwegian University of Science and Technology,
to be defended publicly on 26-08-2025 at 11:30.

Student number:	4856104	TU Delft
	123730	NTNU
Thesis committee:	Dr. ir. P. van der Male,	TU Delft, chair
	Prof. Dr. A. Nejad,	NTNU, supervisor
	Dr. ir. H. Hendrikse,	TU Delft, supervisor
	ir. T. Ouwehand,	HMC, supervisor
	ir. M. Veldhuizen,	HMC, supervisor

Cover: OWT blade installation with Thialf, render by HMC

TU Delft MARINE CONTRACTORS NTNU

Preface

This master's thesis marks the final deliverable of the European Wind Energy Master (EWEM) program, completed in pursuit of a dual degree in Offshore and Dredging Engineering at Delft University of Technology and Wind Energy at the Norwegian University of Science and Technology. The work presented here builds upon the knowledge gained throughout the EWEM curriculum and bridges the gap between academic theory and real-world application through collaboration with Heerema Marine Contractors.

The EWEM program has been an incredible journey, taking me to Copenhagen, Denmark, back to my beloved home base in Delft, and then to Trondheim, Norway, before ultimately leading me to my new home in Amsterdam. With a record of six moves over the past two years, I've learned that home is defined by the people around me, and that I can now pack up my life in just a few hours like a seasoned nomad. This program has provided a truly enriching international experience and the opportunity to meet a wide range of inspiring individuals and form lasting friendships. The thesis process itself has been equally exciting, marking my first deep dive into the operational side of the offshore wind industry.

I would like to express my sincere gratitude to those who supported me during this research. First, I want to thank my academic supervisors, Pim van der Male and Amir Nejad, for their guidance and for offering a critical academic perspective throughout the process. I truly appreciated our meetings and the valuable insights and feedback you shared.

From Heerema Marine Contractors, I am especially grateful to Tim Ouwehand for his daily supervision, for introducing me to the operational aspects of the industry, and for generously sharing his expertise. I thoroughly enjoyed our collaboration and appreciated how your thoughtful questions helped shape the direction of my work. I would also like to thank Maarten Veldhuizen for our technical discussions, your sharp insights encouraged me to think more critically and greatly improved the quality of my research. Finally, my thanks go to everyone at HMC with whom I had the pleasure of working, whether for technical advice or a good conversation over coffee. I truly enjoyed my time at the office and look forward to returning in September.

Lastly, I would like to thank my friends and family for their unconditional support and for always showing enthusiasm for my pursuits. Your encouragement means the world to me.

Ellen Kroon
Amsterdam, July 2025

Summary

This thesis investigates the operability of offshore wind turbine single-blade installation using a semi-submersible crane vessel, with a specific focus on the alignment phase. As turbines grow in size and are installed further offshore, jack-up vessels face limitations due to increasing water depths and challenging soil conditions. SSCVs offer a promising alternative; however, their dynamic response introduces new challenges that warrant detailed analysis.

A numerical model was developed in *OrcaFlex* to simulate the dynamic interaction between the hub of a bottom-fixed 15 MW offshore wind turbine and the root of a suspended blade lifted by the SSCV *Thialf*. Modal and time-domain analyses were conducted to evaluate the dynamic behaviour of both systems, followed by an assessment of their relative displacements. These analyses were performed under environmental conditions representative of a site in the Baltic Sea.

The results showed that wave loading dominated both hub and blade motions, with turbine resonance and vessel dynamics, particularly when coupled with pendulum dynamics, critically affecting operability. Blade root motions were strongly coupled to the SSCVs heave and pitch responses, while hub displacements were significantly amplified near the turbine's natural frequency. Sensitivity analyses revealed the influence of vessel draught, suspension length, blade installation tool mass, and tugger specifications on the system's dynamic response.

Operability was assessed based on relative displacement, defined safety boundaries, and outcrossing frequency criteria. Hub motion emerged as a fundamental limiting factor, particularly for wave peak periods near the turbine's natural frequency. Blade root dynamics were primarily influenced by SSCV motions and the coupling between vessel dynamics and the lifting arrangement. This latter effect can be mitigated through careful tuning of the installation configuration. The installation was found to be operable for peak periods that do not induce resonant hub motion and where vessel motions remain limited, provided the system is properly configured.

These findings underline that the implementation of SSCVs for single-blade installation is not a direct replacement for jack-up vessels but requires a tailored engineering approach. The dynamic behaviour of SSCVs under wave loading necessitates site-specific assessment, particularly with regard to resonance risks. Design adaptations such as draught adjustment and lifting configuration tuning can mitigate dynamic responses, but the feasibility of SSCV-based installation remains constrained under certain environmental conditions.

The numerical model relies on several simplifications and assumptions, and the study is limited to a specific turbine, vessel, lifting configuration, and installation site. As such, the conclusions are not directly generalisable beyond this setup. Future research should focus on experimental validation, improved aerodynamic modelling, and the development of advanced mitigation strategies to enhance installation operability.

This thesis provides a structured methodology for evaluating the environmental and operational effects on the relative dynamic behaviour between the hub and blade root during single-blade installation using an SSCV. It identifies key operational drivers, assesses operability, and highlights critical trade-offs and design considerations for improving offshore wind turbine installation performance.

Contents

Nomenclature

Abbreviations

Abbreviation	Definition
BIT	Blade Installation Tool
DP	Dynamic Positioning
DoF	Degree of Freedom
FA	Fore-Aft
FFT	Fast Fourier Transform
HMC	Heerema Marine Contractors
HTV	Heavy Transport Vessel
MP	Monopile
NREL	National Renewable Energy Laboratory
NTM	Normal Turbulence Model
OWT	Offshore Wind Turbine
RAO	Response Amplitude Operator
RNA	Rotor-Nacelle Assembly
SS	Side-Side
SSCV	Semi-Submersible Crane Vessel
TP	Transition Piece
VIV	Vortex Induced Vibrations
WLL	Working Load Limit

Symbols

Symbol	Definition	Unit
A	Reference area	m^2
$b(f)$	Peakedness function	–
C	Aerodynamic coefficient	–
C_l	Aerodynamic lift coefficient	–
C_d	Aerodynamic drag coefficient	–
C_D	Hydrodynamic drag coefficient	–
C_m	Added mass coefficient	–
c	Chord length	m
D	Diameter	m
$\vec{D}(t)$	Relative displacement vector between hub centre and blade root centre	m
d	Airfoil drag force per unit length	kN/m
dF	Differential hydrodynamic force	N
E	Young's modulus	Pa
F_{aero}	Aerodynamic force	kN
f_m	Wave spectral peak frequency	Hz
f_n	Natural frequency	Hz
g	Gravitational acceleration	m/s^2
G	Shear modulus of soil	MPa
H_s	Significant wave height	m
I	Mass moment of inertia	$t{\cdot}m^2$

Symbol	Definition	Unit
$K(n)$	Normalizing constant for the directional spreading function	–
k_{beam}	Stiffness of the beam	N/m
k_{eff}	Effective stiffness	N/m
k_{soil}	Soil stiffness	N/m
L_{eff}	Effective pendulum length	m
l	Airfoil lift force per unit span	kN/m
m_{eff}	Effective mass	t
m_{beam}	Beam mass	t
m_{tip}	Tip mass	t
n	Wave spreading exponent	–
R_{sb}	Safety boundary	m
r	Radial position along turbine blade	m
$S_d(\theta)$	Directional spreading function of wave energy	1/deg
$S(f)$	Spectral density of sea surface elevation	m^2/Hz
T_p	Wave peak period	s
TI	Turbulence intensity	–
U_{ref}	Reference wind speed	m/s
u	Fluid velocity	m/s
$\dot{u}$	Fluid acceleration	m/s^2
V_{rel}	Relative wind velocity	m/s
V_w	Wind velocity	m/s
α	Angle of attack / scaling factor	$^\circ$ / –
γ	Spectral peak enhancement factor	–
δ	Decay rate	1/s
ζ	Damping ratio	–
ν	Poisson's ratio / outcrossing rate	– / Hz
ν_{cr}	Critical outcrossing rate	Hz
ρ	Fluid density	kg/m^3
ρ_{air}	Air density	kg/m^3
θ_{pitch}	Blade pitch angle	$^\circ$
$\theta_{\text{twist}}(r)$	Local blade twist angle at radial position r	$^\circ$
σ	Motion standard deviation	m / $^\circ$
ϕ_R	Radial velocity potential	m^2/s
ϕ_D	Diffraction potential	m^2/s
Φ	Velocity potential	m^2/s

1

Introduction and Background

This chapter provides a brief introduction to offshore wind energy and offshore wind turbine blade installation. It provides a high-level summary of key findings from the preceding literature study, complemented by updated industry insights. A more detailed background is therefore available in the preceding literature study (Kroon, 2024). The chapter proceeds by stating the problem, followed by a review of existing literature on the subject. Subsequently, the research objectives are outlined, and the research methodology and thesis structure are presented.

1.1. Offshore Wind Energy

Offshore wind energy plays a central role in Europe's renewable energy transition. Between 2025 and 2030, Europe is projected to install 187 GW of new wind power capacity, increasing total capacity to 450 GW across Europe. To meet the EU's 42.5% renewable energy target requires reaching 425 GW by 2030. As shown in Figure 1.1, a substantial share of this growth is expected to come from offshore wind installations. (WindEurope, 2025)

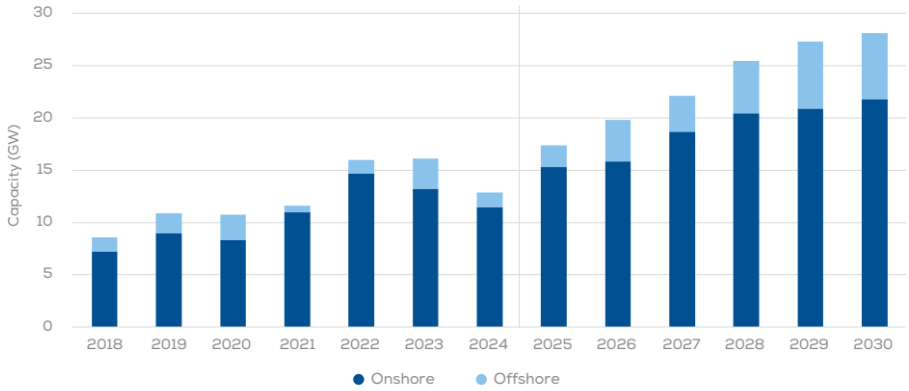

Figure 1.1: Expected increase in wind power capacity in the EU (WindEurope, 2025).

At present, most offshore wind turbines (OWTs) are bottom-fixed (WindEurope, 2025). This type of OWTs requires offshore installation, during which the substructure and all turbine components must be assembled and installed at the designated site. Various installation methods exist for this operation, most of which rely on lifting operations using crane vessels (Zhao et al., 2018). In essence, the installation of bottom-fixed OWTs revolves around three core elements: the substructure, the turbine, and the installation vessel.

Figure 1.2 shows the substructure types used for turbines installed in Europe in 2023. The figure high-

lights that the majority of substructures are bottom fixed and emphasizes the dominance of monopiles (MPs) as the prevailing foundation technology.

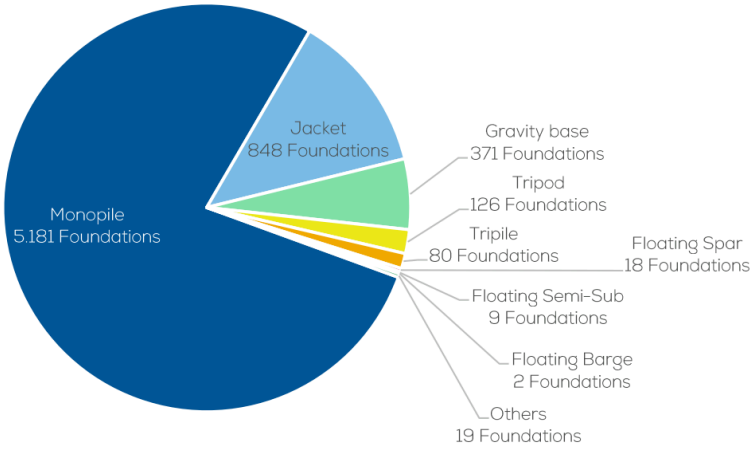

Figure 1.2: Types of substructures for wind turbines installed in 2023 (WindEurope, 2024).

The average power rating of offshore wind turbines in Europe has increased by a factor of 2.4 over the past decade and by more than one quarter since 2022 (WindEurope, 2025). This trend is directly associated with the growth in turbine size and hub height (Zhao et al., 2018). While this increase reflects ongoing efforts to optimize energy capture, it also introduces significant challenges for the offshore installation. Larger turbines demand higher crane capacities, greater lifting heights, and improved resilience to offshore environmental conditions (Zhao et al., 2018).

Different types of crane vessels can be employed for installation operations, including jack-up and floating vessels. Currently, bottom fixed OWTs are predominantly installed using jack-up vessels, which stabilise on the seabed to provide a fixed platform for operations (Jiang et al., 2018; Zhao et al., 2018). For substructure installation, however, floating vessels are also used in the industry.

1.2. Problem Statement

An important trend within the OWT industry is the continuous increase in both average water depth and distance to shore of offshore wind farms (Zhao et al., 2018). Installation costs for OWTs are already substantial, accounting for approximately 19% of the total project budget, which is 16% higher than that typically allocated for land-based wind turbines (Stehly et al., 2018). Moreover, studies indicate that a 10% increase in either water depth or distance to shore leads to a 1% rise in overall investment costs (Kitzing & Morthorst, 2015). Given these high baseline costs and the trend toward deeper installation sites, the need for cost-effective operations is becoming increasingly critical. In this context, the use of an SSCV already present at the installation site could offer a potential economic advantage.

Furthermore, jack-up vessels, which are frequently employed for OWT installation, face several operational constraints that limit their applicability, particularly in light of the anticipated shift toward deeper waters within the offshore wind industry. Their deployment is restricted by water depth, making them unsuitable for deeper installation sites (El-Reedy, 2012). Even in shallow waters, geotechnical challenges such as erodible seabeds can lead to excessive scour around spud cans, potentially resulting in settlement or leg tilting (Raaijmakers & Rudolph, 2007).

In addition, leg deployment and retrieval operations are time consuming and highly sensitive to environmental conditions (Zhao et al., 2018). Operational risks also arise from potential interference between jack-up legs and subsea cables, particularly when turbine installation and cable laying are conducted in close succession (DNV, 2023). This risk is especially critical during maintenance activities at existing offshore wind farms, where the subsea cable infrastructure is already in place.

Furthermore, the limited deck space of jack-up vessels imposes constraints on operational efficiency (Bastiaanssen, 2020), while strict environmental limits, typically mean wind speeds below 10 m/s and significant wave heights between 1.5 m and 2 m, further reduce operability (Zhao et al., 2018), potentially resulting in increased installation costs.

Floating installation vessels present a promising alternative. They are not constrained by water depth and can be rapidly relocated between operations (Zhao et al., 2018). Among floating vessel types, monohull and semi submersible vessels are the most common. In particular, semi submersible crane vessels (SSCVs) appear well suited for single blade installation. A study by Zhao et al. (2018) demonstrated that SSCVs induce significantly lower blade root excitations during installation compared to monohull vessels.

Given their existing role in OWT substructure installation, the potential economic benefits of extending their use to turbine installation, the ongoing shift toward deeper offshore sites, and their operational advantages, further investigation into the feasibility and dynamic behaviour of single blade installation using SSCVs is justified.

As previously noted, various installation methods exist. In many cases, turbine blades are pre-assembled into a complete rotor component prior to installation. This approach reduces offshore lifting operations and offers a relatively cost-effective solution (Jiang et al., 2018).

An example of such an installation method is the Arcadis Ost 1 project by Heerema Marine Contractors (HMC). In 2023, HMC successfully installed 27 wind turbines at the Arcadis Ost 1 wind farm, located in the German sector of the Baltic Sea. The installation method, referred to as the Rotor Nacelle Assembly (RNA) method, involved assembling the complete rotor component on board the SSCV using a support tower positioned on the deck. For blade-to-hub installation, an additional tool, the Guided Root End Positioning (GREP) tool, was employed. This tool mitigated the relative motion between the hub, mounted atop the dummy tower, and the blade root, thereby enhancing precision during this installation phase. (Heerema Marine Contractors, 2022).

However, with the previously named increasing size of OWTs and rotor diameters approaching 250m for the largest announced models (Global Times, 2025), this method is becoming increasingly impractical due to manoeuvring constraints of the complete rotor component.

Furthermore, turbine manufacturers typically do not permit modifications to the turbine structure, making variations on tools such as the GREP not always feasible. Even if such modifications were allowed, installation contractors are typically not involved at that stage to design such a tool. Additionally, the design and fabrication of a suitable tool would need to be adapted for each turbine type, which limits scalability and long-term applicability. Consequently, the single blade installation method, without the aid of specialized tools, remains central to the conventional offshore wind turbine installation process.

This procedure, originally developed for onshore wind turbine blade installation, demands high precision, which is particularly challenging under offshore conditions. Compared to the installation of the substructure and other OWT components such as the tower and nacelle, blade installation presents greater challenges due to the combined effects of high elevation, large dimensions, low structural mass, aerodynamic sensitivity, and the precision required for alignment (Zhao et al., 2018). These factors underscore that blade installation is the most critical and demanding phase of offshore wind turbine installation.

As jack-up vessels are constrained by site-specific conditions and sometimes impractical due to local factors, and with the offshore wind industry moving toward deeper waters, the development and assessment of alternative installation strategies becomes increasingly important. SSCVs offer a promising floating alternative, particularly when already mobilised for substructure or substation installation. However, their dynamic performance and feasibility for turbine blade installation remain insufficiently understood. Blade installation is the most demanding phase of turbine assembly due to its sensitivity to environmental disturbances, large component dimensions, and high precision requirements. Investigating blade installation using SSCVs is therefore a governing operation for evaluating the feasibility

and potential operability of floating offshore wind turbine installation.

The present problem statement focuses on a fixed-to-floater governing installation scenario, in which a floating vessel installs a blade onto a bottom fixed turbine. While grounded in current industry practice, this research also serves as a critical step toward enabling future floater-to-floater installation or maintenance operations, where both the installation vessel and the turbine foundation are floating. Given the trend toward deeper waters, where conventional substructures are limited by depth constraints, floating wind offers a viable pathway for the continued expansion of offshore wind energy. In this context, the study provides insights into the behaviour of a single floater within such a system, contributing to the understanding of dynamic interactions that will play a key role in future floating offshore wind operations.

1.3. Review of Existing Literature

The installation of OWT blades has been studied from various perspectives, including relative motion, aerodynamic behaviour, structural integrity, and mitigation strategies.

Zhao et al. (2018) conducted numerical modelling and dynamic analysis of offshore wind turbine blade installation. While this study provided valuable insights into blade dynamics and vessel-induced motions, it did not account for the influence of OWT hub motions. In contrast, Jiang et al. (2018) performed a parametric study of hub motions during final blade installation under rough environmental conditions. Their model involved a pre-installed MP and nacelle assembly, with a 5 MW blade controlled by tugger lines, but excluded the motion of a floating installation vessel.

From a structural perspective, Verma, Jiang, Ren, et al. (2019) proposed a structural response-based methodology to assess operational limits for single blade installation, introducing a threshold impact velocity below which blade damage does not initiate. Similarly, Verma, Jiang, Vedvik, et al. (2019) focused on blade root impact during mating, underscoring the importance of maintaining structural integrity during installation. These studies highlight the critical role of structural safety in defining operational limits.

From an economic perspective, Gaunaa et al. (2014) demonstrated that increasing the allowable wind speed during installation could significantly reduce overall wind farm costs. Their study focused on first-order aerodynamic and aeroelastic responses of a single-blade setup to define these limits more sharply.

Several mitigation strategies have also been explored. Jiang (2018) investigated the use of a passive tuned mass damper to reduce dynamic loads, while Ren et al. (2018) applied active control through three tugger lines to stabilise the blade during installation.

To date, no study has integrated hub dynamics and blade root motion under the influence of a floating installation vessel such as an SSCV, in the context of a fixed-to-floater configuration. In addition, most existing research has focused on smaller turbines with lower hub heights and shorter blades, which no longer reflect the current scale of offshore wind developments. Given the increasing turbine dimensions, the shift toward deeper waters, and the growing relevance of floating installation strategies, there is a clear need for updated analyses that capture the coupled dynamics governing single blade installation scenarios by floating vessel.

1.4. Research Objectives

This research aims to assess the operability of OWT single blade installation using an SSCV, with particular focus on the relative motion between the hub and the blade root during the alignment phase of the operation.

To this end, a numerical model is developed in OrcaFlex to simulate the dynamic behaviour of the wind turbine, the installation vessel, and the suspended blade under realistic wind and wave conditions for a representative location in the Baltic Sea. The goal is to quantify the relative motions between the hub and the blade root under varying environmental and operational conditions, identify the dominant dynamic contributors, and evaluate the system's sensitivity to key parameters.

The study aims to define the operability of the installation procedure at the selected location by evalu-

ating whether the relative motions between the hub and blade root remain within acceptable limits. In doing so, it provides insight into the limiting environmental conditions that constrain safe and effective installation and identifies key parameters for improving operability through system tuning and installation configuration optimisation.

This study is guided by the following central research question, which captures its overall objective:

> *How do environmental and operational conditions influence the relative motion between the hub of a bottom-fixed offshore wind turbine and the blade root during single blade installation using a semi-submersible crane vessel, and how does this affect installation operability?*

1.5. Research Methodology

This section outlines the research methodology employed in this study. The methodology is structured into three main stages: system definition, modal analysis, and dynamic analysis. Each stage corresponds to specific models, analyses, and chapters of the thesis. A flowchart illustrating the complete methodology, along with its components and corresponding chapters, is provided in Figure 1.3.

The methodology begins with system definition. This stage outlines the scope of the study, followed by the selection of a representative case study and the development of the system configuration. It defines the environmental and operational parameters for both the bottom-fixed offshore wind turbine and the floating installation vessel, as presented in Chapters 1 to 3.

In the second stage, two numerical models are developed to represent the OWT and the lifted blade on the SSCV. Model A represents the bottom-fixed OWT, while Model B represents the lifted wind turbine blade suspended from a SSCV. Modal analysis is used to extract key modal characteristics, including natural frequencies, which are critical for understanding the system's dynamic response. This stage is detailed in Chapters 4 and 5.

The third stage consists of dynamic analysis. Here, the two models are combined into a complete model of the installation system. Time-domain simulations are performed to analyse the dynamic behaviour of both the hub centre and the blade root under varying environmental conditions. From these simulations, relative displacements are computed and key operational drivers are identified. This analysis is covered in Chapter 6.

A sensitivity study follows, in which key operational parameters such as vessel draught, suspension length, and tugger configuration are varied. This identifies the influence of system parameters on relative motion and suggests potential improvements to the installation configuration. These steps are addressed in Chapter 7.

Finally, an improved complete model is developed based on the insights from the sensitivity study. A dedicated operability study is conducted using this improved model to assess feasible environmental conditions under which installation can be safely executed. The findings from this final step are presented in Chapter 8.

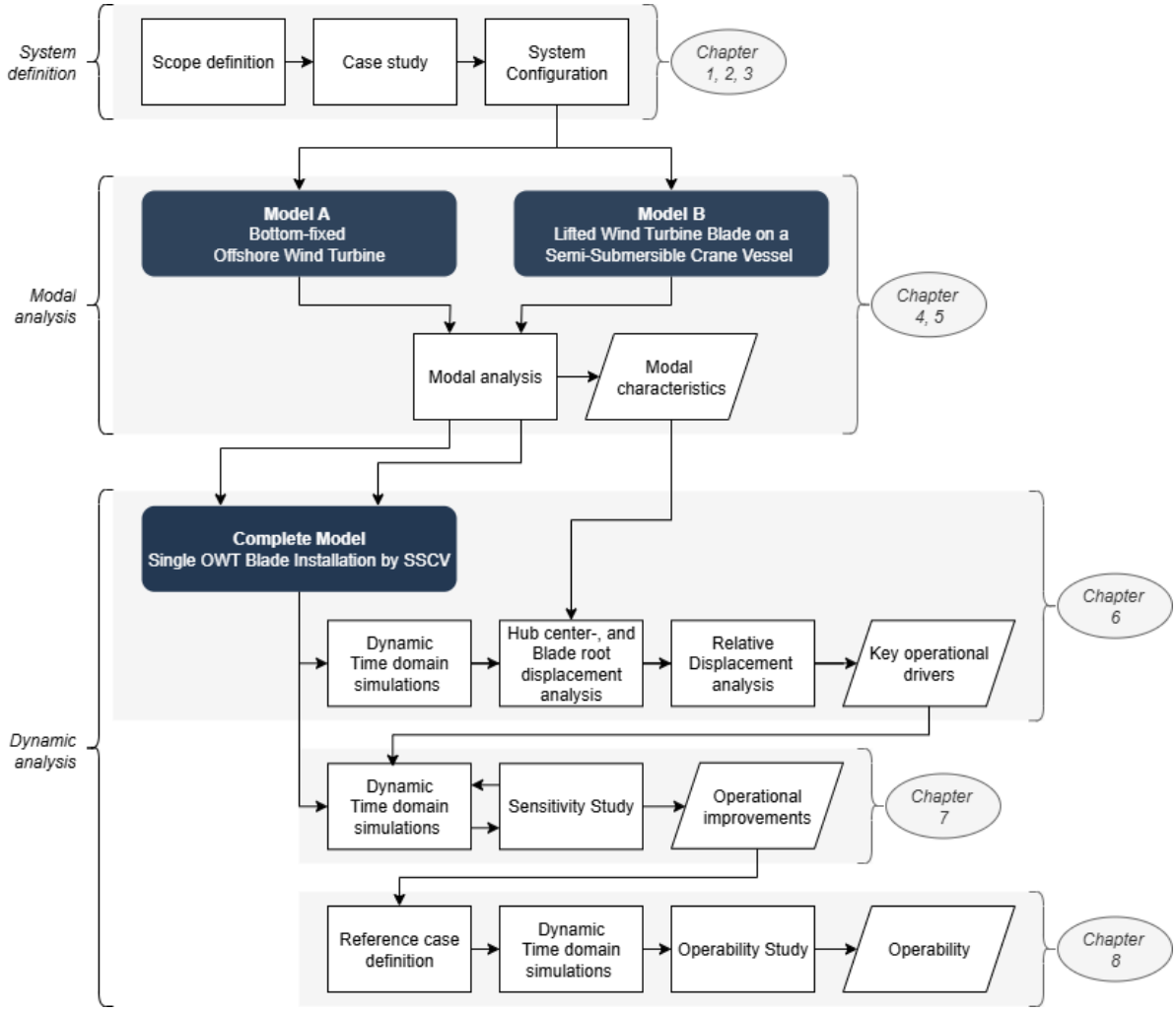

Figure 1.3: Overall research methodology and thesis outline.

1.6. Thesis Outline

Figure 1.4 provides a complete overview of the chapters in this thesis. Chapter 1 introduces the motivation, background, and research objectives. Chapter 2 presents the case study, including site characteristics, environmental conditions, and the hydro- and aerodynamic theories used to translate these conditions into forces acting on the system. Chapter 3 outlines the overall installation procedure, introduces the turbine specifications and the selected installation vessel, and details the dynamic modelling approach used throughout the study.

Chapters 4 and 5 describe the development of the two core models: the bottom-fixed offshore wind turbine (Model A, Chapter 4) and the suspended blade system on a semi-submersible crane vessel (Model B, Chapter 5). These models form the foundation for all subsequent dynamic analyses.

Chapter 6 integrates both models into a complete system model to analyse the dynamic behaviour of the blade root and the hub. Relative displacements are evaluated under varying environmental conditions to examine their effect and identify key operational drivers.

In Chapter 7, a sensitivity study is conducted to examine how key design and operational parameters affect the dynamic response and operability of the system. The insights gained are applied in Chapter 8, where an operability study is performed using an improved model configuration.

Chapter 9 summarises the main findings and presents the conclusions of the research. Finally, Chapter 10 provides a broader discussion of the results, identifies limitations, and offers recommendations for

future work.

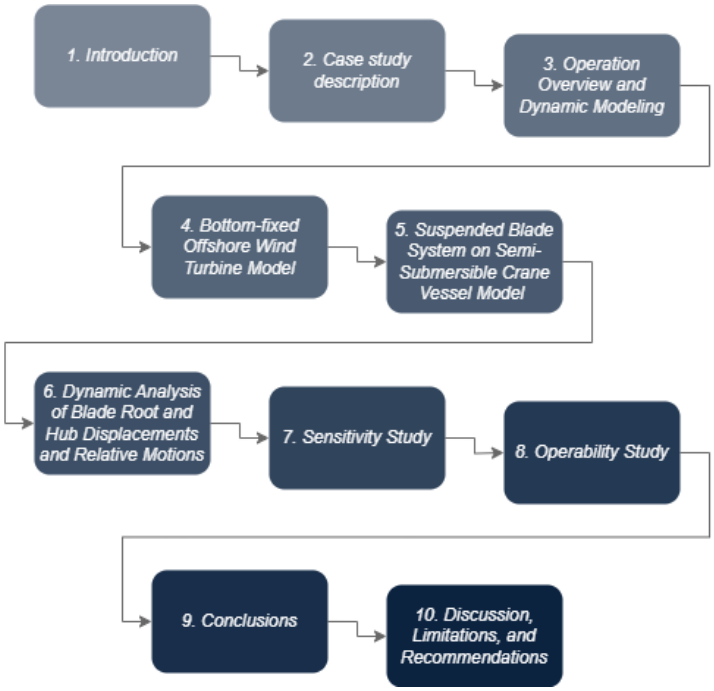

Figure 1.4: Thesis outline.

2

Case Study

The environmental conditions and site characteristics at the installation location establish the boundaries of the study and serve as essential inputs for assessing the installation procedure. To define the scope and ensure consistency in the numerical modelling, a reference site has been selected. This chapter presents the case study, including the selected location, relevant site parameters, and associated environmental conditions. Furthermore, the hydro- and aerodynamic theories used to translate these conditions into forces acting on the system are introduced.

2.1. General Information and Location

The case study provides realistic environmental conditions and site characteristics for a representative offshore location. Site characteristics include key parameters such as water depth, seabed composition, and water density. Environmental conditions describe the wave, current, and wind patterns at the site.

The Baltic Sea is known for its relatively calm environmental conditions compared to other offshore regions, with moderate wave heights and generally steady wind patterns. It is therefore considered a suitable environment for studying this high-precision installation procedure. The environmental data used in this thesis are based on internal knowledge from HMC, collected across several offshore sites in the Baltic Sea with water depths ranging from 25 to 39 metres. Drawing on this expertise, a representative fictional site has been defined off the coast of Poland for the scope of this study. The assumed water depth at this location is 30 metres, and the seabed is considered flat. To represent conditions unsuitable for jack-up vessels, the seabed is assumed to be sandy and thus erodible.

A fictional site is chosen because the operation is evaluated across a range of environmental conditions rather than for a single, fixed scenario. Accordingly, certain environmental parameters are defined as ranges, chosen to remain representative of realistic conditions in the Baltic Sea. This approach enables a systematic evaluation of how variations in environmental loads influence the system response, within the expected boundaries of the region.

Given the relatively short duration of the operation, only short-term environmental conditions are considered. Long-term or extreme conditions, such as snow and ice accumulation, seismic activity, sea ice, or changes in water level due to tides, storm surges, or climate change, fall outside the scope of this study.

2.2. Environmental Conditions

Environmental conditions at offshore sites are dynamic and interdependent; wind speed, wave height, and peak period vary over time and are often correlated. These parameters govern the external loads acting on offshore structures and operations, manifesting as excitation forces. The following sections provide a detailed discussion of each primary excitation source.

2.2.1. Wind

Wind conditions are characterised by a wind spectrum, a wind profile, and a turbulence model, which together form a wind field. More detailed information on the available wind spectra, profiles, and wind fields is provided in the literature review for this study (Kroon, 2024).

The Kaimal spectrum has been found to accurately represent wind conditions in the Baltic Sea. The vertical wind profile is modelled using the power law. All parameters required to define these models are referenced to a height of 150 metres, corresponding to the hub height of the wind turbine to be installed. The selected range of mean wind speeds is defined such that, at a typical site in the Baltic Sea, there is a 90% probability that 1-hour mean wind speeds at the reference height fall within this range. A summary of the wind field parameters is provided in Table 2.1.

Table 2.1: Wind parameters for the selected site in the Baltic Sea, based on internal experience at HMC.

Parameter	Symbol	Value	Unit	Notes
Reference wind speed	U_{ref}	2 - 16	m/s	Step size 2
Turbulence intensity	TI	0.05	-	
Power law exponent	α	0.09	-	

To model the wind conditions at the reference site, a turbulent wind field is generated using the TurbSim software; more information on this software is provided in Subsection 3.3.6. The generated field follows the guidelines set out in IEC 61400-3-1: Design requirements for fixed offshore wind turbines (International Electrotechnical Commission, 2019), and employs the Normal Turbulence Model (NTM) defined in this standard. The wind parameter inputs used to generate the turbulent field in TurbSim are summarised in Table 2.2.

Table 2.2: Turbulent wind field generation parameters.

Parameter	Value	Unit
Turbulence spectrum	IECKAI	-
Vertical wind profile	Power law	-
Turbulence type	NTM	-
Time step	0.05	s
Simulation duration	2500	s
Grid size	31 × 31	-
Grid dimensions	275 × 275	m

2.2.2. Waves

A real sea state consists of irregular, random waves that can be modelled as a superposition of sinusoidal linear wave components. A spectral model describes how the energy of the wave components is distributed relative to each other across the frequency domain, thereby defining which components together represent the sea state. The JONSWAP spectrum is particularly suitable for wind-generated seas in limited-fetch environments, such as the Baltic Sea, and is therefore used to characterise the wave conditions at the fictional reference location. More detailed information on the available wave spectra is provided in the literature review for this study (Kroon, 2024).

The wave heights selected for this study are found to have a 97% probability of falling within this range at a typical site in the Baltic Sea. The peak period and wave height are interdependent. The range of peak periods is chosen such that the lowest peak period corresponds to the lowest value expected for the smallest wave height, and the highest peak period corresponds to the highest value expected for the largest wave height.

Simulation

The JONSWAP spectrum, used for simulating the wave conditions, is defined by Equation 2.1, Equation 2.2, and Equation 2.3. The spectrum is specified in a partially defined form, meaning that the

significant wave height (H_s) and peak period (T_p) are provided as input parameters. For a selected peak enhancement factor of $\gamma = 3.3$, the remaining spectral parameters can be determined automatically. An overview of the wave parameters used in the simulation is provided at the end of this section in Table 2.3.

$$S(f) = \alpha \frac{g^2}{16\pi^4} f^{-5} \exp\left\{-\frac{5}{4}\left(\frac{f}{f_m}\right)^{-4}\right\} \gamma^{b(f)} \tag{2.1}$$

$$b(f) = \exp\left\{-\frac{1}{2\sigma^2}\left(\frac{f}{f_m} - 1\right)^2\right\} \tag{2.2}$$

$$\sigma = \begin{cases} \sigma_1, & f \leq f_m \\ \sigma_2, & f > f_m \end{cases} \tag{2.3}$$

where:

- $S(f)$: spectral density at frequency f,
- f: wave frequency,
- f_m: peak frequency of the spectrum,
- α: scaling parameter,
- g: acceleration due to gravity,
- γ: peak enhancement factor,
- $b(f)$: peakedness function,
- σ: spectral width parameter,

Directional spreading is incorporated in the wave model using a cosine-power distribution, which defines how wave energy is spread around the principal wave direction. The directional spreading function used by OrcaFlex is given in Equation 2.4. The normalising constant ensures that the integral of $S_d(\theta)$ over the domain equals 1. (Orcina Ltd., 2024k)

$$S_d(\theta) = K(n)\cos^n(\theta - \theta_p), \quad \text{for } -\frac{\pi}{2} \leq \theta - \theta_p \leq \frac{\pi}{2} \tag{2.4}$$

where:

- $S_d(\theta)$: directional spreading function,
- θ: wave direction,
- θ_p: principal wave direction,
- n: spreading exponent,
- $K(n)$: normalising constant

In this study, a spreading exponent of $n = 10$ is applied, resulting in a moderate directional distribution centred around the principal wave direction, spanning approximately $\pm 30°$. This choice accounts for possible variations in wave direction during the installation process. The directional range is discretised into 15 wave directions, and the spreading spectrum is constructed using corresponding wave components.

Wave components are selected using the equal energy discretisation method, in which each component represents an equal portion of the total spectral energy. In this model, 100 wave components are used per wave direction to ensure a fine resolution of the wave energy distribution. A relative frequency range is applied, with a minimum of 0.5 and a maximum of 10.0, both relative to the spectral peak frequency f_m. This means that the actual frequency range covered is $[0.5f_m, 10f_m]$, which are usually sufficient to produce a good representation of the spectrum (Orcina Ltd., 2024b).

Kinematic stretching is a method used to extend the predictions of linear airy wave theory to points above the mean water level, where the original theory is not valid. Among the available methods in OrcaFlex, vertical stretching is the simplest approach. This method sets the kinematics above the mean water level equal to those at the mean water level, providing a straightforward and conservative estimation of wave-induced particle motions. (Orcina Ltd., 2024k)

Husain et al. (2017) studied four different kinematic stretching methods and identified significant discrepancies between them, particularly as wave height increases. However, the differences were found to be less critical for moderate wave heights. Since this study focuses on operational conditions with significant wave heights not exceeding 3 m, the vertical stretching method is considered suitable. Moreover, vertical stretching has been shown to overestimate wave-induced loads, which provides a conservative basis for operability assessment by ensuring that the resulting predictions are not underestimated.

Table 2.3: Wave parameters for the selected site in the Baltic Sea, based on internal experience at HMC.

Parameter	Symbol	Value	Unit
Significant wave height	H_s	0 – 3	m
Peak period	T_p	4 – 8	s
Peak enhancement factor	γ	3.3	–
Spectral width parameter 1	σ_1	0.07	–
Spectral width parameter 2	σ_2	0.09	–
Spreading exponent	n	10	–
Number of wave directions	–	15	–

2.2.3. Wind-Wave Misalignment

At the site, wind and wave conditions are statistically correlated through a joint probability distribution. One important aspect of this relationship is the directional misalignment between wind and wave fields, defined as the absolute angular difference between their directions:

$$\Delta\theta = |\theta_{\text{wind}} - \theta_{\text{wave}}| \tag{2.5}$$

Alari and Van Vledder (2016) analysed wind–wave misalignment in the Baltic Sea using 41 years of high-resolution hindcast data. Their results show that misalignment is a persistent feature across all sub-basins. Influenced by swell propagation, heterogeneous wind fields, and restricted fetch, wind and wave directions are often not aligned in deeper regions of the Baltic, where wave refraction is minimal. In waters deeper than 50 m, the average misalignment typically ranges from 20° to 40°, with a mean of approximately 27°.

In contrast, shallower coastal regions, such as the fictional nearshore site considered in this study, experience stronger alignment. Here, wave growth is more directly governed by local wind forcing due to shorter fetch lengths and increased bottom interaction and wave refraction. As a result, wind and wave directions tend to align more closely.

Therefore, directional misalignment is not considered in the present study. Further justification for this assumption is provided in Section 3.4.

2.2.4. Wind Speed and Wave Height

The wave height and wind speed are strongly correlated. This relationship can be observed from a scatter diagram of wind speed versus significant wave height. A commonly used correlation describing the relationship between wind speed and wave height for the Baltic Sea is given in Equation 2.6. This function represents the mean significant wave height for a given 1-hour mean wind speed. It is important to note that this is an average value based on numerous observations rather than an exact measure; in reality, variability exists around this correlation. In this thesis, the correlation is used for approximate estimation of environmental conditions and is therefore considered sufficiently accurate.

$$Hs = 0.03 \times \left(U_{\text{ref @ 150 m}}\right)^{1.4} + 0.1 \tag{2.6}$$

2.3. Environmental Spectral Analysis

The environmental forces described in the previous section act within specific frequency ranges. A spectral density plot provides a useful means of illustrating this, as it shows how the energy or power of a signal is distributed across various frequencies.

The spectral density plot shown in Figure 2.1 illustrates the frequency content of wind and wave conditions at the fictional location, based on a range of mean wind speeds and wave peak periods. The excitation frequency range shows to be $[0,\ 0.4]$ Hz.

In the figure, wave spectral densities are shown for a significant wave height of 1.0 m. While wave height influences the overall energy magnitude, it does not affect the frequency distribution. Increasing the wave height would raise the area under the spectral curve, but the shape, and thus the associated frequency range, remains unchanged. Therefore, for the purpose of determining the excitation frequency range, the specific choice of wave height is not critical.

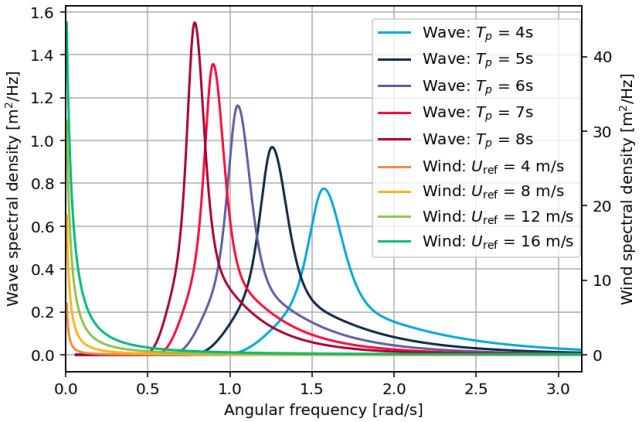

Figure 2.1: Spectral density plots for wind and wave conditions. Wave spectra are shown for various peak periods ($T_p = 4$–8 s), and wind spectra for different reference wind speeds ($U_{\text{ref}} = 4$–16 m/s). The significant wave height is $H_s = 1.0$ m and the turbulence intensity is TI $= 0.05$. Wave spectral density is scaled on the left axis, and wind spectral density on the right axis.

2.4. Aerodynamic and Hydrodynamic Theory

This section outlines the theoretical frameworks used to describe the excitation forces induced by environmental conditions. It begins with the principles of lift and drag, followed by the fundamentals of aerodynamic loading and its application to structures such as turbine blades. Subsequently, hydrodynamic theory is introduced, distinguishing between its application to slender structures, such as MP foundations, and large-volume bodies, such as the SSCV.

2.4.1. Lift and Drag

Lift and drag are the two primary components of fluid forces acting on a body immersed in a flow. Drag acts in the direction of the flow and results from the resistance of the fluid as it moves around the object. It depends primarily on the object's projected area and surface roughness. Lift acts perpendicular to the flow direction and arises from pressure differences across the object's surfaces. While lift is significant for streamlined or inclined bodies, such as airfoils, it is typically negligible for large volume bodies where flow separation dominates and drag becomes the prevailing force. (Orcina Ltd., 2024d)

2.4.2. Aerodynamic Theory

This subsection explains the aerodynamic theories used to mathematically express wind loads, with a focus on general aerodynamic principles and the aerodynamic forces acting on a turbine blade.

General aerodynamic force

A general equation for aerodynamic force is given in Equation 2.7. The aerodynamic coefficient is a dimensionless parameter that represents the complex interactions between the flow and the the object. It accounts for effects such as surface roughness, flow separation, Reynolds number dependence, and the shape and orientation of the object relative to the flow direction. In practice, the aerodynamic coefficient is typically determined through experimental data or computational fluid dynamics simulations, and its value can vary significantly with the angle of attack.

$$F_{\text{aero}} = \frac{1}{2}\rho_{\text{air}} V_{\text{w}}^2 AC \sin(\alpha) \tag{2.7}$$

where:

- F_{aero}: aerodynamic force,
- ρ_{air}: air density,
- V_{w}: wind speed,
- A: reference area,
- C: aerodynamic coefficient,
- α: angle of attack.

Aerodynamic force on a blade

As stated in Subsection 2.4.1, aerodynamic lift and drag effects are relevant for airfoils. A wind turbine rotor blade can be considered as a composition of multiple airfoil sections along its span, as depicted in Figure 2.2.

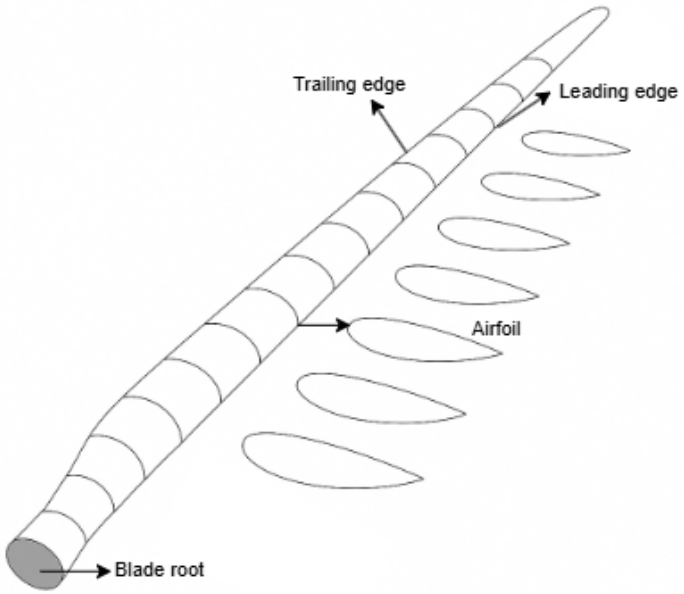

Figure 2.2: Schematic representation of a wind turbine blade and its two-dimensional cross-sections, known as airfoils.

For each airfoil type, tables are provided that give the lift and drag coefficients as functions of the angle of attack, which is defined as the angle between the airfoil chord line and the relative wind velocity. The lift and drag forces on each two-dimensional airfoil section can be calculated using Equation 2.8 and Equation 2.9. To determine the total aerodynamic load on the turbine blade, the distributed forces are integrated along the blade length, accounting for the local chord length of each segment.

$$l_i = C_{l_i} \cdot \frac{1}{2} \rho_{\text{air}} V_{\text{rel}}^2 \cdot c_i \tag{2.8}$$

$$d_i = C_{d_i} \cdot \frac{1}{2} \rho_{\text{air}} V_{\text{rel}}^2 \cdot c_i \tag{2.9}$$

where:

- l_i: lift force on the i-th segment or component,
- C_{l_i}: lift coefficient for the i-th component,
- d_i: drag force on the i-th segment or component,
- C_{d_i}: drag coefficient for the i-th component,
- ρ_{air}: air density,
- V_{rel}: relative wind speed,
- c_i: chord of the i-th cross-section.

The aerodynamic load on a rotating blade differs from that on a stationary blade due to the influence of rotation on the relative wind experienced by the blade. When the blade is stationary or being lifted, the relative wind velocity is simply equal to the incoming wind velocity ($V_{\text{rel}} = V_{\text{w}}$). The decomposition of lift and drag forces for a given angle of attack on a two-dimensional airfoil is illustrated in Figure 2.3.

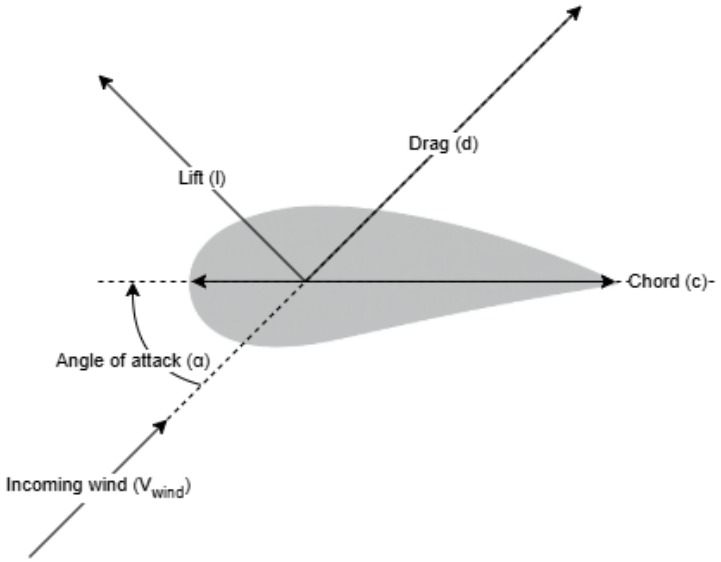

Figure 2.3: Lift and drag on a stationary airfoil.

A widely used approach to determine the wind velocity on a turbine blade is described by Hoerner (1985) and is commonly known as the cross-flow principle. According to this principle, the relative wind acting on the blade can be approximated as purely chordwise, allowing the spanwise component of the wind to be neglected. (Kroon, 2024).

2.4.3. Hydrodynamic Theory

This subsection explains the hydrodynamic theories used to mathematically express wave loads, with a focus on general hydrodynamic principles, the Morison equation, and potential flow theory.

General hydrodynamic loads

Hydrodynamic loading on offshore structures is typically classified based on the structure's size relative to the incident wave field. In this thesis, two distinct approaches are employed: one for the hydrodynamic loading on the MP and another for the SSCV.

For slender components with a small cross-sectional diameter compared to the wavelength, such as the MP foundation, viscous effects and flow separation are generally dominant. In these cases, the Morison equation is applied, as it accounts for both inertial and drag forces. For larger structures, such as the SSCV, the interaction with the incident wave field significantly alters the surrounding fluid motion. In this regime, diffraction and radiation effects become important and are modelled using potential flow theory.

Morison equation

Morison et al. (1950) described the force exerted by unbroken surface waves on a cylindrical structure, such as a pile extending from the seabed above the wave crest, using the Morison equation shown in Equation 2.10. This formulation is applicable when the wavelength is greater than five times the cross-sectional diameter of the structure and provides a means to estimate the hydrodynamic load on the object.

$$dF = \underbrace{C_D \frac{1}{2} \rho D \, dz \, |u| u}_{\text{Drag}} + \underbrace{\rho \frac{\pi D^2}{4} \, dz \, C_M \, \dot{u}}_{\text{Inertia}} \tag{2.10}$$

where:

- dF: differential force on the cylindrical element,
- C_D: drag coefficient,
- ρ: fluid density,
- D: diameter of the cylinder,
- dz: differential element length along the cylinder,
- u: fluid velocity,
- $\dot{u}$: fluid acceleration,
- C_M: inertia coefficient (C_M = 1 + C_a)
- C_a: added mass coefficient

In Equation 2.10, the first term represents the drag force, which is proportional to the square of the fluid velocity relative to the structure and accounts for viscous effects. The second term is the inertia force. The inertia coefficient accounts for the added mass effect arising from the acceleration of the fluid displaced by the structure, and includes the Froude–Krylov force, which is proportional to the undisturbed fluid acceleration and corresponds to the pressure exerted on the structure by the incident wave field (Orcina Ltd., 2024g).

Whether a structure is drag dominated or inertia dominated depends on which force contribution in the Morison equation is more significant. For members with a small cross-sectional area, the term $\frac{\pi D^2}{4}$ is much smaller than the diameter term D, resulting in a relatively small inertia component and a comparatively large drag component. This renders such members drag dominated. The hydrodynamic force in this case is non-linear, as it depends on the square of the relative fluid velocity.

Conversely, for members with a large diameter, the cross-sectional area becomes substantial relative to the diameter, causing the inertia force to dominate the total hydrodynamic loading. Here, the hydrodynamic loading is linear, since it depends linearly on the fluid acceleration.

Potential flow theory

Potential flow theory can be used to model wave–structure interactions for large-volume offshore structures such as an SSCV, where the presence of the body significantly disturbs the surrounding wave field. Potential flow theory is based on the assumptions of inviscid, incompressible, and irrotational

flow (Sheng et al., 2022). Under these assumptions, the fluid motion is described by a velocity potential function $\Phi(x,t)$, from which all wave-induced kinematic and dynamic quantities, such as surface elevation, velocity, and pressure, can be derived. This potential must satisfy the Laplace equation for the incompressible potential flow, which is shown in Equation 2.11 (Sheng et al., 2022).

$$\nabla^2\Phi = 0 \tag{2.11}$$

This potential flow problem can be solved by applying three boundary conditions: the no-penetration condition on the body surface, the condition of no flow through the seabed, and the linearised free surface boundary condition at the water surface. To simplify the solution, the velocity potential is expressed as ϕ, the complex amplitude of the potential function in the frequency domain. By invoking the principle of superposition, the total potential ϕ representing the wave–structure interaction is decomposed into the radiation potential ϕ_R, which accounts for the waves generated by the motion of the structure, and the diffraction potential ϕ_D, which describes the disturbance of the incoming wave field due to the presence of the structure. (Sheng et al., 2022)

In this thesis the potential flow theory is used in WAMIT, an existing software used to perform hydrodynamic analysis of the SSCV. Based on these hydrodynamic analysis and for standard loading conditions of the SSCV. Response amplitude operators (RAOs) are computed across a range of wave frequencies and directions.

These RAOs are frequency-domain transfer functions that describe how a floating structure, responds to regular wave excitation, accounting for the vessel geometry and loading condition. For a given wave frequency and direction, RAOs quantify the amplitude and phase of the vessel's response in six degrees of freedom relative to the amplitude of the incoming wave. These RAOs are used for the numeric model of the SSCV, which is described in Chapter 5.

2.5. Site Characteristics

The site characteristics considered in this study include a water depth of 30 metres and sandy seabed conditions. These parameters define the representative conditions at the fictional installation site.

Soil Model

A MP is designed based on specific soil conditions. The MP considered in this study is tailored to the soil parameters listed in Table 2.4, which correspond to dense sand and dense gravel (Arya et al., 1979). To ensure consistency with the design assumptions, the same soil conditions are adopted in this research.

Table 2.4: Soil parameters for the selected site in the Baltic Sea, based on internal experience at HMC.

Parameter	Symbol	Value	Unit
Shear modulus	G	140	MPa
Poisson's ratio	ν	0.4	–

The soil is modelled using the Elastic Halfspace Model, a fundamental concept in geotechnical engineering and soil mechanics for analysing stress and displacement in soils under external loads. This model assumes the soil to be elastic, homogeneous, and isotropic, with stress–strain behaviour characterised by two elastic constants: the shear modulus and Poisson's ratio. Using the parameters listed in Table 2.4 and the equations provided in Appendix A, the soil stiffnesses are determined. Figure 2.4 shows the resulting soil stiffnesses as a function of depth.

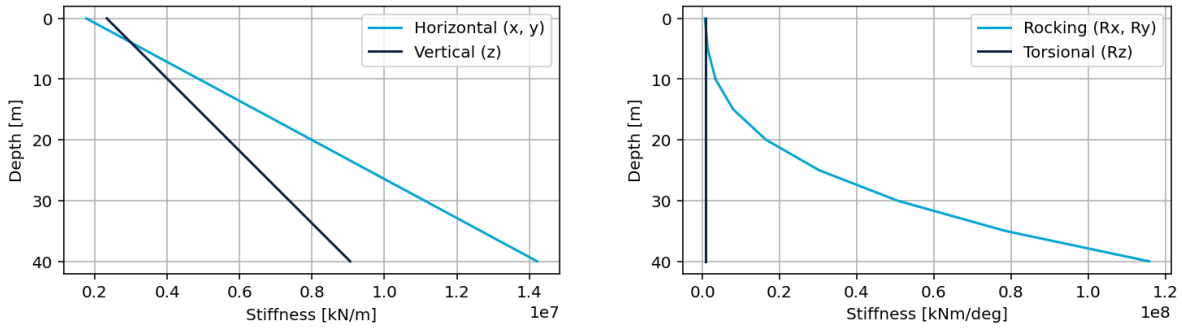

(a) Translational soil stiffness

(b) Rotational soil stiffness

Figure 2.4: Soil stiffness as a function of embedment depth for both translational and rotational degrees of freedom.

The soil damping is not determined individually as a function of depth, as is normally adapted in an elastic halfspace model. Instead, damping is incorporated using Rayleigh damping. Further details are provided in Chapter 4.

3

Operation Overview and Dynamic Modelling

This chapter provides an overview of the offshore single blade installation system, including the key components and procedures that define the operational context. The installation process is outlined step by step, with particular focus on the critical alignment phase. The numerical modelling approach adopted in this study is introduced, detailing the tools and simulation setup used to analyse system dynamics under realistic offshore conditions. Finally, all assumptions made prior to the numerical analysis are presented.

3.1. Description of the Single Blade Installation Operation

This section outlines the procedure for single blade installation, followed by a detailed examination of the specific phase that is the focus of this study. Finally, the key limiting criteria for the operation are discussed.

The procedure is described from the perspective of single blade installation, with the SSCV positioned at the installation site and all necessary components and equipment either on board or nearby on a Heavy Transport Vessel (HTV) or barge. The blades are transported in specially designed blade racks, which ensure safe handling and allow for efficient stacking to optimise deck space.

3.1.1. Installation Procedure

Wind turbine designs vary between manufacturers, each of whom provides specific installation procedures tailored to their technology (De Leeuw, 2019). In this thesis, a representative single-blade installation procedure is adopted, based on the description by Jiang et al. (2018). A simplified flowchart of the typical installation process is shown in Figure 3.1.

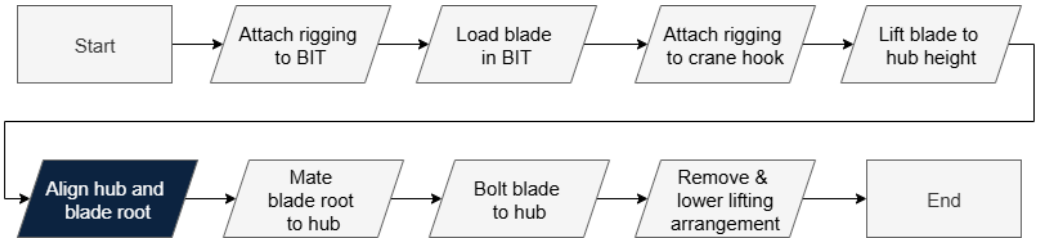

Figure 3.1: Flowchart of a typical single-blade installation.

The installation process begins with the lift-off phase, corresponding to steps 1 through 4. First, the rigging is connected to the Blade Installation Tool (BIT). The blade is then loaded into the BIT, followed

by attaching the rigging to the crane hook. Once the blade is securely fastened, it is lifted from the deck.

When the blade reaches hub height, the alignment phase begins. A typical visualisation of this stage is provided in Figure 3.2a. During this phase, the blade root is aligned with the hub to enable mating. Once the relative motion between the hub and the blade root falls within acceptable limits, manual alignment is carried out, typically by a technician located inside the turbine hub.

The mating phase, illustrated in steps 7 and 8, then commences. The guide pin mounted on the blade root, as schematically shown in Figure 3.2b, first enters the flange hole on the hub. Once mating is achieved, the blade is bolted to the hub. The BIT is subsequently detached and lowered to the deck, concluding the single blade installation operation. The procedure can then be repeated for the remaining blades.

(a) Side view of the alignment phase

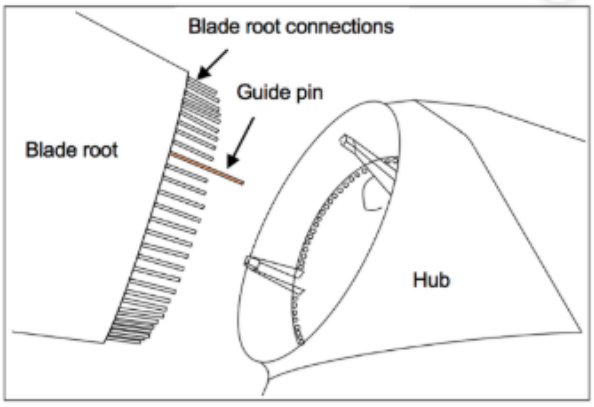

(b) Schematic representation of the blade root and hub prior to mating

Figure 3.2: Blade installation process: (a) Side view of the alignment phase, (b) Schematic representation of the blade root and hub before mating.

3.1.2. Alignment Phase

The alignment phase is a critical part of the single blade installation process. During this step, the root of the lifted blade must be aligned with the turbine hub to enable a successful mechanical connection. For the operation to proceed safely and be successful, the relative motion between the blade root and the hub must remain within predefined thresholds. The environmental conditions, such as wind and wave characteristics, under which these thresholds are expected to be satisfied, are assessed in advance. The installation is carried out only when these conditions are present and expected to remain stable throughout the procedure.

The decision to initiate installation is therefore directly dependent on the relative motion between the blade and the hub during the alignment phase. This makes the alignment phase a critical part of the operation. Accordingly, this research focuses specifically on the alignment phase and evaluates the conditions that enable safe alignment, in order to assess the overall feasibility and operational boundaries of offshore single blade installations.

In contrast to onshore operations, where a blade can be safely returned to its rack if the alignment phase is unsuccessful, offshore installations, particularly those involving floating vessels, pose greater challenges. During installation with a floating vessel, the blade rack moves with the deck, making it significantly more difficult to return the blade once it has been lifted. This scenario is therefore undesirable, underscoring the importance of accurately predicting the relative motion between the hub and blade root. Doing so enables a realistic assessment of the environmental conditions under which the alignment phase can be successfully completed for this installation method.

3.1.3. Limiting Criteria

The thresholds used to assess the relative motion between the blade root and the hub are specific to each turbine design or the installation tool employed, and are typically defined by the respective manufacturers. As this information is confidential, no standard limiting criteria are publicly available. A commonly cited constraint imposed by state-of-the-art lifting equipment is a maximum wind speed of approximately 8–12 m/s (Gaunaa et al., 2014). However, such general criteria do not explicitly account for other environmental or dynamic conditions and may exclude scenarios where installation could still be feasible. As a result, considerable time and financial resources have often been spent waiting for favourable low-wind conditions during the construction of offshore wind farms (Jiang et al., 2018).

In this research, the limiting criteria are defined based on the relative displacement between the hub and the blade root, a safety boundary, and a critical outcrossing rate, in line with the methodologies adopted by De Leeuw (2019), Jiang (2018), and Jiang et al. (2018).

The relative displacement between the centre point of the hub and the blade root is denoted as a time-dependent vector ($\vec{D}(t)$), whose magnitude ($\|\vec{D}(t)\|$) represents the instantaneous, zero-mean spatial separation between the two components. The feasibility of alignment is assessed by evaluating how often this relative displacement magnitude exceeds a specified safety boundary (R_{sb}). Each transition from within the safety region to outside it is considered an outcrossing. The outcrossing rate (ν) is defined as the number of such events per unit time. A lower outcrossing rate indicates more stable relative motion and a greater likelihood of successful alignment. The critical outcrossing rate (ν_{cr}) is defined as the maximum allowable outcrossing frequency for a given safety boundary. This threshold is also typically determined empirically, based on practical experience and operational constraints, and does not have a universally fixed value (Jiang, 2018).

The alignment phase is assumed to have a duration of 30 minutes, consistent with De Leeuw (2019) and Jiang (2018). However, the reported values for the safety boundary and the critical outcrossing rate vary across the literature. De Leeuw (2019) specifies a safety boundary of 0.2 m and a critical outcrossing rate of $1.7 \cdot 10^{-2}$ Hz, corresponding to approximately 30 outcrossings during a 30-minute operation. In contrast, Jiang (2018) adopts a more conservative critical outcrossing rate of $5.5 \cdot 10^{-3}$ Hz, equating to around 10 outcrossings within the same duration, though a fixed safety boundary is not defined in that study. Similarly, Jiang et al. (2018) applies the same critical outcrossing rate of $5.5 \cdot 10^{-3}$ Hz and defines the safety boundary as equal to the blade root diameter, which in that case is 3.54 m. It is noteworthy that this study also introduces a much more stringent safety boundary of 4 mm for the subsequent mating phase, illustrating the variation in how these parameters are defined across different studies.

The limiting criteria are summarised in Table 3.1. The limits defined by De Leeuw (2019) are adopted as the primary criteria in this research. However, the alternative criteria from Jiang (2018) and Jiang et al. (2018) are also considered in the operability assessment presented in Chapter 8.

Table 3.1: Limiting criteria for a 30-minute single blade installation alignment phase as reported in literature.

Reference	Safety boundary (R_{sb})	Critical outcrossing rate (ν_{cr})
De Leeuw (2019)	0.2 m	$1.7 \cdot 10^{-2}$ Hz
Jiang (2018)	–	$5.5 \cdot 10^{-3}$ Hz
Jiang et al. (2018)	3.54 m	$5.5 \cdot 10^{-3}$ Hz

To aid interpretation, an example of the relative displacement is illustrated in Figure 3.3. The grey sphere represents the safety boundary. Instances where the relative motion exceeds this boundary are shown in red, and each outcrossing event is marked with a red cross. The total number of outcrossings in the specific simulation is indicated, and the corresponding outcrossing rate is determined, quantifying how frequently the safety limit is exceeded over time.

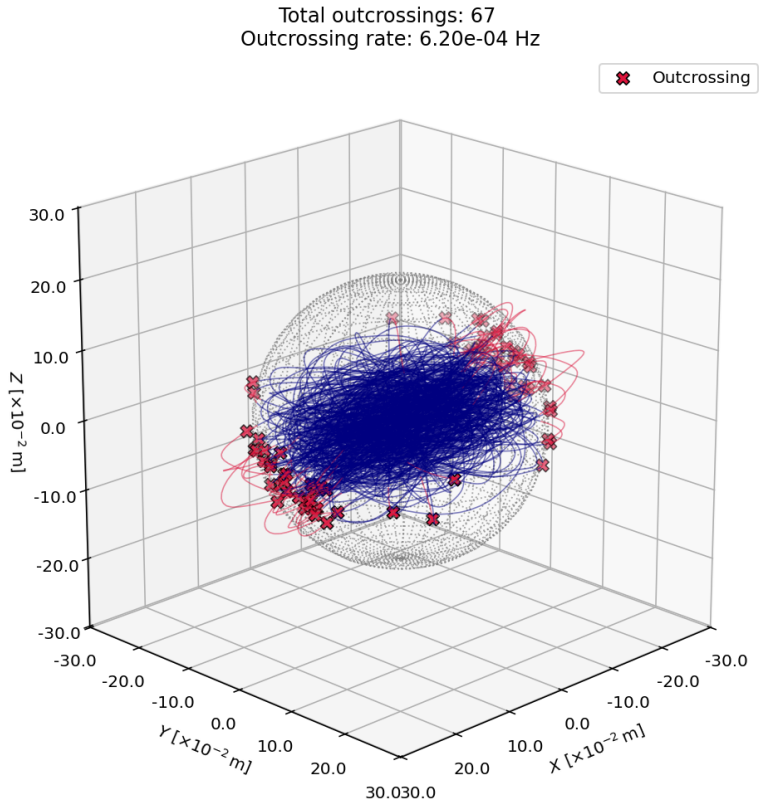

Figure 3.3: Example of three-dimensional relative displacement between the blade root and the hub centre. The grey dotted wireframe represents the safety boundary. Instances where the relative motion exceeds the boundary are shown in red, and outcrossing events are marked with red crosses.

3.2. Installation System and Conventions

This section provides an overview of all components involved in the installation system and defines the local coordinate systems and conventions associated with each element.

3.2.1. Offshore Wind Turbine

The turbine investigated in this thesis is the IEA Wind 15 MW Offshore Reference Wind Turbine (Gaertner et al., 2020), a 15-megawatt offshore wind turbine with a fixed-bottom MP support structure. The OWT consists of a tower, nacelle, hub, and rotor, collectively referred to as the RNA. The MP is divided into three segments: the embedded section located below the seabed, the submerged section within the water column, and the transition piece (TP), which is positioned atop the submerged MP and connects it to the turbine tower. All key parameters relevant to this turbine are listed in Table 3.2, and a visualisation of the turbine is shown in Figure 3.4a.

Table 3.2: Specifications of the IEA 15 MW reference wind turbine (Gaertner et al., 2020).

Parameter	Value	Unit
Airfoil series	FFA-W3	-
Hub height	150	m
RNA mass	1,017	t
TP piece height	15	m
MP embedment depth	45	m
MP base diameter	10	m
Tower mass	860	t
MP mass	1,318	t

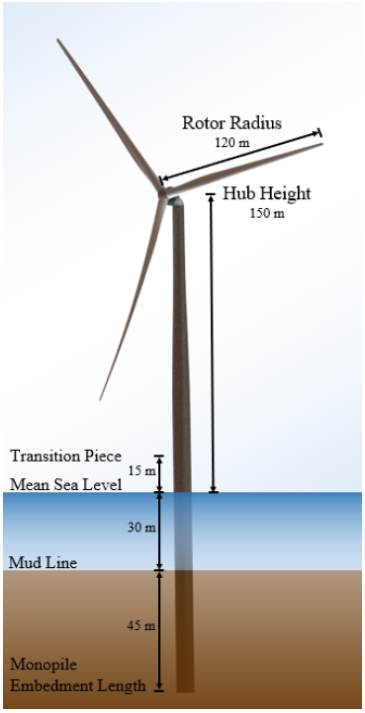

(a) The IEA Wind 15-MW reference wind turbine (Gaertner et al., 2020).

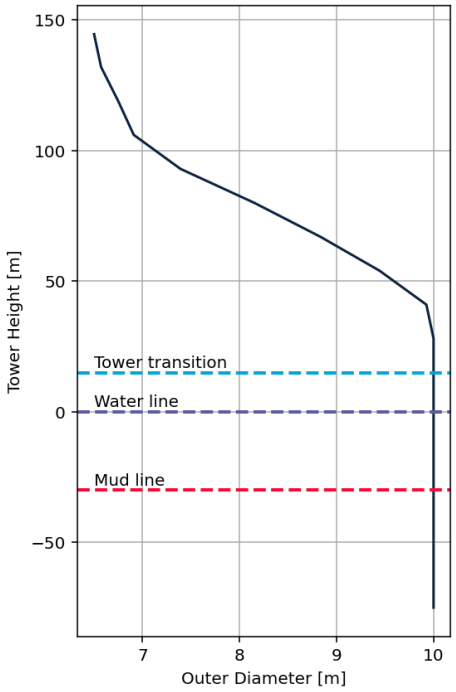

(b) Outer diameter over height as described in Gaertner et al. (2020).

Figure 3.4: Overview and structural dimensions of the IEA Wind 15-MW reference turbine.

Tower and Monopile

The tower and MP serve as the primary support structure of the OWT, anchoring the turbine and transferring loads from the blades and nacelle to the foundation. Their design is primarily governed by the requirement that the first tower–MP eigenfrequency remains between the 1P and 3P blade passing frequency ranges across all wind speeds (Gaertner et al., 2020), placing the turbine in the soft–stiff design regime.

The MP maintains a constant outer diameter along its entire length, whereas the tower exhibits a tapering profile, with its outer diameter varying by more than 3 metres from base to top. The variation in outer diameter along the full height of the support structure is shown in Figure 3.4b.

Nacelle Assembly

The nacelle assembly, located at the top of the tower, consists of the nacelle and the hub. Its primary function is to connect the blades to the main support structure and to house the generator that produces electrical energy. This assembly, illustrated in Figure 3.5, has a total mass of 820 t.

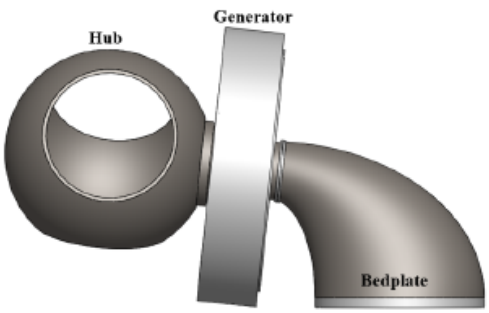

Figure 3.5: CAD model of the nacelle layout of the 15-MW direct-drive wind turbine (Gaertner et al., 2020)

Rotor blade

The rotor blades of the IEA Wind 15-MW reference turbine are based on the DTU FFA-W3 series of airfoils, which have well-documented aerodynamic characteristics and were introduced in the DTU 10-MW offshore reference turbine (Gaertner et al., 2020). These airfoils are distributed along the full 117-meter blade span. Along the blade span, the lift and drag distributions vary according to the local airfoil profile, chord length, and angle of attack. An overview of the blade's geometric, mass, and modal properties is provided in Table 3.3.

Table 3.3: IEA 15-MW blade properties (Gaertner et al., 2020)

Parameter	Value	Unit
Blade length	117	m
Root diameter	5.20	m
Root cylinder length	2.34	m
Max chord	5.77	m
Max chord spanwise position	27.2	m
Tip prebend	4.00	m
Precone	4.00	deg
Blade mass	65.25	t
Blade centre of mass	26.8	m
First flapwise natural frequency	0.555	Hz
First edge-wise natural frequency	0.642	Hz

The pitch of a turbine blade refers to the rotation of the entire blade around its spanwise axis. By adjusting the pitch angle, the blade's angle of attack can be actively controlled to regulate aerodynamic loads. Figure 3.6 illustrates a typical variation of lift and drag coefficients as a function of angle of attack for a specific airfoil located 75 metres from the blade root. This distance, measured along the spanwise direction, is also referred to as the radius. The airfoil at this radius corresponds to airfoil number 23 of the DTU FFA-W3 series.

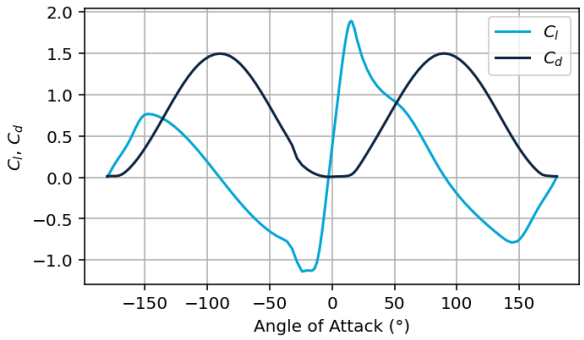

Figure 3.6: Aerodynamic coefficients as a function of angle of attack for an airfoil located at a radius of 75 m along the blade span.

As shown previously in Figure 2.3, the angle of attack is defined as the angle between the chord line of the airfoil and the direction of the incoming wind. For a horizontally incoming wind and a stationary or lifted blade, the relative wind velocity is equal to the incoming wind velocity. Consequently, the angle of attack is equal to the pitch angle of the blade, as illustrated in Figure 3.7.

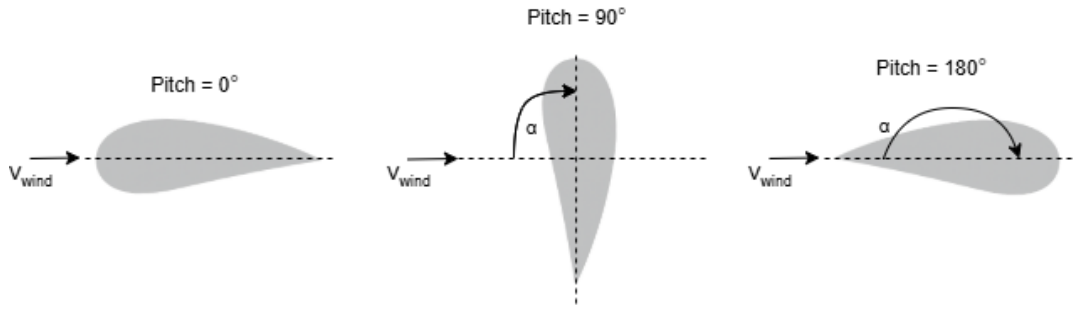

Figure 3.7: Definition of blade pitch: 0 degrees corresponds to feathered (leading edge facing into the wind), 90 degrees to stalled, and 180 degrees to feathered (trailing edge facing into the wind).

At a pitch angle of $0°$, corresponding to an angle of attack of zero (left in Figure 3.7), the blade is in the feathered position, with the leading edge facing into the wind. In this configuration, both the lift and drag coefficients are minimal along the entire blade span. Figure 3.6 illustrates a typical variation of these coefficients for a representative airfoil on the blade. While the exact coefficient values differ between airfoils, their general trends, i.e., the shape of the curves, are similar across most of the blade. An exception occurs near the root, where the blade cross-section is circular rather than airfoil-shaped. At an angle of attack of zero degrees, the coefficients are clearly minimal. However, the figure also shows that small deviations from this angle of attack can cause sharp increases in aerodynamic loads due to the steep gradients of the lift and drag curves.

For the opposite feathered position, where the trailing edge faces into the wind and the angle of attack approaches $180°$ (or $-180°$), as shown on the right in Figure 3.7, the aerodynamic coefficients also remain close to zero, as can be seen in Figure 3.6. In this configuration, the blade is effectively feathered in reverse, and small variations in the angle of attack do not result in such abrupt changes in aerodynamic loading when compared to the configuration at a pitch angle of $0°$.

At a pitch angle near $90°$, the airfoil faces the wind broadside, resulting in a stalled configuration. This position generates high drag and low lift and is generally more stable with respect to variations in pitch or angle of attack. A similar aerodynamic response is observed at a pitch angle near $270°$, where the coefficients exhibit comparable values, as shown in Figure 3.6, leading to similar dynamic behaviour. The choice of blade pitch during installation depends on the desired aerodynamic load characteristics.

The twist of a wind turbine blade refers to the gradual change in orientation of the airfoil sections along the blade span. This geometric adaptation is designed to compensate for the variation in relative wind speed from root to tip that arises during rotation in normal operation. However, when the blade is stationary and exposed only to the incoming wind, this twist prevents all airfoil sections from being uniformly pitched. As a result, the angle of attack is governed not by the blade pitch alone for all airfoils, but by the local twist of the airfoil. The blade of the IEA Wind 15 MW Offshore Reference Turbine exhibits a twist distribution ranging from approximately $+13.31°$ at the blade root to $-3.21°$ near the tip (Gaertner et al., 2020).

The overall angle of attack for the stationary blades examined in this thesis is therefore defined by Equation 3.1.

$$\alpha(r) = \theta_{\text{pitch}} - \theta_{\text{twist}}(r) \tag{3.1}$$

where:

- $\alpha(r)$ is the angle of attack at radius r,
- θ_{pitch} is the blade pitch angle,
- $\theta_{\text{twist}}(r)$ is the local twist angle at radius r.

Lastly, the blade has a significant prebend of 4 m, beginning at the root and curving away from the tower during operation. This design mitigates the risk of tower-blade interaction and satisfies clearance requirements, thereby enabling the use of a large blade radius while maintaining safe operational margins. However, the resulting curvature introduces geometric complexity, which complicates blade handling and transport aboard the vessel.

Conventions

The conventions, key elevations, and primary components of the 15 MW wind turbine are illustrated in the system schematization shown in Figure 3.8. The local coordinate conventions of the turbine blade are depicted in Figure 3.9, where pitch is defined as the rotation about the local x-axis.

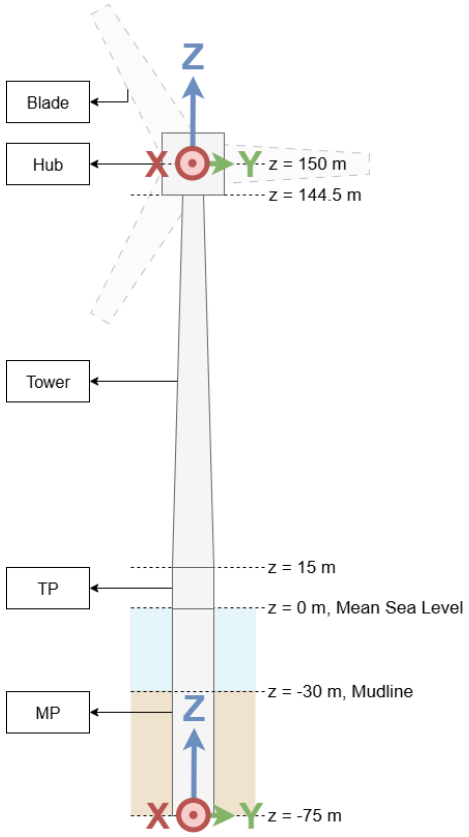

Figure 3.8: Schematisation of the offshore wind turbine with indicated local coordinate axes.

Figure 3.9: Schematisation of the offshore wind turbine blade with indicated local coordinate axes.

3.2.2. SSCV

The SSCV considered in this thesis is the *Thialf*, a dual-crane SSCV equipped with dynamic positioning (DP) capabilities to maintain station during installation operations. Its key characteristics and relevant operational details are presented in the following subsections.

Vessel

The Thialf is an SSCV built in 1985 and operated by HMC. The vessel comprises two pontoons and eight columns, and is equipped with two cranes capable of a combined lifting capacity of up to 14,200 mt, as illustrated in Figure 3.10.

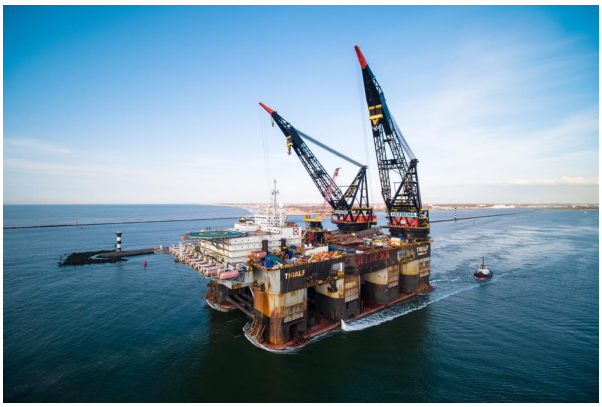

Figure 3.10: Semi-submersible crane vessel Thialf (Heerema Marine Contractors, 2024).

The SSCV can be ballasted to adjust its draught, allowing it to adapt to operational requirements. Selecting an appropriate draught involves balancing water depth constraints with the required stability and deck elevation. Increasing draught alters the vessel's submerged geometry and raises its displacement. As more of the SSCV is submerged, the centre of buoyancy shifts upward relative to the centre of gravity, enhancing the vessel's resistance to tilting. This results in increased initial stability and stronger restoring forces when the vessel is inclined. However, this also shortens the natural roll period, which can cause the vessel to respond more quickly and abruptly to wave-induced motions. As a result, while a deeper draught improves stability, it can also amplify dynamic responses in certain sea states. In addition, a greater draught places a larger portion of the structure in deeper water, where wave-induced velocities and pressures are lower, leading to a reduction in the net wave excitation forces acting on the hull.

For this study, the blade must be installed at an elevation of approximately 150 m above sea level. To achieve this height, while also accommodating the necessary clearance for the lifting arrangement, an initial draught of 16.6 m is selected. Additionally, the lifting point on the whip hoist of the crane is chosen for the installation operation.

This draught, however, introduces certain complexities. As illustrated in Figure 3.11b, at a draught of 16.6 m, the waterline lies approximately 3 m above the pontoons. At this level, the pontoons remain submerged, but under severe wave conditions, water may wash over their surface, potentially inducing complex slamming loads and non-linear hydrodynamic forces. In this study, the wave conditions at the fictional site are mild ($H_s \leq 3\,\text{m}$), such that the lower pontoons remain fully submerged at all times, thereby avoiding the associated hydrodynamic complications.

Cranes

The cranes on the SSCV can be configured by adjusting two angles: the slew angle and the boom angle. For this thesis, commonly used values are selected: 20 degrees for the slew angle and 78.5 degrees for the boom angle. This combination results in a sufficient whip height. Together with the selected draught, the configuration provides a crane tip height of 174.5 m above sea level, leaving approximately 24.5 m for the lifting arrangement. The configuration used is shown in Figure 3.11a and Figure 3.11b, and an overview of the main properties of the SSCV is presented in Table 3.4.

Table 3.4: Main parameters of the semi-submersible crane vessel Thialf.

Parameter	Value	Unit
Length	201.6	m
Breadth	88.4	m
Operational draught	16.6	m
Slew angle	20	deg
Boom angle	78.5	deg
Whip height	174.5	m

Dynamic Positioning

The SSCV is equipped with a dynamic positioning (DP) system, which maintains the vessel's position and heading without the use of anchors or mooring lines. The system incorporates various sensors to measure parameters such as position, heading, vessel motion, wind, and current. Based on these inputs, control algorithms compute the required thrust, which is then applied through the vessel's thrusters and propellers to counteract environmental forces. The DP system compensates for nonlinear, slowly varying forces induced by second-order environmental effects, including steady current forces, mean wave drift loads, and wind forces. It does not mitigate first-order induced motions, which are typically linear and excited around wave frequency. .

Conventions

The most relevant conventions, elevations, and reference directions are illustrated in Figure 3.11, with the top view shown in Figure 3.11a and the side view in Figure 3.11b.

The dynamic motions of a vessel are described in terms of six degrees of freedom, comprising translational and rotational movements along and about the global axes. Translation along the x-, y-, and z-axes is referred to as surge, sway, and heave, respectively. Rotation about the x-, y-, and z-axes is referred to as roll, pitch, and yaw, respectively. The static rotational displacements of a vessel also follow specific terminology. Three commonly referenced vessel orientation angles are heel, trim, and heading, which are typically expressed in degrees. Heel refers to the roll of the vessel, trim describes the pitch, and heading corresponds to the yaw.

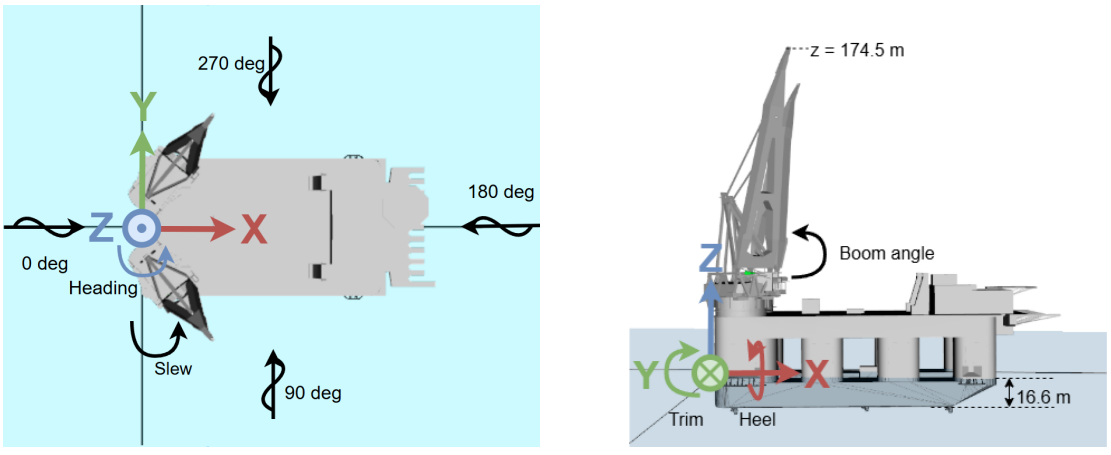

(a) Top view

(b) Side view

Figure 3.11: Top and side views of the semi-submersible crane vessel Thialf with indicated local coordinate axes: (a) top view, (b) side view.

3.2.3. Installation Equipment

The lifting arrangement refers to the complete configuration between the blade and the crane tip, including all related equipment. A classic lifting configuration typically consists of hoist wires, a crane block, rigging, a BIT, also known as a blade yoke, and tuggers. A schematic representation of the lifting configuration is given in Figure 3.12. The properties of the lifting arrangement are thereafter listed in Table 3.5.

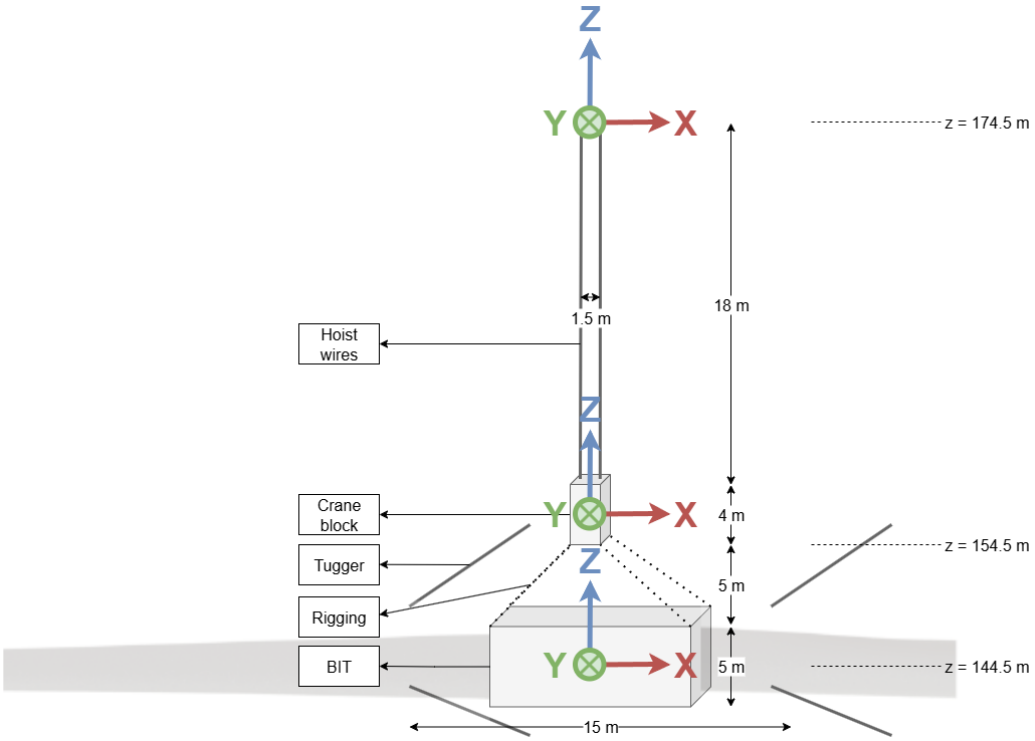

Figure 3.12: Schematic representation of the lifting configuration with indicated components and local coordinate axes.

Table 3.5: Properties of the lifting arrangement used in the installation configuration.

Parameter	Value	Unit
Crane block mass	29.2	t
Hoist wire stiffness	$10 \cdot 10^6$	kN
BIT mass	100	t
Linear tugger stiffness	100	kN/m
WLL tuggers	20	t
Pretension tuggers	10	t

Crane Block and Hoist Wires

From the lifting point at the crane tip, a crane block is suspended using hoist wires. These wires collectively form the reeving system, which runs back and forth between sheaves. Through this configuration, the crane block is connected multiple times to the lifting point, thereby increasing the overall lifting stiffness (Bastiaanssen, 2020).

The hoist wires and crane block set-up adopted in this study corresponds to the classical arrangement of the SSCV. The crane block has a self-weight of 29.2 t. The axial stiffness of the hoist wire is set to 10×10^6 kN. This high value reflects the assumption that elastic deformation of the wire has a negligible effect on the system's behaviour during installation.

Blade Installation Tool

The BIT is used to lift and protect the blade from damaging. The BIT is blade specific and often purpose build for one particular blade. The BIT attaches at the blades centre of mass. The BIT is attached to the blade while located in the blade rack, whereafter the blade can be lifted of the deck.

A wide range of BITs is available on the market, with variations depending on the blade type and the orientation used during installation, which can be horizontal, vertical, or oblique. Some BITs are equipped with active gyration systems that help compensate for blade motions during installation; however, such advanced systems are typically significantly heavier. BITs designed for larger blades are also inherently heavier due to increased structural demands. For example, the Blade Eagle II by Liftra is an advanced remote controlled blade yoke (Liftra, 2025). It can handle blades up to 107 m in length and weighs approximately 160 t (Fenger, 2019). In contrast, the original Blade Eagle is designed for blades up to 73.5 m and weighs around 55 t (Fenger, 2019). These examples highlight the variation in BIT design and weight. A specific BIT can be selected based on blade size, installation method, and operational requirements. In this study, a BIT mass of 100 t is assumed.

Rigging

Rigging is used to connect the BIT to the crane block. A general blade-lifting configuration, including the rigging, is shown in Figure 3.13. In this study, the clearance between the BIT and the crane block, defining the required rigging height, is assumed to be 5 m.

Figure 3.13: Photograph of a turbine blade during lifting. Adapted from Airpes (2025).

Tuggers

Tuggers are auxiliary winches used to control the orientation and position of wind turbine blades during installation. The tugger lines are assumed to maintain constant lengths, while allowing for varying tension to stabilize the blade.

Whenever a tugger line goes slack, snap loads may occur upon re-tensioning. To prevent such snap loads, the tugger lines are pre-tensioned. To allow for additional tension build-up due to environmental excitations, the pre-tension is set to half of the maximum allowable tension of the tuggers, defined by the Working Load Limit (WLL). The WLL of the tuggers is assumed to be 20 t, resulting in a pre-tension of 10 t. The total tension in the tuggers during operation thus consists of the pre-tension and the tension induced by the dynamic behaviour of the system. The tugger lines are further assumed to have a linear stiffness of 100 kN/m.

In practice, control systems are employed to provide damping by continuously adjusting the tugger lines during operation. This non-linear behaviour is difficult to capture in a numerical model. To approximate the practical response, a non-linear damping profile is applied to the tuggers in the simulation.

Two different non-linear damping profiles are considered in this study, which are shown in Figure 3.14. These profiles are derived from operational experience within HMC. In Profile 1, the winch reaches full load at a speed of 10 m/min (0.167 m/s), corresponding to a tension of 80 kN. In Profile 2, the winch operates at half load, reaching a speed of 20 m/min (0.333 m/s) with a corresponding tension of 40 kN. Both profiles are evaluated in the analysis presented in this thesis.

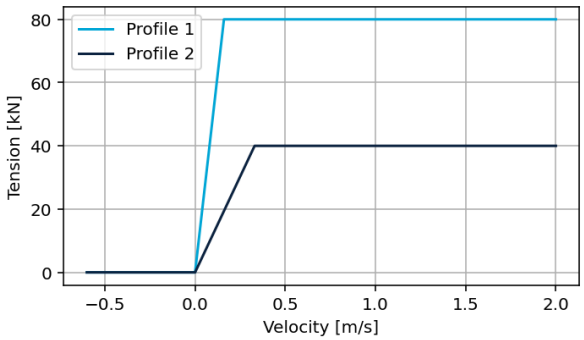

Figure 3.14: Non-linear damping profiles applied to the tugger lines to approximate the non-linear damping behaviour observed in practice.

3.3. Numerical Modelling of the Installation Operation

Numerical modelling is employed to simulate the dynamic behaviour of complex systems by discretising the governing equations and applying suitable numerical methods. This involves representing the system mathematically as a set of coupled, independent objects.In this study, numerical simulations are employed to analyse the dynamic behaviour of the hub and blade root during the installation operation.

3.3.1. Static and Dynamic Analysis

A numerical model supports various types of analyses. In this study, two primary approaches are applied: static analysis and dynamic analysis. Static analysis evaluates the system at a single point in time, without accounting for its temporal evolution. In contrast, dynamic analysis captures the time-dependent behaviour of the system.

Static analysis is primarily used to perform a modal analysis, which provides insight into the system's natural frequencies and mode shapes. Together, these approaches enable a comprehensive evaluation of the system's characteristics and dynamic response. Details of each analysis method are presented in the following subsections.

3.3.2. Modal Analysis

A modal analysis calculates the undamped natural modes of a system, each associated with a specific natural frequency and corresponding mode shape. In a continuous system, where the number of degrees of freedom is infinite, there are likewise infinitely many natural modes. To make this suitable for numerical computation, the system must be discretised, resulting in a finite number of degrees of freedom and a finite set of natural frequencies.

Discretisation involves representing the continuous system with a finite number of elements. For example, a continuous line can be modelled using a series of nodes and segments. A node represents a discrete mass point with associated degrees of freedom, and a segment connects two nodes while capturing the structural properties between them. A finer discretisation, achieved by increasing the number of nodes and segments, leads to a more accurate representation of the continuous system.

For a discretised system, the undamped equation of motion is expressed in matrix form as shown in Equation 3.2. Assuming a harmonic solution, the displacement vector $\mathbf{x}$ can be represented as in Equation 3.3. Differentiating Equation 3.3 twice with respect to time yields Equation 3.4. Substituting this result into Equation 3.2 leads to the eigenvalue problem given in Equation 3.5. This formulation assumes a linear, time-invariant system undergoing free vibration, implying that no external forces are acting on the structure. (Orcina Ltd., 2024e)

$$\mathbf{M}\ddot{\mathbf{x}} = -\mathbf{K}\mathbf{x} \tag{3.2}$$

$$\mathbf{x} = \mathbf{a}\sin(\omega t) \tag{3.3}$$

$$\ddot{\mathbf{x}} = -\omega^2 \, \mathbf{a} \, \sin(\omega t) = -\omega^2 \, \mathbf{x} \tag{3.4}$$

$$\omega^2 \mathbf{M}\mathbf{x} = \mathbf{K}\mathbf{x} \tag{3.5}$$

The natural modes obtained from the discretised model are generally close to those of the true continuous system. As the discretisation becomes finer, meaning that more elements are used to represent the structure, the agreement between the discrete and continuous modes improves. However, for any fixed level of discretisation, the accuracy is not uniform across all modes. The lower modes tend to be significantly more accurate, while the higher modes become progressively less reliable. This is because the higher modes correspond to oscillations with shorter wavelengths, which may be of the same order of magnitude as the segment length used in the discretisation. In such cases, the numerical model may not capture the physical behaviour accurately, and the highest modes often lose physical relevance. (Orcina Ltd., 2024e)

As stated previously, the installation phase considered in this thesis is the alignment phase. During alignment, the blade root and the hub are not in contact but remain in close proximity. Since they are not connected, the installation system can be considered as two separate subsystems for the purpose of modal analysis: the bottom-fixed OWT and the SSCV with the suspended blade. These individual modal analyses are presented in Chapter 4 and Chapter 5 respectively. The coupled model, representing the mating phase, is not included in the scope of this research.

3.3.3. Frequency and Time Domain Analysis

For the dynamic analysis of the system, two different approaches can be considered: the frequency domain and the time domain. In the frequency domain approach, linear transfer functions are derived for both the system and the wave input, which are then used to perform the dynamic analysis. In contrast, the time domain approach computes the dynamic behaviour by evaluating mass, damping, stiffness, external loading, and other effects at each discrete time step, while accounting for the time-varying nature of the system.

Although both methods offer a representation of dynamic behaviour, the frequency domain approach relies on the assumption of linearity and stationarity. As a result, it is limited to linear springs and dampers, stationary environmental conditions, first-order wave loads, and cannot accommodate arbitrary external forces. These simplifications significantly restrict its applicability. On the other hand, the time domain method does not rely on such assumptions. It allows for the evaluation of forces at each time step, supports non-linear spring and damping behaviour, enables property variation over time, and accommodates the use of conditional logic and non-linear external loading. Any form of physical behaviour can be represented, making the method highly flexible and general. However, this also makes it computationally demanding and therefore time-consuming.

While frequency domain analysis is often preferred for its computational efficiency and its ability to provide quick insight into linear system behaviour, it is not suitable for systems that exhibit non-linear dynamics. Given the inherently non-linear nature of turbulent wind fields, frequency domain methods are not capable of providing the required fidelity.

For this reason, this research employs time domain simulation to achieve an accurate representation of the system's dynamic response. Despite its higher computational cost and the increased complexity of pre- and post processing, the time domain approach enables the inclusion of all relevant non-linearities and time-dependent behaviours. This makes it the most appropriate choice for capturing the full range of dynamic phenomena influencing the installation.

During time-domain dynamic analysis, the global equation of motion shown in Equation 3.6 is solved at each time step for the defined system.

$$M(p,a) + C(p,v) + K(p) = F(p,v,t) \tag{3.6}$$

where:

- $M(p,a)$: system inertia load,
- $C(p,v)$: damping load,
- $K(p)$: stiffness load,
- $F(p,v,t)$: external load,
- p: position vector,
- v: velocity vector,
- a: acceleration vector,
- t: simulation time.

Even though time-domain simulations are employed, it remains valuable to examine how the dynamic responses vary with frequency. In this study, spectral density analysis is used to identify which frequency components contribute most significantly to the overall dynamic response, and to assess how different system parameters or configurations influence the distribution of energy across the frequency spectrum. When the spectral response is derived from a fully non-linear time-domain simulation, the effects of system non-linearities are inherently captured in the resulting frequency-domain representation. This enables a more realistic and accurate evaluation of the system's behaviour. The spectral density is obtained by transforming the time-domain simulation results into the frequency domain using a fast Fourier transform (FFT), which yields the power spectral density P_i at each frequency f_i (Orcina Ltd., 2024h).

3.3.4. Accuracy, Stability, and Computational Time

The accuracy of dynamic simulations is primarily influenced by the spatial and temporal discretisation. As with finer discretisations in general, finer meshes and smaller time steps typically yield improved accuracy, but at the expense of increased computational cost. Stability, on the other hand, is largely determined by the choice of time integration scheme. In this thesis, both explicit and implicit time integration methods are considered for time-domain dynamic simulations.

Explicit integration is conditionally stable, requiring the time step to remain below a critical threshold, typically a fraction of the system's smallest natural period, to ensure numerical stability (Orcina Ltd., 2024c). This often necessitates very small time steps, which increases computational cost. Moreover, explicit schemes require all dynamic terms to be expressed in the time domain. When the system includes frequency-dependent effects, such as a vessel's added mass varying with frequency, these must be converted from the frequency domain to the time domain using convolution integrals. This conversion introduces additional computational complexity. Numerical damping may also arise unpredictably as a by-product of the time discretization, potentially distorting the dynamic response. The explicit formulation is shown in Equation 3.7, where all terms on the right-hand side are known from the previous time step, allowing direct computation of the new state.

$$y(t_1) = y(t_0) + \Delta t \cdot f(t_0, y(t_0)) \tag{3.7}$$

Implicit integration are unconditionally stable and allow the use of larger time steps, which reduces the total number of time steps required for a simulation. Furthermore, implicit schemes are more suitable for incorporating frequency-dependent effects without the need for convolution integrals. They also introduce numerical damping naturally, which helps suppress artificial high-frequency responses that can arise from spurious numerical modes in finite element formulations (Orcina Ltd., 2024a). These features lead to greater numerical stability and improved accuracy in dynamic simulations, particularly in complex systems. The implicit formulation is shown in Equation 3.8, where the unknowns appear on both sides of the equation. This requires solving the system iteratively at each time step, but also enables improved stability and flexibility.

$$y(t_1) = y(t_0) + \Delta t \cdot f(t_1, y(t_1)) \tag{3.8}$$

Implicit time integration is employed for the numerical simulations in this study. Its ability to accommodate larger time steps, incorporate frequency-dependent components directly, and maintain numerical stability makes it the preferred approach for efficient and reliable dynamic analysis.

The implicit integration scheme can be configured using parameters such as tolerance, time step, and the maximum number of iterations. Selecting appropriate values for these parameters requires balancing accuracy and computational efficiency. As previously noted, coarse models reduce computational cost but may lack sufficient accuracy, while fine models improve accuracy at the expense of higher computational demand and may introduce non-physical behaviour in higher modes. Therefore, a sensitivity study on the integration parameters is necessary to validate the simulation results and ensure that the chosen configuration does not compromise accuracy.

3.3.5. Simulation Length

The total duration of each numerical time-domain simulation is set to 2500 seconds, comprising multiple distinct phases. The initial 100 s are used for a steady build-up of the excitation conditions, ensuring a smooth transition into the dynamic behaviour of the system. This is followed by a transient period of 600 seconds, allowing the system's initial response to stabilize. The final 1800 seconds correspond to the effective simulation phase, representing the typical 30 minute duration of a single blade installation operation.

The adequacy of this simulation length is verified by performing multiple runs using different random seeds. If the statistical results, such as mean and standard deviation remain consistent across these seeds, the simulation time is considered sufficiently long. The duration of the transient phase is guided by the system's decay characteristics and is chosen to ensure that the initial conditions no longer influence the steady-state response.

3.3.6. Software

The numerical simulations in this study are performed using OrcaFlex, a software widely adopted in the offshore industry and by HMC, selected here for its advanced capabilities in dynamic analysis. Details on the implementation and features of OrcaFlex are provided in the following sections. Additionally, TurbSim is used to generate turbulent wind fields. Each of these tools is described in more detail below.

OrcaFlex

OrcaFlex is a dynamic analysis software package widely used for modelling offshore systems. It supports modal analysis, as well as both time-domain and frequency-domain simulations. To analyse a system in OrcaFlex, a mathematical representation of the physical system is constructed. This model includes both the surrounding marine environment and a coupled set of independently defined objects. The available model object types in OrcaFlex are summarised in Table 3.6.

In OrcaFlex, each object can be defined as free, fixed, anchored, or connected to another object. Most objects have a single connection point, except for lines, which have two, one at each end. An anchored object is connected to a point fixed in space, defined relative to the global coordinate system. A fixed object is fully constrained in both position and orientation, and does not respond to any forces or motions. A free object is completely unconstrained, and can move and rotate in response to environmental loads and system interactions. When an object is connected to another, it becomes a child of the parent object and inherits its motion, including translations and rotations, as determined by the simulation. At each time step, OrcaFlex numerically solves the coupled equations of motion for the entire system, accounting for interactions between all connected objects.

Each OrcaFlex model can be pre-processed and post-processed using Python. During pre-processing, model variables are assigned values, after which a `.dat` file is generated. This file serves as input to the OrcaFlex simulation engine, which can run static or dynamic simulations, producing a `.sim` file containing the results.

In the post-processing phase, the `.sim` file is loaded to extract, analyse, and visualise the simulation output. This automated workflow is employed in this thesis to ensure consistency in simulation setup and improve overall efficiency.

Table 3.6: Overview of object types available in OrcaFlex (Orcina Ltd., 2024f)

Object Type	Description
Vessels	Rigid bodies typically used to simulate floating platforms, barges, or ships. Motion can be user-defined through time histories, RAOs, load RAOs, or QTFs.
3D Buoys	Simplified point-mass objects with three translational degrees of freedom.
6D Buoys	Rigid bodies with six degrees of freedom, with both translational and rotational motion.
Lines	Flexible elements used to represent cables, moorings, and pipes. Lines may have variable properties along their length and have connections at each end.
Links	Massless connectors between two objects. Includes tethers (tension-only) and spring/damper links (tension and compression, possibly nonlinear).
Winches	Mechanisms for controlling connection length between objects using winch wires. Operates in either length-control or tension-control mode.
Shapes	Non-mass objects used to represent geometry and interaction. Elastic solids act as physical barriers, trapped water shapes simulate enclosed water volumes, and drawing shapes are for visualisation only.
Constraints	Massless elements used to define complex mechanical connections between components.
Turbines	Integrated wind turbine models comprising blades, hub, gearbox, and generator. Blades are either rigid or flexible.

TurbSim

TurbSim is a stochastic full-field wind simulator developed by the National Renewable Energy Laboratory (NREL) to generate realistic atmospheric inflow conditions for wind turbine simulations. It produces time-varying, three-dimensional wind velocity fields across a spatial grid, typically aligned with the rotor plane of a wind turbine. The wind field consists of velocity components in the longitudinal (u), lateral (v), and vertical (w) directions, corresponding to the x, y, and z axes respectively. These components form a vector field which varies both spatially and temporally as depicted in Equation 3.9.

$$\vec{V}_{\text{wind}}(t, y, z) = \begin{bmatrix} u(t, y, z) \\ v(t, y, z) \\ w(t, y, z) \end{bmatrix} \tag{3.9}$$

TurbSim reads a input file `.INP` to configure the parameters required for execution. This input file contains detailed information about the model specifications and meteorological boundary conditions. These include the data listed in Table 2.1 and Table 2.2. Together, they define the characteristics and structure of turbulence across the generated wind field.

3.4. General Assumptions

Before constructing the numerical model, a number of assumptions are made to simplify the representation of physical phenomena and ensure computational tractability. Each assumption is motivated by practical considerations, supported where possible by prior studies or preliminary simulations, and assessed in terms of its implications and limitations. The assumptions are grouped by physical domain:

fluid–structure interaction, aerodynamic effects, and vessel modelling.

3.4.1. Fluid–Structure Interaction Assumptions

The following assumptions relate to the interaction between the fluid environment and the structural components of the system. These include simplifications concerning vortex-induced vibrations (VIV), current and second-order wave effects, the applicability of the Morison equation, and wave shielding phenomena. Each assumption is made to balance model fidelity with computational feasibility, while maintaining sufficient accuracy for assessing the system's global dynamic behaviour during installation.

Vortex-Induced Vibrations

VIV occur due to unsteady fluid flow interacting with non-streamlined structures, leading to the periodic formation and shedding of vortices on alternating sides of the body (Chen et al., 2023). When the frequency of vortex shedding approaches the structure's natural frequency, resonance may occur, resulting in significant cyclic loading. Over time, this can degrade structural integrity and adversely impact the performance, reliability, and safety of the system (Sarpkaya, 2004).

VIV can affect several components during wind turbine installation, including the MP, turbine tower, and blades. In standstill conditions, VIV becomes particularly complex and cannot be reliably predicted using low-fidelity modelling techniques (Pirrung et al., 2024). Mitigation strategies are well-established and include tuning natural frequencies to avoid resonance, increasing structural damping, and employing vortex suppression devices such as strakes or rakes. For example, VIV rakes are sometimes installed on turbine towers during installation to limit oscillatory motion (Livanos, 2018).

Given the availability of practical mitigation measures and the modelling complexity required to accurately capture VIV, it is assumed that appropriate damping and suppression strategies are in place during installation. As such, VIV effects are not considered in the present analysis for any component of the system.

Currents and Higher-Order Wave Excitations

Second-order wave forces and moments arise from spatial variations in wave elevation around the structure and from the quadratic velocity components of the water particles. In irregular sea states, pairs of wave components with frequencies ω_i and ω_j interact non-linearly, producing both a steady component, known as wave drift load, and dynamic components. These include low-frequency difference-frequency effects at $\omega_i - \omega_j$ and high-frequency sum-frequency effects at $\omega_i + \omega_j$. The magnitudes of these second-order effects are proportional to the product of the interacting wave amplitudes (Joseph et al., 2014).

Ocean currents are steady or slowly varying and act similarly to the steady wave drift component, primarily inducing a static or quasi-static offset in vessel position. The low-frequency components of wave drift forces may cause slow variations in vessel motion but do not excite the natural frequencies of interest in this study. Furthermore, the SSCV analysed here is equipped with a DP system, as described in Table 3.2.2, which actively mitigates such low-frequency disturbances.

Given their non-oscillatory or slowly varying nature and the presence of the DP system, both ocean currents and wave drift loads are neglected in this analysis.

However, it is important to acknowledge that in practice, the DP system cannot fully compensate for these effects. Oscillatory motions may still occur due to response delays inherent to the DP system, which relies on real-time processing of sensor data and continuous thruster adjustments. These delays can lead to unintended dynamic responses, as the system reacts to rapidly changing environmental conditions. As such, not all second-order effects are fully suppressed in practise. These complex interactions between the vessel control systems and environmental loads are beyond the scope of this study and are therefore neglected in the simulations.

Additionally, second-order sum-frequency effects are also excluded from the analysis. These high-frequency excitations are assumed to be insignificant relative to first-order wave loads, particularly for large, heavy structures like the SSCV considered. The vessel's substantial inertia and hydrodynamic damping are expected to attenuate high-frequency responses, minimizing their influence on system dynamics. It is noted that, in contrast to the SSCV, MPs may be more susceptible to high-frequency

excitations due to their relatively lower mass and higher natural frequencies. However, given the expected low sea states during installation, these effects are assumed to be negligible for the MP in the present study.

Morison Equation

The Morison equation is assumed to be applicable for computing the hydrodynamic loads on the MP across all considered sea states. This assumption is generally valid when the structural diameter is significantly smaller than the incident wavelength, typically by a factor of five or more.

However, based on the site-specific water depth of 30 m, this criterion is not met for wave periods between approximately 4 and 5.66 seconds. In this intermediate regime, a more suitable approach would involve potential flow theory or a hybrid model that incorporates both potential flow and Morison-type loading.

Despite this, the Morison equation is used throughout the present study for the sake of simplicity and consistency. As a result, a slight underestimation of hydrodynamic loads may occur due to the neglect of diffraction and radiation effects inherent to more advanced modelling approaches.

Shielding

Shielding refers to the reduction or modification of wave-induced forces on a structure caused by the presence of a nearby body that disturbs the incoming wave field. The upstream structure partially blocks or diffracts the waves, thereby reducing the wave energy and associated hydrodynamic loads on the downstream structure.

Li et al. (2014) demonstrated that the shielding effect of a vessel can significantly reduce the extreme responses of a MP during continuous lowering operations. Their findings show that the effectiveness of shielding depends on both wave direction and wavelength. For short waves and specific wave approach angles, extreme MP motions were reduced by more than 50% compared to those in undisturbed conditions. For long waves, reductions of over 30% were observed.

These results suggest that the presence of the SSCV can significantly influence MP motion under certain conditions, potentially offering a strategic advantage during installation. However, this effect is not further explored in the present study. Furthermore,

Given that the MP's diameter is only approximately 5% of the Thialf's total length, its influence on shielding the SSCV is considered negligible. Consequently, this analysis focuses on wave directions where the MP is either impacted first or simultaneously with the SSCV. A visual overview of this configuration is provided in Figure 6.2.

Shielding may also occur in this configuration, where waves reaching the MP before the SSCV reflect off the SSCV and subsequently impose additional loading on the MP. This feedback effect is neither included in the numerical model. While such reflections may induce extra loading, the largest excitations of the hub are expected along the primary wave direction. The contribution of the reflected waves to hub excitations is assumed to be negligible or even beneficial with respect to the magnitude of the resulting responses. As such, this effect is also neglected.

3.4.2. Aerodynamic Assumptions

This section outlines the assumptions related to aerodynamic loading on the installation operation. These include simplifications in the representation of aerodynamic forces, such as the use of the cross-flow principle, the exclusion of unsteady aerodynamic effects, and the assumption of wind–wave alignment. These assumptions aim to reduce model complexity while capturing the dominant effects influencing blade motion and alignment under wind loading.

Cross-Flow Principle

As described in Equation 2.4.2, the cross-flow principle neglects the span-wise component of the wind velocity. This assumption is implemented in OrcaFlex and is applied in the simulations presented in this study.

The cross-flow principle is widely adopted in industry due to its simplicity and efficiency, but it only provides a realistic approximation of aerodynamic loading when the wind approaches predominantly in the chord-wise direction. As the angle between the wind and the blade chord increases, the effective wind component in the chord-wise direction decreases, resulting in a reduction in aerodynamic forces. Under these conditions, the model does not compute any force components in the span-wise direction.

While this assumption is practical and widely used, it can lead to an underestimation of aerodynamic loads when the wind is misaligned with the blade chord. In spanwise wind conditions, the model does not generate aerodynamic forces, which does not reflect physical reality. Although preliminary estimates suggest that drag forces remain low in such cases, due to the relatively small projected area of the blade root compared to other components, however even small deviations in wind direction can quickly introduce chordwise components, resulting in abrupt increases in aerodynamic loading. This may compromise the stability and safety of the installation.

Wind approaching perpendicular to the blade may induce higher aerodynamic loads; however, these loads are typically more predictable. For this reason, the present study focuses on perpendicular wind conditions to obtain the most representative results under the cross-flow assumption. The limitations of this assumption are acknowledged and should be considered when interpreting the results.

Unsteady Aerodynamics

In this study, aerodynamic loading on the blade is modelled using a steady-state approach, in which airfoil coefficients are applied directly based on the instantaneous angle of attack and inflow velocity. In reality, however, both the angle of attack and the inflow velocity can fluctuate significantly due to factors such as skewed or turbulent inflow, turbine motion, and controller actions (Orcina Ltd., 2024i).

Additionally, blade flexibility can give rise to unsteady aerodynamic effects through the interaction between structural deformations and aerodynamic forces. These interactions may introduce dynamic behaviours in the aerodynamic loads, such as rapid fluctuations, time delays, and hysteresis (Orcina Ltd., 2024i).

For the purposes of this study, unsteady aerodynamic effects are neglected. As stated previously, the discretised model is best suited for capturing low-frequency behaviour, and therefore does not focus on very high-frequency effects during simulation. This assumption further simplifies the aerodynamic modelling by limiting it to lower-frequency responses. Given the focus on global motion and alignment criteria during the installation procedure, where the influence of unsteady aerodynamic phenomena is expected to be of secondary importance relative to dominant environmental loads and overall system dynamics, this simplification is considered justified.

Wind–Wave Misalignment

This study assumes perfect alignment between wind and wave directions. Given the use of the cross-flow principle, any directional misalignment would primarily result in a reduction of aerodynamic loading on the blade. As such, it is not considered critical in this context and is therefore neglected in the analysis.

3.4.3. Vessel Modelling Assumptions

This section presents the assumptions related to the modelling of the installation vessel. These include simplifications regarding the influence of wind loads on the vessel, as well as the configuration and capabilities of the crane system used during blade installation. The assumptions are made to ensure modelling efficiency while retaining the key dynamic behaviours relevant to the installation procedure.

Wind on the Vessel

Wind loading on the vessel is assumed to have a negligible impact on the dynamic behaviour of the system. This assumption is supported by preliminary simulations, which indicate that wind primarily contributes to a quasi-static offset rather than to dynamic motion. Specifically, the standard deviation of blade root motion changes by only approximately two percent when wind loading on the vessel is included.

Given this minimal dynamic influence, and considering that the vessel's DP system is designed to compensate for steady environmental forces in surge, sway, and yaw, while the ballasting system

addresses heel and trim, the effects of wind on the vessel are neglected in the present simulation.

Crane Block, Hoisting Point, and Reeving Characteristics

The crane system on the Thialf comprises three distinct lifting points: the main hoist, the auxiliary hoist, and the whip hoist. For this operation, the whip hoist, positioned at the highest point on the crane, is selected to achieve the required installation height, as referenced in Subsection 3.2.2. It has a maximum lifting capacity of 200 t, which is sufficient to lift the blade in combination with a BIT weighing up to approximately 120 t. However, since BITs can vary in weight and a safety margin is desirable, the suitability of the whip hoist ultimately depends on the specific installation configuration.

By contrast, the auxiliary hoist offers a significantly higher lifting capacity of up to 900 t, making it suitable regardless of the BITs weight. To satisfy both the height and capacity requirements, this study assumes that the specifications of the auxiliary hoist are applied to the position of the whip hoist. This approach would require structural modifications and reinforcement of the whip hoist prior to execution of the operation.

Furthermore, it is assumed that elastic deformation of the wire has a negligible effect on the system's behaviour during installation.

4

Bottom-fixed Offshore Wind Turbine Model

This chapter presents the development and modal analysis of the bottom-fixed offshore wind turbine model. The objective is to identify the natural frequencies and mode shapes of the turbine structure, which are essential for understanding its dynamic behaviour and evaluating potential resonance with environmental loading in the subsequent dynamic analysis.

4.1. Model Development and Overview

The bottom-fixed OWT described in Subsection 3.2.1 is modelled numerically in OrcaFlex. The process of model development, along with the key considerations involved, is outlined below. This is followed by a detailed description of the numerical model for each component. A summary of the complete model is then provided.

4.1.1. Process and Key Considerations

For the numerical model of the bottom-fixed OWT, several structural components are considered: the MP, TP, tower, nacelle, hub, and the blades. The objective during model development was to achieve a simplified representation without compromising the accuracy of the hub displacement results.

The initial approach used a massless beam to represent the MP, TP, and tower, with a lumped tip mass to account for the RNA. However, the mass of the tower and MP proved too significant to be neglected. To account for this, a beam with distributed mass and a lumped tip mass was implemented. Still, this method assumed uniform mass distribution, which does not reflect reality due to the tower's varying diameter, as illustrated in Figure 3.4b. This discrepancy results in inaccurate mode shapes.

A further simplification attempted to model the MP as a beam fixed at the base, thereby approximating soil embedment. However, this assumption misrepresents the actual interaction between the MP and the soil. In reality, the soil provides distributed stiffness, which influences both the natural frequencies and mode shapes. Modelling the soil as a fixed end leads to unrealistic mode shapes.

Additionally, it was considered to incorporate the blades into the tip mass for simplification. While this would capture the added inertia, it would not allow for the inclusion of aerodynamic loading on the blades, which is crucial for realistic external force simulations.

In conclusion, although various simplifications were evaluated, the complexity of the bottom-fixed system did not allow for a highly reduced model without compromising accuracy. Due to the need for precise prediction of hub motions to assess the feasibility and operability of the installation procedure, the final model consists of multiple coupled, yet independently defined, objects, which are described in the following sections.

4.1.2. Numerical Modelling of the Bottom-Fixed Offshore Wind Turbine

This section describes how each component of the bottom-fixed OWT is represented in OrcaFlex. The modelling is organised by object type, and the connections between these objects are explained. Finally, the implementation of damping within the model is also described.

Monopile, Transition Piece, Tower

The MP, TP, and tower are modelled as two finite element lines: one representing the MP and one representing the tower. The TP is included as part of the MP. Each line is assigned specific properties, including geometry, mass, structural properties, lift and drag coefficients, and structural damping. The MP line is divided into two types: one for the portion in the water and one for the portion in the ground, in order to capture differences in inner diameter and mass per unit length.

The tower line is approximately 130 meters long and divided into segments of 5 meters, resulting in a total of 26 segments. The MP line is 90 meters in length, with 45 meters defined as submersed MP and 45 meters as embedded MP. The MP is also subdivided into 5-meter segments, yielding a total of 18 segments.

Unlike the other lines, the embedded section of the MP features midline connections at each node. These connections are used to model soil interaction. A visualization of the MP and tower is provided in Figure 4.1a.

Nacelle and Hub

The Nacelle and hub are modelled as two lumped buoys. The nacelle-hub assembly is therefore modelled as a rigid body. The nacelle buoy is assigned with the structural properties from the assembly to centralize the information on the assembly, the hub is added as a buoy with a drawing shape for the visual completeness, but no real structural properties are assigned. Structural properties that are assigned to the nacelle are, mass, mass moments of inertia, centre of mass, drag area, volume, height. A visualization of hub and nacelle on top of the tower is provided in Figure 4.1b.

Installed Blades

For each blade that is installed, the model is updated accordingly. The blades are modelled using a turbine object, with all other turbine components removed except for the blades themselves. Each blade is defined by a series of airfoil profiles with specified segment lengths. A total of 50 aerofoils are used to define 58 segments along the full blade span of 117 metres. For each segment, the geometry, inertia-, and structural properties are specified. The blades can be pitched individually and configured as either rigid or flexible. A visualisation of a single blade installed in the hub is shown in Figure 4.1c.

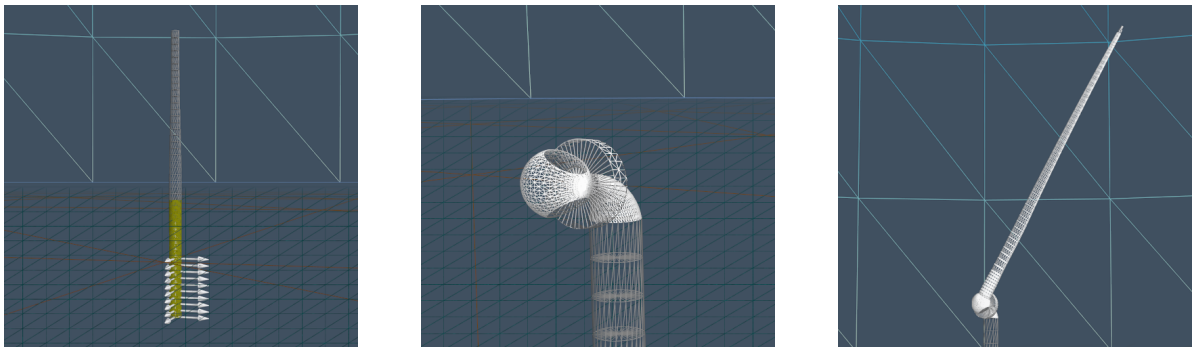

(a) Mesh view of the tower and MP

(b) Mesh view of the hub and nacelle

(c) Mesh view of one installed blade in the hub

Figure 4.1: OrcaFlex mesh configurations of the bottom-fixed OWT model: (a) tower and MP only, (b) hub and nacelle on top of tower, (c) one blade installed in the hub.

Soil

As explained in Section 2.5, the elastic halfspace model is used to compute the soil stiffnesses along the embedded depth of the MP. These stiffness values are incorporated into the model through constraint objects.

The soil is modelled in a manner similar to the OrcaFlex demonstration model for a 10 MW bottom-fixed OWT (International Energy Agency (IEA), 2010), where the interaction between the MP and the soil is represented by linear springs that resist both translational and rotational motion of the embedded MP in all six degrees of freedom.

The soil model is implemented using four chained constraints to represent the full set of translational and rotational stiffnesses. At each of the nine nodes of the embedded MP line, a chain of constraints is connected. The chain begins with the torsional constraint (Rz), which is connected to the rocking constraint (Rx & Ry), followed by the vertical constraint (z), and ends with the horizontal constraint (x & y). The final horizontal constraint in the sequence is anchored to the global axis system, which fixes the entire chain in space and prevents any movement. This method of chaining constraints is strictly valid only for small angular displacements.

Damping

The damping of the model represents the energy dissipation mechanisms within the system. It accounts for the loss of mechanical energy due to several sources. Appropriate damping is essential for capturing realistic dynamic responses and filtering out transient effects.

The overall measured system damping can be approximated as a linear combination of the following contributors in a bottom-fixed wind turbine: material damping of the structure, soil damping due to internal soil friction, aerodynamic damping, and hydrodynamic damping. The latter consists of two components: wave radiation damping, caused by energy loss to the water surface through wave generation, and viscous damping due to hydrodynamic drag (Shirzadeh et al., 2013).

The damping applied to the tower is stiffness-proportional only (Gaertner et al., 2020), meaning that the damping force is proportional to the structural stiffness but not to the mass. This corresponds to a Rayleigh damping model, as described in Equation 4.1, with the mass-proportional coefficient set to zero, i.e., $\alpha = 0$.

$$C = \alpha M + \beta K \tag{4.1}$$

where:

- C: damping matrix,
- α: mass-proportional damping coefficient,
- M: mass matrix,
- β: stiffness-proportional damping coefficient,
- K: stiffness matrix.

A critical damping ratio of 1% ($\zeta = 0.01$) is applied to all line types in the model, consistent with the approach used in Jiang et al. (2018) and supported by experimental findings in Shirzadeh et al. (2013). For the numerical model, the stiffness-proportional damping coefficient β is determined using Equation 4.2. The coefficient is computed for each simulation based on the peak period T_p of the incoming wave.

$$\beta = \frac{\zeta T_p}{\pi} \tag{4.2}$$

4.1.3. Model Summary

As described above, the model includes two buoys, two lines, and a total 36 constraints. The system connectivity is summarized in Table 4.1.

Table 4.1: Overview of connections in the model

Component	Object Type	Connection Description
Nacelle	6D buoy	Free
Hub	6D buoy	Connected to nacelle
Tower	Line	Connected to MP and nacelle
MP line	Line	Free at tower end; connected to soil constraint at embedded nodes
Soil chain of constraints at each of the 9 embedded MP nodes; node(h)		
Rz(h)	Constraint	Rx & Ry(h)
Rx & Ry(h)	Constraint	z(h)
Z(h)	Constraint	x & y(h)
X & y(h)	Constraint	Anchored

The final bottom-fixed OWT model is implemented in three configurations: with two blades, one blade, and no blades, corresponding to the different phases of the installation operation. Visual representations of each configuration, as modelled in OrcaFlex, are shown in Figure 4.2.

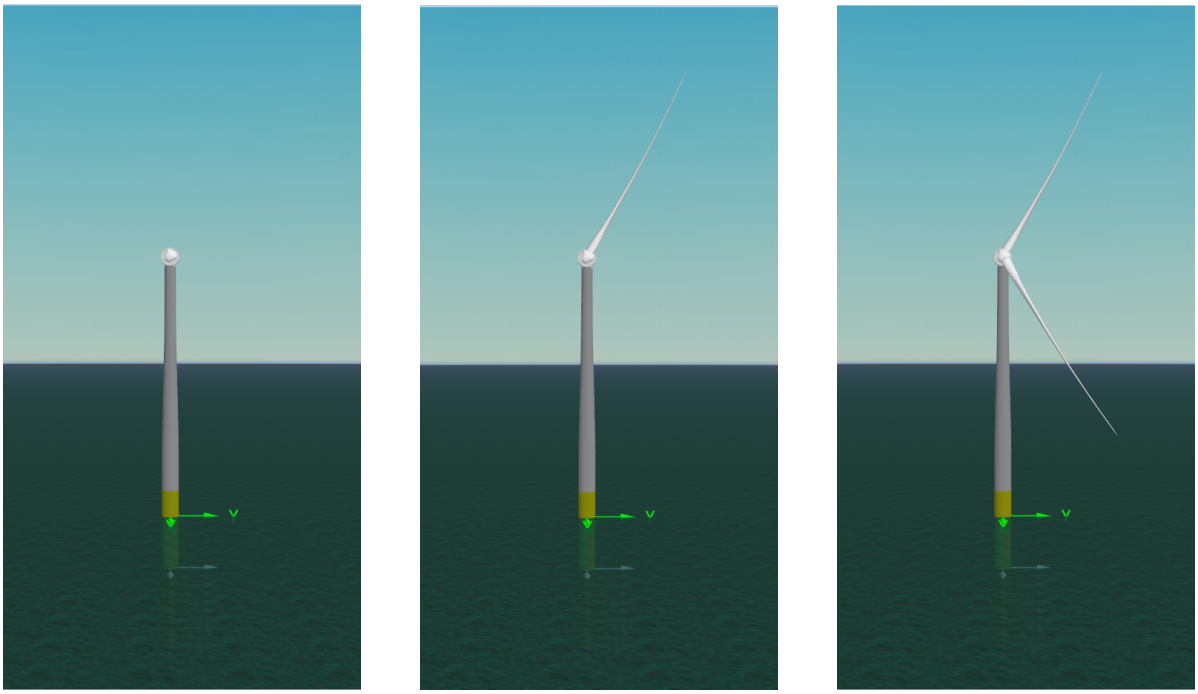

(a) 0 blades installed **(b)** 1 blade installed **(c)** 2 blades installed

Figure 4.2: Bottom-fixed OWT configurations for each installation phase, modelled in OrcaFlex: (a) no blades, (b) one blade installed, (c) two blades installed.

4.2. Assumptions and Limitations

In addition to the assumptions made prior to the numerical modelling, as outlined in Section 3.4, three further assumptions were introduced during the modelling process: the blades are treated as rigid bodies, certain components are assumed to undergo only small deformations, and the embedded MP is assumed to experience only minor angular deflections. These assumptions are discussed in more detail in the following subsections.

Rigid Installed Blades

The installed blades are modelled as rigid bodies in the numerical model. This simplification is justified after examining the dynamic characteristics of the blades relative to the expected excitation range.

According to the turbine specifications, the first natural frequency in the flapwise direction is 0.555 Hz, and in the edgewise direction it is 0.642 Hz (Gaertner et al., 2020). These frequencies are significantly higher than the dominant excitation frequencies identified in Chapter 2. Because the excitation does not coincide with the natural frequencies, resonance is not expected to occur.

Given this frequency separation and the prior exclusion of unsteady aerodynamic effects on the blade, the dynamic flexibility of the blades has a negligible influence on the overall system response. Therefore, modelling the blades as rigid components is considered a reasonable and efficient simplification.

Small Deformations

The nacelle and hub are modelled as rigid bodies based on the assumption that their structural deformations are negligible. Due to their high stiffness relative to the applied loads and expected dynamic responses, no significant deformation is anticipated. As a result, incorporating structural flexibility into the model is unnecessary for these components.

Small Angular Deflection of Embedded MP

The chained constraint approach used to model soil stiffness is valid only for small deflections of the MP. Considering the high stiffness of the overall system, the large geometric scale, and the stiffness characteristics of the soil, it is assumed that angular deflections remain small. Therefore, this soil modelling approach is deemed appropriate for the current application.

4.3. Modal Analysis and Model Verification

A modal analysis is conducted for each configuration shown in Figure 4.2. The results are compared to those of a single degree-of-freedom cantilever beam with a tip mass. Damping characteristics are evaluated to verify system behaviour and to gain insight into the transient response.

4.3.1. Natural Frequencies and Mode Shapes

The first two natural frequencies for each blade configuration are presented in Table 4.2, corresponding to the first Side-Side (SS) and Front-Aft (FA) modes. Higher-order modes are not considered, as they fall outside the expected excitation frequency range and are therefore unlikely to be significantly excited.

Table 4.2: First natural frequencies and corresponding periods of a bottom-fixed OWT for each installation phase.

Number of blades	SS frequency [Hz]	SS period [s]	FA frequency [Hz]	FA period [s]
0	0.1845	5.42	0.1847	5.41
1	0.1739	5.75	0.1743	5.74
2	0.1560	6.41	0.1566	6.39

The first tower–MP mode of the 15 MW IEA reference turbine is reported as 0.170 Hz (Gaertner et al., 2020), which closely matches the values obtained from the modal analysis. This agreement indicates that the OrcaFlex model accurately represents the dynamic characteristics of the referenced turbine.

In addition, the mode shapes can be visually inspected in OrcaFlex. The SS and FA modes are shown in Figure 4.3a and Figure 4.3b, respectively. These mode shapes correspond with those reported by Pezeshki et al. (2023), who derived an analytical solution for the dynamic response of offshore wind turbines under wave loading, incorporating non-linear Stokes wave theory as well as wave–structure and soil–foundation interactions.

Together, these results verify that the numerical turbine model exhibits natural frequencies consistent with reference data and demonstrates the expected dynamic behaviour in terms of mode shapes.

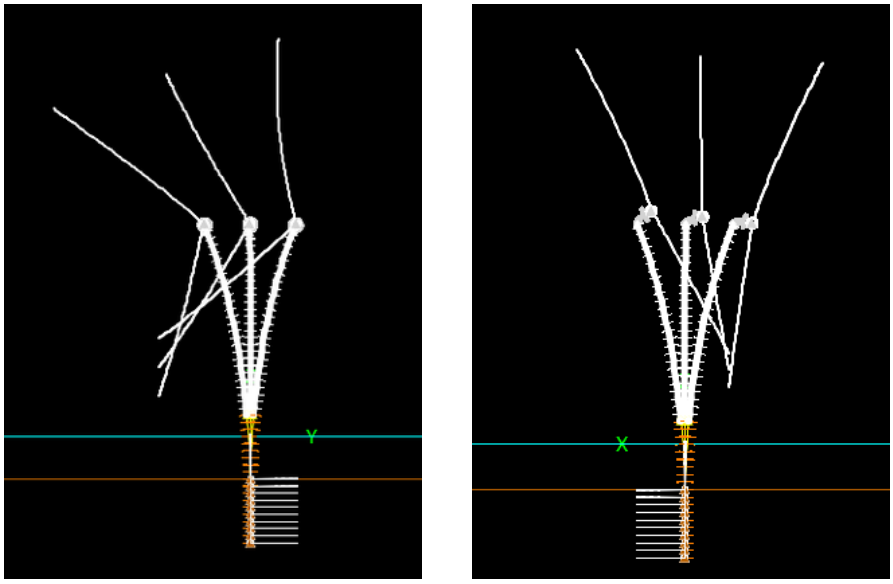

(a) First Side-Side mode of the OWT **(b)** First Front-Aft mode of the OWT

Figure 4.3: First two mode shapes of the offshore wind turbine: (a) side–side mode, (b) fore–aft mode.

Comparison to a One Degree of Freedom Cantilever Beam with Tip Mass

A simplified one-degree-of-freedom (1-DoF) analysis is conducted to estimate the global natural frequency of a bottom-fixed offshore wind turbine structure and to validate it against the results from the numerical model. This estimate also serves as a reference in the sensitivity study presented in Chapter 7.

In this approach, the system is idealised as an equivalent cantilever beam with a flexible base, represented by the soil's lateral stiffness. The tower and MP are homogenised by calculating an average bending stiffness, EI, and an average mass per unit length. The equivalent beam stiffness is computed using the standard cantilever expression, as shown in Equation 4.3.

$$k_{\text{beam}} = \frac{3EI}{L_{\text{eff}}^3}, \tag{4.3}$$

In this equation, L_{eff} represents the effective length, which is an idealized representation of the total vertical length over which lateral flexibility occurs. In this model it includes the tower, the submerged portion of the MP, and half of the embedded MP. This simplification accounts for the fact that while soil stiffness increases with depth, the lateral displacement of the pile decreases, resulting in the upper portion of the embedded MP contributing most significantly to lateral resistance. Including the full embedded length would overestimate the flexibility, while ignoring it altogether would underestimate the foundation's contribution. Taking half strikes a practical balance. The total effective stiffness is then modelled as a series combination of the equivalent beam stiffness and the soil's lateral stiffness, as shown in Equation 4.4.

$$k_{\text{eff}} = \left(\frac{1}{k_{\text{beam}}} + \frac{1}{k_{\text{soil}}} \right)^{-1}. \tag{4.4}$$

The effective mass includes a fraction of the distributed mass and the specified tip mass configuration, as defined in Equation 4.5. The fraction $\frac{33}{140}$ is derived under the assumption that the vibration mode shape of the beam is the same as the static deflection curve produced by a point load applied at the free end (Timoshenko et al., 1974).

$$m_{\text{eff}} = \frac{33}{140} m_{\text{beam}} + m_{\text{tip}}. \tag{4.5}$$

Finally, the global natural frequency is then determined using the Rayleigh approximation for a cantilever beam with an added tip mass, as shown in Equation 4.6. The results are given in Table 4.3.

$$f_n = \frac{1}{2\pi}\sqrt{\frac{k_{\text{eff}}}{m_{\text{eff}}}}, \tag{4.6}$$

Table 4.3: First natural frequencies and corresponding periods of the simplified single degree-of-freedom bottom-fixed OWT for each installation phase.

Number of blades	Natural frequency [Hz]	Natural period [s]
0	0.151	6.62
1	0.147	6.79
2	0.144	6.95

This idealised 1 DoF formulation provides a practical means to approximate the fundamental frequency but does not fully capture the coupled translational and rotational dynamics that are accounted for in the full numerical model.

The natural frequencies predicted by the simplified 1 DoF analysis are consistently lower than those computed using the full six degrees of freedom (6 DoF) numerical model. For instance, the hybrid 1 DoF model estimates the fundamental frequency at approximately 0.14 Hz with all three blades installed, increasing slightly as blades are removed: 0.14 Hz (2 blades), 0.15 Hz (1 blade), and 0.15 Hz (0 blades).

In contrast, the numerical model, which includes the full stiffness matrix and coupling between all six degrees of freedom, predicts higher values: 0.16 Hz (2 blades), 0.17 Hz (1 blade), and 0.18 Hz (0 blades). The inclusion of rotational degrees of freedom and coupled rocking-bending interaction in the numerical model leads to a stiffer global response than captured by the simplified model, resulting in higher natural frequencies.

The simplified 1 DoF model, which accounts only for horizontal translational stiffness and a lumped tip mass, underestimates the system's overall dynamic compliance because it neglects the soil–structure interaction's rotational flexibility and other relevant degrees of freedom. Nevertheless, the 1 DoF model provides a useful first-order estimate of the offshore wind turbine's natural frequency and confirms the expected trend when varying the rotor mass due to blade removal. However, the full 6 DoF numerical model remains essential for accurately predicting the dynamic response, particularly when assessing the coupled effects of translational and rotational motions and the influence of changing rotor configurations.

4.3.2. Decay Tests

The damping of the system is evaluated using decay tests. These tests are performed on the turbine configuration with zero blades by applying an impulse force of 100 kN for 0.1 seconds to the hub, after which the force is removed, allowing the system to vibrate freely. For the FA decay test, the force is applied along the x-axis, while for the SS decay test, it is applied along the y-axis. The total duration of each decay test is 800 seconds, with the impulse force applied at $t = 11$ s.

The resulting time trace is analysed to determine the decay rate, which quantifies how quickly the oscillations diminish over time. The decay rate, denoted by δ, is calculated using Equation 4.7. For the turbine configuration with no blades installed ($f_n = 0.185$ Hz), the decay rate in both the SS and FA directions is found to be approximately $\delta \approx 0.0118\,\text{s}^{-1}$.

$$\delta \approx 2\pi\zeta f_n \tag{4.7}$$

where:

- δ: decay rate,
- ζ: damping ratio,
- f_n: natural frequency.

From the time-domain results shown in Figure 4.4, the decay rate in both directions is consistently found to be approximately 0.0114 1/s, which deviates by only 3% from the expected value, thereby confirming the expected damping behaviour of the model.

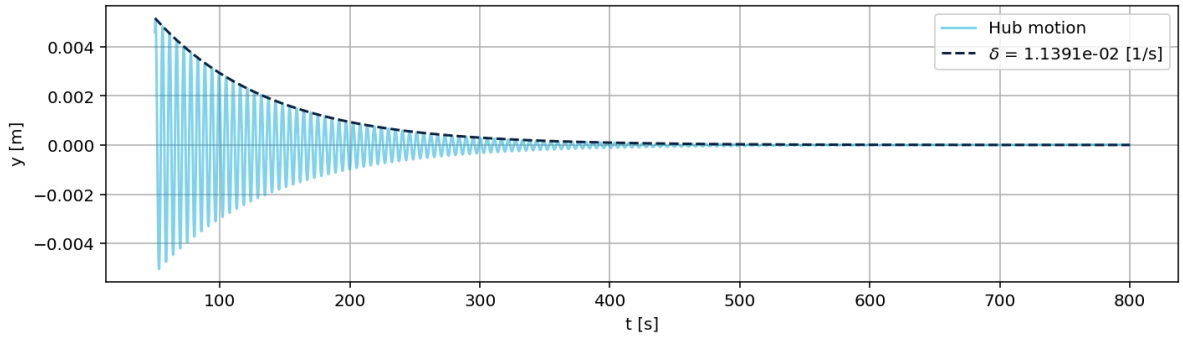

(a) Side-side decay test of hub motions.

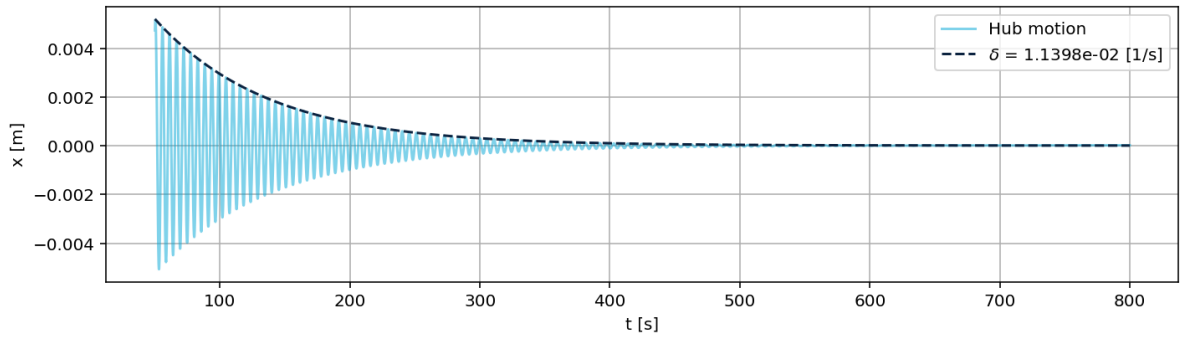

(b) Fore-aft decay test of hub motions.

Figure 4.4: Decay tests of nacelle displacement under a 100 kN impulse force: (a) hub displacements along y-axis, (b) hub displacements along x-axis.

5

Suspended Blade System on Semi-Submersible Crane Vessel Model

This chapter investigates the suspended blade system on the SSCV through modal analysis. Similar to the previous chapter, the objective is to find the system's natural frequencies and corresponding mode shapes, which will serve as a foundation for understanding the dynamic behaviour.

5.1. Model Development and Overview

The second sub-model of the overall installation system consists of two coupled subsystems: the vessel and the suspended blade within the lifting arrangement. The process of model development, is outlined below. Followed by a detailed description of the numerical model for each component. Lastly, a summary of the complete model is then provided.

5.1.1. Process and Key Considerations

For the SSCV Thialf, HMC already maintains validated models, which can be accessed, configured, and modified within Python.

Before implementation of one of these models, a simplification step was considered in which the vessel's motion would be captured in the motion of the crane tip directly. However, due to the phase characteristics of the RAOs, it was preferred to retain visual access to the full vessel response. Therefore, the entire vessel model is included in the simulations to ensure realistic motion behaviour and enable visual verification.

Furthermore, different configurations were evaluated for the tuggers. The initial setup consisted of two horizontal tuggers aligned along the x-axis, primarily intended to constrain yaw motion of the blade. However, testing showed that this configuration permitted rotation around the y-axis of the BIT, leading to large displacements at the blade root and was therefore deemed unsuitable. This occurred because the line of action of the tuggers was confined to the x-axis, providing no constraint against motion in the z-direction, thereby allowing rotation about the y-axis. Consequently, the final configuration employs two pairs of tuggers to effectively suppress rotation about both the y- and z-axes.

5.1.2. Numerical Modelling of the SSCV

This section describes how each component of the suspended blade system is represented in OrcaFlex. The modelling is described per object type, whereafter the connections between these objects are explained.

Vessel

The vessel is modelled using the vessel object in OrcaFlex. This object includes definitions for the RAOs, as introduced in Subsection 2.4.3, along with specifications for stiffness, added mass, damping, and wind area. These specifications account for the contributions of all components on the vessel.

The RAOs characterising the vessel response to incident waves are load RAOs. These represent the wave-induced loads on the vessel across a range of frequencies and directions, and are used to simulate the resulting motions. The vessel is modelled as a rigid body. Resistance to sway, surge, yaw, heave, roll and pitch are modelled through constraints with high stiffness.

Cranes

The cranes are modelled using 6D buoy objects and are therefore treated as rigid bodies. Each crane assembly consists of a crane house and a crane boom, both represented as individual 6D buoys with defined mass, centre of mass, and mass moments of inertia. The crane house and boom are connected via a hinge constraint, allowing relative rotation. Two winches represent the suspension wires linking the crane house to the boom. These winches are assigned specific lengths and a very high axial stiffness of 5.19×10^6 kN, reflecting the fact that the crane is designed for extremely heavy offshore lifts, far exceeding the weight of a single blade. As a result, while the connection is modelled with a hinge, the suspension system strongly constrains the relative motion between the crane components, maintaining near-rigid behaviour under operational loads.

DP

The DP system is modelled by neglecting second-order wave effects on the vessel.

5.1.3. Numerical Modelling of the Lifting Arrangement and Blade

The components of the lifting arrangement are labelled in Figure 3.12. The modelling approach for each component is outlined below. A visualisation of the numerical model, with each component identified, is provided at the end of this section in Figure 5.1.

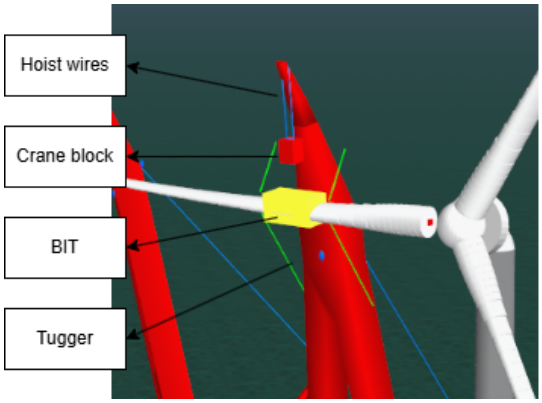

Figure 5.1: OrcaFlex model of the lifting configuration with indicated components.

Hoist wires

The hoist wires are modelled using one winch with four connections to capture the lifting operation. The spacing between the winch connection points is set equal to the breadth of the reeving.

Crane Block and BIT

The crane block and the BIT are each modelled as 6D buoys, with defined mass properties and mass moments of inertia. The BIT is assumed to have a mass of 100 t and dimensions of $5 \times 10 \times 5$ m. The mass moments of inertia are calculated based on the assumption of a uniform rectangular prism, as shown in Equation 5.1, with a scaling factor of α = 1.3 applied to account for the mass being concentrated toward the outer regions of the BIT. The impact of this assumption is further examined in the sensitivity study presented in Chapter 7.

$$I = \frac{1}{12} m(a^2 + b^2)\alpha \tag{5.1}$$

where:

- I: mass moment of inertia about the axis of rotation
- m: mass of the object
- a, b: dimensions of the object perpendicular to the axis of rotation
- α: scaling factor

Suspended turbine blade

The suspended blade employs the same model as the installed blades described in Subsection 4.1.2. It is fixed at its centre of mass within the BIT to maintain a horizontal orientation and to ensure proper handling through balanced weight distribution. A dimensionless and massless 6D buoy is added at the blade root to enable tracking of the blade root centre. This buoy is connected to the root end of the blade.

Tuggers

Four tuggers are included in the model, arranged in two pairs. One pair connects the blade yoke to a lower point on the crane boom, while the other pair connects the blade yoke to a higher point on the crane boom. Both tugger pairs are attached at a distance of 7.5 m from the centre of the BIT, resulting in a total spacing of 15 m, hereafter referred to as the tugger width.

The pre-tensioned tuggers are modelled using spring-damper links. Each link has a fixed unstretched length and a defined linear stiffness. Pre-tension is introduced by shortening the unstretched length. Additionally, the damping behaviour is modelled with a non-linear profile to capture the dynamic response, as previously explained in Subsection 3.2.2.

5.1.4. Model Summary

All objects and their connections are listed in Table 5.1, organized by subsystem. For the Thialf, the table includes the primary components of the model. The complete model also contains additional 6D buoys representing deck loads and other auxiliary elements. A visual representation of the OrcaFlex model is shown in Figure 5.2a, and a separate visual of the lifting configuration is provided in Figure 5.2b.

The two subsystems, the SSCV and the lifting configuration, are connected as follows: the auxiliary wire is attached to the whip of the crane, and the tuggers are connected to the boom of the crane, the full system is depicted in Figure 5.2c.

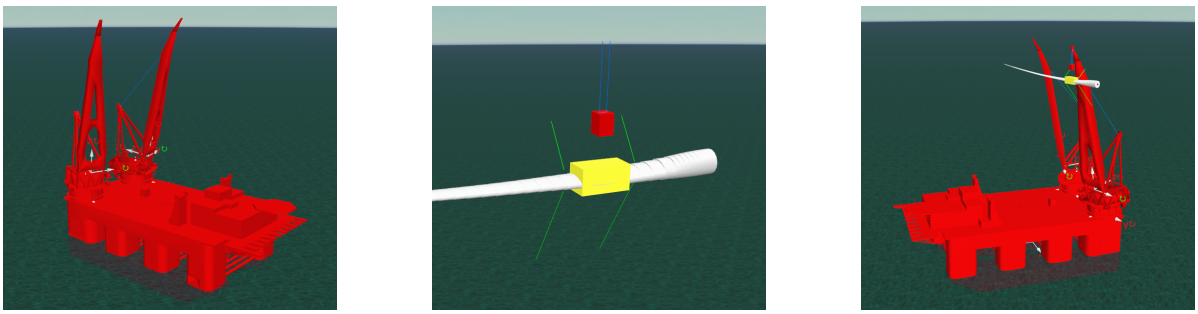

(a) Thialf overview **(b)** Lifting arrangement **(c)** Total sub-model overview

Figure 5.2: Visualisations of the numerical SSCV lifting configuration model.

Table 5.1: Overview of connections in the suspended blade system on the semi-submersible crane vessel model

Component	Object Type	Connection Description
DP Chain of constraints & Thialf		
Setpoint	Constraint	Fixed
X	Constraint	Setpoint
Y	Constraint	X
Z	Constraint	Y
Control Point	Constraint	Z
Thialf	Vessel	Control Point
Starboard-side crane (SB)		
Slew (SB)	Constraint	Thialf
House (SB)	6D Buoy	Slew (SB)
Hinge (SB)	Constraint	Slew (SB)
Boom (SB)	6D Buoy	Hinge (SB)
Suspension Wire (SB)	Winch	House (SB), Boom (SB)
Port-side crane (PS)		
Slew (PS)	Constraint	Thialf
House (PS)	6D Buoy	Slew (PS)
Hinge (PS)	Constraint	Slew (PS)
Boom (PS)	6D Buoy	Hinge (PS)
Suspension Wire (PS)	Winch	House (PS), Boom (PS)
Lifting arrangement		
Auxiliary Wire	Winch	Boom (PS), Craneblock, Craneblock, Boom (SB)
Craneblock	6D Buoy	Free
BIT	6D Buoy	Craneblock
Turbine Blade	Turbine Object	BIT
Blade Root	6D Buoy	Turbine Blade
Tuggers	Spring/Damper Links	BIT, Boom (PS)

5.2. Assumptions and Limitations

As outlined in Chapter 3, several assumptions were defined prior to the numerical modelling. Additional assumptions specific to this model are introduced below, accompanied by explanations and discussions of their potential implications.

Light Lifts

A lift is classified as a light lift when the weight of the lifted object is negligible compared to the displacement of the crane vessel, typically less than 1 to 2% of the vessel's displacement, corresponding to a mass of only a few hundred tonnes (Det Norske Veritas, 2011). In such cases, the dynamics of the vessel, remain effectively unchanged by the presence of the lifted load.

The total weight of the lifting configuration in this study is approximately 200 tonnes, which qualifies it as a light lift. Consequently, the criteria and modelling approaches applicable to light lifts are adopted. The RAOs of the vessel thus remain unchanged whether or not a blade is suspended in the crane.

Furthermore, in this category of lifts, the crane boom can be modelled as a rigid structure. As a result, the motion of the crane tip is governed solely by the wave induced rigid body motion of the vessel (Det Norske Veritas, 2011). This supports the assumption of a rigid crane in the numerical model.

Rigging

The dynamic effect of the rigging is neglected, as its mass and stiffness are small relative to the overall system and thus have minimal influence on the dynamic behaviour of the installation. The rigging

primarily transfers load from the crane block to the BIT without introducing significant compliance or dynamic amplification. As a result, the BIT is modelled as rigidly connected to the crane block.

Additionally, the degrees of freedom of the crane hook are neglected. Although the hook can swivel and rotate about the horizontal axes in reality, this motion is constrained in the model. This assumption is justified by the high effective stiffness provided by the combined action of the hoist wires and the four pre-tensioned tuggers, which apply continuous tension and are assumed to sufficiently constrain the blade yoke, effectively limiting its motion relative to the crane block.

Rigid Blade

The suspended blade is modelled as a rigid body. This assumption is supported by two main considerations. First, when the blade is fixed at its centre of mass, such as in the blade yoke, rather than at the root, its effective stiffness increases. This leads to a corresponding rise in the natural frequencies, which are expected to shift further outside the excitation range, toward approximately 0.8 to 0.9 Hz. Second, unsteady aerodynamic effects are assumed to be negligible during the installation process, as previously stated in Subsection 3.4.2. Given that the excitation frequencies remain well below these elevated natural frequencies, the risk of resonance is minimal. Therefore, representing the blade as a rigid body is considered a valid simplification.

Wind Loading on Lifting Configuration

Wind loading on the lifting configuration is neglected in the model. This includes the BIT, crane block, winches, and rigging, for which the drag area is assumed to be zero. The aerodynamic load on the blade is significantly greater, making the influence of wind on these components negligible. Additionally, the projected areas of the lifting components are not well defined, introducing uncertainty into load estimations. Given their minimal influence and the lack of precise geometric data, this assumption is made.

Mass of Winches and Links

The winches and links, including the auxiliary wire and the tuggers, contribute only a small mass relative to the overall system. Their influence on the dynamic response is therefore minimal. It is therefore assumed that their mass can be neglected.

Tuggers

Snap loads must be avoided in the tuggers, which is why they are pre-tensioned in the system. In the numerical model, the tuggers are represented by links, which can mimic their behaviour under tension. However, these link objects can also transmit compressive forces, which is not physically realistic, as actual tuggers cannot sustain compression and would instead go slack. As a result, the model is only valid for analysing the tuggers while they remain in tension. Any occurrence of compressive force in a tugger indicates that the simulation no longer reflects a physically realistic scenario and should be considered invalid for that period.

Blade Orientation on Deck

The blade's pre-bend causes a tip displacement of approximately 4 meters relative to the root. This large offset makes it impractical to store the blade with the pre-bend oriented downward. Therefore, it is assumed that the pre-bend points upward or sideways in the on-deck configuration, which is considered when evaluating the blade pitch angles.

5.3. Modal Analysis and Verification

The model characteristics are obtained from a modal analysis of the complete sub-model shown in Figure 5.2c. The natural frequencies and corresponding mode shapes are presented, followed by verification steps to assess the model validity.

5.3.1. Natural Frequencies and Mode Shapes

The natural frequencies are listed in Table 5.2. Modes 1 through 4 correspond to the expected pure vessel modes: surge, yaw, sway, and roll. The mode shapes show that the pitch and heave modes of the vessel couple with pendulum-like swinging of the suspended assembly about the y-axis.

Modes 5, 8, and 9 represent the pendulum modes and torsional modes of the lifting configuration. Modes 10 and 11 correspond to pendulum-like swinging of the segment between the crane whip and the crane block within the lifting configuration. Modes 12 and 13 represent rotational modes of the crane booms, which may rotate either out of phase or in phase.

Finally, mode 14 represents the pure vertical heave motion of the suspended lifting arrangement. However, this mode is unlikely to occur in reality due to the flexibility of the blade, as further explained in the following subsection.

Table 5.2: Natural frequencies and corresponding periods for each mode.

Number	Mode	Natural frequency [Hz]	Natural period [s]
1	Surge	0.0079	126.83
2	Yaw	0.0082	121.77
3	Sway	0.0096	104.24
4	Roll	0.0550	18.19
5	Blade yaw	0.0667	14.98
6	Pitch and blade pendulum y	0.0880	11.37
7	Heave and blade pendulum y	0.1082	9.25
8	Blade pendulum y	0.1127	8.88
9	Blade pendulum x	0.1751	5.71
10	Crane block pendulum y	0.1908	5.24
11	Crane block pendulum x	0.5648	1.77
12	Out-of-phase boom rotation	0.8285	1.21
13	In-phase boom rotation	0.8521	1.17
14	Blade heave	13.3713	0.07

5.3.2. Flexible Blade

The blade is modelled as a rigid body, as previously explained. To validate this assumption, a modal analysis is conducted for a configuration with a flexible blade. The results show that the first eleven modes remain largely unchanged in both shape and frequency, indicating that blade flexibility does not significantly influence the global dynamic behaviour in these modes.

However, the higher modes associated with boom rotation are altered in the flexible blade case. Blade flexibility introduces additional deformation modes that absorb part of the system's dynamic energy. Consequently, the boom rotation modes become coupled modes, characterised by minor boom motion combined with significant blade deformation.

Mode 14, present in the rigid blade system, no longer appears in the same form, as it transforms into a pure blade deformation mode. In addition, the flexible blade introduces extra higher-frequency modes, all corresponding to blade bending shapes.

5.3.3. Vessel RAOs

RAOs, particularly their phase components, are abstract and prone to error, even in data from well-respected sources (Orcina Ltd., 2024j). It is therefore essential to verify them. The RAOs of the SSCV were validated by simulating an airy wave and observing the vessel response at both short and long wave periods. At short periods ($T = 1$ s), the vessel remains effectively stationary due to its inertia, as expected. At long periods ($T = 30$ s), the vessel follows the wave motion: in the crest, it reaches maximum heave while moving in the direction of wave propagation; in the trough, it reaches minimum heave while moving against the wave direction. This confirms that both the amplitude and phase behaviour of the RAOs are physically consistent with expectations.

5.3.4. Pendulum

The natural frequency of a pendulum can be determined using Equation 5.2, where the effective pendulum length L_{eff} is defined as the distance from the suspension point to the centre of mass. The centre of mass is calculated based on the masses of the crane block, the BIT, and the blade.

$$f = \frac{1}{2\pi}\sqrt{\frac{g}{L_{\text{eff}}}} \tag{5.2}$$

where:

- f: natural frequency of the pendulum,
- g: acceleration due to gravity ,
- L_{eff}: effective pendulum length.

For this lifting arrangement, the calculated natural period of the pendulum mode is 9.74 s. The pendulum motion in the model about the y-axis appears as 8.88 s, as depicted in Table 5.2. The pendulum natural period in the numerical model is thus lower than that of the pendulum calculation. This can be attributed to the tuggers, which contribute to the stiffness of the system. Furthermore, it is found that the pendulum mode along the y-axis couples with the pitch and heave modes of the vessel.

Overall, the pendulum mode shape in the y-axis and its natural frequency are of the same order of magnitude as the theoretical natural frequency of a pendulum. However, the system does not behave as a conventional pendulum due to the influence of the tuggers, which is particularly evident in the x-axis pendulum mode. This also shows that the tuggers have the most effect on the dynamic behaviour along the x-axis, which aligns with their line of action.

5.3.5. Tugger Decay Tests

The damping behaviour of the tuggers is evaluated using decay tests, following the same methodology described in Chapter 4. This test is done to evaluate the damping behaviour of the two non-linear damping profiles, and select the most suitable damping profile.

The test involves applying a force along the global y-axis of the BIT and a moment about the same axis. This is selected because these motions are the least constrained, and thus the least damped by the tuggers. The decay test will therefore show the longest transient. A force of 10 kN and a moment of 100 kNm are applied for 0.1 s at t = 11 s. After the load is removed, the system is allowed to vibrate freely, enabling observation of its decay characteristics.

Figure 5.3 presents the results of the tugger decay test. The top row shows the translational response of the BIT to a force applied along the global y-axis, while the bottom row shows the rotational response to a moment about the global y-axis. In translation (Figure 5.3a and Figure 5.3b), both show stretching of the tuggers to the stretched baseline after which the tuggers return to the original length at t = 52.5 s. Thereafter, Profile 1 exhibits a longer settling time of 104 s, compared to 73 s for Profile 2. This indicates that Profile 2 achieves faster energy dissipation. In rotation (Figure 5.3c and Figure 5.3d), both profiles show damped oscillatory behaviour. Profile 1 settles in 43 s, whereas Profile 2 requires 54 s, indicating slightly slower damping in rotational motion for Profile 2.

Overall, the damping behaviour is pretty similar for both profiles, where Profile 2 exhibits more effective damping in vertical translation but slightly reduced damping in rotation around the y-axis compared to Profile 1. However, the excitations observed for Profile 2 are larger, indicating greater flexibility in the system under this damping configuration. Given the high accuracy required for the operation, Profile 1 is selected for this thesis. For verification, a sensitivity study is conducted for both profiles in Subsection 7.3.4.

As defined in Subsection 3.3.5, the transient period for the dynamic simulations is set to 600 s. This duration covers the transient behaviour observed in all tugger decay tests, ensuring that the transient response of the tuggers is excluded from the final analysis.

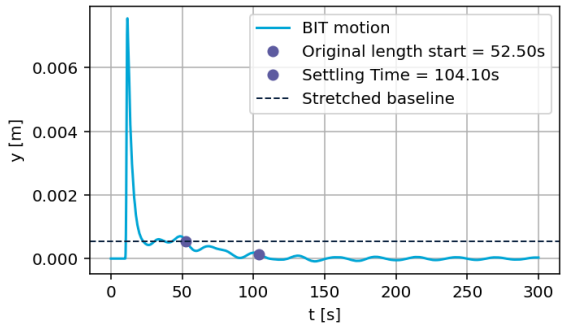

(a) Profile 1: translational decay test of BIT motion

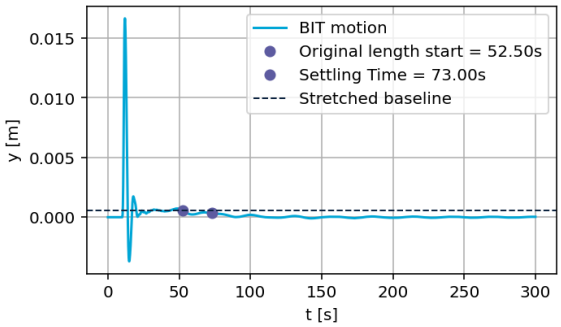

(b) Profile 2: translational decay test of BIT motion

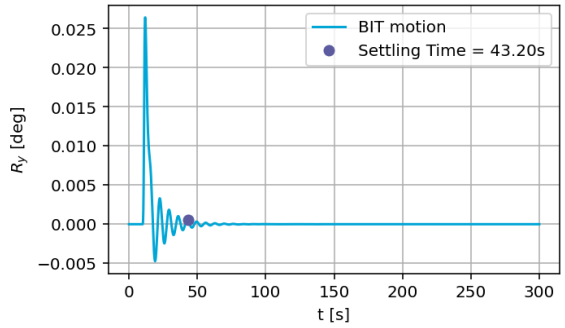

(c) Profile 1: rotational decay test of BIT motion

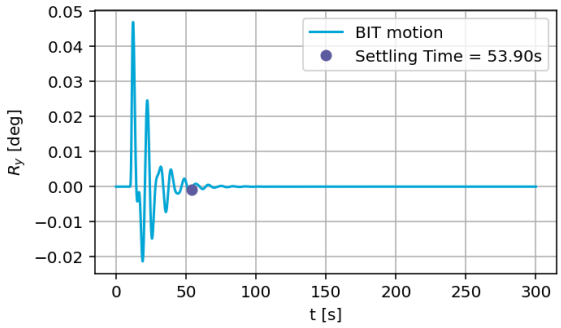

(d) Profile 2: rotational decay test of BIT motion

Figure 5.3: Tugger decay tests used to evaluate damping behaviour. Top row: translational response to a force applied along the global y-axis for two damping profiles. Bottom row: rotational response to a moment about the global y-axis for the same profiles.

6

Dynamic Analysis of Blade Root and Hub Motions

This chapter presents a dynamic analysis of the complete installation system, combining the two models described in Chapter 4 and Chapter 5. This dynamic analysis is performed to investigate the dynamic behaviour of the hub and blade root under varying environmental conditions, and to examine how these responses relate to one another.

6.1. Model Design Summary

The complete model combines the sub-systems described in Chapter 4 and Chapter 5. Both sub-systems are modelled independently and are not mechanically connected; thus, no coupling is present. Only their relative orientation and spacing are considered when assembling the complete model.

Due to the crane's slew angle, the blade is rotated out of the global axis frame. To integrate the models, the heading of the SSCV in Model B is adjusted to compensate for this angle, thereby aligning the blade with the global y-axis. Additionally, the vessel is translated along the global y-axis to ensure sufficient clearance between the blade and the hub. This configuration aligns the length of the suspended blade along the global y axis. An overview of the complete model is shown in Figure 6.1.

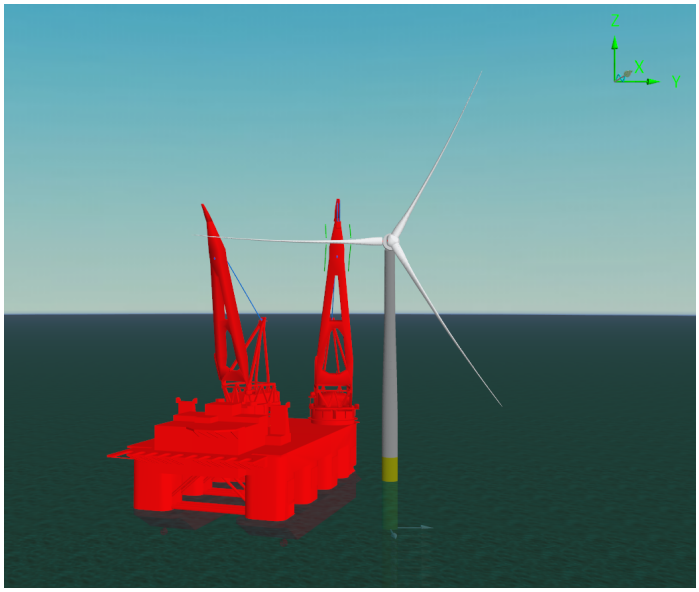

Figure 6.1: Overview of the final numerical model of the single blade installation system

6.1.1. Wind and Wave Directions

As outlined in Section 3.4, this study focuses on wave directions in which the MP is not affected by wave shielding from the vessel. Directions are evaluated at 45-degree intervals, with two additional orientations corresponding to perfect head and beam seas included where relevant. The wind and wave directions analysed in this study are illustrated in Figure 6.2.

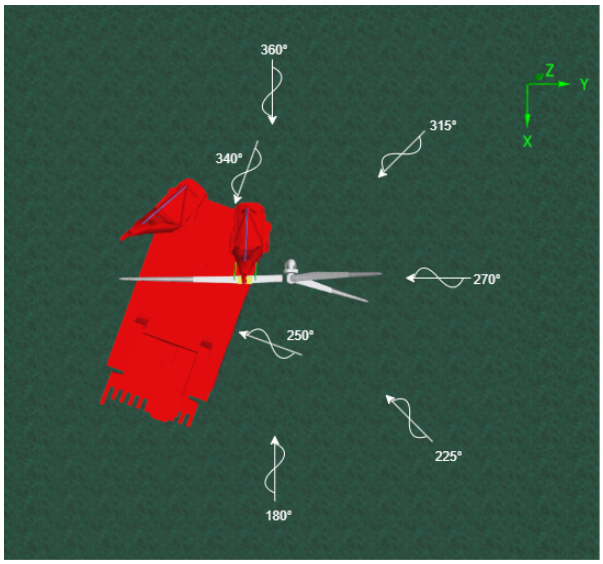

Figure 6.2: Top view of the complete numerical model with the wave directions considered in the analysis.

6.1.2. Analysis Method

The dynamic analysis is performed by running simulations in OrcaFlex for the full operational duration of 30 minutes, covering the complete installation configuration for the range of environmental conditions on the fictional site defined in Chapter 2. After the simulations are completed, the time histories of all model components are extracted for detailed post-processing and analysis. To quantify the motions of the components, the standard deviation of the time histories is computed. Since it captures how much a signal deviates from its mean position, it provides a consistent basis for comparing motion across different conditions, directions, or components.

The standard deviations are analysed under wind and wave excitation separately to examine the individual effects of each. Additionally, the influence of blade pitch and wind and wave direction is considered to determine the most suitable operational configuration within the given environmental conditions.

Given that the standard deviation only provides information about the magnitude of motion and does not capture direction nor information about the spatial displacements of components, the standard deviation analyses are accompanied by three-dimensional trajectories of the components.

The most suitable operational configuration, defined as the one resulting in the lowest overall standard deviations for both the hub and blade root, is then further analysed. The relative spatial behaviour of these components is examined to understand their motion in both magnitude and direction under varying environmental loading. This analysis aims to identify environmental conditions that are favourable for the operation and to highlight those that may pose challenges.

Figure 6.3a shows the points of interest (POIs) for this dynamic analysis. The dynamic behaviour of the hub is examined through the motion of the hub centre. The blade root behaviour is investigated via the vessel response and the motions of the whip, BIT, and blade root centre. The relative dynamic behaviour is assessed based on the blade root centre and hub centre motions as depicted in Figure 6.3b.

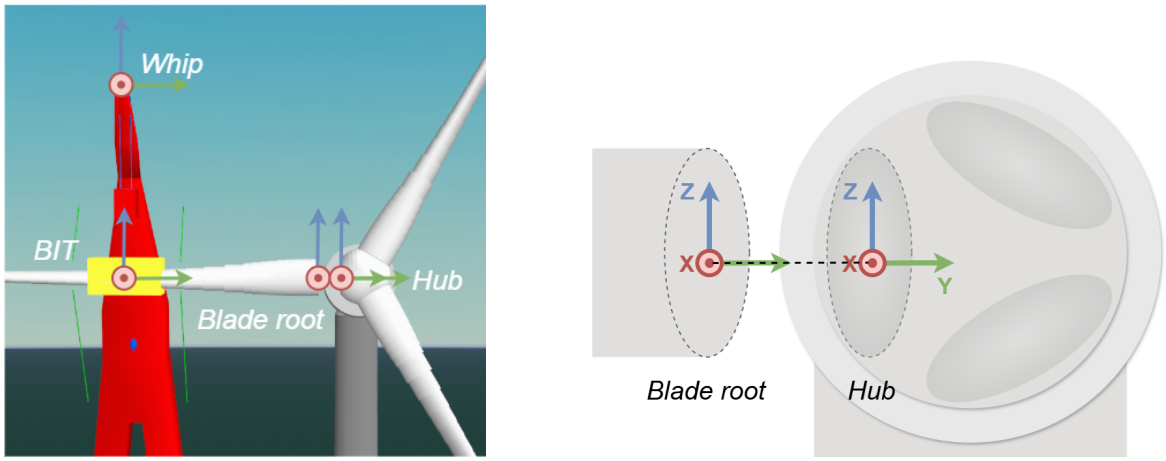

(a) POIs dynamic analysis

(b) POIs relative hub and blade root dynamic analysis

Figure 6.3: Points of interest for the dynamic analysis, including coordinate axis conventions.

6.2. Dynamic Analysis of the Hub Motions

The first dynamic analysis focuses on the hub motions of the OWT. The influence of waves on the hub is examined first, followed by the effect of wind. Finally, a summary is provided, identifying the main factors driving the dynamic behaviour of the hub.

6.2.1. Wave Effect

As described in Chapter 2, a range of peak periods and wave heights representative of conditions at the fictional location is considered to analyse their effect on the dynamic response of the structure. To assess the turbine's behaviour under these varying sea states and varying wave directions, dynamic simulations are conducted for a configuration with two feathered installed blades ($\theta_{\text{pitch}} = 90°$). For a wave direction of $180°$, the standard deviation of hub motion along the global x-axis is shown in Figure 6.4a, with corresponding results for the y-axis and z-axis presented in Figure 6.4b and Figure 6.4c, respectively.

The results demonstrate a clear linear response of the hub displacements with respect to significant wave height for each wave direction, confirming that the hydrodynamic forces acting on the structure are linear and inertia-dominated, as discussed in Subsection 2.4.3.

Furthermore, larger standard deviations are observed around peak periods of 6 and 7 seconds, corresponding to the first FA and SS natural periods of the turbine, which are 6.41 s and 6.39 s, respectively. These elevated standard deviations thus result from resonant behaviour of the OWT.

Due to directional wave spreading, wave excitations are not confined strictly to the principal wave direction; however, they are most pronounced along this direction, which explains the higher standard deviations of hub motions observed along the y-axis. Displacements along the z-axis remain very small, which is typical for the OWT configuration, given that the hub remains positioned at the top of the tower. The tower experiences slight bending under lateral loading, resulting in minimal vertical hub motion as a secondary effect.

Given that the hub motion response is linear with respect to wave height, the subsequent hub motion analyses are conducted for a representative wave height of 1 metre.

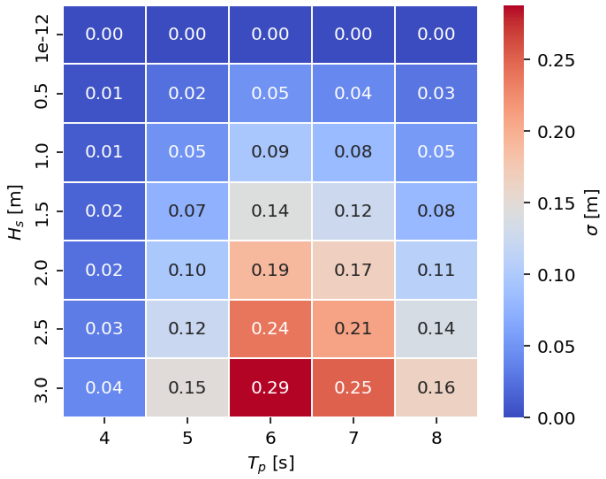

(a) x-direction

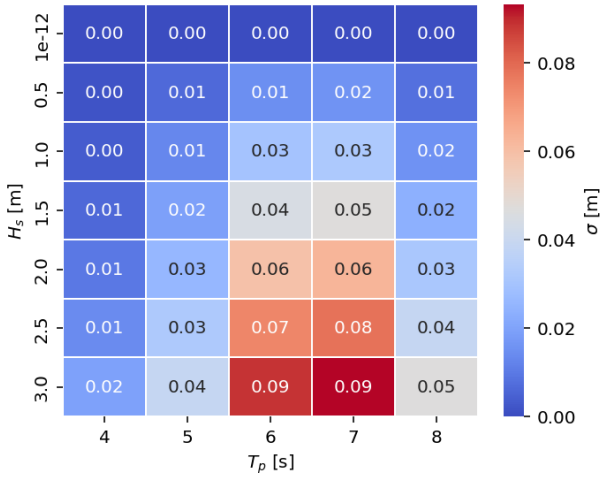

(b) y-direction

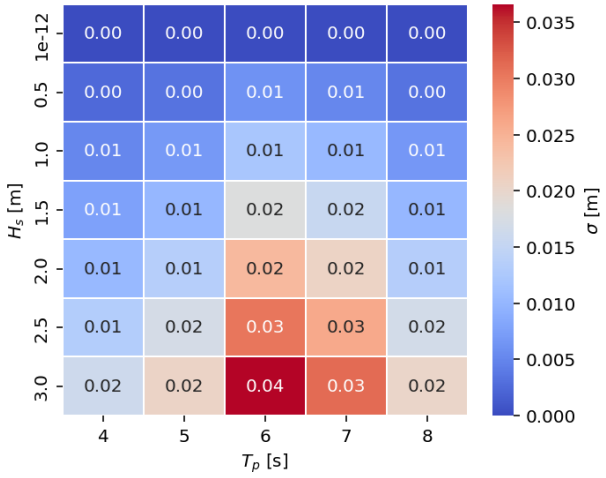

(c) z-direction

Figure 6.4: Standard deviation of hub centre motions in the x-, y-, and z-directions as a function of significant wave height H_s and peak period T_p. The wave direction is $180°$, with no wind.
The installation configuration includes two feathered installed blades ($\theta_{\text{pitch}} = 90°$).

The H_s–T_p plots reveal that the hub motions vary notably over range of peak periods. To understand the spatial response of hub under these varying wave conditions, three-dimensional trajectories of the hub over the full operational duration of 30 minutes is examined. The illustrated wave direction is $180°$, indicating that the primary wave propagation occurs along the x-axis.

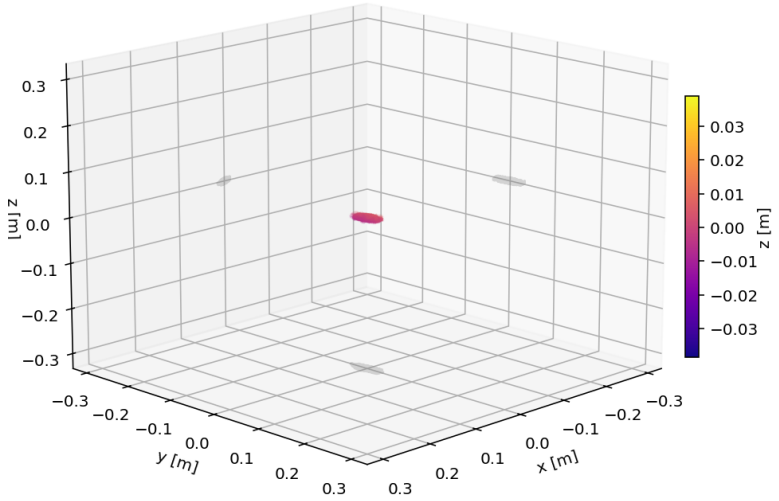

(a) $T_p = 4\,\text{s}$

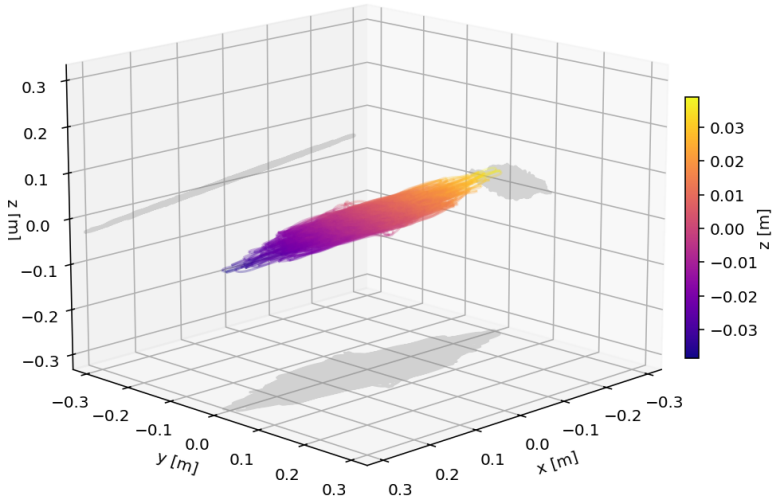

(b) $T_p = 6\,\text{s}$

Figure 6.5: Three-dimensional trajectories of the hub relative to its static position for $H_s = 1\,\text{m}$ and two peak period values, for a wave direction of $180°$, with no wind.
The installation configuration includes two feathered installed blades ($\theta_{\text{pitch}} = 90°$).

For a peak period of 4 seconds, the time trace of the hub's motion is shown in Figure 6.5a. The H_s–T_p plots indicates that, for this peak period, only small standard deviations are expected along all three

axes, which is confirmed by the compact three-dimensional trajectory.

For a peak period of 6 seconds, the standard deviations in the H_s–T_p plots, increase in all directions, with the largest values occurring along the axis aligned with the incoming wave direction, as expected. The three-dimensional trajectory for this case is shown in Figure 6.5b, which clearly demonstrates that the hub moves substantially along the wave direction (x-axis), which corresponds to the FA mode of the OWT. Furthermore, displacements along the y-axis are induced by directional wave spreading. The little asymmetry observed in the x-y displacement field can be attributed to the uneven mass distribution resulting from only two blades being installed. Furthermore, the plot highlights the small vertical motion that arise as secondary effect of the lateral motions.

Wave Direction

The previous section shows that hub motions are most pronounced along the axis of wave propagation. Wave direction therefore has a significant influence on the dynamic behaviour of the hub. To investigate this effect, the standard deviations of hub motions along the global axes for the selected wave directions, as described in Subsection 6.1.1, are presented in Figure 6.6.

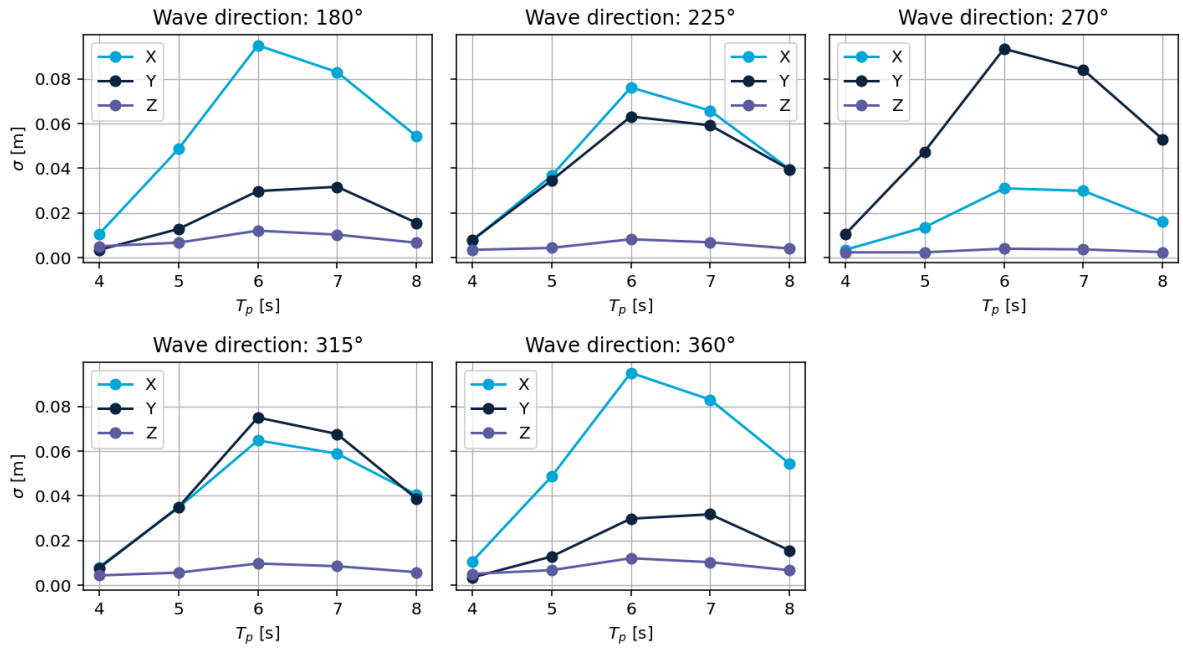

Figure 6.6: Standard deviation of hub motions for H_s = 1 m, as a function of peak period T_p for selected wave directions.

For wave directions differing $90°$, the turbine exhibits similar response patterns, shifted along the principal axes according to the wave direction. For instance, at $180°$ and $270°$, the standard deviation patterns are very similar. This highlights the symmetrical nature of the dynamic behaviour of the hub, indicating that asymmetries of the OWT, such as the two installed blades or excentric rotor, do not significantly affect the hub motions. For all wave directions, the largest hub motions occur along the wave propagation axis.

Figure 6.7a and Figure 6.7b show three-dimensional trajectories of the hub for a peak period of 5 seconds and wave directions of $270°$ and $180°$, respectively. These conditions are close to the FA and SS natural periods of the OWT. The figures illustrate that the dynamic response varies slightly with wave direction. In particular, the eccentricity of the rotor in the FA mode, observed for the $180°$ wave direction, introduces a marginal increase in vertical hub motion. However, this difference remains very small, confirming the symmetrical dynamic behaviour.

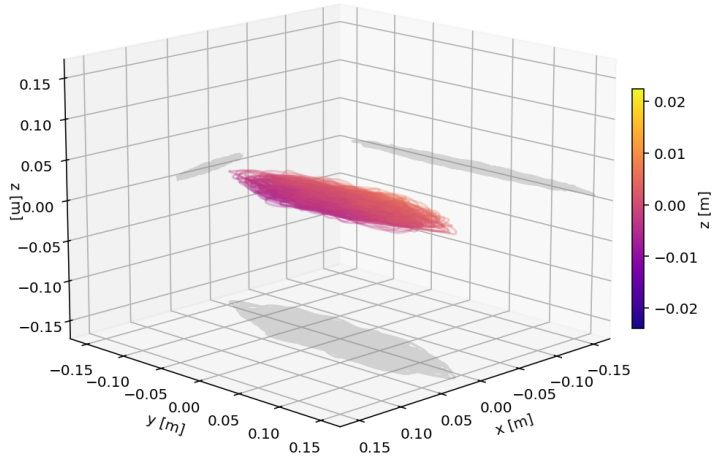

(a) Wave direction: 270°

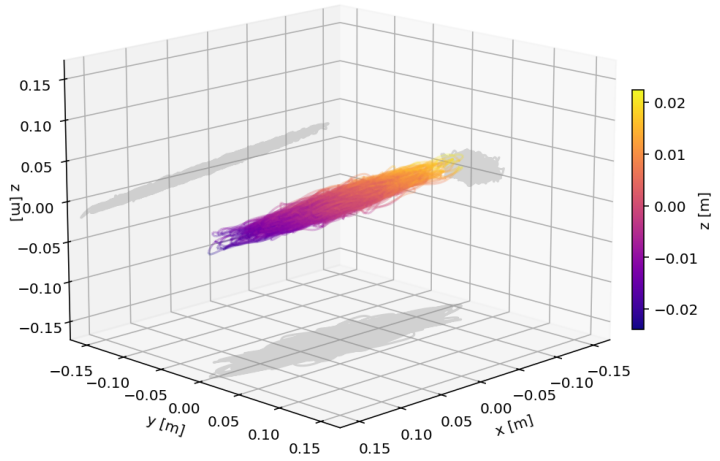

(b) Wave direction: 180°

Figure 6.7: Three-dimensional trajectories of the hub relative to its static position for $H_s = 1\,\text{m}$ and $T_p = 5\,\text{s}$, for two wave directions 270° and 180°, with no wind.
The installation configuration includes two feathered installed blades ($\theta_{\text{pitch}} = 90^\circ$).

6.2.2. Wind Effect

The effect of wind on the standard deviation of the hub displacements is determined for a OWT with no installed blades and a OWT with two installed blades for three blade pitches. The installed blades are positioned in feathered and stalled configurations as described in Chapter 3.

The wind effects are analysed for a wind direction of 180°. For other wind directions, the aerodynamic loading on the installed blades decreases due the cross-flow principle. Therefore, this case represents the governing scenario. For the first case, where no blades are installed, the standard deviations of the hub motions are provided in Figure 6.8.

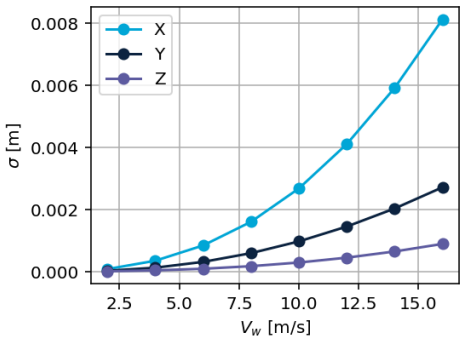

Figure 6.8: Standard deviation of hub motions over mean wind speed V_w for no waves, and an installation configuration with 0 installed blades.

The standard deviation of the hub displacements increases quadratically with wind speed, as the aerodynamic loading scales with the square of the mean wind speed. The largest standard deviation is observed along the global x-axis, which aligns with the direction of the incoming wind, as expected. Notably, even for the highest mean wind speed considered (16 m/s), the standard deviation reaches only approximately 8 millimetres in this configuration, indicating that the influence of wind on hub motions through tower loading remains relatively small.

Installed Blade Pitch

When the blades are installed, the aerodynamic loading on the installation configuration increases, as the blades also experience aerodynamic forces. These loads can be influenced by the blade pitch angle.

Given that hub motions are undesirable, the aerodynamic load should be minimised. This can be achieved by feathering the blades, which can be implemented in two ways. Furthermore, to investigate the effect of maximized aerodynamic loading of the blades, a stalled pitch configuration is also considered. To assess the impact of the overall increased aerodynamic loading on the dynamic behaviour of the hub, the standard deviation of hub displacements is evaluated for the installed pitch angles shown in Figure 3.7.

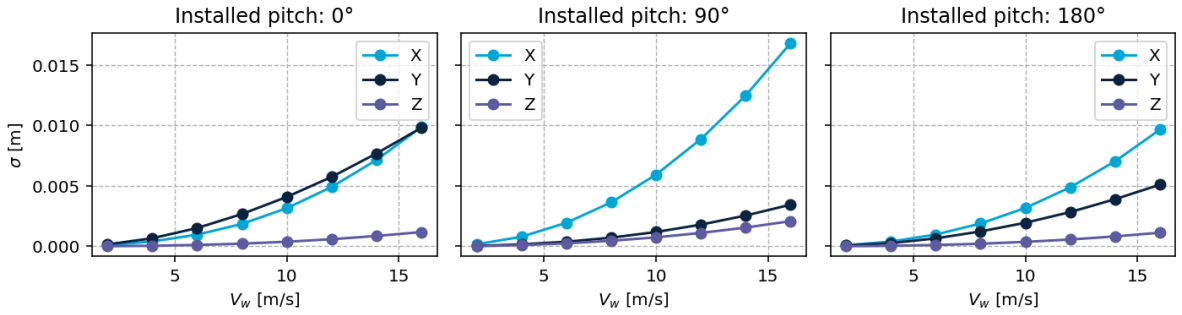

Figure 6.9: Standard deviation of hub motions over a range of mean wind speed V_w for a configuration with two installed blades, comparing three installed pitch settings: feathered at $90°$ with the leading edge facing into the wind, feathered at $270°$ with the trailing edge facing into the wind, and stalled at $0°$.

The middle graph shows that the stalled blades generate the highest standard deviations. The increased drag forces on the blades lead to greater hub motions, with the largest displacements occurring predominantly along the wind direction. Both feathered configurations show a small increase of standard deviation compared to Figure 6.8. Showing that feathering is an effective way of minimizing the aerodynamic loading of the blades.

For the feathered blade with the leading edge facing into the wind ($\theta_{\text{pitch}} = 0°$), motions arise along the y-axis. This occurs because small fluctuations in the angle of attack cause the airfoil to generate lift, as

illustrated in Figure 3.6. For the second feathered position ($\theta_{\text{pitch}} = 180°$) the trailing edge cause flow separation and suppresses lift generation. Consequently, the resulting displacement pattern shows lower standard deviations.

6.2.3. Hub Dynamics Summary

The analyses indicate that the hub motions are symmetrical under wave loading, with dominant motion occurring along the wave propagation axis. The maximum standard deviation of hub motion is approximately 9 cm for a wave height of 1 m.

Furthermore, wind has a smaller overall effect on hub motions. For feathered blades with the trailing edge facing into the wind, this effect is further reduced. The largest wind-induced standard deviation of hub motion, observed at a wind speed of 16 m/s, is approximately 1 cm.

These results demonstrate that wave-induced loading is the dominant factor governing the displacement behaviour of the hub.

6.3. Dynamic Analysis of the Blade Root Displacements

The second dynamic analysis focuses on the blade root motions of the suspended blade on the SSCV. To understand the dynamic behaviour of the blade root displacements, it is important to recognise that the overall motion is affected by two components: the motions of the SSCV and the motions of the blade relative to the SSCV.

The influence of wave height and peak period on the system is examined first. To clarify the contribution of each component, the wave-induced excitations are then analysed sequentially: starting at the vessel level, followed by the crane whip, and finally at the blade root. This stepwise approach highlights how each object moves and contributes to the overall blade root motions. For wind-induced excitations, this sequential analysis is not performed, as wind effects on the vessel are neglected.

6.3.1. Wave Effect

Similar to the previous dynamic analysis, to understand how the vessel and blade root behave under the varying sea states and wave directions defined in the case study, dynamic simulations are carried out, after which the standard deviations are determined across the full range of wave heights and peak periods.

The standard deviation of the blade root displacement along the global x-axis is shown in Figure 6.10a; the corresponding results for the y- and z-axes are presented in Figure 6.10b and Figure 6.10c, respectively.

Similar to the hub, the standard deviation increases linearly with H_s for all wave directions, consistent with the expected hydrodynamic loading on the SSCV, which is inertia-dominated and therefore linear. Consequently, the response behaviour is examined in detail for a representative wave height of 1 m across several peak periods.

Furthermore, the H_s–T_p plots reveal that the blade root motions increase for larger peak periods along the x-, y-, and z-axes. The increase of standard deviation in x-axis and y-axis are similar, whereas the increase of in z-axis is smaller. The largest standard deviations are observed around the peak period of 8 seconds.

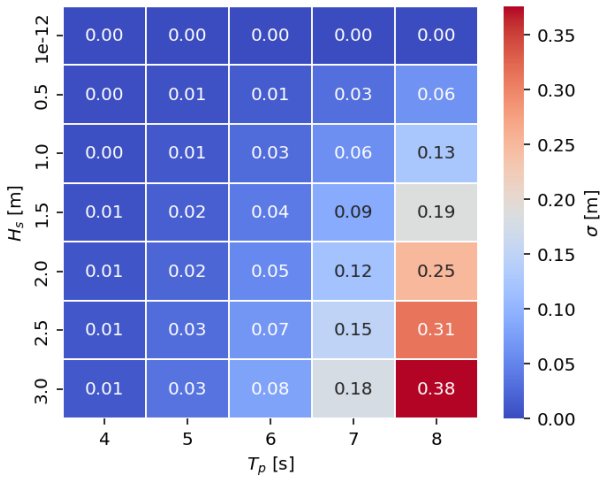

(a) x-direction

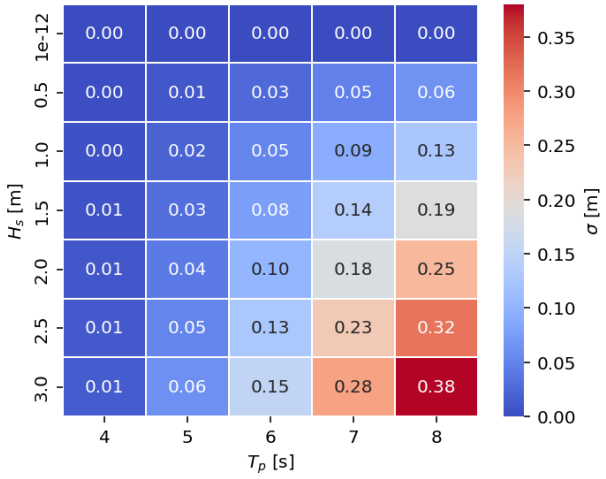

(b) y-direction

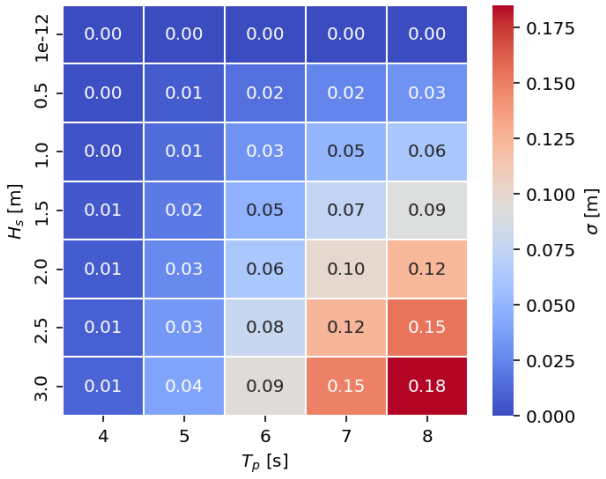

(c) z-direction

Figure 6.10: Standard deviation of blade root motions in x-, y-, and z-directions as a function of significant wave height H_s and peak period T_p for a wave direction of $180°$ and no wind.
The installation configuration consists of a feathered suspended blade, a crane block height of 159.4 m, tugger stiffness of 100 N/m, and a tugger width of 15 m.

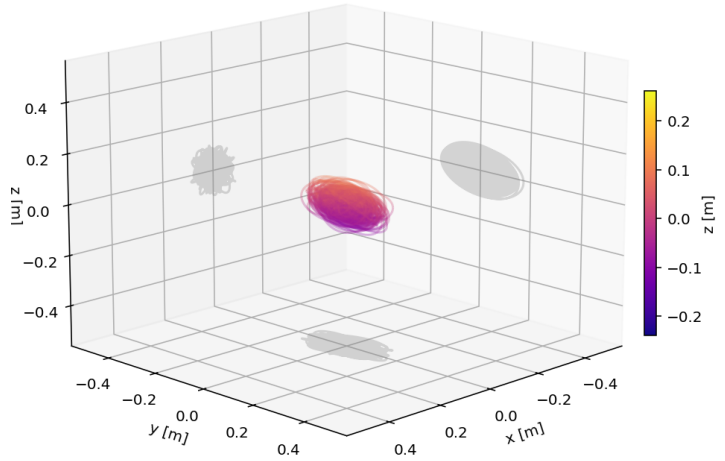

(a) $T_p = 6\,\text{s}$

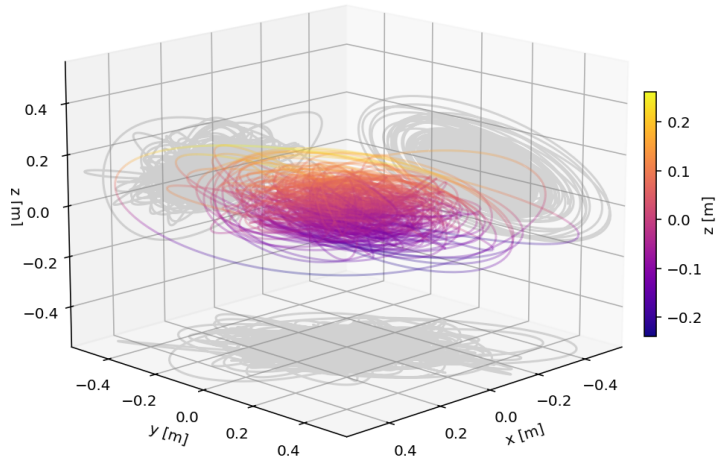

(b) $T_p = 8\,\text{s}$

Figure 6.11: Three-dimensional trajectories of blade root motions relative to its static position for $H_s = 1\,\text{m}$ and two peak periods for a wave direction of $180°$ and no wind.
The installation configuration consists of a feathered suspended blade, a crane block height of 159.4 m, tugger stiffness of 100 N/m, and a tugger width of 15 m.

Figure 6.11a shows that for a peak period of 6 seconds, the blade root exhibits motion along all three axes. Figure 6.11b demonstrates that as the peak period increases, these motions also increase along all axes.

Wave Direction Effect on SSCV motions

To analyse the vessel's dynamic behaviour, the translational and rotational standard deviations are analysed for a extended range of peak periods, which are presented in Figure 6.12 for different wave directions. The analysis is conducted in the SSCVs local coordinate system and the results are given for the origin of this local system as depicted in Figure 3.11. In this configuration, wave directions $180°$

and $360°$ correspond to head seas, $270°$ to beam seas, and $225°$ to oblique seas.

Given that the SSCV is a rigid body, the rotation of the SSCV is the same for each point on the Thialf. The translational motions however differ for each point depending on the distances from the local origin.

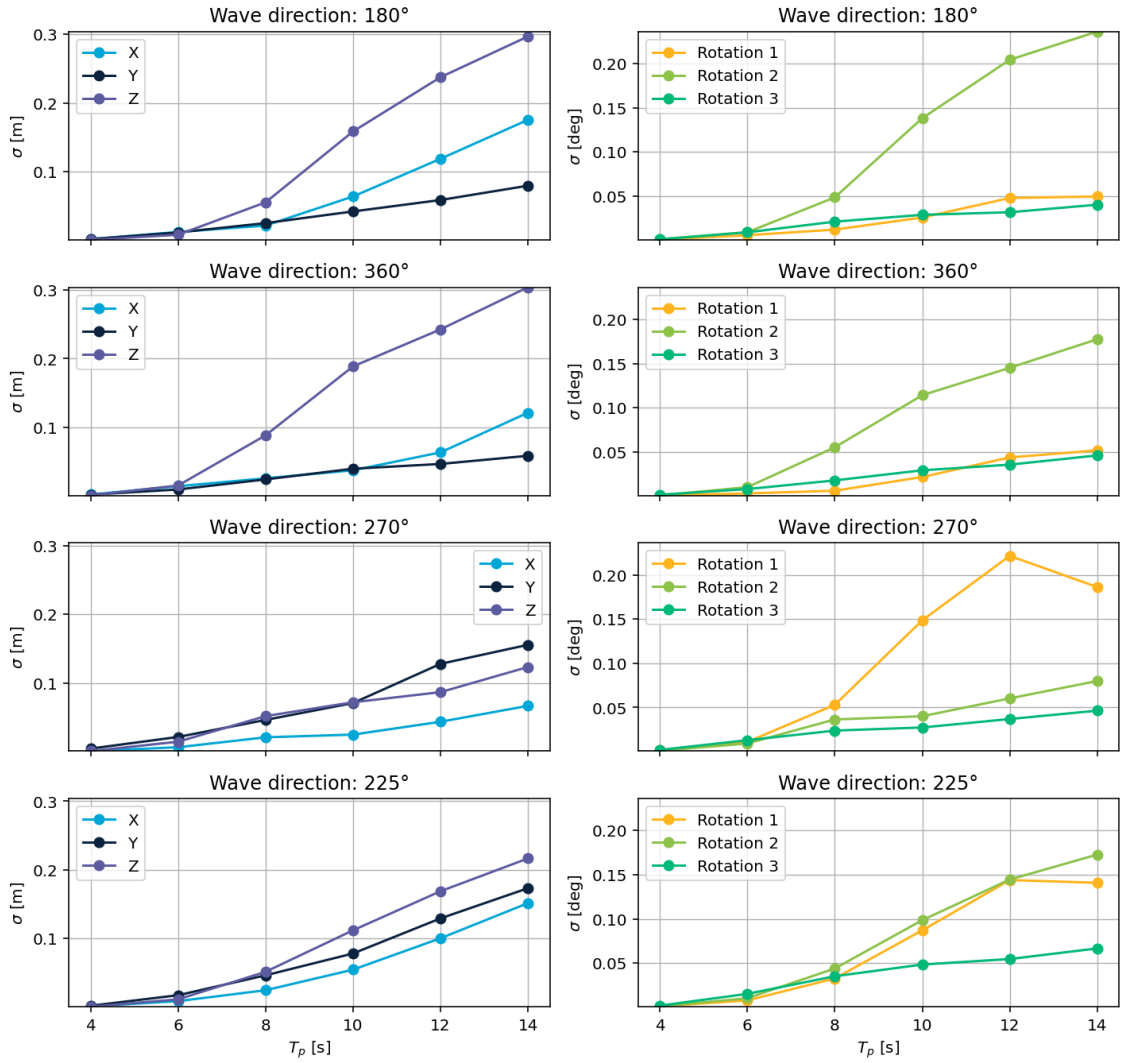

Figure 6.12: Standard deviation of the SSCV motions as a function of peak period T_p for different wave directions in local SSCV coordinate system.

The figure shows that both translational and rotational standard deviations increase with peak period. The two upper plots, representing head seas, produce different dynamic responses due to asymmetry of the hull and also due to the asymmetric placement of the cranes on one side of the vessel. These head sea conditions predominantly generate SSCV pitch (Rotation 2) and heave (Z) in the local origin.

In contrast, the beam sea predominantly result in considerable rotations about the local x-axis, which corresponds to roll. Furthermore, the oblique sea results in a combination of head and beam sea effects, resulting in translational and rotational motions along and about all principal axes.

Wave Direction Effect on Whip Motions

The next dynamic analysis focuses on the motions of the whip. Since the crane and vessel are modelled as rigid bodies, with booming motion as the only permitted relative movement constrained by the

suspension wire, the high axial stiffness of the wire ensures that these relative motions remain minimal. As a result, the whip motions primarily consist of the SSCVs translational motions and rotational motions, scaled by the distance between the whip and the SSCVs local origin. Figure 6.13 shows the standard deviations of the whip translational motions over the same extended peak period range applied in the previous section. Note that these are given in the local axes of the SSCV.

What stands out is that the whip motions primarily arise due to the rotation of the vessel, which can be derived by comparing of the standard deviations trends to Figure 6.12. Which can be attributed to the considerable length of the crane, due to which the rotationally induced displacements are significant.

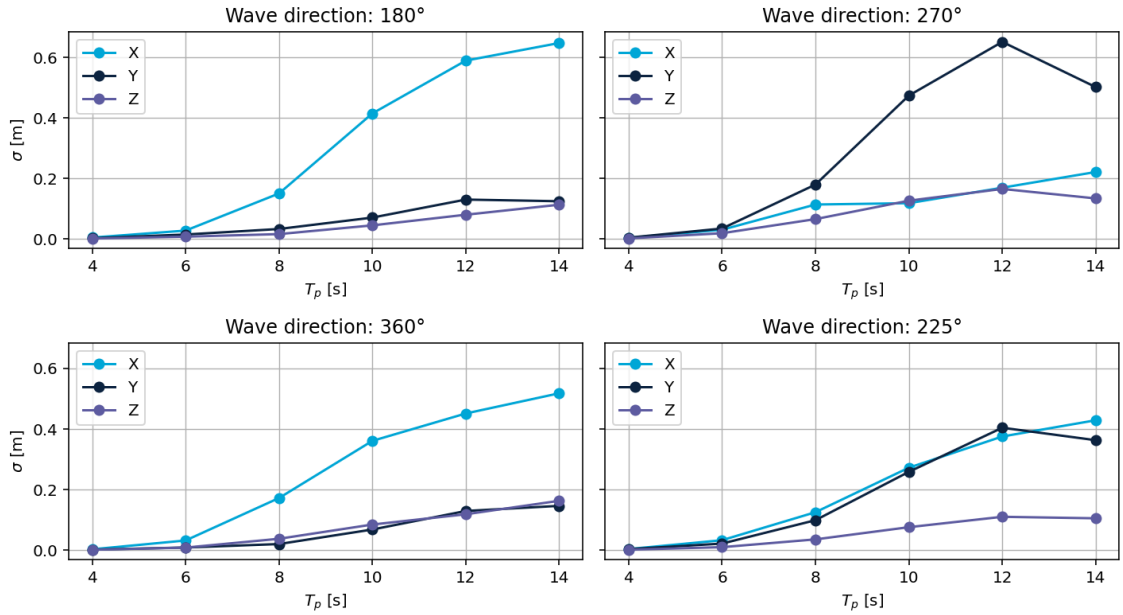

Figure 6.13: Standard deviation of the SSCV whip motions as a function of peak period T_p, H_s = 1 m/s and no wind, for different wave directions in local SSCV coordinate system.

Now that it is established that the whip motions are primarily induced by the SSCV rotations, the remainder of this dynamic analysis examines the displacements in the global coordinate system within the expected peak period range of the case study. This allows for an assessment of the influence of various wave headings on the overall installation system and the identification of a preferred wave direction for this configuration. The whip displacements in the global coordinate system are presented in Figure 6.14.

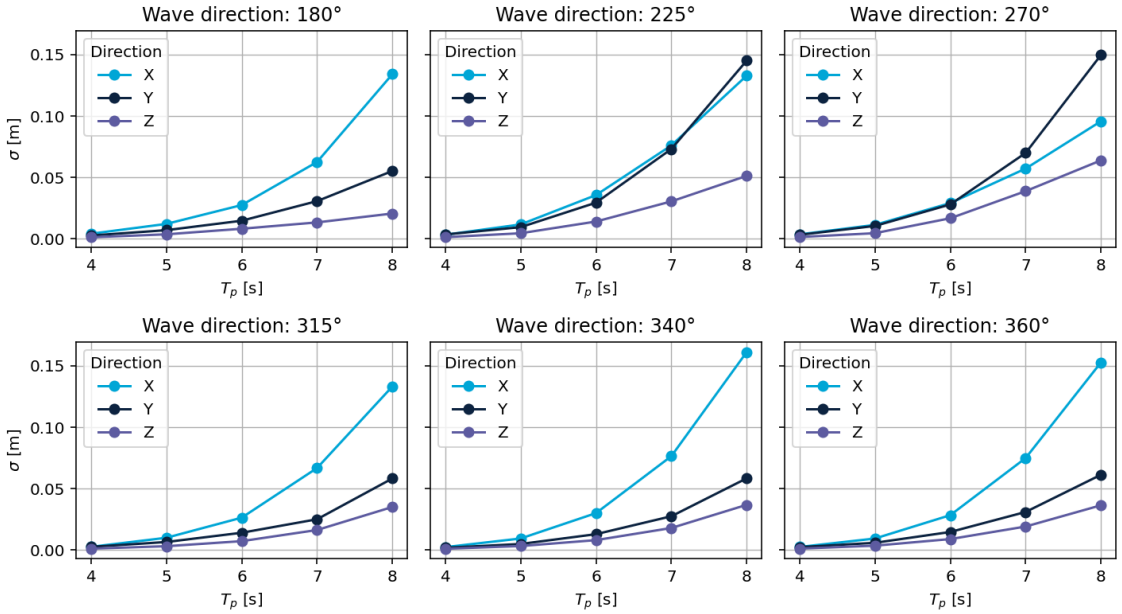

Figure 6.14: Standard deviation of the SSCV whip motions as a function of peak period T_p, H_s = 1 m/s and no wind, for different wave directions in global coordinate system.

It can be clearly observed that the predominant head seas at $180°$, $315°$, $240°$, and $360°$ follow the standard deviation trend characteristic of the full head seas, as illustrated in Figure 6.13 for the representative directions of $180°$ and $360°$. In these head sea conditions, the most significant signal deviations occur along the x-axis.

These trend also show for the predominant beam seas, $225°$ and $270°$, however for these seas large standard deviations of whip motions also arise along the y-axis.

Wave Direction Effect on Blade Root

Lastly, the dynamic response of the blade root is analysed, which is presented in Figure 6.15.

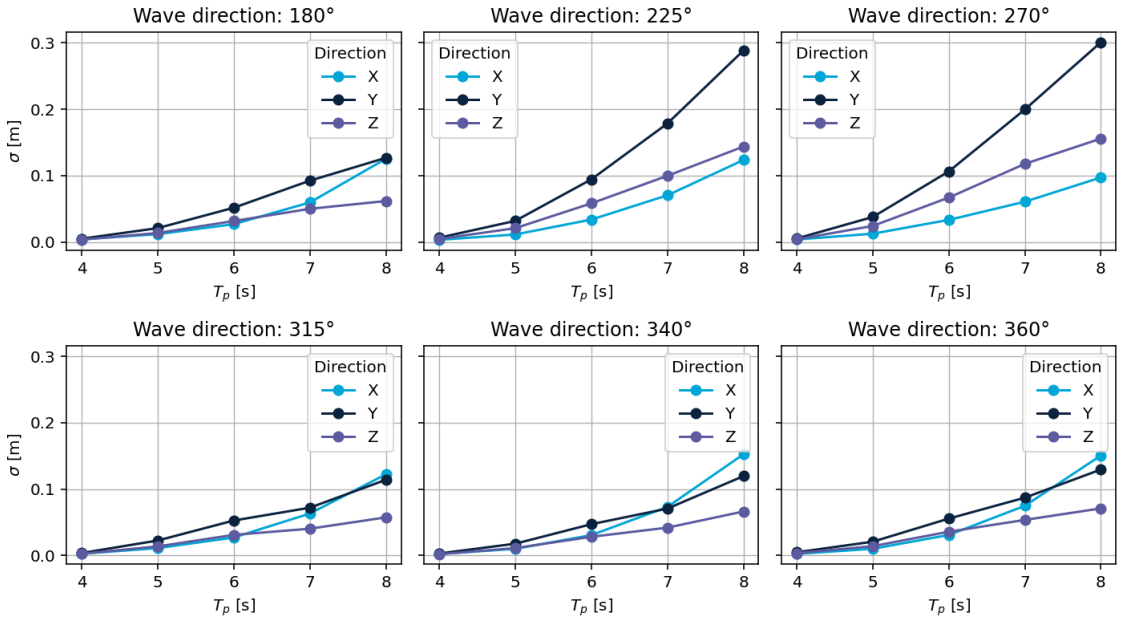

Figure 6.15: Standard deviation Blade Root motions as a function of peak period T_p, H_s = 1 m/s and no wind, for different wave directions.

The tuggers are effective along their own line of action and therefore primarily act along the global x-axis of the system. Consequently, the standard deviation for the blade root motion along the x-axis is the same as that of the whip, showing that the blade does not move significantly relative to the crane in this direction, but rather follows it motions.

However, for all wave directions, the motion in y-axis is larger than that of the whip. This can be attributed to the pendulum motion of the lifting configuration along the y-axis and the fact that the tuggers do not constrain this motion as effectively as they do along the x-axis. The relative motion between blade root and crane is governed by the pendulum mode.

This indicates that the displacement pattern of the blade root matches that of the whip along the x-axis. However, in the y- and z-axes, the standard deviations are greater, which is attributable to the flexibility of the lifting arrangement in these directions. This flexibility results from the selected tugger configuration and could therefore be modified by adjusting the tugger setup.

To assess the spatial effect of different wave directions on the whip and blade root motions, the whip and blade root motions relative to their static positions are depicted for wave directions of $180°$ and $270°$ in Figure 6.16a and Figure 6.16b, respectively.

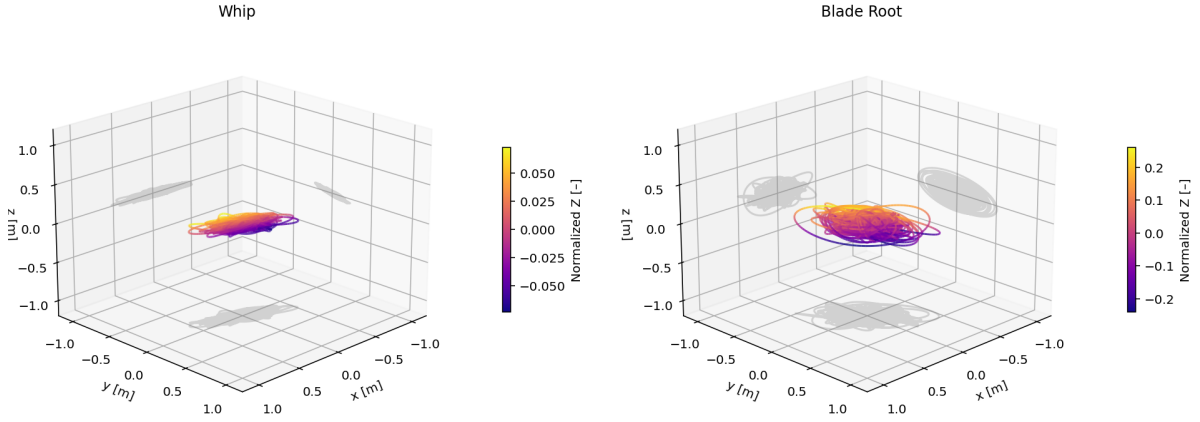

(a) Wave direction: $180°$

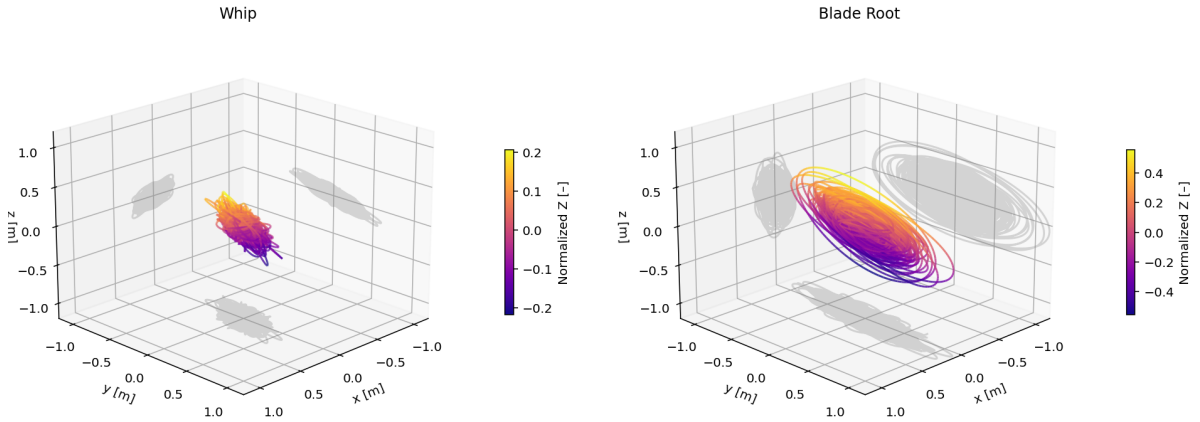

(b) Wave direction: $270°$

Figure 6.16: 3D trajectories of the whip motions and blade root motions for $H_s = 1$ m and $T_p = 8$ s for two wave directions $180°$ and $270°$.
The installation configuration consists of a feathered suspended blade, a crane block height of 159.4 m, tugger stiffness of 100 N/m, and a tugger width of 15 m. No wind is considered.

For the wave direction of $180°$, the whip trajectory show larger motions along the x-axis as a result of

vessel pitching. The blade root exhibits relatively increased motions along the y-axis compared to the whip, which can be attributed to the pendulum motion of the blade as previously explained.

Then for the wave direction of $270°$, the whip shows largest motions in the y-direction due to vessel rolling. In this case the blade root shows even greater motions along the y-axis, also due to the pendulum motion of the blade.

The motions along the x-axis remain similar for the whip and blade root for both wave directions, indicating that the blade root closely follows the whip displacements and is effectively restrained in this direction.

Overall this shows that the blade is effectively constrained by the tuggers in x-axis, however in y-axis, and z-axis the blade root shows larger motions, showing relative displacement between SSCV and blade due to pendulum motions.

Tugger Check

As explained previously in Section 5.2, compression in the tuggers is not permissible in the simulation, as it would render the results invalid. These compression occur when the blade undergoes significant excitations and moves towards the crane boom, in reality this would lead to slacking of the tugger. The simulations in which compression occurred at any point during the 30-minute operation simulations are listed in Table 6.1.

Table 6.1 shows that for beam seas with wave heights of 2 m or greater and longer wave periods, compression occurs in the tuggers. In contrast, oblique to head-sea wave directions exhibit smaller standard deviations and consequently fewer instances of compression, indicating that these wave directions are preferred with respect to maintaining tension in the tuggers.

The least compression instances occur for the dominantly head-sea of $180°$. Only wave conditions with a peak period of 8 s and a significant wave height of 3 m lead to compression and thus unrealistic simulation results. Also, in reality this would lead to slacking of the tuggers, making the operation under these conditions is not feasible.

Therefore, adjustments to the configuration are necessary to prevent snap loads in these conditions. Possible measures to mitigate snap loads are explored in the sensitivity study presented in Chapter 7.

Table 6.1: Tuggers with negative tension in simulation grouped by wave direction and sea state (H_s, T_p)

Wave Direction	H_s, T_p	Tuggers with negative tension
$180°$	3.0, 8	4_Down_SB
$225°$	2.0, 8	4_Down_SB
	2.5, 8	4_Down_SB, 4_Down_PS
	3.0, 7	4_Down_SB, 4_Down_PS
	3.0, 8	4_Down_SB, 4_Down_PS
$270°$	2.0, 8	4_Down_PS
	2.5, 7	4_Down_PS
	2.5, 8	4_Down_SB, 4_Down_PS
	3.0, 6	4_Down_SB, 4_Down_PS
	3.0, 7	4_Down_SB, 4_Down_PS
	3.0, 8	4_Up_SB, 4_Down_SB, 4_Down_PS

6.3.2. Wind Effect

The dynamic effect of wind on the blade root motion is examined a direction of $180°$, given that for other wind directions, the aerodynamic loading is reduced, as the wind approaches at an angle and the cross-flow principle applies. Therefore, this case represents the governing scenario. The standard deviations of the blade root motions are depicted in Figure 6.17.

The aerodynamic centre of the blade does not align with the centre of mass, therefore for tugger systems with lower pre-tension, blade yaw is likely to arise. In this case, the tuggers are highly pre-tensioned due to which the blade does not yaw under the de-centralized aerodynamic load. Furthermore, the considered wind range does not lead to negative tension values in the simulation.

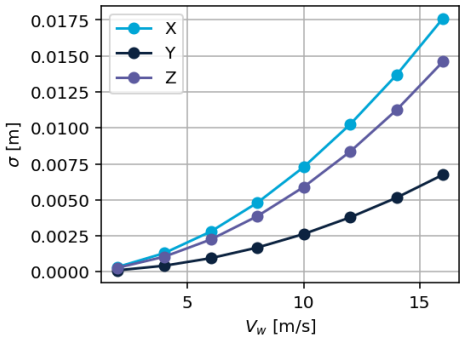

Figure 6.17: Standard deviation of blade root motions as a function of peak mean wind speed Vw. The suspended blade is feathered with the trailing edge into the wind

The increase in standard deviation is consistent with theoretical expectations, as aerodynamic loads scale quadratically with wind velocity. Therefore, an increase in the mean wind speed leads to a quadratic increase in the displacement of the blade root. The standard deviations of the blade root motions induced by the wind are however relatively small, similar to the wind effect on the hub motions.

Suspended Blade Pitch

The pitch of the suspended blade is evaluated for two configurations: feathered ($180°$) and stalled ($270°$). The feathered configuration is expected to produce the smallest standard deviations, as the aerodynamic loading on the blade is minimised. However, to assess the overall effect of aerodynamic loading on blade root motion, both pitch settings are examined. The resulting lift and drag distributions along the blade for a constant wind speed of 10 m/s are shown in Figure 6.18 for both pitches.

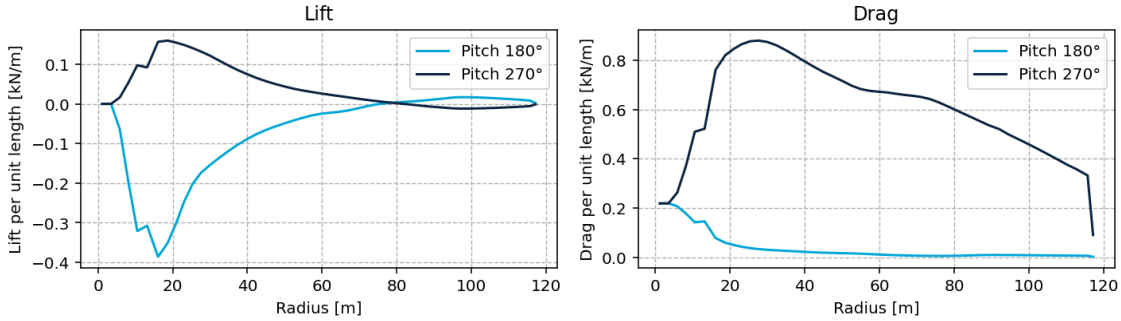

Figure 6.18: Lift and drag distribution along an OWT turbine blade for two different pitch angles: $180°$ and $270°$.

At a pitch angle of $180°$, the trailing edge faces directly into the wind, resulting in negative lift and negligible drag forces. At $270°$, the blade is stalled, producing maximum drag and only a small lift component. This shows that for the different pitches the aerodynamic loading of the suspended blade differs, as expected. The effect these different aerodynamic loading has on the on the blade root motion is presented by the standard deviation of the blade root motion in Figure 6.19 for both pitches.

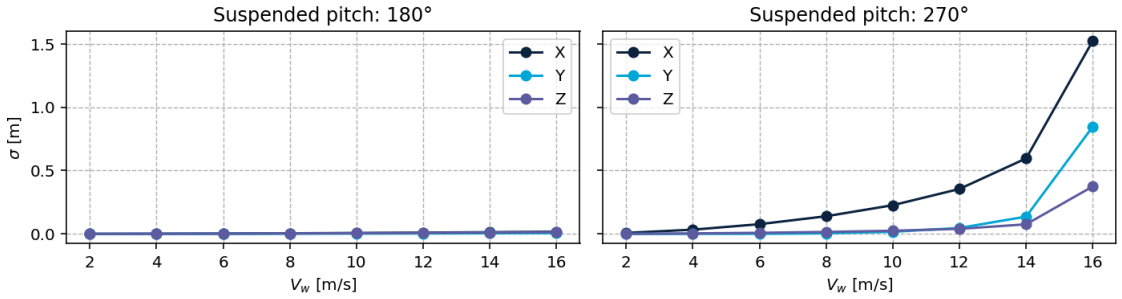

Figure 6.19: Standard deviation of blade root motion as a function of mean wind speed V_w for different pitch angles of the suspended blade. Results are shown for a pitch of $180°$ (trailing edge into the wind) and for a pitch of $270°$ (blade stalled with the broadside facing the wind).

For the configuration where the trailing edge faces into the wind, the standard deviation of the blade root displacement is negligible, indicating that the wind has no effect on the blade root motion across all wind speeds. In contrast, for the stalled configuration, the standard deviation of the blade root motions become very high at higher wind speeds.

Therefore, the feathered position is preferred, as it minimises the aerodynamic loads and, consequently, the wind-induced excitations of the blade root.

6.3.3. Blade Root Dynamics Summary

The dynamic analysis of the blade root motions indicates that predominantly head seas result in smaller displacements and optimal performance of the tugger system.

For these wind-wave direction, the maximum standard deviation of the wave-induced blade root motion reaches approximately 12.5 cm for a significant wave height of 1 m.

The wind-induced excitations are smaller in comparison. The standard deviation of the blade root motions induced by wind about 2 cm in the x-direction at a mean wind speed of 16 m/s. Note however that this is the case for the optimal pitch configuration, where the blade is pitched with the trailing edge facing the wind.

For a differently pitched suspended blade, for example a stalled blade, the blade root motion would be governed by wind-induced motions at higher mean wind speeds.

For the installation configuration, with a feathered suspended blade, the wave-induced loading is the dominant factor governing the displacement behaviour of the blade root.

6.4. Dynamic Analysis of the Relative Motions Between Hub and Blade Root

This section presents the relative spatial dynamic behaviour between the blade root and the hub, highlighting how different environmental factors influence each component. The relative effect on the dynamic behaviour of both components is induced by waves is examined first, followed by the effect of wind.

The installation configuration considered is one where all blades are feathered with the trailing edge facing into the wind, as this setup yielded the most favourable results in the preceding analyses, for both the hub motions as well as the blade root motions.

Furthermore, a wind and wave direction of $180°$ is selected based on the outcomes of the previous sections. Another consideration in selecting this wave direction is that wave reflections from the SSCV back to the MP, which could induce additional loading, are unlikely to occur in this configuration. Since such effects are not modelled, it is preferable to choose a configuration in which such effects are not expected to arise.

6.4.1. Wave Effect

The spatial relative motions between the hub and blade root for waves from $180°$ are shown in Figure 6.20. The figure illustrates that the hub primarily moves along the wind-wave direction, while the blade root exhibits motion along all three axes, indicating distinct dynamic behaviour for each component.

Notably, the dynamic behaviour is strongly influenced by the peak period of the waves. As the peak period approaches a natural period of the system, the motion of the corresponding component increases. The component exhibiting the largest motion therefore depends on the peak period. As a result, the relative dynamic behaviour is not governed by a single component, but rather by the combined dynamic behaviour of both systems. Therefore the dynamic behaviour of both the hub and the blade root need consideration for the installation operation.

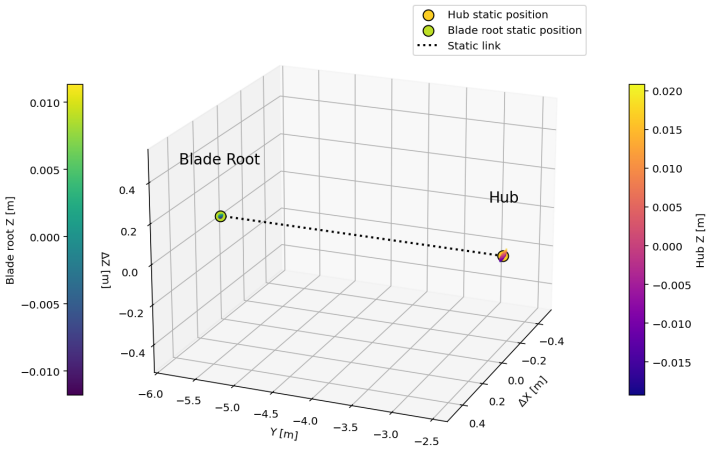

(a) $T_p = 4\,\text{s}$

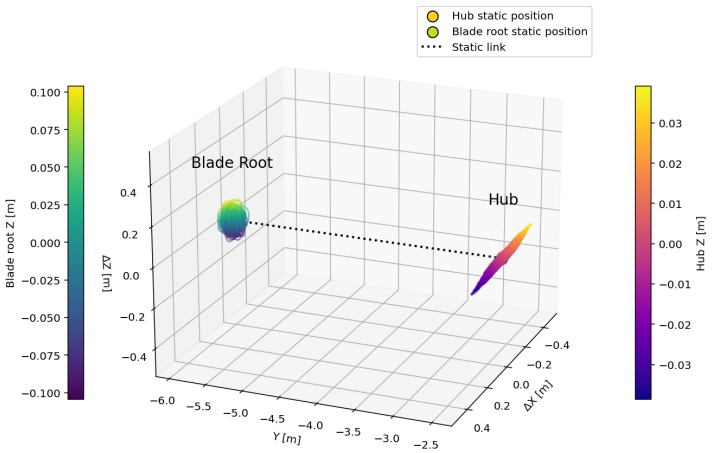

(b) $T_p = 6\,\text{s}$

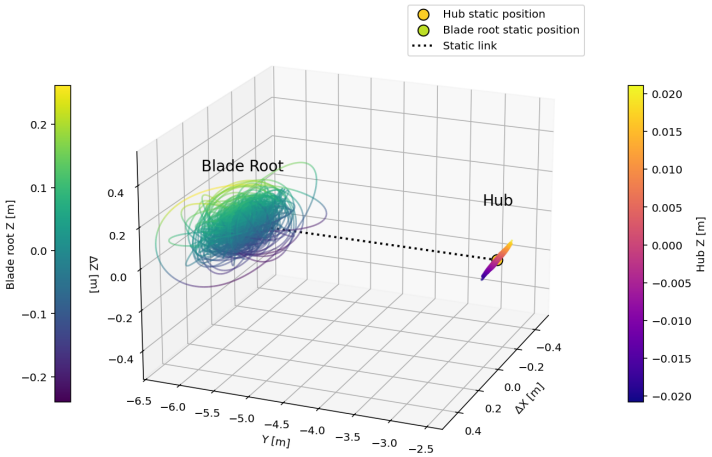

(c) $T_p = 8\,\text{s}$

Figure 6.20: Three-dimensional trajectories of hub and blade root motions for $H_s = 1\,\text{m}$ and three peak period values ($T_p = 4, 6, 8\,\text{s}$). No wind is considered. The configuration includes two feathered installed blades pitched and a feathered suspended blade, a crane block height of 159.4 m, tugger stiffness of 100 N/m, and a tugger width of 15 m.

6.4.2. Wind Effect

The spatial relative motions between the hub and blade root for wind from $180°$ are shown in Figure 6.21. In this case the wind is perpendicular on the blade resulting in the governing loading case. The figure illustrates that, similar to the wave effect, the hub primarily moves along the wind-wave direction, while the blade root exhibits motion along all three axes, indicating different dynamic behaviour for each component. Furthermore, the wind-induced motions are greater for the blade root than for the hub.

Figure 6.21a shows that for low mean wind speeds, the standard deviations of both the hub and blade root displacements are small. Figure 6.21b shows that as the wind speed increases, the displacements of both the hub and blade root increase due to the greater aerodynamic forces acting on the system. The hub motions occur primarily along the x-axis wind propagation direction, whereas the blade root experiences motions along all three axes. Particularly for the blade root motions, these higher wind speeds can result in excursions from the static position of up to 3 cm.

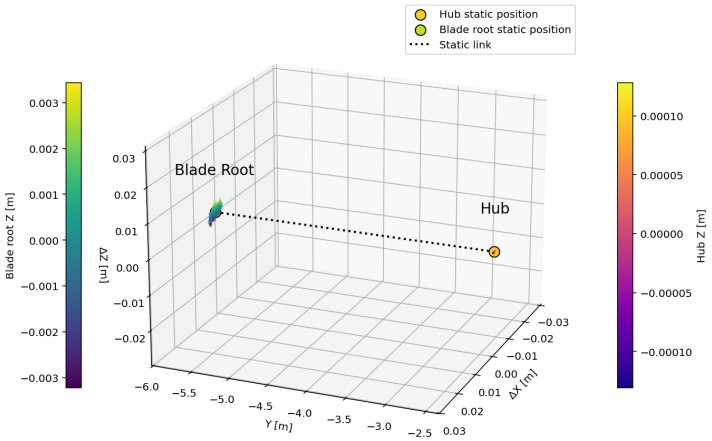

(a) $V_w = 4$ m/s

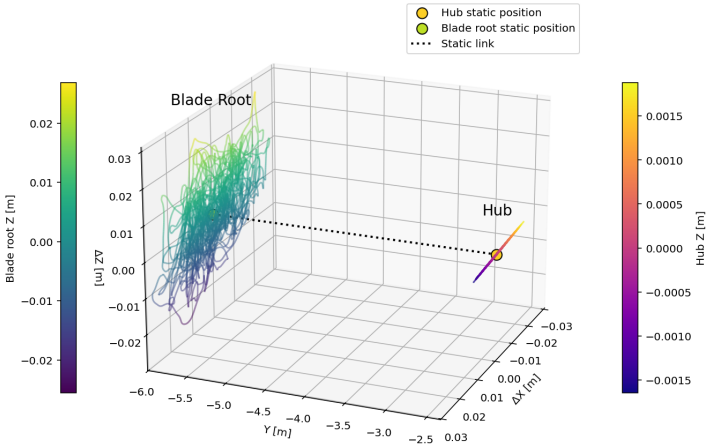

(b) $V_w = 12$ m/s

Figure 6.21: Three-dimensional trajectories of the hub and blade root motions for two wind speeds: $V_w = 4$ m/s and $V_w = 12$ m/s from direction $180°$. No waves are considered. The configuration includes two installed blades and one suspended blade, all feathered with the trailing edge facing into the wind.

6.4.3. Relative Hub and Blade Root Dynamics Summary

The hub and blade root both show different dynamic behaviour both under wave-, and wind loading. Where the hub moves along the primary excitation axes, the blade root moves along all principle axes.

Whether the hub motions or the blade root motions are dominant depends on the peak period of the

waves: for peak periods close to the first natural period of the OWT, the hub motion are more significant, whereas for larger peak periods, the blade root motion are largest due to the increased SSCV and possible pendulum motions. It is therefore essential to account for both components during the installation process.

Furthermore, for the relative dynamic behaviour, the effect of wind remains relatively small compared to that of waves when considering the standard deviations of both components. However, examining the three-dimensional trajectories reveals that at a wind speed of 12 m/s, wind-induced blade root motions can result in peak excursions of up to 3 cm.

Given that the operability assessment is based on how often the relative displacement between the hub and blade root exceeds a defined safety boundary of 20 cm, as described in Subsection 3.1.3, blade root excursions of 3 cm are of the same order of magnitude and therefore significant in this context. Although the overall wind-induced motions are small, the impact of wind-induced maximum excursions cannot be neglected in the subsequent sensitivity and operability studies.

6.4.4. Key Operational Drivers

Based on the dynamic analysis conducted in this chapter, the key operational drivers have been identified to guide the selection of parameters for the subsequent sensitivity study in the next chapter. These include: (i) the *natural frequency of the turbine*, since the largest hub displacements occur due to wave excitations near this frequency; (ii) the *SSCV response*, as a substantial portion of the blade excitations is induced by the vessel's motions; (iii) the *natural frequency of the pendulum*, which governs larger excitations transverse to the action line of the tuggers.

7

Sensitivity study of the operation

This chapter presents a sensitivity study aimed at understanding the influence of various parameters on the dynamic analyses from the preceding chapter.

The dynamic response derived from the numerical simulations depends on many parameters, making the system inherently complex. Identifying the most influential parameters is essential for validating the simulation results, gaining insight into the key factors driving system behaviour, and identifying potential improvements.

The parameters analysed in this chapter are categorised into three subgroups: simulation parameters, operational parameters, and environmental parameters, as outlined in Figure 7.1. The simulation and environmental parameters are examined to evaluate the sensitivity of the results to these factors. This assessment determines whether the parameters have a significant impact on the simulation outcomes and whether the results can be considered robust.

The operational parameters are investigated to assess how the relative motions respond to different configuration settings. Parameters related to the bottom-fixed OWT are evaluated qualitatively, while the remaining operational parameters are examined through sensitivity analyses using time-domain simulations. Understanding these sensitivities is essential for identifying the most critical factors to consider when planning and executing the operation. To support the interpretation of certain sensitivities, spectral density plots are provided in Appendix B and are referenced in the text where relevant.

This chapter concludes with a summary of all sensitivities. Based on the findings, a selection is made of parameters that demonstrate a positive impact on relative motion between the hub and the blade root. These insights form the basis for an improved configuration studied in the operability study presented in Chapter 8.

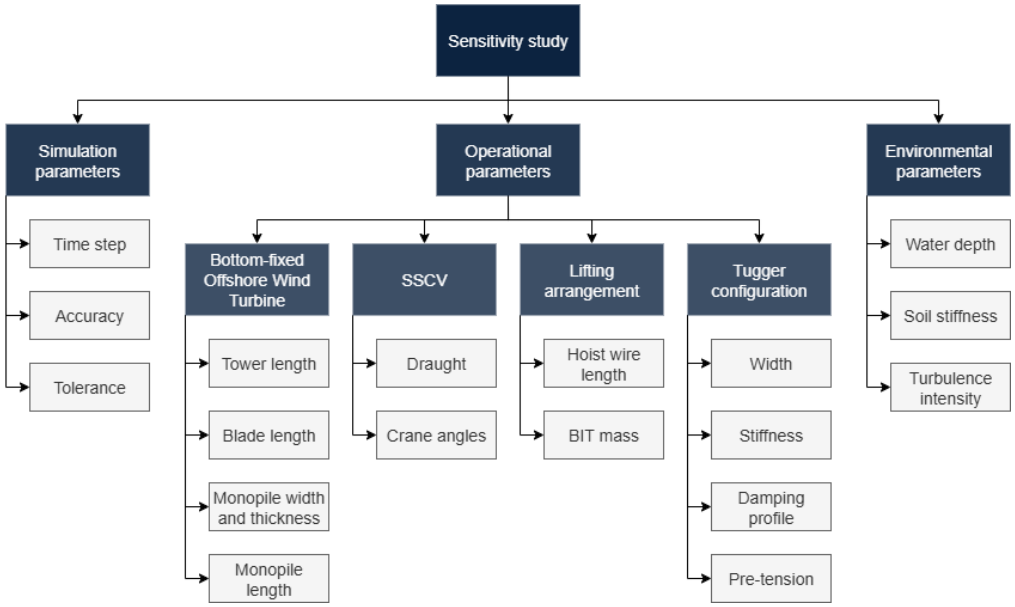

Figure 7.1: Overview of the parameters analysed in the sensitivity study presented in this chapter.

7.1. Reference Case

This section introduces the reference case used as the baseline for the sensitivity study. The reference case is selected to represent typical environmental conditions at the fictional site. The operational parameters are based on those used in the previous chapter, with adjustments made where improvements in dynamic behaviour were identified.

The considered wind speed is 12 m/s, and the significant wave height is 1 m, corresponding to a realistic wind-wave combination at the fictional site, derived from Equation 2.6. The full range of peak periods T_p is evaluated, given the strong influence of this parameter on the relative behaviour, as demonstrated in the previous chapter.

The wind and wave directions are both set to $180°$. The configuration includes two installed blades in the hub and one blade suspended by the crane. All blades are feathered, with their leading edges facing into the wind. The tugger system is characterised by a tension stiffness of 100 kN/m, a pretension of 100 kN, and a tugger width of 15 m. Damping profile 1 is applied to represent the system's damping characteristics.

The standard deviations of the hub and blade root motions for the reference case are presented in Figure 7.2a and Figure 7.2b, respectively.

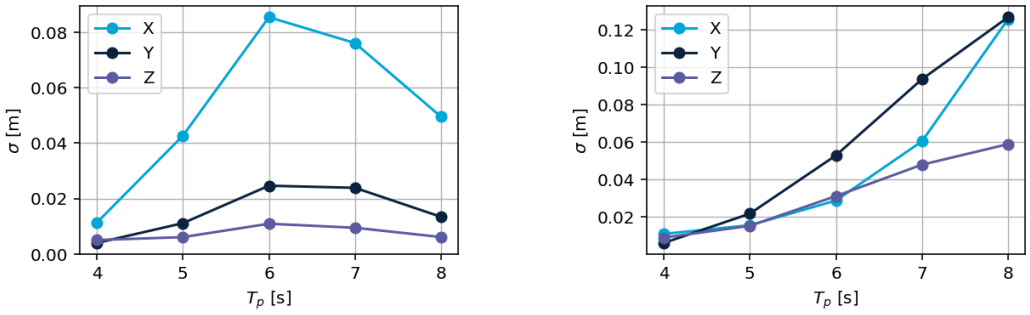

(a) Standard deviation of the hub motions for the reference case

(b) Standard deviation of the blade root motions for the reference case

Figure 7.2: Sensitivity study reference case motions

7.2. Simulation Parameters

A sensitivity study was conducted to verify the adequacy of the selected configurations for the dynamic simulations, as outlined in Subsection 3.3.4. The parameters varied during this investigation included the time step, the number of iterations, and the tolerance level. Specifically, the time step was reduced from the original value of 0.1 seconds to 0.01 seconds and 0.001 seconds. The number of iterations was increased from 100 to 200 and 400, while the tolerance was tightened from $100 \cdot 10^{-6}$ to $10 \cdot 10^{-6}$ and $1 \cdot 10^{-6}$.

Smaller time steps and tighter tolerances generally lead to more precise simulation results. However, fewer iterations typically reduce the solution accuracy. If the refined simulations with smaller time steps and tighter tolerances had produced significantly different outcomes, it would suggest that the original configurations missed important details and required adjustment. In this study, the results remained consistent, indicating that the original simulation parameters are adequate.

7.3. Operational Parameters

This section presents the operational parameters considered in the sensitivity analysis, which are derived from the identified key operational drivers from the previous chapter.

The first sensitivity study focuses on the natural frequency of the offshore wind turbine. Parameters examined include structural characteristics of the turbine, such as variations in tower height and blade length, as well as modifications to the MP, including changes in outer diameter, wall thickness, and embedment depth.

For the second key operational driver, the response of the SSCV, the analysis considers variations in vessel draught and crane boom angle to assess their effect on vessel motions and the resulting influence on blade dynamics.

Finally, the natural frequency of the pendulum system is examined by varying the lifting configuration and tugger line properties to assess their effect on the blade dynamics. For the lifting configuration, the hoist wire length and the mass of the BIT are studied. For the tugger arrangement, parameters such as the tugger width, stiffness, damping characteristics, and pretension levels are evaluated.

7.3.1. Turbine Structural Parameters

Given that the detailed specifications of the turbine and MP lie outside the scope of HMC, and recognising that these components are typically designed to meet specific site constraints and performance requirements, it is assumed that the turbine and MP design will generally require favourable conditions for installation. However, in light of the industry trend towards larger turbines, a theoretical sensitivity study is presented to examine how key structural parameters influence the dynamic response of a bottom-fixed OWT, based on the principles outlined in Chapter 2 and the 1 DoF model described in Chapter 4.

A general sensitivity overview for the key parameters is provided at the end of this section, which also reflects on current industry trends and their implications for installation operations. For reference, the turbine parameters used in the analysis are illustrated in the schematic representation of the OWT shown in Figure 7.3. Note that in this analysis, the symbol $\propto$ denotes a direct proportional relationship, whereas $\sim$ indicates that the variables scale similarly, though the relationship may be influenced by other factors or hold only approximately.

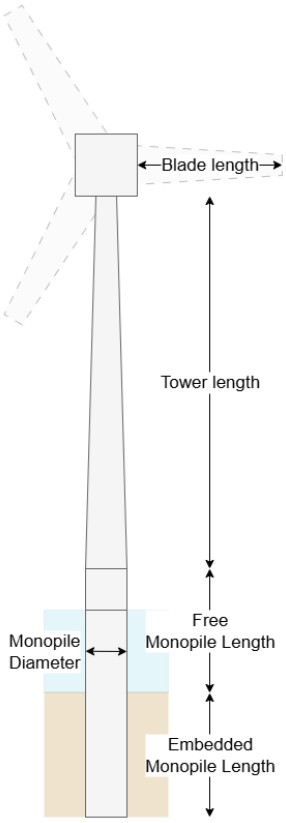

Figure 7.3: Schematic overview of the OWT, highlighting studied parameter definitions.

Longer Tower

The total length of the support structure is given by

$$L = L_{\text{tower}} + L_{\text{MP, free}} + L_{\text{MP, embedded}}.$$

Increasing the tower length extends the cantilevered portion above the seabed, which reduces the structural bending stiffness. This relationship for the tower segment, is described by

$$k_{\text{beam}} \propto \frac{1}{L_{\text{tower}}^3}.$$

Since the soil stiffness remains constant, this reduction in bending stiffness lowers the overall effective system stiffness, denoted as k_{eff}. Assuming a constant average distributed mass per unit length, the total effective mass increases linearly with tower length. As a result, the combined effect of decreased stiffness and increased mass leads to a reduction in the natural frequency of the system.

Larger Blade

A larger blade results in greater wind-induced excitations due to the increased aerodynamic surface area exposed to the flow. However, when the blade is feathered with the trailing edge facing into the wind, these excitations remain minimal because the aerodynamic forces are significantly reduced in this orientation. Additionally, increasing the blade length increases the mass at the blade tip,

$$m_{\text{tip}} \sim L_{\text{blade}},$$

causing the effective mass to scale proportionally, as

$$m_{\text{eff}} \propto m_{\text{tip}}.$$

The combined effect of the larger blade is a lower natural frequency of the system and a tendency for larger dynamic responses under unsteady wind loading.

A larger blade results in greater wind-induced excitations due to the increased aerodynamic surface area exposed to the flow. However, when the blade is feathered with the trailing edge facing into the wind, these excitations remain minimal because the aerodynamic forces are significantly reduced in this orientation. Additionally, increasing the blade length increases the mass at the blade tip,

$$m_{\text{tip}} \sim L_{\text{blade}},$$

causing the effective mass to scale proportionally, as

$$m_{\text{eff}} \propto m_{\text{tip}}.$$

The combined effect of the larger blade is a lower natural frequency of the system and a tendency for larger dynamic responses under unsteady wind loading. Furthermore, for a larger blade within the lifting configuration, rotations of the BIT result in greater motions due to the increased lever arm.

Increased MP Diameter and Wall Thickness

An increase in the MP outer diameter D_o, while keeping the wall thickness t constant, affects both the soil–structure interaction and the overall turbine dynamics. According to the soil stiffness model presented in Appendix A, the translational soil stiffness components, k_x and k_z, are directly proportional to the pile radius, implying that

$$k_{\text{soil, translational}} \propto D_o.$$

The rotational soil stiffness components, k_ψ and k_ϕ, scale with the cube of the pile radius, leading to

$$k_{\text{soil, rotational}} \propto D_o^3.$$

For the structural response, the bending stiffness of the MP scales with the fourth power of the diameter,

$$EI \propto D_o^4,$$

which implies that the structural beam stiffness k_{beam} similarly scales as

$$k_{\text{beam}} \sim D_o^4.$$

Assuming a thin-walled cylinder where $D_o^2 - D_i^2 \approx 2D_o t$, the distributed mass of the MP, m', is proportional to the outer diameter, so the effective mass of the system, m_{eff}, also scales with diameter:

$$m_{\text{eff}} \sim D_o.$$

Combining the soil and structural stiffness in series, the effective stiffness of the system scales with

$$k_{\text{eff}} \sim \frac{1}{\frac{1}{D_o^4} + \frac{1}{D_o}}.$$

Consequently, the natural frequency of the system, given by Equation 4.6, increases with a larger MP diameter, since the scaling of the effective stiffness outweighs the linear scaling in effective mass.

If the wall thickness does differ and scales with the diameter, such that $t \propto D_o$, then the distributed mass becomes proportional to the square of the outer diameter,

$$m' \propto D_o^2,$$

and the effective mass of the system scales accordingly as

$$m_{\text{eff}} \sim D_o^2.$$

In this case, the natural frequency still increases with diameter, but less steeply than for constant thickness, as the increase in effective stiffness continues to dominate over the quadratic growth in effective mass. Therefore, a larger MP diameter generally results in a stiffer system with a higher natural frequency.

Longer MP

The effect of increasing the MP length depends on which portion of the MP is extended. The free length, $L_{\text{MP, free}}$, is the submerged portion above the seabed, while the embedded length, $L_{\text{MP, embedded}}$, is the portion below the seabed within the soil. As stated before, the total length of the support structure is given by

$$L = L_{\text{tower}} + L_{\text{MP, free}} + L_{\text{MP, embedded}}.$$

When increasing the free length of the MP, $L_{\text{MP, free}}$, while keeping the embedded length constant, the cantilevered portion below the tower is extended. This reduces the structural bending stiffness of the free length segment according to

$$k_{\text{beam}} \sim \frac{1}{L^3_{\text{MP, free}}}.$$

This behaviour is thus similar to the effect of increasing the tower length. With the soil stiffness unchanged, this reduction in beam stiffness decreases the overall effective stiffness, k_{eff}. The distributed mass per unit length remains constant, so the total effective mass grows linearly with the free MP length. As a result, the combination of lower stiffness and greater mass reduces the natural frequency of the system.

Conversely, if the embedded length $L_{\text{MP, embedded}}$ is increased, the soil stiffness rises due to the greater soil–structure interaction depth. According to the translational soil stiffness model, the horizontal soil stiffness scales quadratically with embedment depth, so

$$k_{\text{soil}} \propto h^2,$$

for a fixed pile diameter. Therefore, increasing the embedded length enhances soil stiffness, which raises the effective stiffness of the system, assuming that the beam stiffness remains unchanged.

However, regardless of which length is increased, the distributed mass per unit length remains constant. Thus, the total effective mass m_{eff} increases linearly with the total MP length:

$$m_{\text{eff}} \sim L_{\text{MP}}.$$

Consequently, when only the free length is increased, the combination of reduced structural stiffness and increased mass results in a lower natural frequency. If the embedded length increases, the gain in soil stiffness partially compensates the reduction in beam stiffness, but the larger effective mass still leads to an overall decrease in the natural frequency, as given by Equation 4.6.

In summary, extending the MP generally lowers the system's natural frequency, with the magnitude of this effect depending on whether the free or embedded length is increased.

Overall Turbine Sensitivities

The key parameters discussed above demonstrate that they influence both the stiffness and the mass of the system and, consequently, affect the natural frequencies of the turbine structure. A shift in natural frequencies results in different dynamic response of the hub. These key parameters can therefore be adjusted such to achieve a configuration that best meets the site-specific boundary conditions. For example, designing a larger MP (increased stiffness, k) to support a heavier turbine (increased mass, m) will shift the natural frequency depending on the relative change in these two parameters: if the stiffness increases faster than the mass, the natural frequency rises; if the mass increases more than the stiffness, the natural frequency decreases.

The dynamic analysis presented in Chapter 6 shows that the first natural frequencies of the bottom-fixed OWT significantly influence the hub's dynamic response when the peak wave period approaches the natural period of the structure. Therefore, to minimise the hub's dynamic response, it is preferable to ensure that the natural frequencies lie outside the dominant excitation range, thereby avoiding resonance.

In line with the industry trend towards larger turbines, it has been observed that larger turbines generally exhibit lower natural frequencies due to increased structural mass (Varghese et al., 2022). To minimise

dynamic response, the system stiffness must be increased proportionally, which can be achieved, for example, by enlarging the MP dimensions and increasing the embedment depth. However, these measures entail additional costs and may introduce fabrication and transportation challenges due to the larger structural dimensions. It therefore cannot be assumed that the turbine and MP will always be designed such that the natural frequencies fall outside the excitation range. Consequently, the natural frequency of the bottom-fixed OWT should be carefully considered when preparing the installation procedure.

7.3.2. SSCV Parameters

The parameters examined for the SSCV are the draught and the crane angles. For the draught, simulations are performed to assess its effect on the blade root motions, as it does not influence the displacement of the hub. The impact of the crane angles is addressed through a theoretical approach.

Draught

Changing the vessel draught alters its dynamic behaviour, particularly its natural frequencies, which in turn affect both the magnitude and character of the vessel's motions under wave loading. To investigate the impact of draught on the dynamic behaviour of the SSCV and its implications for the installation operation, a deeper draught of 26.6 m is compared to the base configuration draught of 16.6 m. The corresponding modes, natural frequencies, and periods of the SSCV for both draughts are presented in Table 7.1.

Table 7.1: Comparison of natural frequencies and corresponding periods of the suspended blade on the SSCV model for two draught configurations.

#	Mode	26.6 m draught		16.6 m draught	
		Frequency [Hz]	Period [s]	Frequency [Hz]	Period [s]
1	Yaw	0.0065	153.90	0.0082	121.77
2	Surge	0.0065	153.07	0.0079	126.83
3	Sway	0.0080	124.67	0.0096	104.24
4	Roll	0.0529	18.91	0.0550	18.19
5	Blade yaw	0.0663	15.08	0.0667	14.98
6	Pitch	0.0686	14.58	0.0880	11.37
7	Heave	0.0838	11.94	0.1082	9.25
8	Pendulum in y-axis	0.1114	8.98	0.1127	8.88
9	Pendulum in x-axis	0.1722	5.81	0.1751	5.71
10	Crane block pendulum y	0.1884	5.31	0.1908	5.24
11	Crane block pendulum x	0.5434	1.84	0.5648	1.77
12	Out-of-phase boom rotation	0.8248	1.21	0.8285	1.21
13	In-phase boom rotation	0.8412	1.19	0.8521	1.17
14	Blade heave	13.7740	0.07	13.3713	0.07

The vessel natural periods of yaw, surge, sway, pitch, and heave increase significantly. The resulting effects on the translational and rotational motions of Thialf for are illustrated in Figure 7.4 and Figure 7.5, respectively, alongside the reference case draught of 16.6 m.

Given the change in dynamic behaviour caused by the increased draught, this sensitivity study also considers multiple wave directions to evaluate the combined effects of beam, head, and oblique seas together with draught on the vessel response. Wave directions of $180°$, $225°$, and $270°$ are considered, which are illustrated in Figure 6.2.

Furthermore, to isolate the effect of draught, the lifting arrangement remains unchanged. Consequently, the blade is positioned 10 meters below the installation height. This approach ensures that only the impact of draught variation is assessed, excluding lifting arrangement effects already addressed in the previous section. It is important to note that if Thialf were to be used for the actual installation, the lifting arrangement or crane tip height would need to be adjusted to position the blade at the required installation height.

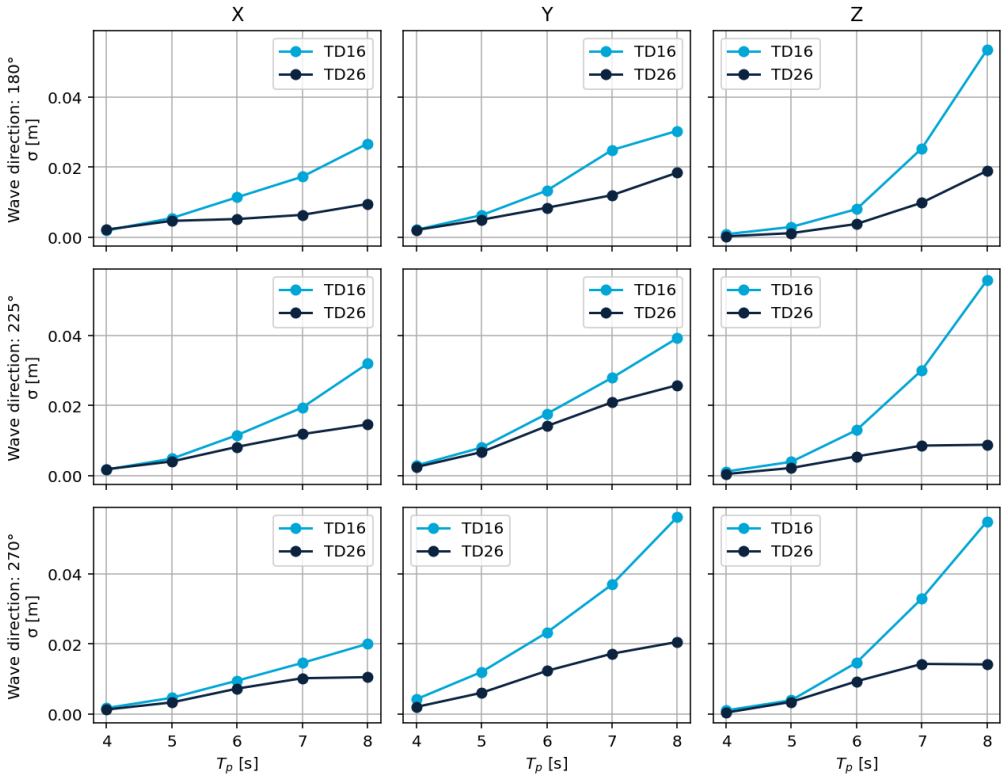

Figure 7.4: Standard deviations of the SSCV translational motions over peak periods T_p at draughts of 16.6 m and 26.6 m, for wave directions of $180°$, $225°$, and $270°$

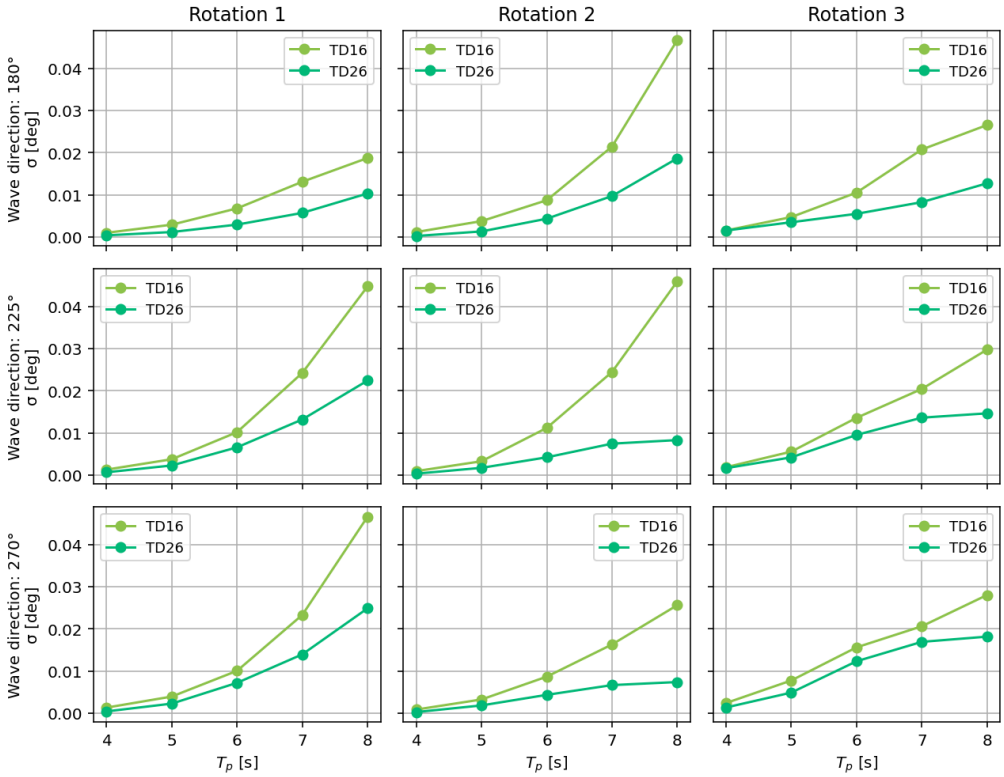

Figure 7.5: Standard deviations of the SSCV rotational motions over peak periods T_p at draughts of 16.6 m and 26.6 m, for wave directions of $180°$, $225°$, and $270°$

Examining the translational and rotational motions of Thialf, it is evident that the overall responses are larger for the 16.6-meter draught compared to the 26.6-meter draught configuration across all degrees of freedom.

Furthermore, the different sea conditions, namely head seas, beam seas, and oblique seas, result in varying responses of the Thialf. To assess whether this affects the installation configuration, the blade root responses for the three wave directions and both draught conditions are presented in Figure 7.6. The results show that, regardless of draught, a wave direction of $180°$ leads to the smallest blade root motions and is therefore the most favourable orientation for installation.

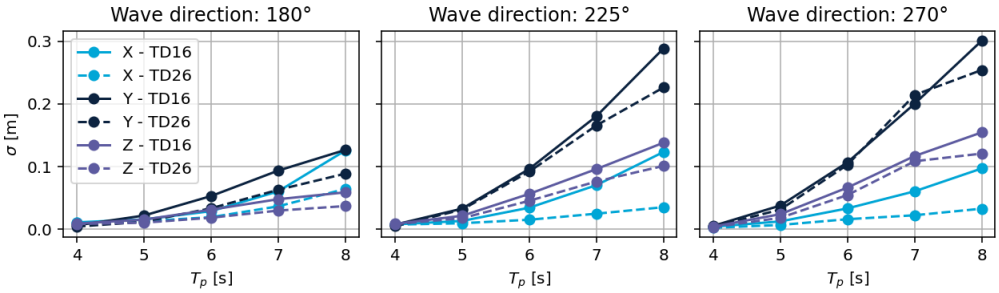

Figure 7.6: Standard deviation of the blade root translational motions for different wave directions.

To assess the effect on the increased draught on the installation configuration, the dynamic behaviour of the SSCV is first analysed, followed by the evaluation of the BIT motions. Finally, the blade root motions are assessed. This analysis is conducted for a wave direction of $180°$.

The dynamic response of the SSCV is governed by the combined characteristics of the load RAOs and the wave spectrum. A response occurs at frequencies where both the RAOs and the wave spectrum have non-zero values, leading to peaks in the spectral density. These peaks indicate the frequencies at which energy is transferred from the waves to the vessel.

The vessel response can be amplified by resonant behaviour, which occurs when wave frequencies align with the vessel's natural frequencies. In such cases, a distinct peak appears in the spectral density at the corresponding natural frequency.

A clear trend observed in the standard deviations of the translational and rotational responses for both draughts, shown in Figure 7.4 and Figure 7.5, respectively, is that the overall motion amplitudes of the vessel increase with larger peak wave periods. This indicates that, at longer wave periods, more wave energy falls within the frequency range where the load RAOs are significant, leading to amplified vessel motions.

Furthermore, the spectral densities for the larger peak periods ($T_p = 6$, 7, and 8 s) of the translational and rotational motions of the SSCV, shown in Subsection B.1.1, reveal that for the 16.6 m draught, significant peaks in z-translation and Rotation 2 occur at $T_p = 7$ and 8 s. These correspond to heave and pitch motions, with peaks occurring around 0.1 Hz, which matches the heave natural frequency (0.1 Hz) and is close to the pitch natural frequency (0.09 Hz). This indicates that the heave and pitch motions of the vessel are coupled and experience resonant amplification when the wave energy aligns with these natural frequencies. As a result, in addition to the general increase in motion amplitudes due to the longer wave periods, resonance further amplifies the z-translation and Rotation 2 responses for the 16.6 m draught.

The overall translational and rotational motion of the BIT are given in Figure 7.7 and Figure 7.8. These graphs also show larger motions for the increasing peak periods, similar to the SSCV. Furthermore, the spectral densities for the larger peak periods ($T_p = 6$, 7, and 8 s) of the translational and rotational motions of the BIT, shown in Subsection B.1.2, show that the BIT exhibits similar spectral peaks in the

translation in x-axis, and in Rotation 2, as the vessel pitch. This is due to the BIT being well constrained by the tuggers in these degrees of freedom, causing it to closely follow the vessel's motion. Additionally, the large length of the crane boom amplifies the effect of the Thialf's pitch rotation, resulting in significant BIT translations along the x-axis.

The BIT also exhibits significant peaks in Rotation 1, with frequencies aligning with both the pitch and roll frequencies of the vessel. Similarly, the y-translation shows peaks near the pitch frequency, and Rotation 3 corresponds to the vessel's yaw motion. These observations indicate that the BIT is influenced through multiple coupling mechanisms with the vessel's dynamic motions.

In contrast, no significant motions or spectral density peaks are observed in the z-translation of the BIT compared to the other directions, indicating that the vessel's heave motion is not directly transmitted as pure heave to the blade. Instead, coupling between the vessel's heave and the pendulum-like motion of the blade contributes to the Rotation 1 response observed in the BIT.

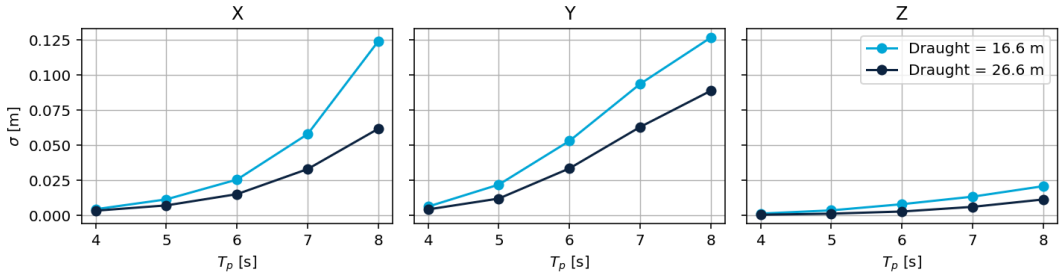

Figure 7.7: Standard deviations of the translational motions of the BIT for draughts of 16.6 m and 26.6 m at a wave direction of $180°$

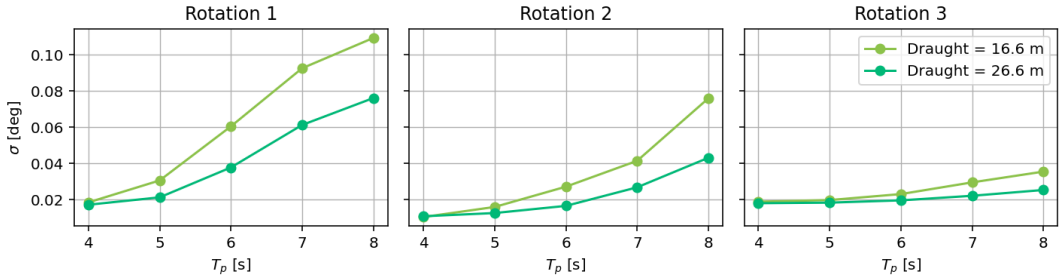

Figure 7.8: Standard deviations of the rotational motions of the BIT for draughts of 16.6 m and 26.6 m at a wave direction of $180°$

The resulting blade root motions for this configuration are presented in Figure 7.9, which shows that the blade root motions along the x- and y-axes closely follow those of the BIT. The displacement along the z-axis is primarily caused by the roll motion (Rotation 1) of the BIT.

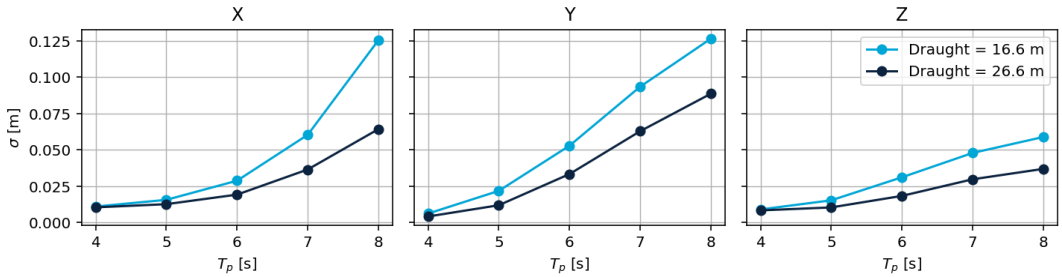

Figure 7.9: Standard deviations of the translational motions of the blade root for draughts of 16.6 m and 26.6 m at a wave direction of $180°$

It is important to note that reaching the required installation height would require adjustments, such as increasing the crane tip height. This would not only involve modifications to the crane itself but would also amplify the impact of Thialf's rotations on the blade displacements due to the increased lever arm. As a result, translational motions are expected to slightly increase in this scenario. A second option is to shorten the lifting arrangement. The effects of this modification are examined in Subsection 7.3.3.

This sensitivity study demonstrates that the dynamic response of the SSCV is governed by the vessel's natural frequencies and the frequency content of the incoming waves, as expressed through the load RAOs. For both draught configurations, the overall motion amplitudes increase with larger peak wave periods. However, the deeper draught results in reduced vessel motions, due to the downward shift of the SSCV's natural frequencies, moving them away from the dominant energy in the wave spectrum. Spectral densities of the BIT motions indicate that they are driven by the vessel's dynamics and transmitted through coupling mechanisms. As a result, the reduced vessel motions at greater draught also lead to decreased motions of the BIT and blade root. Among the wave directions considered, a heading of $180°$ produces the smallest blade root excitations and is therefore selected for further analysis.

Crane Angles

The sensitivity of blade root motions to crane angles arises from the crane functioning as a geometrical extension of the vessel, while the connection between the crane whip and the suspended blade allows limited hinging. This motion is strongly constrained by the suspension wire, which has a very high axial stiffness. This extreme stiffness is due to the crane being designed for very large offshore lifts, far exceeding the weight of a single blade. As a result, the crane tip closely follows the vessel's deck motions combined with the crane's rigid-body geometry.

As previously stated, vessel rotations can result in significant whip motions. The manner in which these rotations manifest at the whip is governed by the crane angles. The slew and boom angles together define the spatial configuration of the crane relative to the vessel's centre of gravity and therefore influence the rigid-body dynamics of the system.

The crane angles are primarily determined by the reach required for the operation. During the planning and selection process, the impact of these angles on the dynamic response should be evaluated to achieve the most favourable configuration. The current reference case represents a well-balanced setup, providing an effective compromise between operational reach and motion sensitivity.

7.3.3. Lifting Configuration

The parameters examined for the lifting configuration include the suspension length and the effect of increasing the mass of the BIT, as illustrated in Figure 7.10. These parameters influence the blade root motions, but do not affect the displacements of the hub. Therefore, only the blade root displacements are considered in this part of the sensitivity study.

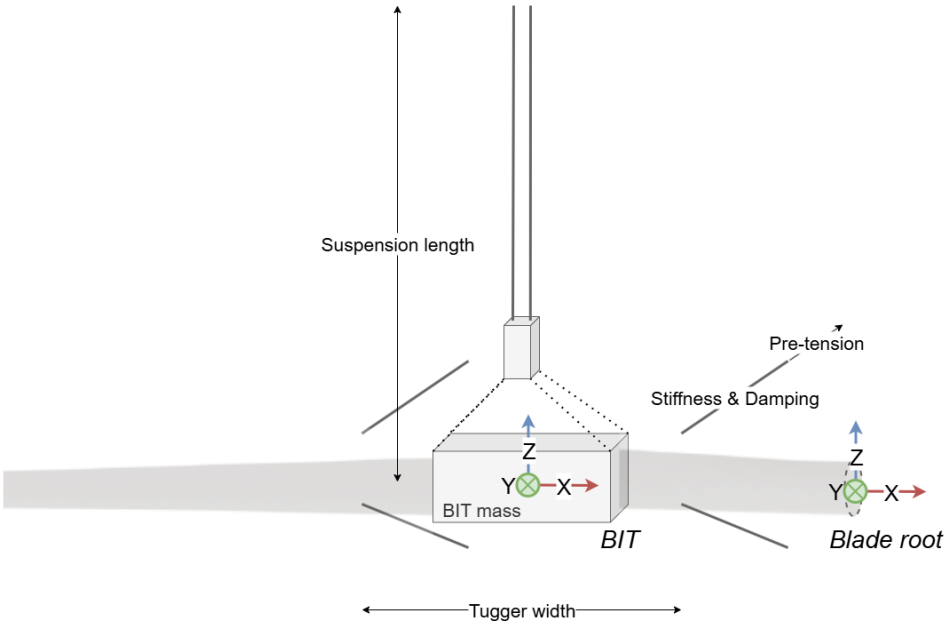

Figure 7.10: Schematic overview of the lifting configuration and tuggers, highlighting studied parameter definitions.

Suspension Length

The suspension length is defined as the distance between the crane tip and the centre of the BIT. This subsection examines how variations in this length affect the blade root motions.

Although the lifting arrangement does not behave as a conventional pendulum, it exhibits similar dynamic characteristics. The suspension length directly influences the effective pendulum length, as described in Equation 5.2, and thus affects the associated natural frequency. Increasing the suspension length is expected to result in a longer natural period, shifting the pendulum mode further away from the dominant excitation frequencies and potentially reducing resonant amplification.

In the reference case, the pendulum-like motion in the y-axis couples with both the vessel's pitch and heave motions, amplifying blade root displacements. Modifying the suspension length alters the natural frequency of the pendulum mode and, consequently, the nature and strength of this dynamic coupling. This sensitivity study therefore focuses on the pendulum mode in the y-axis, vessel pitch, and heave, to assess how changes in suspension length influence blade root motions through their interaction.

Table 7.2 presents the natural frequencies and corresponding natural periods for the three modes: heave, pitch, and pendulum in y-axis, as derived from the modal analysis for the systems with the varying suspension lengths. The natural period of the pendulum indeed increases for longer suspension lengths. Note that the suspension length of 25 m corresponds to the reference case.

Table 7.2: Natural periods and corresponding frequencies of SSCV heave and pitch modes along with the blade pendulum mode in the y-direction for different suspension lengths.

Suspension Length [m]	Mode	Frequency [Hz]	Period [s]
15	Vessel Pitch	0.0879	11.372
	Vessel Heave	0.1082	9.246
	Blade Pendulum y	0.1177	8.498
25	Vessel Pitch	0.0879	11.372
	Vessel Heave	0.1081	9.248
	Blade Pendulum y	0.1127	8.872
35	Vessel Pitch	0.0880	11.367
	Vessel Heave	0.1083	9.233
	Blade Pendulum y	0.1074	9.314
45	Vessel Pitch	0.0880	11.363
	Vessel Heave	0.1082	9.243
	Blade Pendulum y	0.1029	9.719

To examine the impact of these different natural frequencies on blade root motions, the BIT translations and rotations are first analysed, as shown in Figure 7.11 and Figure 7.12, respectively. Subsequently, the blade root translations are considered.

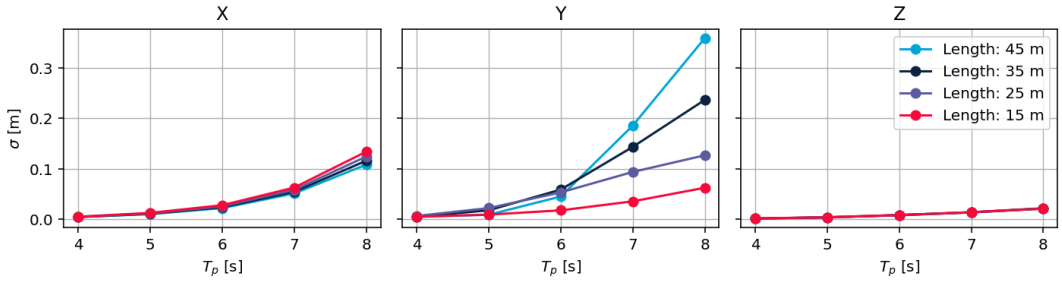

Figure 7.11: Standard deviations of the translational motions of the BIT at a wave direction of $180°$, for varying suspension lengths.

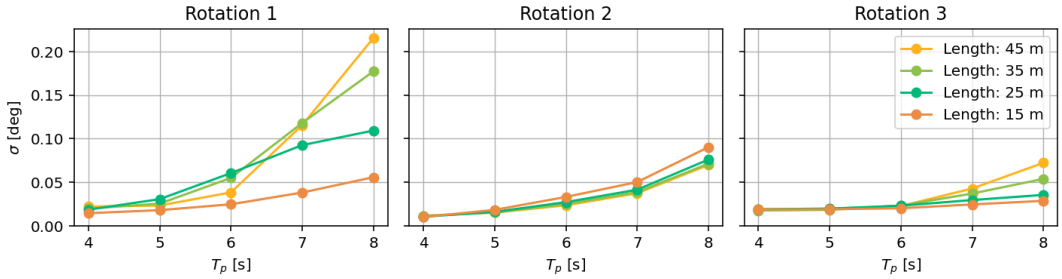

Figure 7.12: Standard deviations of the rotational motions of the BIT at a wave direction of $180°$, for varying suspension lengths.

The BIT motion along the x-axis are larger for shorter suspension lengths. This is attributed to the blade being positioned closer to the crane tip and farther from the vessel's centre of gravity, which amplifies the effect of vessel rotations on the BIT. More pronounced, however, are the motions in translation along the y-axis and rotation about the x-axis (Rotation 1).

The spectral density plots in Subsection B.2.1 for $T_p = 7$ and 8 s exhibit clear peaks in these degrees of freedom for suspension lengths of 45, 35, and 25 m, corresponding to the observed increased motions.

The peak spectral density value increases with decreasing suspension length, consistent with the rise in natural frequency of the pendulum mode, as shown in Table 7.2. Furthermore, the spectral density peaks decrease for shorter suspension lengths, indicating that less energy is present in this mode, which corresponds to the reduced BIT motions observed.

For a draught of 16.6 m, the Thialf exhibits dominant heave and pitch responses near 0.1 Hz. When the blade pendulum frequency approaches this value, increased spectral energy is observed, demonstrating that the vessel's motion excites the pendulum mode. As the suspension length decreases, the pendulum frequency diverges from the vessel's dominant frequency, leading to less BIT motion.

These findings indicate that significant pendulum excitation occurs when the vessel's dynamics couple with the pendulum mode. Longer suspension lengths align more closely with the vessel's heave and pitch frequencies, resulting in larger responses. In contrast, shorter suspensions experience less coupling and smaller motions.

The standard deviations of the blade root motions are shown in Figure 7.13. As expected, since the blade and BIT are rigidly connected, the blade root translations in the x- and y-directions closely follow those of the BIT. The translations along the z-axis can be attributed to BIT rotations about the x-axis, which cause the blade to rotate accordingly, resulting in z-displacements at the blade root.

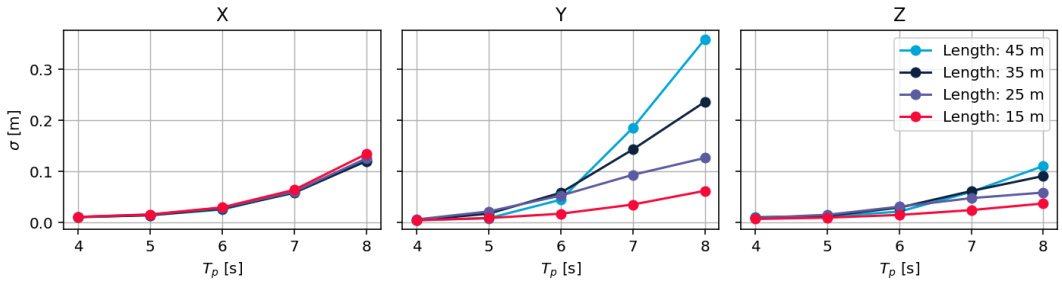

Figure 7.13: Standard deviations of the translational motions of the blade root at a wave direction of $180°$, for varying suspension lengths.

In summary, the suspension length directly influences the natural frequency of the pendulum mode. This mode is effectively excited when its natural frequency aligns with the vessel's dominant response frequencies. For the longer suspension lengths studied, the pendulum mode frequency approaches that of the SSCV's heave and pitch motions, resulting in significant blade root motions.

BIT Mass

The effect of the BIT mass is examined by comparing the standard deviations of BIT and blade root motions for BIT masses equal to two and three times the original mass of 100 tonnes. The mass moments of inertia of the BIT are adjusted accordingly, with the corresponding values presented in Table 7.3.

Table 7.3: Moments of inertia for BIT for various masses

Mass [t]	I_x [t·m²]	I_y [t·m²]	I_z [t·m²]
100	1,354.17	541.67	1,354.17
200	2,708.33	1,083.33	2,708.33
300	4,062.50	1,625.00	4,062.50

Similar to the suspension length, an increase in BIT mass alters the pendulum characteristics and consequently affects the coupling of the pendulum with the SSCV motions. The natural frequencies for the pendulum and heave and pitch of the SSCV for the three BIT masses are presented in Table 7.2.

Table 7.4: Natural periods and corresponding frequencies of coupled and uncoupled blade pendulum modes in the y-direction for different BIT masses.

BIT mass [t]	Mode	Frequency [Hz]	Period [s]
100	Pitch	0.0879	11.372
	Heave	0.1082	9.246
	Pendulum y	0.1177	8.498
200	Pitch	0.0874	11.447
	Heave	0.1081	9.255
	Pendulum y	0.1125	8.890
300	Pitch	0.0867	11.530
	Heave	0.1080	9.264
	Pendulum y	0.1123	8.903

The effect of these changes on the the translational and rotational motion of the BIT, is shown in Figure 7.14 and Figure 7.15.

Only minor differences are observed in the x-translation, which can be attributed to slight shifts in the pendulum natural frequency. A heavier BIT shifts this frequency closer to the vessel's heave and pitch response frequencies, resulting in higher spectral density peaks at the peak periods where heave and pitch are dominant, as shown in Subsection B.2.2. A similar effect is observed in Rotation 2.

The y-translations exhibit distinct dynamic behaviour depending on the BIT mass. The spectral density plots in Subsection B.2.2 show that, for the lighter BIT, y-translations are primarily driven by the sway and roll motions of the SSCV, resulting in larger responses at shorter peak periods (up to 7 seconds). In contrast, for the heavier BITs, clear spectral density peaks appear near the pendulum natural frequency, which is excited by the vessel's heave and pitch motions, as previously discussed. This occurs because the pendulum natural frequency shifts closer to the vessel's dominant response frequencies. As a result, y-translations increase for the larger peak periods of 7 and 8 seconds.

The same phenomenon affects Rotation 1. While sway and roll dominate for the reference BIT, the heavier BITs exhibit additional contributions from pendulum motion at the wave peak periods where pitch and heave motions of the vessel are amplified.

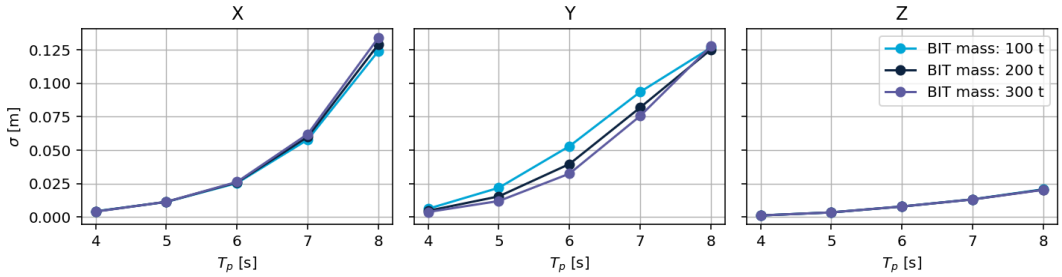

Figure 7.14: Standard deviations of the translational motions of the BIT at a wave direction of $180°$, for varying BIT mass.

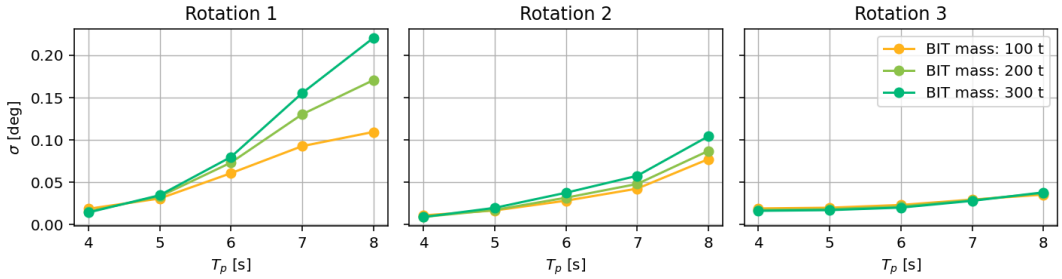

Figure 7.15: Standard deviations of the rotational motions of the BIT at a wave direction of $180°$, for varying BIT mass.

It is important to note that increasing the BIT mass also alters the pre-tension in the tuggers. The corresponding tugger tensions are shown in Figure 7.16 for both the upper port-side tugger at a peak period of 8 seconds. The figure indicates that the mean tension in the tuggers increases with BIT mass, along with greater deviations from the initial pre-tension. This suggests that the increased BIT motions lead to higher tension in the tuggers. The effect this has on the dynamic behaviour is further investigated in the subsection on tugger pre-tension in Subsection 7.3.4.

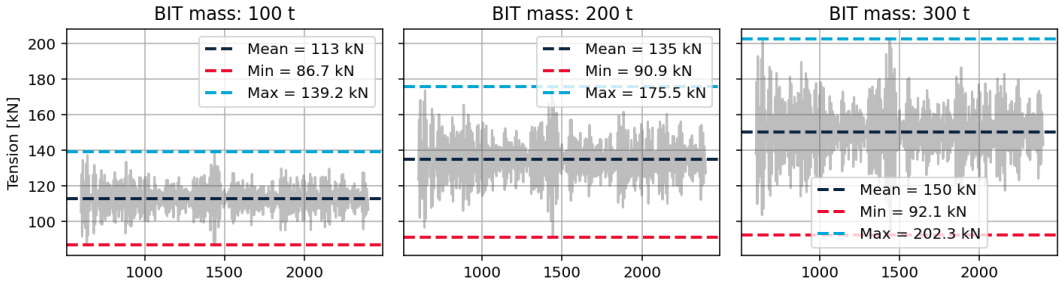

Figure 7.16: Tugger tension in the upper port-side tugger of the lifting arrangement for different BIT masses, for the reference case and T_p = 8 s.

Figure 7.17 shows the translational motions of the blade root. The motions in the x- and y-directions are similar to those of the BIT. However, the z-displacement exhibits distinct behaviour for different BIT masses, driven by BIT rotations about the x-axis (Rotation 1). These rotations induce increased blade root displacements in the z-direction, resulting in the largest z-translations for the heaviest BIT.

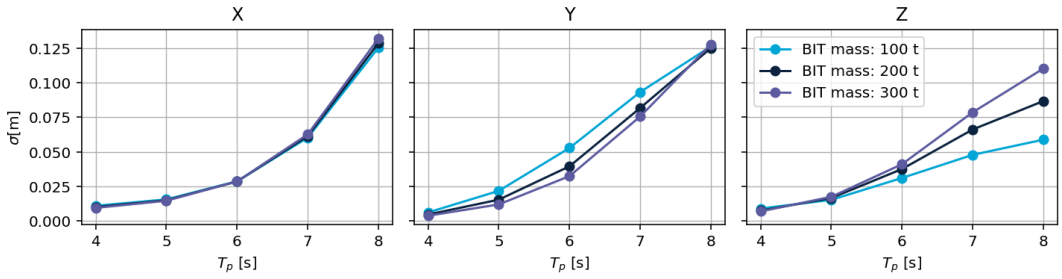

Figure 7.17: Standard deviations of the translational motions of the blade root at a wave direction of $180°$, for varying BIT mass.

Overall, increasing the BIT mass lowers the natural frequency of the pendulum mode and affects the tension in the tuggers. The considered heavier BITs align closer to the heave and pitch frequencies of the SSCV leading to larger BIT and blade root motions.

7.3.4. Tugger Specifications

The tuggers have a significant influence on the dynamic behaviour of the blade root. The parameters of the tugger configuration have been shown to strongly affect blade root motions during the setup of the model. In this study, several key parameters are examined, including the tugger width, line stiffness, damping characteristics, and pretension.

It is important to note that while the parameters of the current tugger setup can be adjusted, it is also possible to modify the overall configuration entirely. This alternative is discussed at the end of this subsection; however, detailed simulations and quantitative assessment of such a redesign fall outside the scope of this research.

Tugger Width

The tugger width is defined as the distance between the two tuggers, measured both at the BIT and at the crane boom, such that the overall tugger configuration remains consistent. The wider the tuggers are positioned along the y-axis, the greater the rotational moment they can resist, particularly in yaw, due to the increased lever arm. The effect of tugger widths of 5, 15, 25, and 35 m is evaluated, with the 15 m configuration serving as the reference case. This width approximately corresponds to the breadth of the crane. For configurations with tugger widths exceeding 15 m, additional structural elements would be required to support the extended span.

Adjusting the tugger widths alters the dynamic behaviour of the pendulum motion in the y-direction. As shown in Table 7.5, increasing the tugger width leads to an increase in the natural frequencies of both blade yaw and y-direction pendulum motion, while the natural frequency in the x-direction remains nearly constant. This indicates that wider tugger spacing introduces a stronger restoring moment about the vertical axis, increasing yaw stiffness and thereby raising the natural frequency from approximately 0.022 Hz at 5 meters to 0.153 Hz at 35 meters. Similarly, the increased lateral restraint limits swing in the y-direction, enhancing stiffness and thus increasing the natural frequency of the pendulum mode in that direction.

Table 7.5: Natural frequencies and corresponding periods for blade yaw and blade pendulum motions in the x- and y-directions for different tugger widths.

Tugger Width [m]	Mode	Frequency [Hz]	Period [s]
35	Blade Pendulum y	0.1423	7.028
	Blade Yaw	0.1526	6.553
	Blade Pendulum x	0.1746	5.728
25	Blade Pendulum y	0.1316	7.598
	Blade Yaw	0.1091	9.172
	Blade Pendulum x	0.1746	5.729
15	Blade Pendulum y	0.1126	8.880
	Blade Yaw	0.0667	14.980
	Blade Pendulum x	0.1751	5.710
5	Blade Pendulum y	0.0943	10.605
	Blade Yaw	0.0221	45.339
	Blade Pendulum x	0.1745	5.730

First the translational motions and rotational motions for the BIT are given in Figure 7.19 and Figure 7.18. Whereafter the resulting translational displacements of the blade root are shown in Figure 7.20.

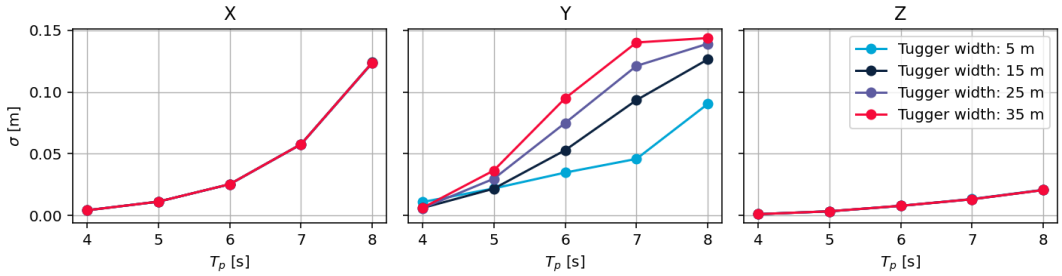

Figure 7.18: Standard deviations of the translational motions of the BIT at a wave direction of $180°$, for varying tugger widths.

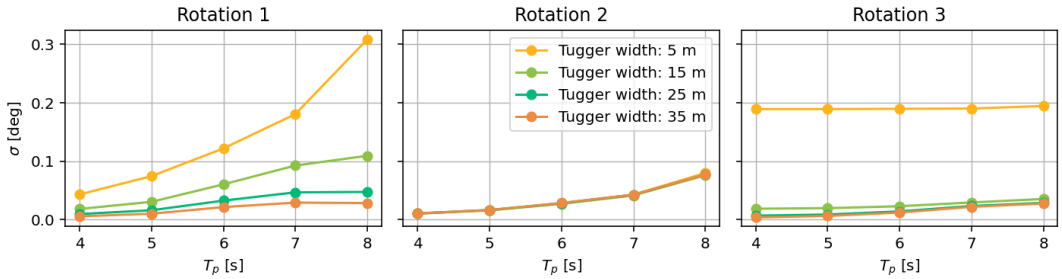

Figure 7.19: Standard deviations of the rotational motions of the BIT at a wave direction of $180°$, for varying tugger widths.

These graphs show that the translation along the x-axis and the rotation about the y-axis (Rotation 2), both aligned with the tugger action line, are strongly constrained due to the pre-tension in the tugger lines acting in these directions. As a result, the BIT closely follows the vessel's motion in these degrees of freedom. The tugger width has little influence on these responses, as they remain consistent across all configurations.

The rotation around the z-axis (Rotation 3), corresponding to the yaw motion of the blade, is effectively constrained for tugger widths greater than 5 m. At 5 m, the lever arm is too short to generate sufficient yaw resistance, resulting in a large yaw response. Wider tugger spacings provide a longer moment arm, enabling greater resistance to yaw motion.

The translations along the y-axis are larger for wider tugger configurations. The spectral density plots, as shown in Subsection B.3.1, reveal distinct peaks in y-translation near the pendulum natural frequencies for these configurations. The increased tugger width raises the natural frequency, thereby shifting the corresponding natural period into the excitation range. As a result, even modest vessel responses at these frequencies lead to pronounced spectral peaks in the y-translation due to resonance effects.

The rotation about the x-axis (Rotation 1), however, is more effectively constrained at larger tugger widths. Despite the presence of a resonant pendulum response, the increased spacing enhances the lever arm of the tuggers, thereby increasing the restoring moment that resists this rotation and compensating for the pendulum associated rotational effects.

The dynamic behaviour of the blade root, depicted in Figure 7.20, results from a combination of BIT translations and rotations. Motions along the x-axis arise from both x-translations and rotations about the z-axis (Rotation 3). The configuration with the smallest tugger width exhibits significantly larger motion in this direction, while the configurations with tugger widths of 15, 25, and 35 m show comparable x-axis motions.

Motions along the z-axis are primarily influenced by rotations about the x-axis (Rotation 1), as previously explained, which are largest for the smallest tugger width and decrease with increasing width. Displacements along the y-axis are dominated by the resonant pendulum motion, with higher amplitudes observed for larger tugger widths due to better alignment of the natural frequency with the wave excitation range.

Overall, the configuration with a tugger width of 15 m yields the smallest motions along the y-axis while maintaining acceptable behaviour in the other directions. This suggests that it provides the most favourable dynamic response among the configurations considered.

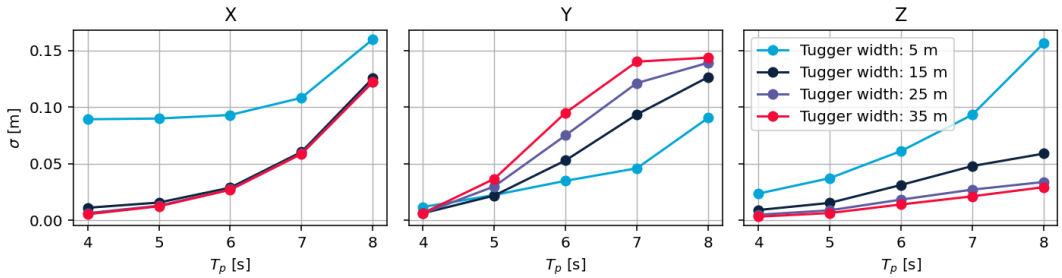

Figure 7.20: Standard deviations of the translational motions of the blade root at a wave direction of $180°$, for varying tugger widths.

Tugger Stiffness

Increasing the tugger stiffness enhances the restoring forces generated in response to displacements, thereby increasing the overall system stiffness. This results in higher natural frequencies for the pendulum motions in both the x- and y-directions, as well as for blade yaw mode. The corresponding natural frequencies and periods are presented in Table 7.6, where a stiffness of 100 kN/m represents the reference case.

Table 7.6: Natural periods and corresponding frequencies for blade yaw and blade pendulum motions in x and y directions at different tugger stiffnesses.

Tugger Stiffness [kN/m]	Mode	Period [s]	Frequency [Hz]
100	Blade Pendulum y	8.880	0.1126
	Blade Yaw	14.980	0.0667
	Blade Pendulum x	5.710	0.1751
200	Blade Pendulum y	7.719	0.1295
	Blade Yaw	11.679	0.0856
	Blade Pendulum x	4.767	0.2097
300	Blade Pendulum y	7.156	0.1398
	Blade Yaw	9.970	0.1003
	Blade Pendulum x	4.227	0.2365

Figure 7.21 and Figure 7.22 show the standard deviations of the translational and rotational motions of the BIT. It can clearly be seen that the systems exhibit similar dynamic behaviour for the different tugger stiffnesses.

For the translations in the y-direction, the highest tugger stiffness values result in slightly larger motions at peak periods of 6 and 7 seconds. This is also reflected in the modestly elevated spectral density peaks shown in Subsection B.3.2. At a peak period of 8 seconds, the y-translations are predominantly driven by the pendulum motion induced by the vessel's heave and pitch, resulting in a similar response across all three stiffness configurations.

For the rotations, it is observed that higher tugger stiffness leads to smaller motions in Rotation 1 and Rotation 2. This is also reflected in the larger spectral density peaks for the stiffer configurations, as shown in Subsection B.3.2. Higher tugger stiffness more effectively constrains the rotational movements of the BIT, as it can absorb greater forces and thereby resist larger rotational moments. Additionally, the resonant response in the y-direction pendulum motion decreases with increasing stiffness, as the corresponding natural frequency shifts further away from the vessel's heave and pitch response frequencies.

However, for the yaw motion (Rotation 3), the configuration with the highest stiffness results in slightly larger excitations compared to the lower-stiffness cases. This is attributed to the yaw natural frequency increasing with higher stiffness, causing it to align more closely with the vessel's response frequencies and leading to a minor resonant response at higher peak periods. Nevertheless, these yaw motions are effectively constrained by the very stiff tuggers, which prevent them from developing into significant rotational displacements along this axis.

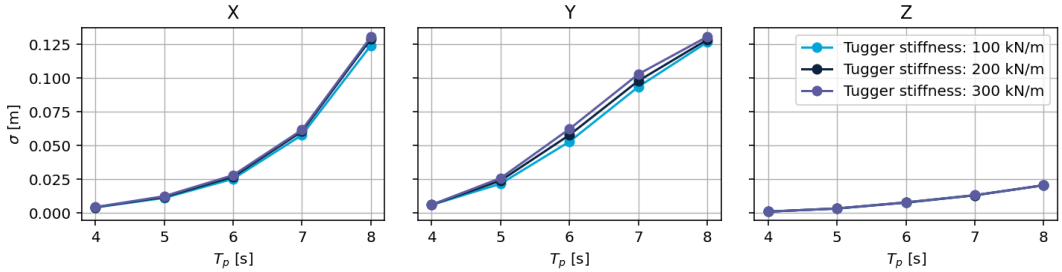

Figure 7.21: Standard deviations of the translational motions of the BIT at a wave direction of $180°$, for varying tugger stiffnesses.

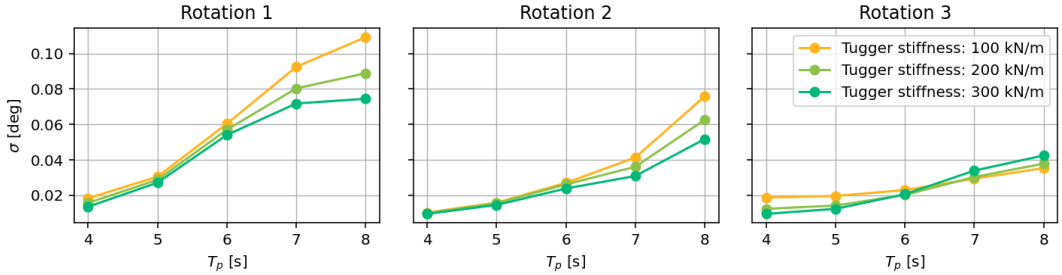

Figure 7.22: Standard deviations of the rotational motions of the BIT at a wave direction of $180°$, for varying tugger stiffnesses.

Figure 7.23 shows the standard deviations of the translational motions of the blade root. The translations in the x- and y-directions closely follow those of the BIT, with minor differences arising from the contributions of BIT rotational motions. The translation along the z-axis arise from the rotation of the BIT about the x-axis (Rotation 1).

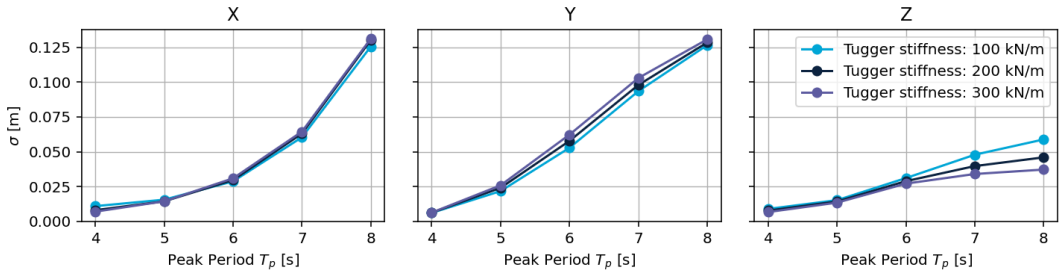

Figure 7.23: Standard deviations of the translational motions of the blade root at a wave direction of $180°$, for varying tugger stiffnesses.

Overall, the dynamic behaviour remains largely consistent across the different tugger stiffness configurations. Stiffer tuggers more effectively constrain rotational motions, resulting in slightly reduced blade root displacements along the z-axis. However, the effect is minimal.

Tugger Damping Profile

This section evaluates the influence of two damping profiles on the system's dynamic response, as illustrated in Figure 3.14. As previously discussed in Subsection 5.3.5, a decay test was used to assess their transient behaviour. Profile 1 showed a shorter transient time and was therefore selected as the baseline configuration throughout this research.

Damping primarily influences the amplitude of oscillations and the transient decay time, rather than altering the natural frequencies. The effect of the two profiles on the system's motion is evaluated using the BIT translational and rotational motions shown in Figure 7.24 and Figure 7.25, respectively. The resulting blade root motions are presented in Figure 7.26.

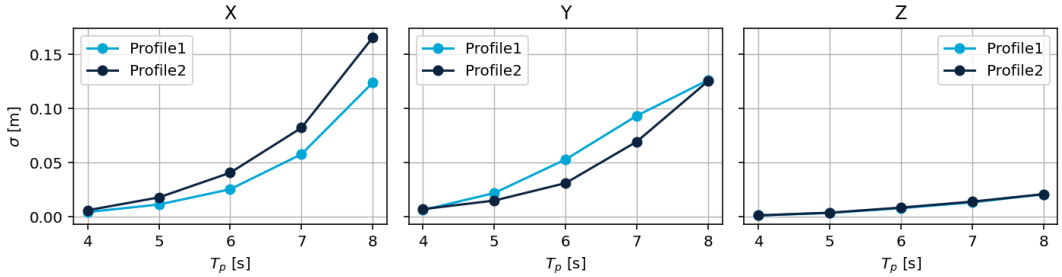

Figure 7.24: Standard deviations of the translational motions of the BIT at a wave direction of $180°$, for varying tugger damping profiles.

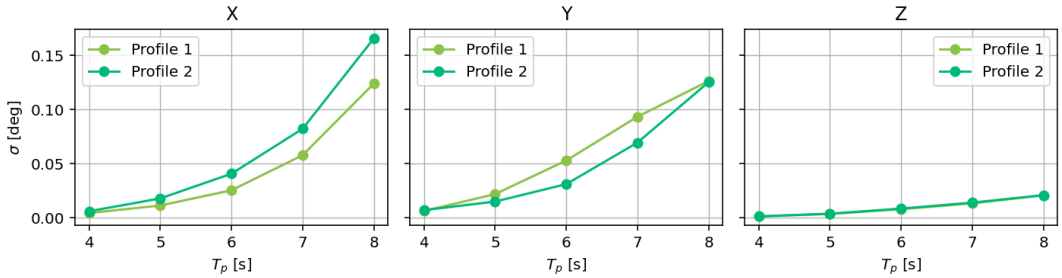

Figure 7.25: Standard deviations of the rotational motions of the BIT at a wave direction of $180°$, for varying tugger damping profiles.

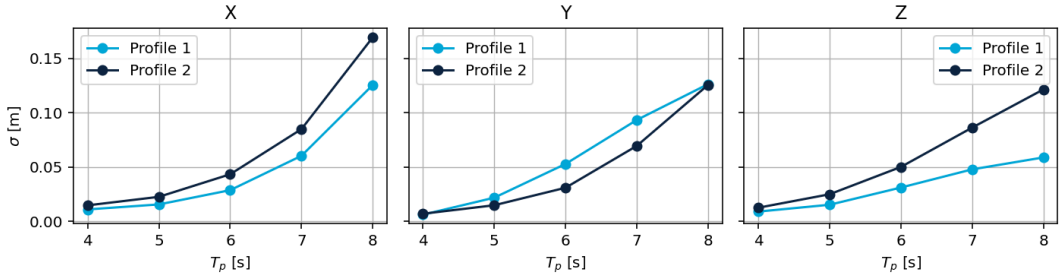

Figure 7.26: Standard deviations of the translational motions of the blade root at a wave direction of $180°$, for varying tugger damping profiles.

Profile 2 results in larger blade root motions in the x- and z-directions across the full range of peak periods. The increased motion in the z-direction arises from enhanced rotation around the x-axis (Rotation 1). In contrast, for the y-direction, Profile 2 shows slightly reduced motion compared to Profile 1 between $T_p = 5$–8 s. This indicates that Profile 2's lower but more progressive damping response is more effective at mitigating y-axis motion during regular non-resonant conditions.

However, near the natural frequency of the pendulum in the y-direction, excited by the heave and pitch motions of the vessel as previously discussed, the resonant behaviour becomes the dominant factor. In this regime, the differences between the two damping profiles diminish, as the damping force becomes less effective relative to the energy input from the vessel. Consequently, Profile 1 remains the preferred configuration due to its faster transient response and more effective suppression of BIT and blade root motions.

Pretension

Increasing the tugger pretension enhances the restoring force available to counteract displacements of the suspended blade. While pretension alone does not directly alter the natural frequencies, in this case the increase in pretension is achieved by reeling in the tugger lines. This modifies the static configuration of the system, resulting in slight changes in the effective stiffness and geometry, which in turn lead to small shifts in the natural frequencies of the pendulum-like modes. The corresponding natural periods and frequencies for various pretension levels are summarized in Table 7.7, with 100 kN representing the reference configuration.

Table 7.7: Natural periods and corresponding frequencies for blade yaw and blade pendulum motions in the x- and y-directions at different tugger pretensions.

Tugger Pretension [kN]	Mode	Period [s]	Frequency [Hz]
100	Blade Yaw	14.980	0.0667
	Blade Pendulum y	8.880	0.1126
	Blade Pendulum x	5.710	0.1751
150	Blade Yaw	15.696	0.0637
	Blade Pendulum y	8.186	0.1222
	Blade Pendulum x	5.817	0.1719
200	Blade Yaw	15.812	0.0633
	Blade Pendulum y	7.717	0.1296
	Blade Pendulum x	5.849	0.1710

The effect of increasing pretension on the BIT motions is illustrated in Figure 7.27 and Figure 7.28. Notably, the translations in the y-direction and the rotation around the x-axis (Rotation 1) show significant changes. These motions initially increase with pretension up to a peak period of approximately 6 seconds, beyond which higher pretension results in reduced motions. The increased pretension causes the natural frequency of the pendulum motion in the y-direction to shift closer to the vessel's roll response frequency, leading to a moderate resonant response around $T_p = 6$ s. However, this resonance remains limited due to the relatively low energy content of the vessel response at this frequency. As a result of this frequency shift, the pendulum mode is no longer strongly excited at $T_p = 7$ and 8 s for the higher pretension cases, leading to reduced BIT motions.

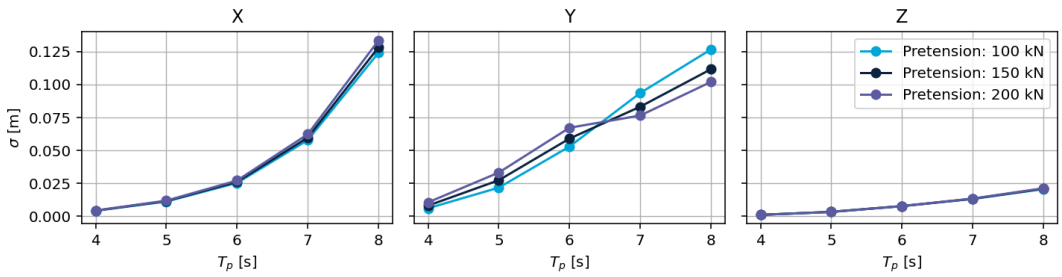

Figure 7.27: Standard deviations of the translational motions of the BIT at a wave direction of $180°$, for varying tugger pretension.

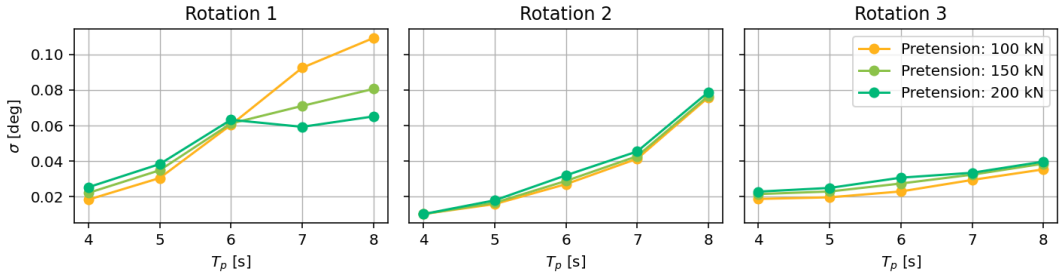

Figure 7.28: Standard deviations of the rotational motions of the BIT at a wave direction of $180°$, for varying tugger pretension.

Figure 7.29 shows the resulting motions at the blade root, which arise from the combined translational and rotational dynamics of the BIT. Increased pretension leads to reduced displacements along the y- and z-axes at larger peak periods. This reduction is attributed to the shift in the natural frequency of the y-direction pendulum mode, which moves away from the dominant vessel excitation frequencies, thereby limiting resonant amplification. In contrast, the motions in the x-direction remain largely unaffected by pretension. This is expected, as the x-axis motion is primarily driven by the vessel's global movement, which is not influenced by the tugger line pretension.

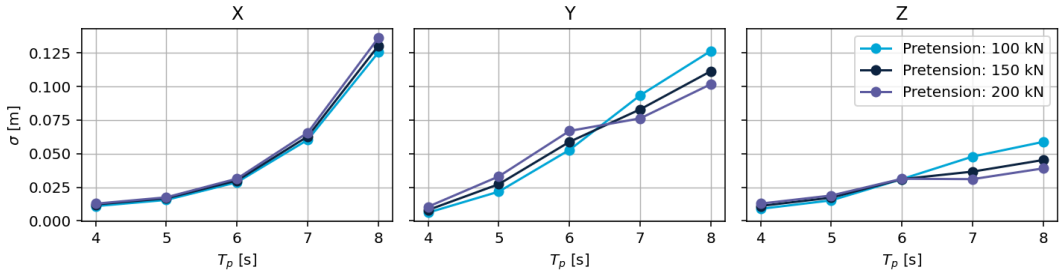

Figure 7.29: Standard deviations of the translational motions of the blade root at a wave direction of $180°$, for varying tugger pretension.

Finally, Figure 7.30 illustrates the time history of the tugger tensions. While the overall fluctuation pattern remains similar across pretension levels, higher pretension results in an elevated mean tension. This ensures that the tuggers remain under tension throughout the operation, effectively preventing the slack conditions presented in Table 6.1, which resulted resulting in simulations that are not representative of operational conditions. Both the 150 kN and 200 kN pretension configurations are sufficient to avoid these undesired effects and ensure reliable system behaviour for the conditions considered for the investigated site.

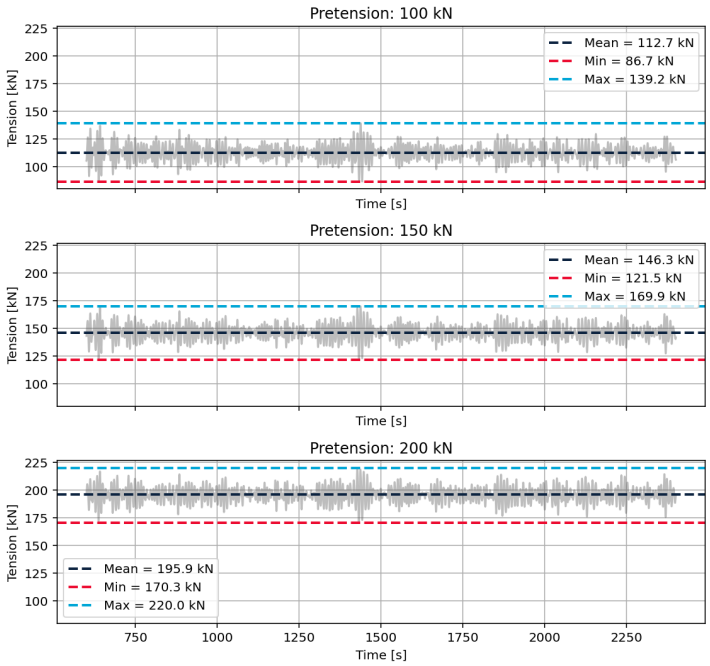

Figure 7.30: Tugger tension in the upper port-side tugger of the lifting arrangement for varying pretension levels, for the reference case and Tp = 8 s

Overall, the increase in pretension in the tuggers results in a modified static configuration of the system, which in leads to a shift in the natural frequencies of the pendulum motion in the y-direction. Additionally, increasing the pretension helps maintain continuous tension in the tugger lines, preventing them from going slack. This reduces the risk of snap loads, which can cause sudden and potentially damaging dynamic effects. Overall, a higher pretension contributes to a more stable and controlled dynamic response during blade installation.

7.4. Environmental Parameters

To assess the extent to which the results are influenced by the chosen site characteristics of the fictional location, a sensitivity study is conducted on water depth and soil stiffness.

Water Depth

The water depth determines the hydrodynamic loading on the turbine and influences the structural dynamics of the support structure. As the water depth increases, the submerged length of the MP also increases, resulting in a greater effective cantilever length, L_{eff}. This increase in L_{eff} reduces the overall bending stiffness of the structure, assuming all other parameters remain constant, and consequently lowers the natural frequencies. The natural frequencies of the OWT for each water depth are presented in Table 7.8, which shows that both side-side and fore-aft natural frequencies decrease with increasing depth. Figure 7.31 illustrates the effect of increasing water depth on the dynamic response of the hub. Note that a water depth of 30 meters corresponds to the reference configuration.

Table 7.8: First natural frequencies and periods of a bottom-fixed OWT with two installed blades, for different water depths.

Water depth [m]	Mode	Frequency [Hz]	Period [s]
30	Side-side	0.1560	6.41
	Fore-aft	0.1566	6.39
40	Side-side	0.1463	6.83
	Fore-aft	0.1469	6.81
50	Side-side	0.1372	7.29
	Fore-aft	0.1377	7.26
60	Side-side	0.1286	7.78
	Fore-aft	0.1290	7.75

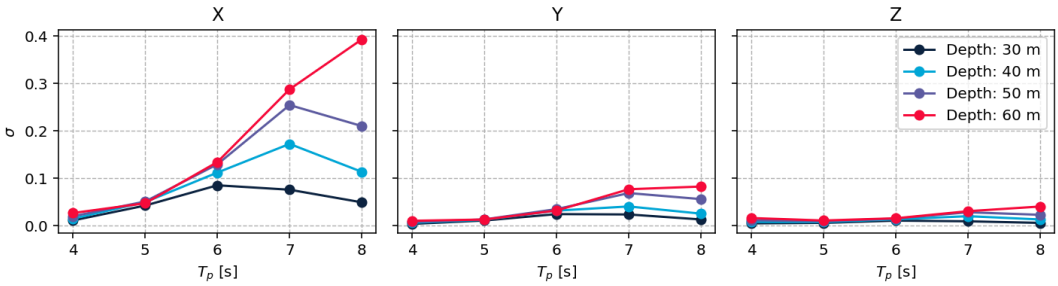

Figure 7.31: Standard deviations of the translational motions of the hub at a wave direction of $180°$, for varying water depths.

Figure 7.31 shows that the hub motions of the turbine increase with water depth, driven by enhanced resonance effects caused by increased hydrodynamic loading. Additionally, the shift in natural frequencies results in the largest hub responses occurring at different wave peak periods.

Jiang et al. (2018) report similar findings, noting that for a MP with an embedment depth of 25 m, the resonant response remains relatively limited. However, for deeper foundations where the embedment depth is 40 meters, the resonance becomes more pronounced and significantly contributes to the standard deviation of the hub motion. This supports the observation that a longer submerged MP length leads to increased hub motions due to enhanced dynamic amplification.

Furthermore, at greater water depths, different vessel load RAOs describe the wave effect on the vessel, reflecting how the vessel behaves under those conditions. These altered RAOs can influence the vessel's motion characteristics and, consequently, affect the blade root dynamics. However, the impact of increased water depth on vessel motions and the resulting effects on blade root behaviour are not addressed in this study.

Overall, an increase in water depth for a similar OWT configuration decreases the natural frequencies of the structure and increases the potential for resonant response due to greater hydrodynamic loading. For the assumed water depth of 30 m, the resulting hub motions remain relatively limited. However, this sensitivity study shows that hub motions are significantly influenced by water depth.

However, the current OWT is designed for a water depth of 30 m, and its performance is therefore not well suited for deeper waters. In reality, at greater depths, the MP would be dimensioned differently to ensure suitable structural and dynamic performance. This study does not consider alternative MP designs for varying depths. Additionally, the response of the SSCV may also be affected by water depth, which in turn could influence the dynamics of the installation operation.

Soil Stiffness

The influence of soil stiffness is investigated to assess whether the assumed soil properties yield reliable and representative results. Three different soil stiffness configurations are analysed: reference, double, and four times the reference stiffness. The resulting natural frequencies and periods for the fundamental modes are summarised in Table 7.9, and the motion standard deviations are shown in Figure 7.32.

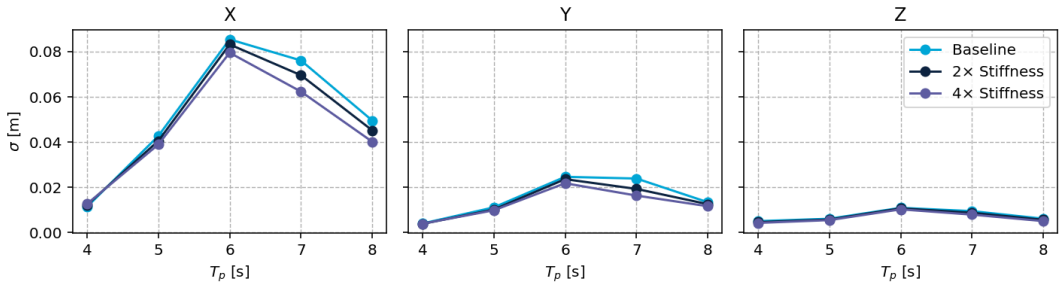

Figure 7.32: Standard deviations of the translational motions of the hub at a wave direction of $180°$, for varying soil stiffnesses.

Table 7.9: First natural frequencies and corresponding periods of a bottom-fixed OWT with two installed blades, evaluated for varying soil stiffness conditions.

Soil stiffness	Mode	Frequency [Hz]	Period [s]
Reference	Side-side	0.1560	6.41
	Fore-aft	0.1566	6.39
Double	Side-side	0.1576	6.34
	Fore-aft	0.1583	6.32
Four times	Side-side	0.1591	6.29
	Fore-aft	0.1597	6.26

Stiffer soil results in a stiffer overall system, thereby increasing the natural frequency. For less stiff soil, increased hub motions are observed around peak periods that more closely align with the system's natural frequency. Further more, the weaker soil lead to a more flexible support, which leads to a wider frequency bandwidth where resonance effects are observed around these natural frequencies. However, the observed differences across configurations are minor, and the overall effect on hub motions is limited. Even a fourfold increase in soil stiffness yields only a modest reduction in motion amplitudes.

Considering the influence of site-specific characteristics, this sensitivity study confirms that, within the tested range, soil stiffness is not a dominant factor in determining the turbine's dynamic response. It should be noted, however, that the MP design is tailored to the reference soil conditions. In practical applications, significantly different soil properties would likely necessitate a re-dimensioning of the MP.

Extreme Wind

The turbulence intensity (TI) at the fictional location is assumed to be 5% based on internal experience. This average TI has been observed to remain relatively stable across varying wind speeds and

is therefore applied uniformly in assessments. To evaluate the sensitivity of the installation process to variations in turbulence intensity, a dedicated sensitivity study was performed. In this study, a higher TI of 8% was tested. Operational experience indicates that this level of turbulence is exceeded only 10% of the time at the reference site, thereby representing an upper bound of typical conditions. To isolate the effect of wind turbulence, the sensitivity analysis was conducted without the influence of waves.

The results showed that the standard deviation of the wind load scales linearly with turbulence intensity, as expressed in Equation 7.1. This finding is consistent with the work of Gaunaa et al. (2014), who investigated the first-order aerodynamic and aeroelastic behaviour of a single-blade installation setup and demonstrated that the standard deviation of aerodynamic loads scales linearly with turbulence intensity.

$$\sigma_{F_{\text{aero}}} = k \cdot \text{TI} \tag{7.1}$$

In the simulations, this linear scaling also applied to the blade root motions, which aligns with the findings of Jiang et al. (2018). For the hub, motions were likewise higher under increased turbulence intensity. However, due to the asymmetric structure with two blades already installed, the scaling of the motions was not strictly linear. It is important to note that at sites with higher turbulence intensity, increased hub and blade root motions can be expected.

In the investigated installation, where wind loading on the blades is minimised through feathering, the overall wind-induced motions remain minimal. However, as shown in Chapter 6, wind loading can still lead to large extreme excitations, particularly at the blade root, which may pose challenges for operability. A higher turbulence intensity could further amplify these extreme blade root excitations.

7.5. Sensitivity Study Summary

This section summarizes the sensitivity study from the previous sections and proposes an improved installation configuration based on its findings.

7.5.1. Overview

A summary of the most important sensitivities for each studied parameter is presented in Table 7.10.

7.5.2. Operational Configuration Improvements

For the operability study in Chapter 8, a second reference case is defined by applying several modifications to the original configuration, aimed at reducing the motions of both the hub and blade root. Specifically, the draught is increased to 26.6 metres and the suspension length is reduced to 15 metres. These changes are based on findings from the sensitivity study, which showed that each adjustment individually leads to reduced standard deviations in blade root motions. The combination of these two modifications still allows the required hub height to be achieved. Additionally, the pretension in the tuggers is increased to 150 kN to prevent slack in the lines and to ensure more reliable simulation results under demanding conditions.

The decreased suspension length is limited, reducing the available space for the lifting configuration. The feasibility of this setup depends on the size of the lifting equipment and the required clearances between the crane tip and the BIT.

All other key parameters were maintained from the reference case, including a tugger width of 15 metres, the blade tip mass, damping profile 1, tugger stiffness, crane angles, and environmental conditions. This strategy preserves consistency to enable comparison, while targeting crucial adjustments that affect operability. The corresponding natural frequencies for the new configuration are given in Table 7.11.

Table 7.11: Natural frequencies and corresponding periods for each mode in the improved model.

Number	Mode	Natural frequency [Hz]	Natural period [s]
1	Yaw	0.0065	153.878
2	Surge	0.0065	153.067
3	Sway	0.0080	124.674
4	Roll	0.0529	18.902
5	Blade Yaw	0.0630	15.867
6	Pitch	0.0686	14.581
7	Heave	0.0838	11.940
8	Pendulum y	0.1221	8.190
11	Pendulum x	0.1811	5.523
12	Crane block pendulum y	0.3373	2.964
13	Crane block pendulum x	0.6972	1.434
14	Crane out of phase	0.8300	1.205
15	Crane in phase	0.8770	1.141

Table 7.10: Summary of Parameter Sensitivities on System Dynamics

Parameter	Effect on Modal Properties	Remarks	Changed dynamics
OWT structure parameters			
Tower length	Longer tower reduces the OWT natural frequency	Assumes constant distributed mass per unit length; leads to increased hub motions	✓
Blade length	Longer blade lowers the OWT natural frequency	Increases aerodynamic loading, which results in larger hub motions	✓
MP diameter	Larger diameter increases the OWT natural frequency	Increases structural stiffness	✓
MP submerged length	Longer submerged length reduces the OWT natural frequency	Decreases structural stiffness and increases hydrodynamic loading; increases hub motions	✓
MP embedded length	Longer embedded length slightly lowers the OWT natural frequency	Soil stiffness increase partially offsets reduced structural stiffness; net increase in motions	✓
SSCV parameters			
Draught	Affects vessel natural frequencies	Larger draught reduces vessel and blade root motions; resonance observed near $T_p = 7$–8 s for 16.6 m draught	✓
Crane angles	Alters whip motions through rigid-body geometry	Mostly governed by operational constraints	✗
Lifting configuration parameters			
Suspension length	Longer length lowers the pendulum natural frequency	Coupling of pendulum frequency with vessel heave and pitch leads to large blade root motions	✓
BIT mass	Heavier BIT reduces pendulum frequency	Alters dynamic coupling with the vessel; affects tension distribution in tuggers	✓
Tugger parameters			
Width	Wider spacing adjust BIT motions	Narrow width causes yaw instability; wider tuggers induce y-resonance but better constrain Rotation 1; 15 m is optimal	✓
Stiffness	Higher stiffness increases natural blade frequencies in x-, and y-pendulum, and yaw	Reduces rotational response; lowers blade root motions	✓
Damping profile	No change in natural frequencies	Reduces blade root motion amplitudes	✗
Pretension	Larger pretension increases y-pendulum frequency via altered static equilibrium	Higher pretension prevents slack in tuggers and reduces snap loads	✓
Environmental parameters			
Water depth	Increased depth lowers OWT natural frequency	Leads to increased hydrodynamic loading and thus larger hub motions; OWT configuration is designed for reference water depth	✓
Soil stiffness	Minor effect on modal properties within tested range	Even a 4× increase causes marginal motion change; OWT configuration is designed for reference soil conditions	✗
Turbulence intensity	Does not affect structural natural frequencies	Higher TI leads to stronger aerodynamic forcing and increased hub/blade root response	✗

8

Operability study of the operation

In the preceding chapters, the influence of environmental and operational parameters was examined by evaluating the motion of the hub and blade root individually, using their respective standard deviations as indicators. This approach provided insight into the sensitivity of each component to varying external conditions. However, the limiting criteria that govern the system's feasibility are not defined for the individual motions of the hub or blade root, but rather for their relative displacement. Therefore, this chapter shifts focus to the relative motion between the hub and the blade root.

By quantifying this relative displacement and comparing it against the predefined limiting criteria, as introduced in Chapter 3, the operability of the system is assessed to determine whether the installation operation is possible under the different operating conditions.

The operability is assessed for both the reference case from the previous chapter, as well as the improved configuration derived from the sensitivity study. First, the method used to compute the relative displacement and its evaluation against the limiting criteria is described. Subsequently, the operability assessment for the operation is given.

8.1. Relative Displacement Between Hub and Blade Root

The relative displacement between the hub centre point and the blade root centre point at time step t is computed along each Cartesian direction. To remove any static offset, a zero-mean correction is applied. For a given direction $p \in \{X, Y, Z\}$, the relative displacement signal is defined as given in Equation 8.1.

$$D_p(t) = (r_{\text{hub},p}(t) - \overline{r}_{\text{hub},p}) - (r_{\text{blade},p}(t) - \overline{r}_{\text{blade},p}) \tag{8.1}$$

where:

- $r_{\text{hub},p}(t)$ is the position of the hub centre point in direction p at time t,
- $r_{\text{blade},p}(t)$ is the position of the blade root centre point in direction p at time t,
- $\overline{r}_{\text{hub},p}$ and $\overline{r}_{\text{blade},p}$ are the time-averaged positions in direction p for the hub and blade root, respectively.

The resulting 3D relative displacement vector $\vec{D}(t)$ is defined in Equation 8.2. A schematic visualisation of the relative displacement vector is provided in Figure 8.1.

$$\vec{D}(t) = \begin{bmatrix} D_X(t) \\ D_Y(t) \\ D_Z(t) \end{bmatrix} \tag{8.2}$$

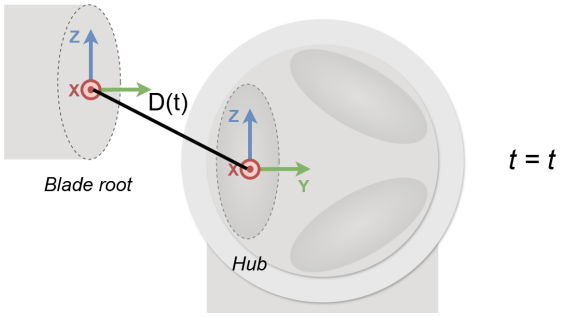

(a) $D(t)$ at a time step t

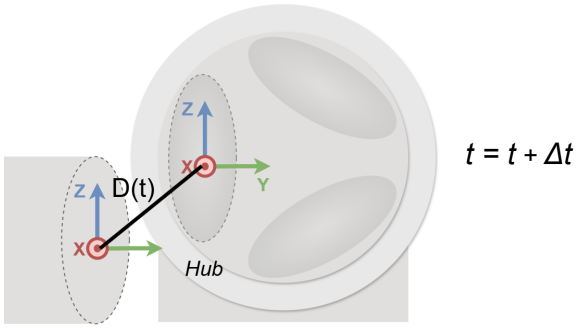

(b) $D(t)$ at a time step $t + \Delta t$

Figure 8.1: Schematic representation of the relative displacement vector at two different time steps.

The magnitude of the relative displacement vector can be derived from Equation 8.3. This quantity represents the instantaneous, zero-mean spatial separation between the hub centre and the blade root centre in 3D space.

$$\|\vec{D}(t)\| = \sqrt{D_X(t)^2 + D_Y(t)^2 + D_Z(t)^2} \tag{8.3}$$

To assess the exceedances of the defined safety limit, the magnitude $\|\vec{D}(t)\|$ is compared against a safety boundary R_{sb}. Each time $\|\vec{D}(t)\|$ transitions from inside the safety boundary to outside, this event is classified as an outcrossing.

To detect such events during operation, a binary array s_t is computed. This array contains a binary value for each time step t of the numerical simulation. A value of 1 indicates that the relative displacement exceeds the safety boundary, while a value of 0 indicates it remains within bounds, as defined in Equation 8.4.

$$s_t = \begin{cases} 1, & \text{if } \|\vec{D}(t)\| > R_{\text{sb}} \\ 0, & \text{otherwise} \end{cases} \tag{8.4}$$

In the event of an outcrossing, the array s_t transitions from 0 to 1. The total number of outcrossings, N, is then computed by counting the number of such transitions over the full array length T, as shown in Equation 8.5.

$$N = \sum_{t=1}^{T-1} \max\left(0,\, s_{t+1} - s_t\right) \tag{8.5}$$

Finally, the outcrossing rate ν is determined by normalizing the number of outcrossings by the total duration of the operation T_{op} (in seconds), as given in Equation 8.6:

$$\nu = \frac{N}{T_{\text{op}}} \tag{8.6}$$

8.2. Environmental Parameters

Considering the significant influence of varying peak periods, the full range of the fictive location is evaluated for each combination of wave height and wind speed. The pairing of wave height H_s and the 1-hour mean wind speed V_w is derived from Equation 2.6. The environmental conditions used in the operability study are summarized in Table 8.1.

Table 8.1: Considered environmental conditions for the operability study.

Wave height H_s [m]	Peak Period, T_p [s]	Mean Wind Speed, V_w [m/s]
0	4–8	0
0.5	4–8	7
1	4–8	11
1.5	4–8	15
2	4–8	18
2.5	4–8	21
3	4–8	24

8.3. Reference Cases

To assess the effect of the adjustments made following the sensitivity study, the relative displacements between the blade root and hub are examined for both reference case configurations. The first reference case corresponds to the configuration described in Section 7.1, while the second incorporates the modifications outlined in Subsection 7.5.2. An overview of the operational parameters for both cases is provided in Table 8.2.

Furthermore, a third reference case is considered in which the SSCV is fixed in position. All six degrees of freedom are constrained, resulting in a fixed crane tip. In this configuration, the only factors influencing operability are the aerodynamic loading on the suspended blade and the hub motions induced by wave and wind loading. By comparing this reference case with others, the contribution of the SSCV to the relative displacements within the overall installation system can be evaluated.

Table 8.2: Summary of operational parameters for each reference case used in the operability analysis.

Parameter	Unit	Reference Case 1	Reference Case 2	Reference Case 3
Operational Parameters				
6 DOFs SSCV	–	✓	✓	✗
Thialf Draught	m	16.6	26.6	16.6
Suspension Length	m	25	15	25
BIT Mass	t	100	100	100
Tugger Width	m	15	15	15
Tugger Stiffness	kN/m	100	100	100
Tugger Damping Profile	–	1	1	1
Tugger Pretension	kN	100	150	100

For each reference case, the three-dimensional trajectory of the instantaneous, zero-mean spatial separation between the hub centre and the blade root centre is presented. As long as the trajectory remains within a sphere defined by the safety boundary radius, no outcrossings occur. When the trajectory crosses this sphere, the event is classified as a single outcrossing. The safety boundary is visualised in grey, while trajectory segments outside the boundary are highlighted in red. Additionally, a histogram is included to show the total number of outcrossings for each peak period. The results are presented for each reference case at $H_s = 1\,\text{m}$ and $V_w = 12\,\text{m/s}$, across the range of studied peak periods.

8.3.1. Reference Case 1: 16.6 m draught

The three-dimensional trajectories for $T_p = 4$, 6, and 8 s are presented in Figure 8.2. For the smallest peak period, the spatial separation between the hub centre and the blade root centre remains well within the safety boundary. At $T_p = 6\,\mathrm{s}$, a total of 67 outcrossings is observed, primarily along the x-axis, indicating dominant fore-aft motion of the wind turbine. In contrast, the trajectory for $T_p = 8\,\mathrm{s}$ exhibits 228 outcrossings, which are large in magnitude and distributed across all axes.

Figure 8.3 presents the histogram corresponding to these conditions. An increasing number of outcrossings is observed for larger peak periods. This trend is consistent with the analysis in Chapter 6, which demonstrated that the relative motion is primarily driven by blade root excitations, increasing with peak period except near the natural period of the OWT.

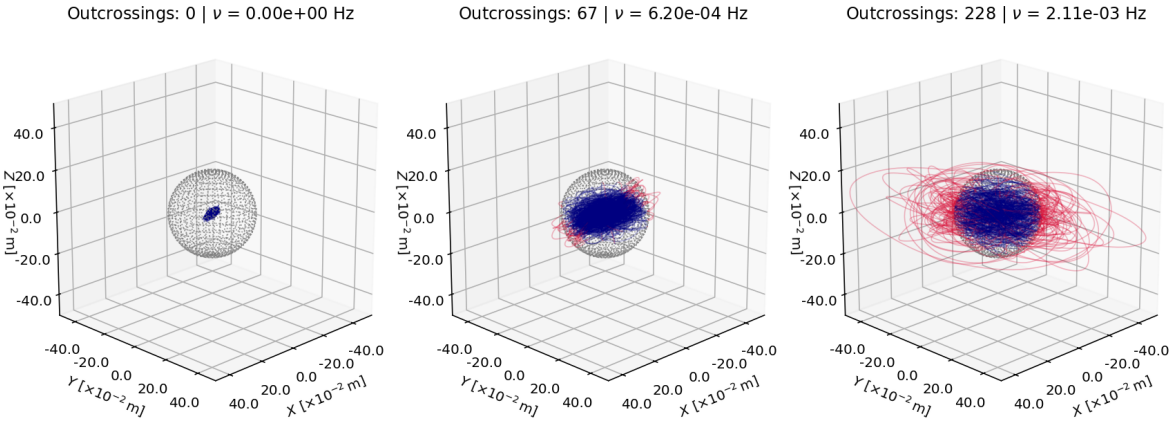

Figure 8.2: Three dimensional trajectories of the relative displacement between the blade root and the hub with a safety boundary of 0.2 m, shown for wave peak periods $T_p = 4$, 6, and 8 s for Reference Case 1. The grey sphere indicates the safety boundary, blue shows the time trace within the boundary, and red highlights instances where the relative displacement exceeds the limit.

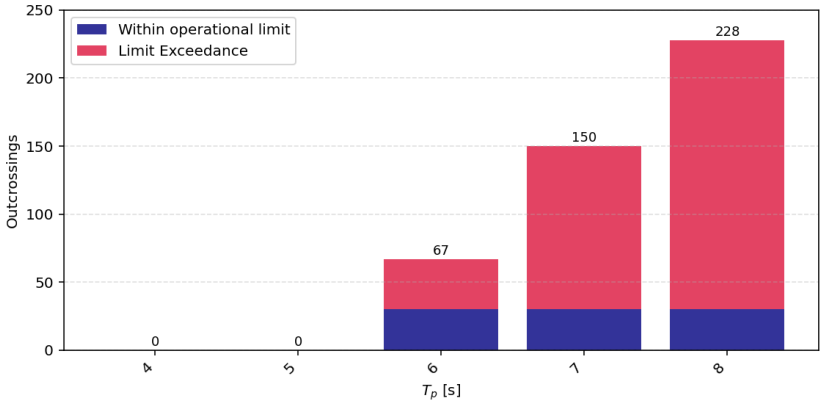

Figure 8.3: Outcrossings of the relative displacement between the blade root and the hub for a safety boundary of 0.2 meters for Reference Case 1. Bars highlighted in red indicate cases where the number of outcrossings exceeds the critical maximum.

8.3.2. Reference Case 2: 26.6 m draught

For the second reference case, which incorporates improvements over the first, improved performance is expected. Figure 8.4 shows the trajectories of the spatial separation. For $T_p = 4\,\mathrm{s}$, the behaviour is similar to the first case, with no breaches of the safety boundary. At $T_p = 6\,\mathrm{s}$, a total of 40 threshold exceedances is observed, primarily along the x-axis, indicating dominant fore-aft motion of the wind turbine. This directional dominance suggests that blade root excitations are reduced in this case, as anticipated. The trajectory for $T_p = 8\,\mathrm{s}$ shows 42 exceedances, again mostly along the x-axis, though less pronounced than at $T_p = 6\,\mathrm{s}$. This reduction in directional dominance can be attributed to a lower

resonant response of the wind turbine. The comparable number of exceedances at $T_p = 8\,\mathrm{s}$ indicates increased blade root activity at that peak period.

Figure 8.5 presents the corresponding histogram, which clearly illustrates the improvement in performance.

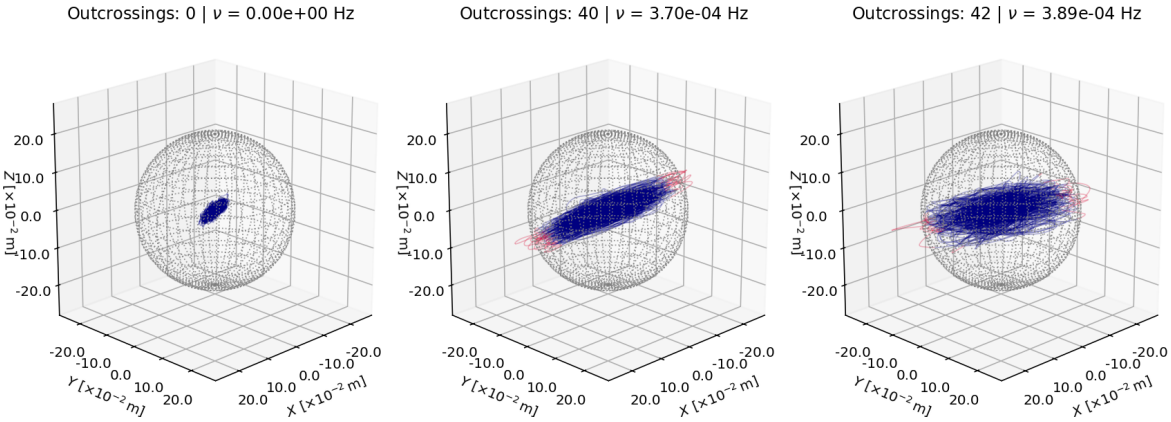

Figure 8.4: Relative displacement between the blade root and the hub for a safety boundary of 0.2 m, shown for wave peak periods $T_p = 4$, 6, and 8 s for Reference Case 2. The grey sphere indicates the safety boundary, blue shows the time trace within the boundary, and red highlights instances where the displacement exceeds the limit.

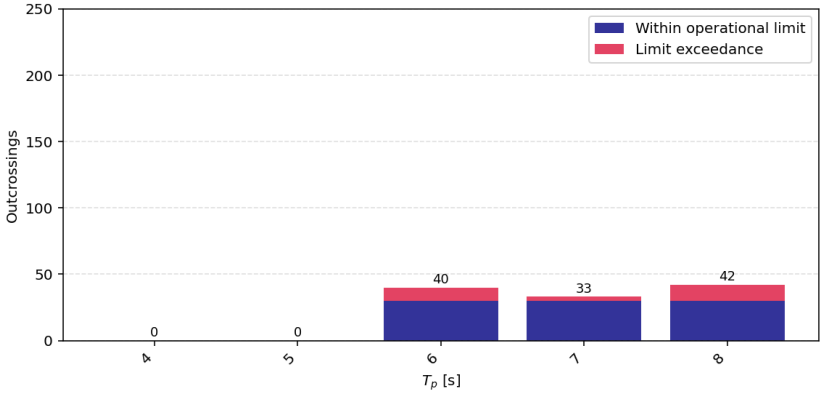

Figure 8.5: Outcrossings of the relative displacement between the blade root and the hub for a safety boundary of 0.2 meters for Reference Case 2. Bars highlighted in red indicate cases where the number of outcrossings exceeds the critical maximum.

8.3.3. Reference Case 3: Fixed SSCV

For the third reference case, the SSCV is fixed in position. This eliminates the influence of vessel motion, allowing operability to be evaluated independently of vessel dynamics. In this configuration, blade root motions are solely induced by wind, while the OWT remains subject to both wave and wind loading. The case thus represents a fundamental scenario for all single blade installations on this site, which can only worsen due to the vessel motions and dynamic coupling leading to extra blade excitations. By comparing this reference case to the other reference cases enables a clear assessment of how much vessel motion affects operability under defined conditions. And what the base operability of this installation procedure on this location would be for every installation vessel.

Figure 8.6 shows the time series of the spatial separation between the blade root and the hub for wave peak periods of 4, 6, and 8 seconds. Exceedances beyond the safety threshold occur only near the natural frequency of the turbine. For the other peak periods, the relative separation remains within acceptable limits. Figure 8.7 presents the overall histogram of exceedances across the range of peak periods, confirming that significant exceedances occur only in the vicinity of the turbine's natural frequencies.

The same operability is observed for a fixed blade root, indicating that hub displacements alone dominate the operability and can, on itself, lead to non-operable conditions.

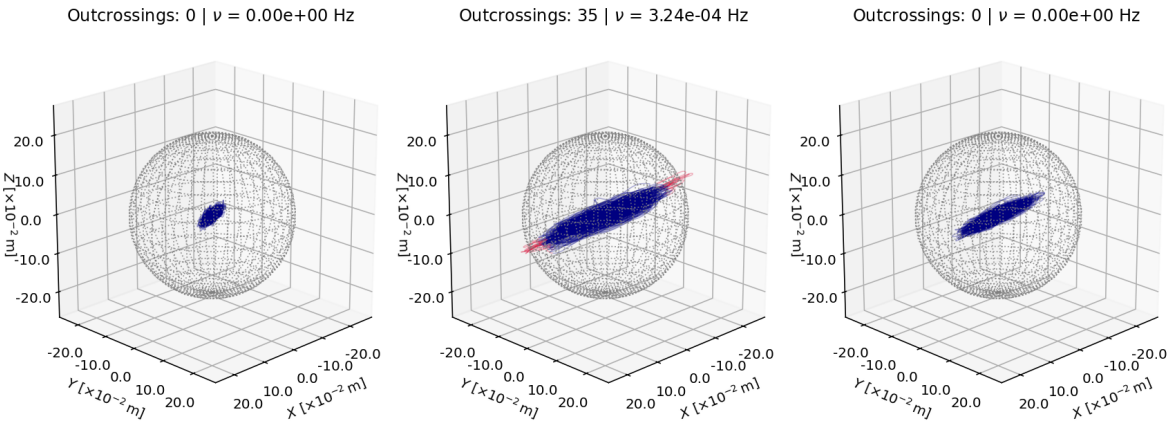

Figure 8.6: Relative displacement between the blade root and the hub for a safety boundary of 0.2 m, shown for wave peak periods $T_p = 4$, 6, and 8 s for Reference Case 3. The grey sphere indicates the safety boundary, blue shows the time trace within the boundary, and red highlights instances where the displacement exceeds the limit.

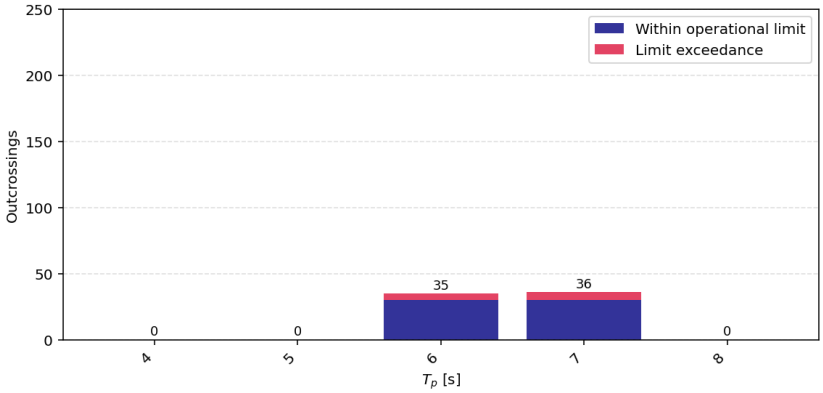

Figure 8.7: Outcrossings of the relative displacement between the blade root and the hub for a safety boundary of 0.2 meters for Reference Case 3. Bars highlighted in red indicate cases where the number of outcrossings exceeds the critical maximum.

8.3.4. Reference Case Comparison

This section presents a side-by-side comparison of the behaviour observed in Reference Cases 1, 2, and 3. First, the three-dimensional trajectories are analysed for wave peak periods of 6 and 8 s to evaluate the impact of the implemented adjustments and to identify the dominant motions affecting operability. This is followed by a general assessment comparing all reference cases.

Figure 8.8 illustrates the relative behaviour at a peak period of 6 s, which is close to the natural frequency of the OWT. In all cases, exceedances occur primarily along the x-axis, corresponding to the fore-aft motion of the OWT. Reference Case 1 exhibits the greatest deviations along all axes, driven by blade root motions occurring in all directions, not only along the x-axis. Reference Case 2 shows reduced deviations in the transverse and vertical directions, indicating that the blade root motions have decreased. The modifications introduced in Chapter 7 therefore have a positive impact on the blade root motions, reducing the number of exceedances from 67 to 40.

However, the relative displacement remains dominated by the fore-aft motion of the hub, and the number of exceedances still exceeds the operability threshold. In Reference Case 3, vessel motions are entirely excluded. Despite this, 35 outcrossings are observed, which is five more than the allowed maximum for the operation to be considered operable. This confirms that, even in the absence of vessel-induced dynamics, the installation is not feasible in this configuration. The time trace of the

relative displacement shows that the exceedances are caused by the fore-aft motion of the OWT along the x-axis.

This comparison highlights that, regardless of the installation vessel used, the operation is not operable due to resonant fore-aft motions of the OWT induced by waves with a peak period near the structure's natural frequency.

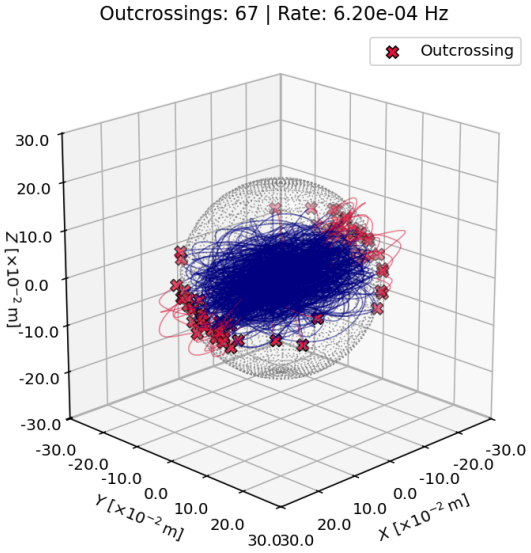

(a) Reference case 1; $T_p = 6$ s

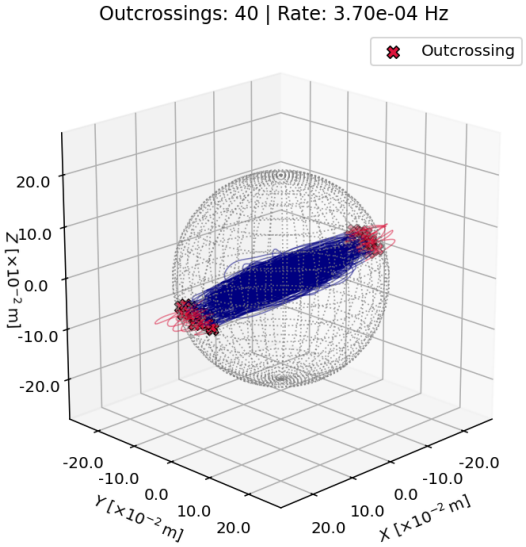

(b) Reference case 2; $T_p = 6$ s

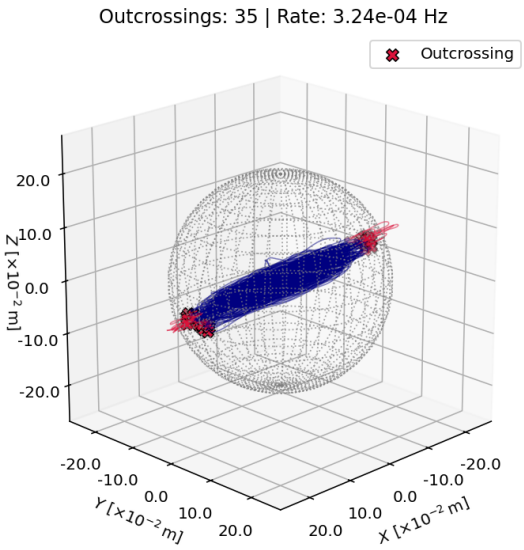

(c) Reference case 3; $T_p = 6$ s

Figure 8.8: Comparison of reference cases for $T_p = 6$ s. Outcrossings are marked with red crosses; the total number of outcrossings is noted for each case.

Figure 8.9 shows the relative behaviour at a peak period of 8 s. At this period, vessel responses are larger, and the associated response frequencies are known to induce resonant pendulum-like motions. Reference Case 1 clearly exhibits excessive relative displacements between the hub and the blade root. The fact that exceedances occur along all axes confirms that the response is dominated by blade root motion. The amplitude of the relative displacement is notably larger compared to the other cases. It is important to note that, under conditions where the relative displacement between the hub and the blade root exceeds the safety threshold by this margin, proceeding with the installation could pose significant risks, including potential structural collisions.

In Reference Case 2, most exceedances still occur along the fore-aft direction, indicating that fore-aft bending of the OWT remains a significant contributor to the relative displacement. In the absence of vessel motion, such OWT bending remains within acceptable limits, as demonstrated by Reference Case 3, rendering the installation operable. However, when the hub is already in motion, only minimal additional relative excitation of the blade root can be tolerated for the operation to remain within safety boundaries. Despite the improvements introduced in Reference Case 2, the combined effects of vessel motion and dynamic coupling with the blade result in excessive relative displacements. This leads to too many exceedances for the operation to be considered operable.

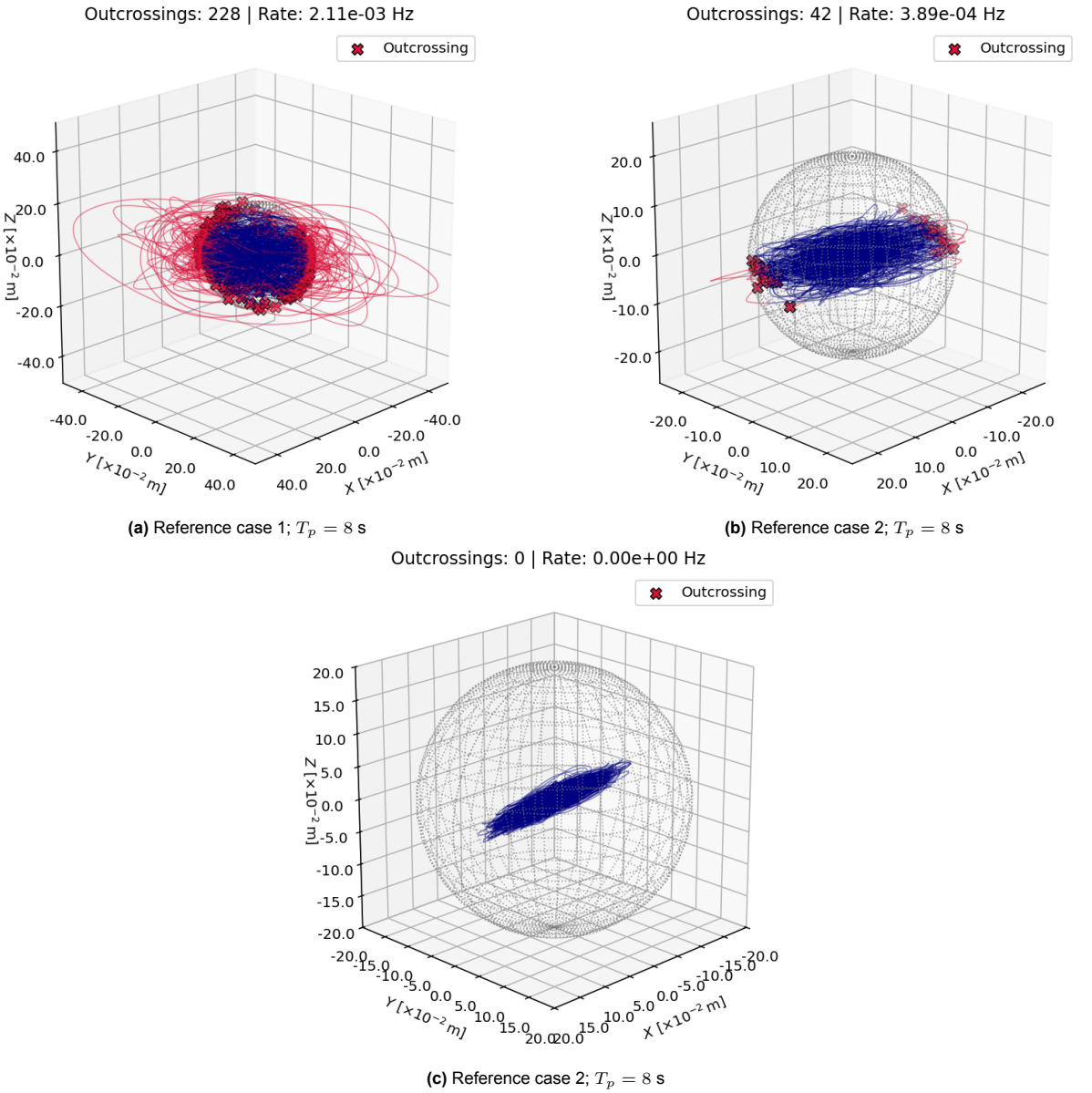

(a) Reference case 1; $T_p = 8$ s

(b) Reference case 2; $T_p = 8$ s

(c) Reference case 2; $T_p = 8$ s

Figure 8.9: Comparison of reference cases for $T_p = 8$ s. Outcrossings are marked with red crosses; the total number of outcrossings is noted for each case.

The improvements made following the sensitivity study have had a positive effect on the blade root motions. Comparing Figure 8.3 and Figure 8.5, Reference Case 2 results in fewer outcrossings due to the reduction in blade root motion. However, the overall operability within this range remains unchanged; operation is feasible for both cases only at $T_p = 4\,\mathrm{s}$ and $T_p = 5\,\mathrm{s}$.

Reference Case 3, which excludes vessel motion and is therefore independent of vessel type, shows

that the operation is not operable at peak periods of 6 and 7 seconds due to OWT motions near its natural frequency, regardless of the vessel used. At $T_p = 7\,\mathrm{s}$, the SSCV-induced blade root motion in Reference Case 2 even results in fewer outcrossings than in Case 3. This suggests that vessel-induced blade motion can,in some cases even reduce the relative displacement between the blade root and the hub.

Reference Case 3 further shows that, even without vessel-induced excitations, the installation is already near the operability threshold. As the hub motions dominate, only very limited blade root excitation can be tolerated. Although blade root motions from other vessel types are beyond the scope of this study, it is reasonable to assume that other vessels also induce blade root motions, potentially also resulting in low operability.

Overall, by comparing the three reference cases, it can be concluded that under the studied conditions (a wave height of 1 m and a wind speed of 12 m/s), even in the absence of vessel motions influencing the relative displacement, the operation can become inoperable due to excessive hub motions. Furthermore, in the improved reference case with the larger draught, fewer exceedances of the safety boundary occur compared to the installation using the SSCV with the smaller draught. However, the overall operability of both reference cases remains the same. This indicates that while the improvements had a positive effect, they were not sufficient to significantly enhance the operability of the operation.

8.4. Operability

This section evaluates the operability of both reference cases for the full range of environmental conditions. First, the operability is assessed in detail based on the main limiting criteria: a safety boundary of 0.2 m and a maximum of 30 outcrossings per 30-minute operation. Subsequently, alternative limiting criteria defined in Table 3.1 are also considered to evaluate their impact on the operability.

8.4.1. Primary Limiting Criteria

The operability, based on a safety boundary of 0.2 m and a maximum of 30 outcrossings per 30-minute operation, is shown for Reference Case 1 in Figure 8.10a and for Reference Case 2 in Figure 8.10b. The figures show that the operation is feasible only for low wave heights ($H_s = 0$–$0.5\,\mathrm{m}$) and short peak periods ($T_p = 4\,\mathrm{s}$). Reference Case 2 exhibits fewer outcrossings than Reference Case 1, however both reference cases lead to similar overall operability.

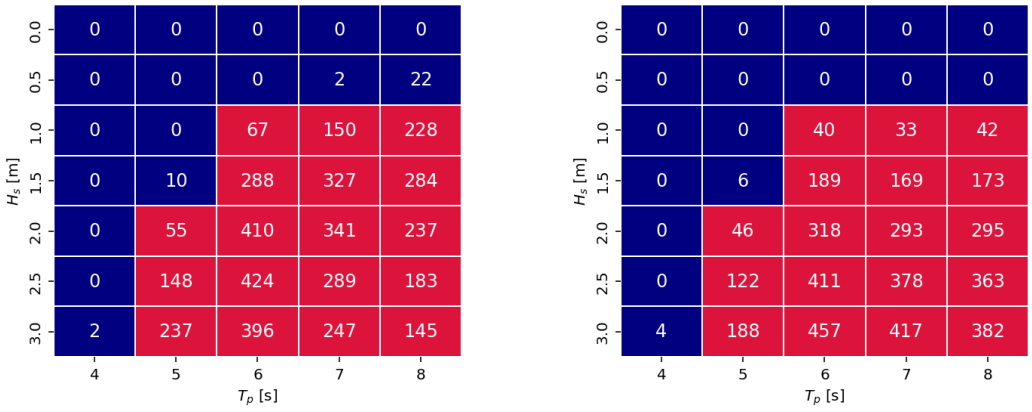

(a) Reference Case 1

(b) Reference Case 2

Figure 8.10: Operability of the installation for $R_{\mathrm{sb}} = 0.2\,\mathrm{m}$ and $\nu_{\mathrm{cr}} = 30$ outcrossings per 30-minute operation, for Reference Cases 1 and 2.

Hub Motion Contribution

To examine the impact of hub motions on operability, operability results are presented in Figure 8.11b for both reference cases, purely based on the hub motions. These plots highlight that substantial hub motions near the turbine's natural frequency result in frequent violations of the limiting criteria and

inoperable conditions. Note that the hub motions, independently of the effect of vessel motions, can lead to inoperable conditions for the installation.

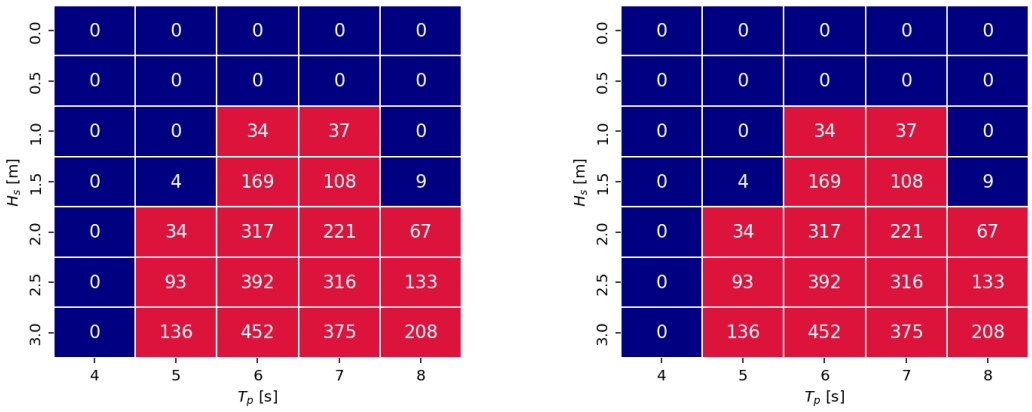

(a) Reference Case 1

(b) Reference Case 2

Figure 8.11: Illustrative operability based solely on hub motions relative to a fixed blade root, assuming $R_{\mathrm{sb}} = 0.2\,\mathrm{m}$ and $\nu_{\mathrm{cr}} = 30$ outcrossings per 30-minute operation, for Reference Cases 1 and 2. Trends shown are indicative only and not representative of actual operability.

Blade Root Contribution

To investigate the effect of blade root displacements on operability, illustrative operability results are presented in Figure 8.12b for both reference cases. These results clearly demonstrate the positive impact of the improvements implemented in Reference Case 2 compared to Reference Case 1. Furthermore, the figures show that if the hub remains stationary, installation using the SSCV can be operable under a wider range of environmental conditions, particularly in Reference Case 2.

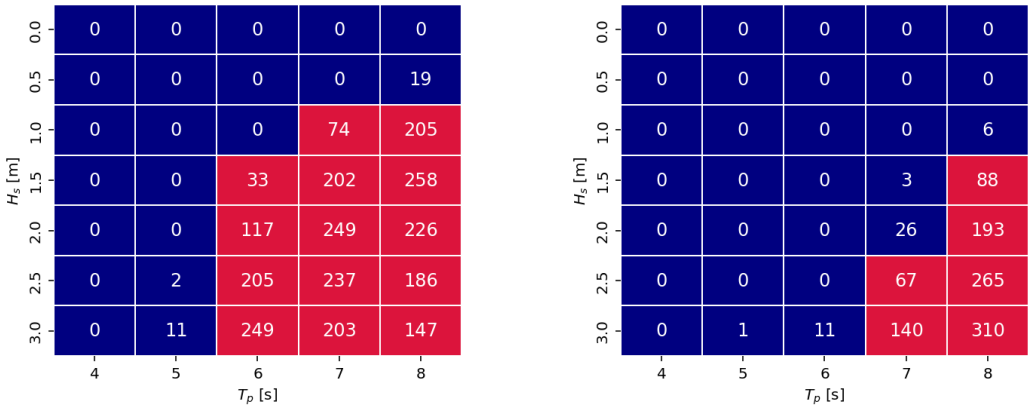

(a) Reference Case 1

(b) Reference Case 2

Figure 8.12: Illustrative operability based on blade root motions relative to a fixed hub, assuming $R_{\mathrm{sb}} = 0.2\,\mathrm{m}$ and $\nu_{\mathrm{cr}} = 30$ outcrossings per 30-minute operation, for Reference Cases 1 and 2. Trends shown are indicative only and not representative of actual operability.

Overall, this operability study shows that, within the current setups, the operability of the installation is low when the relative motion between the hub and blade root is taken into account. Furthermore, the results indicate that hub motions contribute significantly to this limited operability. When the hub is assumed to be stationary, the operability improves, particularly for the installation using the SSCV with the larger draught and shorter suspension length.

8.4.2. Alternative Limiting Criteria

This subsection examines the effect of the limiting criteria themselves on the operability of the operation. The next limiting criterion, defined as a maximum of 10 outcrossings per 30-minute operation by Jiang (2018) and Jiang et al. (2018), is now evaluated. No specific safety boundary was defined in the study by Jiang (2018); therefore, these criteria are assessed using safety boundaries equal to twice and three times the primary safety boundary, i.e. 0.4 m and 0.6 m. The safety boundary defined by Jiang et al. (2018) was 3.54 m, equal to the blade root diameter.

The operability of the operation for a safety boundary of 0.4 m is shown in Figure 8.13. Under these limiting criteria, a clear difference in operability is observed between the two reference cases, in contrast to the results under the primary limiting criteria. For these operational limits, the improvements made following the sensitivity study have a positive effect on the operability of the operation.

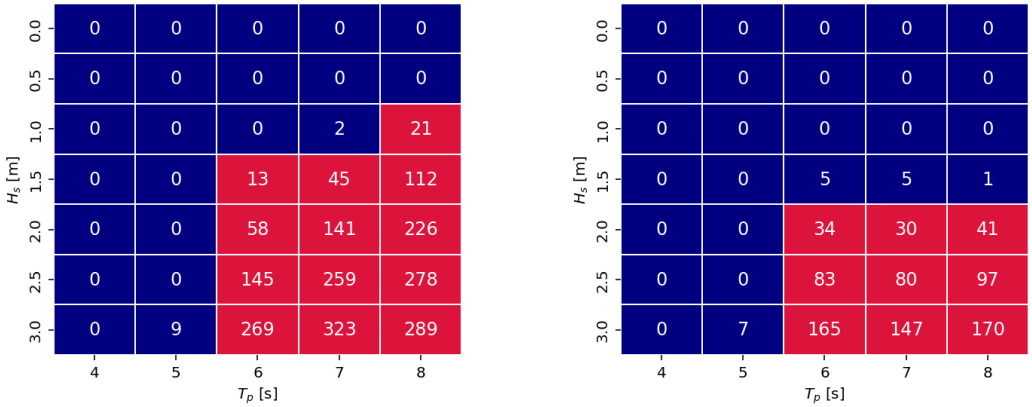

(a) Reference Case 1 **(b)** Reference Case 2

Figure 8.13: Operability of the operation for $R_{\mathrm{sb}} = 0.4\,\mathrm{m}$ and $\nu_{\mathrm{cr}} = 10$ outcrossings per 30-minute operation, for Reference Cases 1 and 2.

Figure 8.14 shows the operability for a safety boundary of 0.6 m. Under this condition, Reference Case 2 is highly operable, except for wave heights of 3 m in combination with peak periods of 6, 7, and 8 s. The operability of Reference Case 1 also improves, though not as significantly.

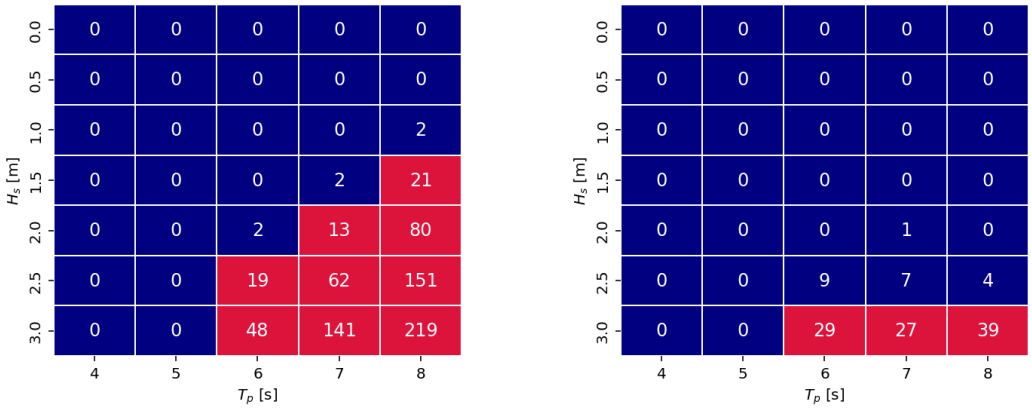

(a) Reference Case 1 **(b)** Reference Case 2

Figure 8.14: Operability of the operation for $R_{\mathrm{sb}} = 0.6\,\mathrm{m}$ and $\nu_{\mathrm{cr}} = 10$ outcrossings per 30-minute operation, for Reference Cases 1 and 2.

For the largest safety boundary, $R_{\mathrm{sb}} = 3.54\,\mathrm{m}$, no outcrossings are observed for either reference case. Under these limiting criteria, the operation is considered fully operable across all site conditions for both

reference cases.

Overall, it is evident that the operability of the installation varies across different configurations. It is therefore advantageous to optimise the configuration in order to maximise operability and minimise weather-related delays. Moreover, the defined limiting criteria have a significant influence on the operability outcome. When the limiting criteria are less strict, the operation becomes significantly more operable. This highlights the importance of how limiting criteria are defined, as they can greatly influence the feasibility and operability of the considered installation.

8.4.3. SSCV Reflection

To evaluate the SSCVs performance in this installation scenario, a comparison is made to an idealised installation vessel, for example a rigid stationary jack-up vessel, that does not contribute to the motion of the suspended blade. This idealised case is represented by Reference Case 3 in Subsection 8.3.4. Comparing Reference Case 3 with the cases where the SSCV is implemented provides insight into the impact the SSCV has on the installation operability.

What stands out in Reference Case 3 is that, even with the idealised installation vessel, the operational limits are exceeded. This is attributed to excessive hub motions occurring near the natural period of the OWT. Consequently, this same effect influences the operability of Reference Cases 1 and 2, where the SSCV is implemented. At larger peak periods, comparison between the SSCV cases and the idealised installation vessel reveals that the additional motions introduced by the SSCV can lead to inoperable conditions, whereas the operation remains operable with the idealised vessel.

This can be further explained by the blade root displacement contributions shown in Figure 8.12b. These plots reveal that, for the larger peak periods within the studied range, excessive blade root motions can render the operation inoperable. Previous chapters showed that these blade root motions are induced by the SSCVs dynamic response. When comparing Reference Case 1 and Reference Case 2, the results indicate that blade root motions can be mitigated through certain design changes. Particularly by decoupling the pendulum natural frequency of the lifting configuration from the vessel's natural response frequencies, by shortening the suspension length of the lifting configuration. But also by increasing the draught of the SSCV, which leads to overall decreased SSCV motions. These findings again highlight the critical role the SSCV motions play in the operability of the installation operation.

From this, it can be concluded that installation using the SSCV is only feasible under environmental conditions where vessel motions remain limited. This can be achieved by adjusting the draught so that the vessel's natural frequencies lie outside the excitation frequency range present at the installation site. However, this strategy is constrained by other operational requirements, such as the necessary installation elevation. If it is not possible to avoid overlap between the SSCV's natural frequencies and the dominant wave frequencies at the location, the operation becomes unfeasible under those conditions. The feasibility of the operation by SSCV is therefore limited by the SSCVs response at a certain installation location.

Returning to the comparison to other installation vessels. It is important to note that these same consideration applies to other installation vessels. Any vessel will exhibit increased motions when wave frequencies approach its natural frequency, and if these response frequencies are close to the pendulum natural frequencies, that will also inherently result in large blade root motions. Also, for the comparison to the idealised vessel, it should be acknowledged that real-world installation vessels inherently experience motion, which may translate to blade root displacements and affect operability.

What this study clearly shows for the SSCV is that installation can be carried out using the SSCV, provided that vessel motions are limited and coupling between the lifting arrangement and the vessel's dynamic response is avoided.

9

Conclusion

This thesis investigates how environmental and operational conditions influence the relative motion between the hub of a bottom-fixed offshore wind turbine and the blade root during single-blade installation using a semi-submersible crane vessel, and how these motions affect the operability of the installation. This is achieved through the development of a numerical model of the installation in *OrcaFlex*. The model is used to perform dynamic analyses to study the behaviour and motion of the installation components under varying environmental and operational conditions. The main conclusions drawn from this study are presented in this chapter.

Impact of Environmental Conditions on the Relative Motions

The environmental conditions at the site were characterised by irregular JONSWAP waves and a turbulent wind field. From dynamic analyses the dynamic response of the hub and blade root were analysed and compared.

The hub motions were found to increase linearly with wave height, driven by inertia-dominated wave loading on the MP. Resonant response occurred when the wave peak period approached the natural frequencies of the OWT, resulting in large hub motions. Among the studied configurations, the case with two blades already installed proved to be most critical due to increased aerodynamic loading. However, when the blades were feathered, particularly with the trailing edge facing into the wind, the influence of wind on hub motion was minor compared to that of waves. Hub motion predominantly followed the direction of wave and wind propagation, and the dynamic response was found to be largely symmetrical, resulting in similar motion patterns across wave and wind directions.

The blade root motions were also found to increase linearly with wave height, as the hydrodynamic loading on the vessel also is inertia-dominated. Larger peak periods resulted in increased vessel responses, which, through various coupling mechanisms, translated into higher blade root motions. The blade root response varied with wave direction, reflecting the vessel's different behaviour in head, beam, and oblique seas. Predominantly head seas were found to result in the smallest blade root motions. As with the hub, applying the same feathered pitch configuration effectively minimised the influence of wind loading on the blade root. While the standard deviations of blade root motions were relatively small compared to those induced by wave loading, fluctuations due to the turbulent wind resulted in considerable maximum excursions. The dynamic behaviour of the blade root exhibited significant components along all three spatial axes.

For both the hub and blade root motions, wave loading was identified as the dominant driver. Whether hub or blade root motions governed the relative displacement pattern was found to depend on the wave peak period. The key parameters influencing operability were identified as the turbine's natural frequency, the dynamic response of the SSCV, and the pendulum frequency of the suspended blade.

Impact of Operational Parameters on the Relative Motions

To investigate the impact of operational parameters a sensitivity study was conducted on various operational parameters of the OWT, SSCV and lifting configuration. This study showed that the blade root

motions depend on the SSCV motions and the coupling of the pendulum mode of the lifting configuration and the SSCV response frequencies.

For the SSCV parameters, it was found that increasing the SSCV draught changed the natural frequencies of the vessel and reduced overall vessel motions, which led to decreased blade root motions.

For the lifting configuration it was found that adjusting the suspension length and the BIT mass affected the pendulum frequency. These parameters can therefore be adjusted to avoid coupling between the pendulum and SSCV natural frequencies to prevent resonant response.

Wider tugger spacing improved yaw control but shifted the pendulum frequency toward vessel response frequencies which introduced potential for resonant response; a width of 15 meter was found to offer a favourable balance between both effects. Increased tugger stiffness had limited impact on translational blade root motions, but dit effectively reduce rotational motions. Different damping profiles showed to affect the amplitude of the blade root motions. And increasing the pretension was found to prevent the risk of slack lines and possible snap loads in the tuggers.

This sensitivity study considered a selection of operational parameters. From this study it followed that it is good to avoid any coupling between the lifting arrangement natural frequencies and vessel response frequencies, as this would lead to resonant motions and thus increased blade root motions. Many parameters can be adjusted to tune the installation system.

Impact of Operational Parameters on the Relative Motions

To investigate the influence of operational parameters, a sensitivity study was conducted on key characteristics of the OWT, SSCV, and lifting configuration. The results showed that blade root motions depend strongly on the SSCVs dynamic response and the coupling between the pendulum mode of the lifting configuration and the vessel's natural frequencies.

For the SSCV, increasing the draught shifted the vessel's natural frequencies and reduced overall motion, which in turn led to smaller blade root motions. For the lifting configuration, adjustments to the suspension length and BIT mass were found to affect the pendulum frequency. These parameters can be tuned to avoid coupling with the SSCV's natural frequencies and thereby prevent resonant behaviour. Wider tugger line spacing improved yaw control but shifted the pendulum frequency closer to the vessel's response range, introducing potential for resonance. A spacing of 15 meters was identified as a favourable balance between control and resonance risk. Increasing the tugger stiffness had limited effect on translational blade root motions but did reduce rotational motion effectively. Variations in damping profiles were found to influence the amplitude of blade root motions, while increasing pretension helped prevent slack lines and potential snap loads in the tuggers.

Although this sensitivity study considered only a selection of operational parameters, it clearly showed that avoiding coupling between the natural frequencies of the lifting arrangement and the vessel response is critical to preventing resonant amplification of blade root motions. Multiple parameters can be tuned to optimise the dynamic behaviour of the installation system.

Overall Operability Evaluation

The operability of the installation system was evaluated by assessing the relative displacement between the hub and blade root over the full operational duration and comparing it to the defined operational limits.

The analysis revealed that hub motions near the natural frequencies of the offshore wind turbine contributed significantly to inoperable conditions. Even in the idealised vessel scenario, where no vessel-induced dynamics influence the blade root motions, the operation was found to be inoperable primarily due to large hub excitations. Furthermore, when using the SSCV, operability was shown to be limited for peak periods associated with increased vessel response. The study concluded that the operation remains operable only under conditions with low peak periods ($T_P = 4$s) and low wave heights ($H_s \leq 1$m).

When the contribution of hub motion was excluded from the relative displacement calculation, the SSCV-based operation became operable across a wider range of environmental conditions. This was particularly true for configurations featuring increased draught and parameter tuning aimed at avoiding

coupling between vessel motion frequencies and the blade pendulum frequencies. When considering only SSCV-induced effects, the operation was found to be operable for peak periods up to 6 seconds and wave heights up to 3 meters.

The study also highlighted the importance of the limiting criteria themselves. As expected, stricter criteria result in reduced operability. A more detailed investigation into what constitutes a realistic operational limit could offer a completely different perspective on the installation's feasibility and allowable conditions.

Influence of the SSCV on Installation Dynamics

Due to its floating nature, the SSCV is susceptible to wave-induced motions, which are transferred to the suspended blade and result in blade root displacements. These vessel motions can also couple with the suspended blade system, amplifying the relative motion and potentially leading to significant dynamic responses. This study demonstrated that the operability of the installation using an SSCV is highly sensitive to environmental conditions, particularly when wave excitation frequencies approach the vessel's natural frequencies. Although design modifications, such as increasing the draught or adjusting the suspension length, can help mitigate these effects, the overall feasibility of installation using an SSCV remains constrained under certain sea states.

These findings underscore the importance of evaluating vessel characteristics in relation to site-specific environmental conditions to accurately assess the feasibility of conducting the installation by SSCV.

In response to the central research question, how environmental and operational conditions influence the relative motion between the hub of a bottom-fixed offshore wind turbine and the blade root during single-blade installation using a semi-submersible crane vessel, and how this affects installation operability, this study has shown that both hub and blade root motions are primarily governed by wave-induced dynamics. Environmental conditions, particularly wave height and peak period, were found to significantly affect relative motion through the excitation of the natural frequencies of both the OWT and the SSCV. Operational parameters such as suspension length, tugger configuration, and SSCV draught were shown to either amplify or mitigate these effects, depending on their tuning. Operability was found to be influenced by different dominant mechanisms at different peak periods, with hub resonance being the most critical factor. In addition, SSCV motions and coupling between the natural frequencies of the lifting arrangement and the vessel response further limited operability.

Ultimately, the operability of single-blade installation using an SSCV depends on a carefully configured installation system, site- and vessel-specific characteristics, and the defined limiting criteria. For the SSCV *Thialf*, such an operation is feasible, but only within a moderate envelope of environmental conditions.

10

Discussion of Findings, Limitations, and Recommendations for Future Work

This chapter discusses the results, outlines the main limitations of the study to clarify the scope of its conclusions, and presents recommendations for future research on the topic.

10.1. Discussion

This first section reflects on the findings of the study, placing them in the context of real-world offshore wind turbine installation practices.

Applicability of SSCVs in Deep Water and Soft Soil Conditions

In offshore wind turbine installations, jack-up vessels are constrained by both water depth and seabed conditions (El-Reedy, 2012; Raaijmakers & Rudolph, 2007). In deep waters, jack-up legs may be too short to reach the seabed, while at sites with soft or erodible soils, excessive scour around the spud cans can result in settlement, leg tilting, or potentially unsafe conditions. In such scenarios, SSCVs offer a viable alternative, as they are not limited by soil structure interaction for station keeping and can operate independently of both water depth and geotechnical constraints.

Beyond technical feasibility, SSCVs provide notable logistical and commercial advantages. In many offshore wind projects, SSCVs are already deployed for foundation installation (Zhao et al., 2018). Leveraging the same vessel for turbine installation can eliminate the need for additional mobilisation, streamline project scheduling, and reduce overall installation costs. This dual-use capability strengthens the business case for HMC to extend SSCV operations beyond foundation installation to include turbine installation as well, positioning SSCVs as flexible and cost-effective assets for multi-phase offshore campaigns.

Operationally, SSCVs can relocate more rapidly than jack-up vessels in response to changing environmental conditions. Given the preference for perpendicular wind on the blade during installation due to aerodynamic load predictability, and the sensitivity of vessel dynamics to wave direction, this ability to maintain a favourable heading is beneficial for minimizing blade root motions and preserving operability during the alignment phase.

Although jack-up vessels are generally regarded as more stable installation platforms, they also experience dynamic excitation due to wave loading on their legs, wind forces acting on the elevated hull, and soil-structure interaction. Zhao et al. (2018) demonstrated that a selected SSCV can exhibit motion responses comparable to those of jack-ups in head seas, with similar standard deviations in vessel and blade motions for peak periods up to 7 seconds. Furthermore, that study reported increased vessel and blade root motions at higher peak periods. These findings support the results of the present

study, which demonstrated minimal blade root motions and operable conditions at lower peak periods for installations using an SSCV. This further shows that, under such conditions, SSCVs can perform comparably to jack-up vessels.

For moderate sea states where vessel responses remain limited, SSCVs offer operable conditions with dynamic behaviour similar to that of jack-up vessels. Their mobility, adaptability, and potential for multi-use across installation phases position SSCVs as strong candidates for full-scope turbine installation campaigns, assuming blade installation represents the most critical phase of the full-scope OWT installation.

Overall, the applicability of the SSCV for this installation is highly dependent on the environmental conditions at the installation site. When vessel responses remain limited and the overall dynamic behaviour resembles that of a jack-up vessel, the installation is feasible. In contrast, under conditions with larger peak periods, the increased response of the floating vessel renders the installation inoperable.

Hub Motions

It is well established that turbine blades can be installed offshore independently of the installation vessel. Considering the limiting effect that hub motions have on operability in this study, this either suggests that the applied limiting criteria may be overly conservative, or that resonant hub motions are relatively rare in real-world conditions.

Offshore wind turbines are typically designed so that their natural frequencies lie outside the dominant environmental excitation range. Therefore, it can be reasonably assumed that the peak periods leading to resonant hub responses do not occur frequently for a properly designed turbine.

A detailed investigation into the probability of occurrence of specific environmental conditions would constitute a workability analysis, which lies beyond the scope of this study. Nevertheless, it is important to note that the conditions under which hub motions significantly impair operability are likely infrequent at typical installation sites.

Turbine Structural Dynamics: Soft-Stiff vs. Stiff-Stiff Design

The turbine considered in this study follows a soft–stiff design philosophy, with its first natural frequency positioned between the wave excitation range and the rotor's 1P excitation frequency. This soft–stiff configuration is commonly adopted for large offshore wind turbines, as it results in cost-effective foundation designs (Wan et al., 2023). However, as demonstrated in this thesis, soft–stiff designs are vulnerable to resonant excitation when the wave peak period approaches the turbine's natural frequency. This resonance significantly amplifies hub displacements, often rendering the installation procedure non-operable under such sea states.

An alternative is the stiff–stiff design, where the first natural frequency is shifted above both the dominant wave excitation and the rotor-induced (1P and 3P) frequencies. This increased structural rigidity reduces susceptibility to dynamic amplification and effectively suppresses resonant hub motion. The resulting reduction in tower bending under wave and wind loading yields smaller amplitude responses and improves hub stability during blade installation. As such, a stiff–stiff design would substantially reduce the turbine's dynamic contribution to relative displacements and could expand the range of sea states under which installation is operable.

These advantages, however, come at the cost of greater structural requirements. Achieving higher natural frequencies necessitates stiffer and heavier support structures, often requiring larger-diameter MPs or alternative foundations, driving up overall project costs (Lian et al., 2022). Thus, while a stiff–stiff design presents clear dynamic benefits for single-blade installation by SSCV, its adoption needs to be weighed against economic considerations.

Vessel Response and Generalisability

A key finding of this study is the critical influence of vessel response on blade root motion and, by extension, the overall operability of the blade installation process. Since the suspended blade is dynamically coupled to the motions of the SSCV, any vessel movement directly affects the relative displacement between the blade root and the hub.

This vessel response is highly sensitive to hydrodynamic properties, which vary not only with sea state but also between different SSCV designs. The results presented in this thesis are based on the hydrodynamic load RAOs of the SSCV *Thialf*. While representative of a large semi-submersible, these findings are not universally applicable. Differences in hull geometry, mass distribution, draught, and damping characteristics can lead to different vessel responses under identical environmental conditions. Therefore, operability assessments for other SSCVs must be based on case-specific hydrodynamic modelling.

Additionally, vessel response is inherently site- and configuration-specific. Hydrodynamic behaviour, and consequently the load RAOs, varies with water depth, while changes in vessel draught and heading can significantly influence response characteristics and, in turn, operability outcomes.

In summary, vessel response should not be treated as a fixed parameter, but rather as a critical, configuration-dependent variable. To assess operability for a given SSCV, each unique combination of site and vessel must be evaluated individually. Although this research offers a structured framework for evaluation, its conclusions are applicable only within the scope of the investigated configuration.

Validity of the Numerical Model and Assumptions

The numerical model developed in this study provides valuable insights into the dynamic behaviour of offshore blade installation using a SSCV. However, several simplifications and modelling assumptions were required to make the simulations tractable, and these inherently affect the fidelity and generalisability of the results.

For the SSCV, linear Response Amplitude Operators (RAOs) were used, assuming small-amplitude motions and linear hydrodynamic behaviour. Assumptions such as an effective DP system and the exclusion of current loads simplified vessel station-keeping but do not fully capture realistic vessel response under environmental loading.

Furthermore, the whip of the crane is used as the lifting point to reach the required elevation of the OWT. While this crane point is sufficient for lifting the blade in the studied lifting configuration, it is not strong enough to lift other OWT components nor the blade in heavier lifting arrangements. To enable the SSCV to perform full OWT installation, reinforcement of the whip hoist lifting point is necessary. In addition, clearances between the lifted object and the crane structure have not been considered in this study. These spatial constraints may also require crane modifications, such as a boom extension. Such upgrades would alter the dynamics of the installation process and could therefore affect the operability of the installation.

The lifting configuration was modelled in a simplified manner, omitting detailed rigging geometry and real-world winch dynamics. Tugger systems were approximated with a non-linear damping profile, which adds realism over purely linear models but does not represent the complex tugger behaviour.

The wind turbine structure itself was modelled as a linear elastic system, sufficient for modal analysis but unable to capture potential non-linearities, such as tower deformation or soil-structure interactions. Also, due to the blades being modelled as rigid bodies, aeroelastic effects are not accounted for. Additionally, several environmental effects were simplified or excluded: like VIV effects, wind–wave misalignment, and wave shielding interactions between the SSCV and the OWT.

The numerical model remains a simulation of the real-world situation, in which components are simplified and certain effects are neglected. While the current model presents an overview of the dominant dynamic behaviour during the alignment phase, its results should be interpreted with consideration of the underlying assumptions and limitations. The main limitations are summarised in Section 10.2.

Operational Limits

The operability assessment in this study is based on predefined safety criteria. While these thresholds provide a consistent and objective basis for evaluating different configurations and environmental conditions, it is important to consider whether such criteria are overly conservative or realistically reflect the demands and tolerances of real-world offshore operations.

In the absence of widely standardised industry values for single-blade installation, these safety limits are

often informed by engineering judgement, expert experience, or extrapolation from related procedures. However, the high sensitivity of operability to these criteria, as demonstrated in this study, emphasises the need for careful calibration. Even small relaxations in the displacement threshold or outcrossing frequency can significantly increase the range of operable sea states, while stricter thresholds may lead to overly cautious decisions that unnecessarily reduce installation windows and raise project costs.

Ultimately, the safety margin must reflect not only theoretical design tolerances, but also the practical realities of offshore execution. The crew's confidence in proceeding with the operation is critical, particularly given the precision and timing required during blade-to-hub alignment. As such, operational limits should ideally be defined through a combination of dynamic simulation, industry best practices, and field measurements from comparable operations.

10.2. Limitations

This study presents a dynamic analysis of offshore wind turbine single-blade installation using an SSCV, based on a numerical model of the installation system. However, several limitations of the study are acknowledged:

- *Case-specific applicability:* The analysis was performed for a single turbine model (IEA 15 MW), a specific installation vessel (SSCV *Thialf*), and a defined environmental context (Baltic Sea, 30 m depth). While the results offer valuable insights, they are not directly generalisable to other turbine types, vessel designs, or site conditions without case-specific adaptation.
- *Scope of installation phase:* This study focused exclusively on the alignment phase of single-blade installation. Other critical stages of the OWT installation, such as blade mating or tower-top bolting, were not addressed and may introduce additional dynamic considerations and operational constraints.
- *Analysis method:* The motions are analysed using the standard deviation to quantify and compare different dynamic effects. While this is an effective way to capture the average magnitude of motion, it does not account for extreme values. These extremes are visualised in the presented three-dimensional trajectories and relative motions, but they are not considered in the evaluation of environmental and operational effects.
- *Environmental conditions:* Simulations were limited to a representative but narrow set of wind and wave conditions. Only one site was analysed, and directional variability was constrained. Broader environmental conditions or alternative excitation frequencies could activate different resonant modes or dynamic behaviours not captured here.
- *Linear modelling assumptions:* The structural and hydrodynamic responses of both turbine and vessel were modelled under linear assumptions. The SSCV response was based on linear load RAOs, neglecting second-order wave effects, sum–difference frequency interactions, and current-induced forces. The DP system was assumed ideal, without accounting for drift or wind-induced motion. Crane dynamics were treated as rigid-body responses, excluding structural deformations. The turbine was modelled as a linear elastic system, omitting large deflections, joint flexibility, and non-linear soil–pile interaction. Non-linear blade flexibility and aeroelastic effects were also excluded by modelling the blades as rigid bodies.
- *Aerodynamic loading simplification:* Aerodynamic excitation was modelled using the cross-flow principle, assuming wind perpendicular to the blade plane. While this is reasonable for blades oriented perpendicularly to the wind, other wind directions were not considered. Consequently, the potential influence of wind directional changes on blade excitation was omitted from the analysis.
- *Shielding effects:* Potential hydrodynamic interactions between the SSCV and the OWT, such as wave shielding, diffraction, and wave reflections, were not included in the numerical model. In practice, the presence of a large vessel in close proximity to the turbine can alter the local wave field. The SSCV may partially block or diffract incoming waves, potentially reducing wave loading on the turbine (beneficial shielding). Conversely, wave energy reflected from the vessel hull could amplify hub motion through constructive interference. These complex, position-dependent interactions require detailed hydrodynamic coupling simulations which were out of scope for this study. However, they may play a non-negligible role in real-world conditions and should be addressed

in higher-fidelity models.

- *Tugger system modelling:* Tuggers were approximated using a simplified non-linear damping profile. While this approach is more representative than linear models, it remains an idealisation. In reality, tugger dynamics are governed by complex mechanisms whose behaviour is difficult to accurately capture in time-domain simulations.

10.3. Recommendations for Future Work

This section presents recommendations for future research on the topic.

Validation through Field Measurements

While this study provides a detailed numerical assessment of the blade installation process, the results have not been validated against real-world data. Future research could address this by incorporating experimental validation through offshore measurement campaigns or scaled physical testing.

Such validation could involve capturing vessel motions, blade dynamics, and hub displacements during the alignment phase. These data would enable verification of key modelling assumptions, including the use of linear RAOs, the damping behaviour of the tuggers, and simplifications in the structural and aerodynamic representations. For instance, motion tracking of the blade root and crane tip could reveal discrepancies between predicted and observed dynamic coupling, offering insight into the accuracy of the lifting configuration model.

Experimental validation can enhance confidence in the numerical model's predictive accuracy and provide critical insights for model refinement and the correction of underlying assumptions.

Limiting Criteria Assessment

It is recommended that future research investigates what constitutes realistic operational limits for the single-blade installation process. As demonstrated in this study, these limits have a significant impact on the assessed operability of the installation. A more refined understanding of these thresholds could offer a fundamentally different perspective on the feasibility of the operation and the range of allowable environmental conditions.

Improved Estimation of Aerodynamic Loads

This study employed simplified aerodynamic loading assumptions based on the cross-flow principle, considering wind only perpendicular to the blade and assuming a feathered blade orientation. While this approach is reasonable for an initial assessment, it neglects important aerodynamic effects such as varying wind directions, transient gusts, unsteady flow regimes, altered angle-of-attack distributions, and flow interactions near the hub and crane components. These simplifications may lead to inaccurate load predictions and limit the applicability of the study to wind directions that are strictly perpendicular to the turbine blades.

Although wind showed a limited effect on the overall motions of the hub and blade root, it did result in considerable maximum excursions of the blade root. The above listed neglected aerodynamic effects could further amplify such excursions, which could be critical for the operability of the installation.

It is therefore recommended that future research focus on developing more accurate methods for estimating aerodynamic loads during blade installation. Improved load predictions would allow for better estimation of the fluctuating and extreme blade root motions. This, in turn, would support more effective design of the lifting configuration and help mitigate these adverse effects on installation operability.

Optimisation of the Tugger Configuration

The sensitivity analyses conducted in this study identified the pendulum-like motion of the suspended blade in the global y-direction as a significant contributor to relative displacement and potential operability loss under certain sea states and vessel response conditions. The current tugger configuration primarily constrains motion within the x–z plane and provides limited resistance to transverse movement in the y-direction. Consequently, resonant responses may occur when the blade's pendulum frequency aligns with vessel-induced excitations.

It is recommended that future research explore alternative spatial arrangements of the tuggers to enhance control in all translational directions. Modifying the angles of application or introducing additional lateral constraint lines could increase stability and damping, thereby mitigating pendulum-like motions.

Ideally, the blade should remain stationary relative to the crane tip, eliminating coupled resonant blade root motions. Leaving the vessel motion as the dominant contributor to relative displacement between the blade root and the hub.

Investigation of Mitigation Strategies

Literature exists on possible mitigation strategies for limiting the relative motion between the hub and blade root during single-blade installation. Jiang (2018) investigated the use of a passive tuned mass damper to reduce hub motions, while Ren et al. (2018) applied active control through three active tugger lines to stabilise the blade and limit the blade root motions during installation.

This research did not account for any mitigation strategy to show the true dynamic behaviour of the hub and blade root whilst suspended from a future vessel. It is however recommended for future research to further explore mitigation strategies and their effect on the investigated operation. Each of the following methods targets specific limitations identified in this study:

- *Active tugger control:* As investigated by Ren et al. (2018), active tugger control has the potential to mitigate blade oscillations by dynamically adjusting restoring forces in response to vessel and blade root motions. This strategy could effectively reduce the relative displacement not only between the blade root and the vessel, but also between the blade root and the hub. As a result, it would improve the relative motion characteristics and enhance the operability of the installation process.
- *Tuned Mass Dampers (TMDs):* As investigated by Jiang (2018), installing TMDs on OWT could reduce hub motions. Given the substantial influence of hub motions on installation operability, the implementation of TMDs could significantly enhance overall operability.
- *Motion compensation in lifting arrangement:* Incorporating active heave compensation or motion-suppression systems in the crane or lifting configuration could help mitigate the transfer of vessel-induced motions to the blade root, thereby reducing relative displacements and improving installation operability.
- *Blade alignment stabbing cone:* A passive guidance structure around the hub, such as a stabbing cone, could support the alignment phase by helping to guide and 'catch' the incoming blade, thereby easing the alignment process. This feature may facilitate the alignment under less stringent limiting criteria, potentially allowing larger misalignments without causing damaging contact and thereby improving overall operability.

References

Airpes. (2025). Wind Turbine Blade Materials Handling Clamp GE-ASBI25t [Accessed: 2025-07-09].

Alari, V., & Van Vledder, G. P. (2016). Spatial variability of directional misalignment between waves and wind in the baltic sea – model study [41-year high-resolution hindcast analysis of wind–wave misalignment in the Baltic Sea]. *Marine Systems Institute at Tallinn University of Technology and Delft University of Technology*. http://waveworkshop.org/13thWaves/Papers/WW2013_Alari_VanVledder_Final.pdf

Arya, S. C., O'Neill, M. W., & Pincus, G. (1979). *Design of structures and foundations for vibrating machines*. Gulf Publishing Company.

Bastiaanssen, P. (2020, September). *Modelling the dynamic behaviour of a rotor nacelle assembly during installation using a floating vessel* [Master's thesis]. Delft University of Technology, Norwegian University of Science, and Technology [Dual degree: MSc in Offshore and Dredging Engineering (TU Delft), MSc in Technology - Wind Energy (NTNU)]. http://repository.tudelft.nl/

Chen, C., Zhou, J.-w., Li, F., & Gong, D. (2023). Nonlinear vortex-induced vibration of wind turbine towers: Theory and experimental validation. *Mechanical Systems and Signal Processing*, *204*, 110772. https://doi.org/https://doi.org/10.1016/j.ymssp.2023.110772

De Leeuw, K. (2019). Single lift blade alignment for large offshore wind turbines.

Det Norske Veritas. (2011, April). DNV-RP-N103: Modelling and Analysis of Marine Operations [Recommended Practice, DNV-RP-N103]. http://www.dnv.com

DNV. (2023, December). DNV-ST-N001: Marine Operations and Marine Warranty [Standard, DNV-ST-N001. Edition December 2023]. https://www.dnv.com

El-Reedy, M. A. (2012). *Offshore structures: Design, construction and maintenance*. Gulf Professional Publishing.

Fenger, P. (2019). Upscaling – the game changers: Smart installation and service tool solutions [Presentation at WindEurope Offshore 2019].

Gaertner, E., Rinker, J., Sethuraman, L., Zahle, F., Anderson, B., Barter, G. E., Abbas, N. J., Meng, F., Bortolotti, P., Skrzypinski, W., Scott, G. N., Feil, R., Bredmose, H., Dykes, K., Shields, M., Allen, C., & Viselli, A. (2020). Iea wind tcp task 37: Definition of the iea 15-megawatt offshore reference wind turbine. *OSTI*. https://doi.org/10.2172/1603478

Gaunaa, M., Bergami, L., Guntur, S., & Zahle, F. (2014). First-order aerodynamic and aeroelastic behavior of a single-blade installation setup. *The Science of Making Torque from Wind (TORQUE 2014)*, *524*, 012073. https://doi.org/10.1088/1742-6596/524/1/012073

Global Times. (2025, July). Offshore wind turbine with the largest rotor diameter in the world unveiled in coastal fujian, east china [Accessed: 2025-07-10]. https://www.globaltimes.cn/page/202507/1338041.shtml

Heerema Marine Contractors. (2022). Arcadis ost 1 offshore wind project [Accessed: 2025-07-10]. https://www.heerema.com/heerema-marine-contractors/offshore-wind/arcadis-ost-1

Heerema Marine Contractors. (2024). Thialf [Accessed: 2024-11-07]. https://www.heerema.com/heerema-marine-contractors/fleet/thialf

Hoerner, S. F. (1985). *Fluid dynamic lift: Practical information on aerodynamic and hydrodynamic lift*. Hoerner Fluid Dynamics. https://archive.org/details/FluidDynamicLiftHoerner1985/page/n299/mode/2up

Husain, M. K. A., Zaki, N. I. M., & Najafian, G. (2017). Various methods of simulating wave kinematics on the structural members of 100-year responses [Email: mohdkhairi.kl@utm.my]. *Proceedings of the International Conference on Engineering Technology (ICET)*.

International Electrotechnical Commission. (2019). IEC 61400-3-1:2019 wind energy generation systems – part 3-1: Design requirements for fixed offshore wind turbines [IEC Standard]. *International Electrotechnical Commission*.

International Energy Agency (IEA). (2010). *10mw fixed-bottom offshore wind turbine (owt) model* (tech. rep.) (The system design basis is documented by the Systems Engineering Wind Energy -

WP2.1 Reference Wind Turbines technical report, available from the open-source IEA-10.0-198-RWT GitHub repository). International Energy Agency (IEA). https://www.orcina.com/wp-content/uploads/examples/k/k02/K02%2010MW%20fixed-bottom%20OWT.pdf

Jiang, Z. (2018). The impact of a passive tuned mass damper on offshore single-blade installation. *Journal of Wind Engineering and Industrial Aerodynamics*, *176*, 65–77. https://doi.org/10.1016/j.jweia.2018.03.008

Jiang, Z., Gao, Z., Ren, Z., Li, Y., & Duan, L. (2018). A parametric study on the final blade installation process for monopile wind turbines under rough environmental conditions. *Engineering Structures*, *172*, 1042–1056.

Joseph, A., S., A., & Viswanathan, S. (2014). Second order wave force effects on a semisubmersible platform. *INTERNATIONAL JOURNAL OF DESIGN AND MANUFACTURING TECHNOLOGY*, *5*. https://doi.org/10.34218/IJDMT.5.3.2014.30320140503002

Kitzing, L., & Morthorst, P. E. (2015). Trends in offshore wind economics – the past and the future [Peer reviewed version]. *Proceedings of the 14th Wind Integration Workshop*. https://backend.orbit.dtu.dk/ws/portalfiles/portal/117692803/Trends_in_offshore_wind_economics.pdf

Kroon, E. (2024, December). Operability of an offshore wind turbine blade installation operation by floating vessel [TMR4590 - Wind Turbine Energy - Offshore Engineering, Specialization Project].

Li, L., Gao, Z., Moan, T., & Ormberg, H. (2014). Analysis of lifting operation of a monopile for an offshore wind turbine considering vessel shielding effects. *Marine Structures*, *39*, 287–314. https://doi.org/https://doi.org/10.1016/j.marstruc.2014.07.009

Lian, J., Zhou, H., & Dong, X. (2022). A theoretical approach for resonance analysis of wind turbines under 1p/3p loads. *Energies*, *15*(16), 5787. https://doi.org/10.3390/en15165787

Liftra. (2025). Blade handling brochure [Accessed June 2025].

Livanos, D. (2018). *Investigation of vortex induced vibrations on wind turbine towers* [Master's thesis]. Delft University of Technology [Faculty of Mechanical Engineering]. http://resolver.tudelft.nl/uuid:90b62a9f-0740-4798-8a9a-7b2708756268

Morison, J., Johnson, J., & Schaaf, S. (1950). The force exerted by surface waves on piles. *Journal of Petroleum Technology*, *2*(05), 149–154. https://doi.org/10.2118/950149-G

Orcina Ltd. (2024a). Dynamic analysis: Time domain solution – orcaflex documentation [Accessed: 2025-05-29]. https://www.orcina.com/webhelp/OrcaFlex/Default.htm#GeneralTimeSteps

Orcina Ltd. (2024b). Environment: Data for random waves – orcaflex documentation [Accessed: 2025-06-29]. https://www.orcina.com/webhelp/OrcaFlex/Content/html/Environment,Dataforrandomwaves.htm

Orcina Ltd. (2024c). General data: Explicit integration – orcaflex documentation [Accessed: 2025-05-29]. https://www.orcina.com/webhelp/OrcaFlex/Content/html/Generaldata,Explicitintegration.htm#GeneralTimeSteps

Orcina Ltd. (2024d). Line theory: Hydrodynamic and aerodynamic loads [Accessed: 2025-07-14]. https://www.orcina.com/webhelp/OrcaFlex/Content/html/Linetheory%2CHydrodynamicandaerodynamicloads.htm?utm_source=chatgpt.com

Orcina Ltd. (2024e). Modal analysis – orcaflex documentation [Accessed: 2025-05-26]. https://www.orcina.com/webhelp/OrcaFlex/Content/html/Modalanalysis,Theory.htm

Orcina Ltd. (2024f). Modelling introduction – orcaflex documentation [Accessed: 2025-06-01]. https://www.orcina.com/webhelp/OrcaFlex/Content/html/Modellingintroduction.htm

Orcina Ltd. (2024g). Morison's equation – orcaflex documentation [Accessed: 2025-06-02]. https://www.orcina.com/webhelp/OrcaFlex/Content/html/Morison%27sequation.htm

Orcina Ltd. (2024h). Results: Spectral density graphs – orcaflex documentation [Accessed: 2025-07-05]. https://www.orcina.com/webhelp/OrcaFlex/Content/html/Results,Spectraldensitygraphs.htm

Orcina Ltd. (2024i). Turbine theory: Aerodynamic load – orcaflex documentation [Accessed: 2025-06-08]. https://www.orcina.com/webhelp/OrcaFlex/Content/html/Turbinetheory,Aerodynamicload.htm

Orcina Ltd. (2024j). Vessel theory: Rao quality checks – orcaflex documentation [Accessed: 2025-06-09]. https://www.orcina.com/webhelp/OrcaFlex/Content/html/Vesseltheory,RAOqualitychecks.htm

Orcina Ltd. (2024k). Wave theorys – orcaflex documentation [Accessed: 2025-06-29]. https://www.orcina.com/webhelp/OrcaFlex/Content/html/Wavetheory.htm

Pezeshki, H., Pavlou, D., Adeli, H., & Siriwardane, S. C. (2023). Modal analysis of offshore monopile wind turbine: An analytical solution. *Journal of Offshore Mechanics and Arctic Engineering*, *145*(1), 010907. https://doi.org/10.1115/1.4055402

Pirrung, G. R., Grinderslev, C., Sørensen, N. N., & Riva, R. (2024). Vortex-induced vibrations of wind turbines: From single blade to full rotor simulations. *Renewable Energy*, *226*, 120381. https://doi.org/https://doi.org/10.1016/j.renene.2024.120381

Raaijmakers, T., & Rudolph, D. (2007). Scour protection of spud cans – a new design approach. *Proceedings of the 11th International Conference "The Jack-Up Platform Design, Construction & Operation"*, 1–13.

Ren, Z., Jiang, Z., Skjetne, R., & Gao, Z. (2018). Single blade installation using active control of three tugger lines. *Proceedings of the Twenty-eighth (2018) International Ocean and Polar Engineering Conference*.

Sarpkaya, T. (2004). A critical review of the intrinsic nature of vortex-induced vibrations. *Journal of Fluids and Structures*, *19*(4), 389–447. https://doi.org/https://doi.org/10.1016/j.jfluidstructs.2004.02.005

Sheng, W., Tapoglou, E., Ma, X., Taylor, C. J., Dorrell, R., Parsons, D., & Aggidis, G. (2022). Hydrodynamic studies of floating structures: Comparison of wave-structure interaction modelling. *Ocean Engineering*, *249*, 110878. https://doi.org/10.1016/j.oceaneng.2022.110878

Shirzadeh, R., Devriendt, C., Bidakhvidi, M., & Guillaume, P. (2013). Experimental and computational damping estimation of an offshore wind turbine on a monopile foundation. *Journal of Wind Engineering and Industrial Aerodynamics*, *120*, 96–106. https://doi.org/https://doi.org/10.1016/j.jweia.2013.07.004

Stehly, T., Beiter, P., Heimiller, D., & Scott, G. (2018). *2017 cost of wind energy review* (tech. rep. No. NREL/TP-6A20-72167). National Renewable Energy Laboratory. Golden, CO. https://www.nrel.gov/docs/fy18osti/72167

Timoshenko, S., Young, D. H., & Jr., W. W. (1974). *Vibration problems in engineering* (4th). Wiley.

Varghese, R., Pakrashi, V., & Bhattacharya, S. (2022). A compendium of formulae for natural frequencies of offshore wind turbine structures. *Energies*, *15*(8), 2967. https://doi.org/10.3390/en15082967

Verma, A. S., Jiang, Z., Ren, Z., Gao, Z., & Vedvik, N. P. (2019). Response-based assessment of operational limits for mating blades on monopile-type offshore wind turbines [adapted figure] [Figure adapted from the original publication].

Verma, A. S., Jiang, Z., Vedvik, N. P., Gao, Z., & Ren, Z. (2019). Impact assessment of a wind turbine blade root during an offshore mating process. *Engineering Structures*, *180*, 205–222. https://doi.org/https://doi.org/10.1016/j.engstruct.2018.11.012

Wan, J.-H., Bai, R., Li, X.-Y., & Liu, S.-W. (2023). Natural frequency analysis of monopile supported offshore wind turbines using unified beam-column element model. *Journal of Marine Science and Engineering*, *11*(3), 628. https://doi.org/10.3390/jmse11030628

WindEurope. (2024, April). *Offshore wind energy 2023 statistics* (Accessed: 2024-11-07). WindEurope.

WindEurope. (2025, February). *2024 statistics and the outlook for 2025–2030* (Accessed: 2025-07-10). WindEurope.

Zhao, Y., Cheng, Z., Sandvik, P. C., Gao, Z., Moan, T., & Van Buren, E. (2018). Numerical modeling and analysis of the dynamic motion response of an offshore wind turbine blade during installation by a jack-up crane vessel. *Ocean Engineering*, *165*, 353–364. https://doi.org/https://doi.org/10.1016/j.oceaneng.2018.07.049

A

Soil Model

This appendix presents the analytical stiffness formulations for soil-structure interaction, based on the theory of an elastic half-space. These expressions are derived from the work of Arya et al. (1979) and are applicable to circular foundations such as monopiles. The stiffness components are provided for vertical, horizontal, rocking, and torsional directions.

A.1. Elastic half-space model

A.1.1. Vertical Stiffness

The vertical stiffness of the soil represents the resistance in the axial direction of the structure. For monopiles and towers, this contribution is often considered negligible due to their relatively high axial rigidity:

$$\eta_z = 1 + 0.6(1-\nu)\frac{h}{r_0} \tag{A.1}$$

$$k_z = \frac{4Gr_0}{1-\nu}\eta_z \tag{A.2}$$

where:

- η_z: vertical stiffness factor,
- ν: Poisson's ratio of the soil,
- h: embedded depth of the structure,
- r_0: radius of the circular foundation,
- G: shear modulus of the soil,
- k_z: vertical stiffness.

A.1.2. Horizontal Stiffness

The horizontal stiffness characterizes the soil's resistance to lateral movement of the structure:

$$\eta_x = 1 + 0.55(2-\nu)\frac{h}{r_0} \tag{A.3}$$

$$k_x = \frac{32(1-\nu)Gr_0}{7-8\nu}\eta_z \tag{A.4}$$

where:

- η_x: horizontal stiffness factor,
- k_x: horizontal (lateral) stiffness,
- η_z: vertical stiffness factor, defined in Equation A.1.

A.1.3. Rocking Stiffness

The rocking stiffness accounts for the soil resistance to rotational motion about the horizontal axis:

$$\eta_\psi = 1 + 1.2(1-\nu)\frac{h}{r_0} + 0.2(2-\nu)\left(\frac{h}{r_0}\right)^3 \tag{A.5}$$

$$k_\psi = \frac{8Gr_0^3}{3(1-\nu)}\eta_\psi \tag{A.6}$$

where:

- η_ψ: rocking stiffness factor,
- k_ψ: rocking stiffness.

A.1.4. Torsional Stiffness

The torsional stiffness defines the soil's resistance to rotation around the vertical axis:

$$k_\phi = \frac{16Gr_0^3}{3} \tag{A.7}$$

where:

- k_ϕ: torsional stiffness.

B

Spectral Densities

The spectral densities in this appendix are presented for both translational and rotational motions, defined along the X, Y, and Z axes. Rotational components are labelled as Rotation 1, Rotation 2, and Rotation 3, corresponding to rotation about the X, Y, and Z axes, respectively

B.1. SSCV Parameters

B.1.1. SSCV Spectral Densities for two SSCV draughts

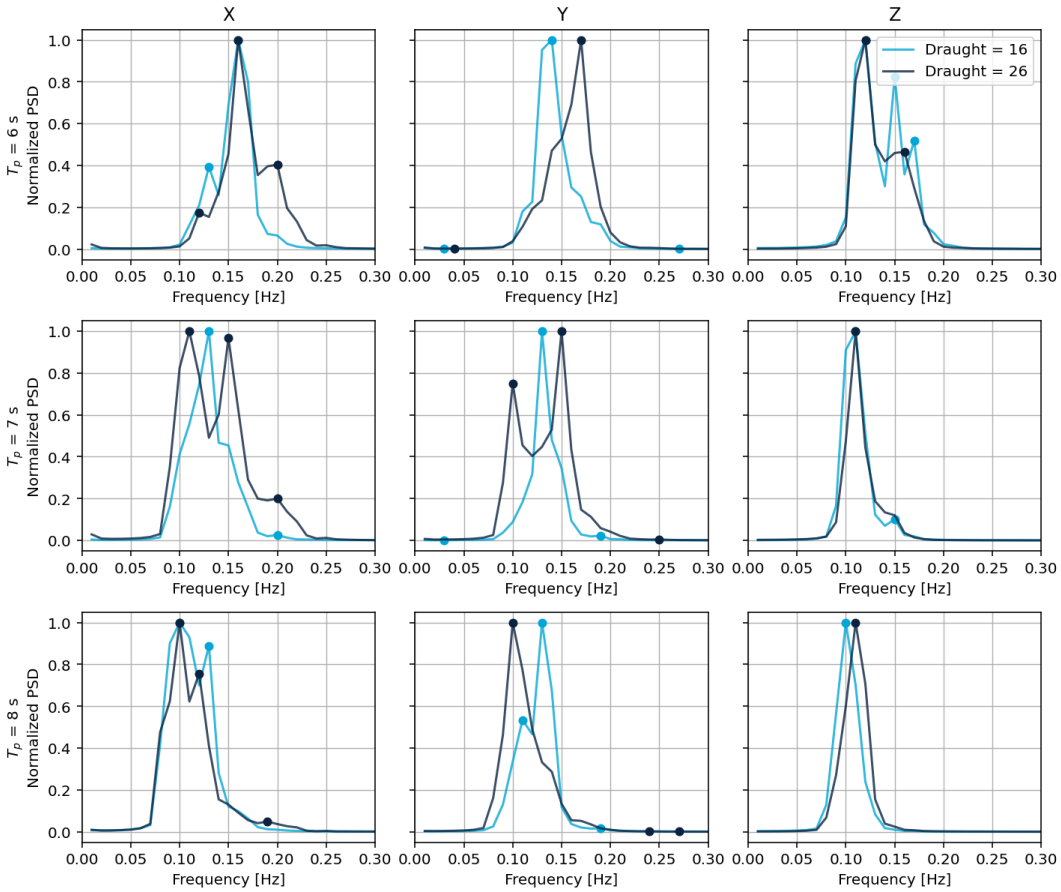

Figure B.1: Normalized spectral density for $T_p = 6$ s, $T_p = 7$ s and $T_p = 8$ s for the translational response of the Thialf where H_s = 1 m, V_w = 12 m/s, and a wind-wave direction of $180°$, for two SSCV draughts.
(The spectral density has been normalized due to confidentiality of the HMC vessel data.)

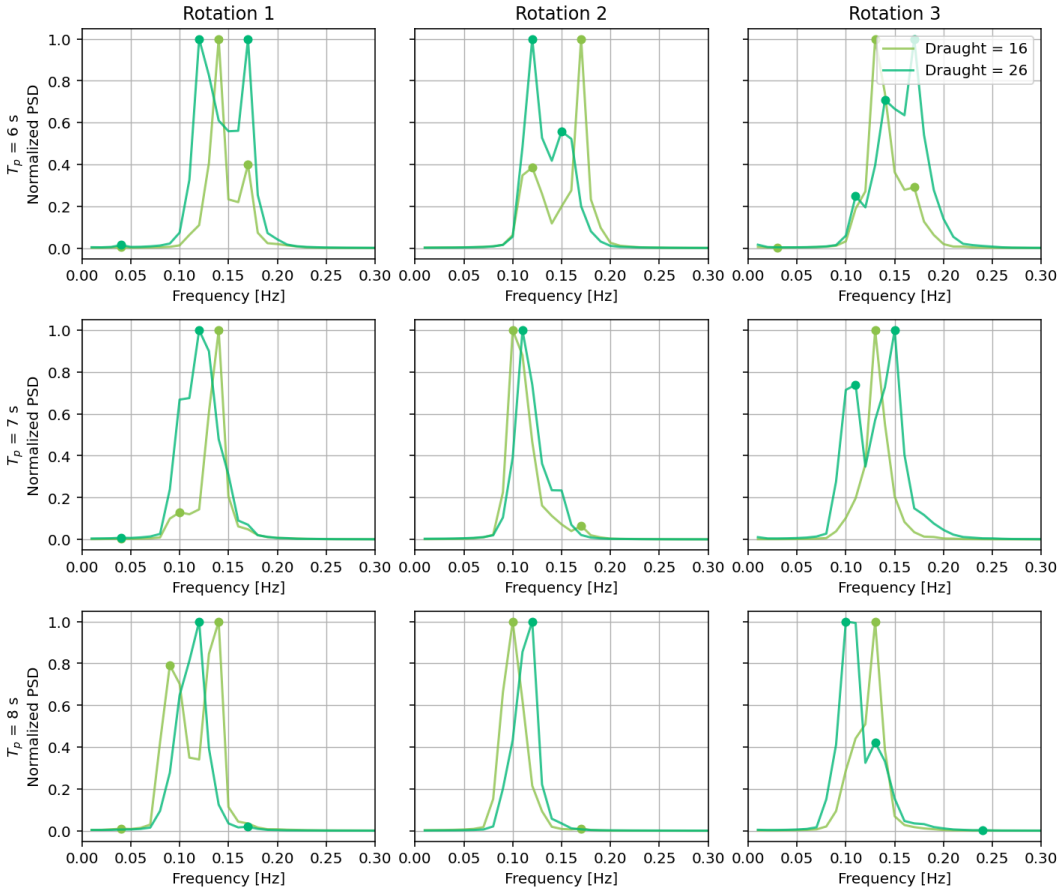

Figure B.2: Normalized spectral density for $T_p = 6$ s, $T_p = 7$ s and $T_p = 8$ s for the rotational response of the Thialf where H_s = 1 m, V_w = 12 m/s, and a wind-wave direction of $180°$, for two SSCV draughts.
(The spectral density has been normalized due to confidentiality of the HMC vessel data.)

B.1.2. BIT Spectral Densities for two SSCV draughts

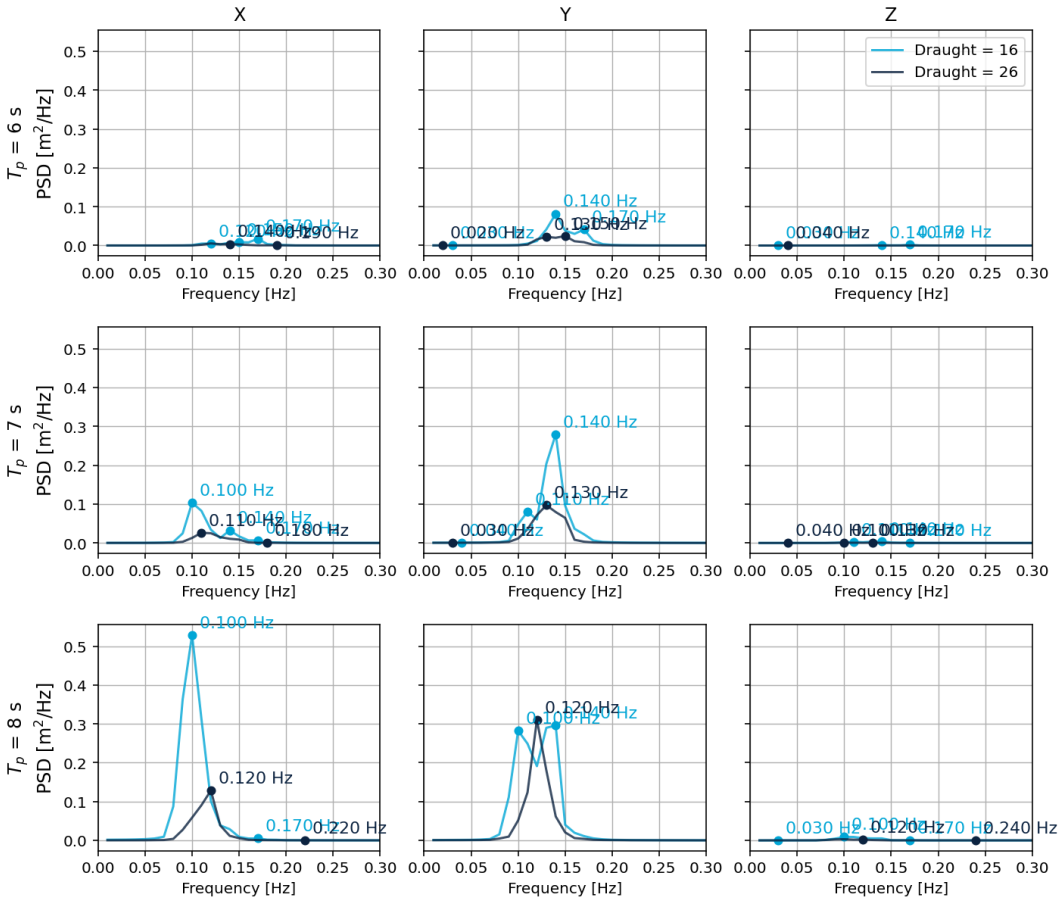

Figure B.3: Spectral density for $T_p = 6$ s, $T_p = 7$ s and $T_p = 8$ s for the translational response of the BIT at a wave direction of $180°$, for two SSCV draughts.

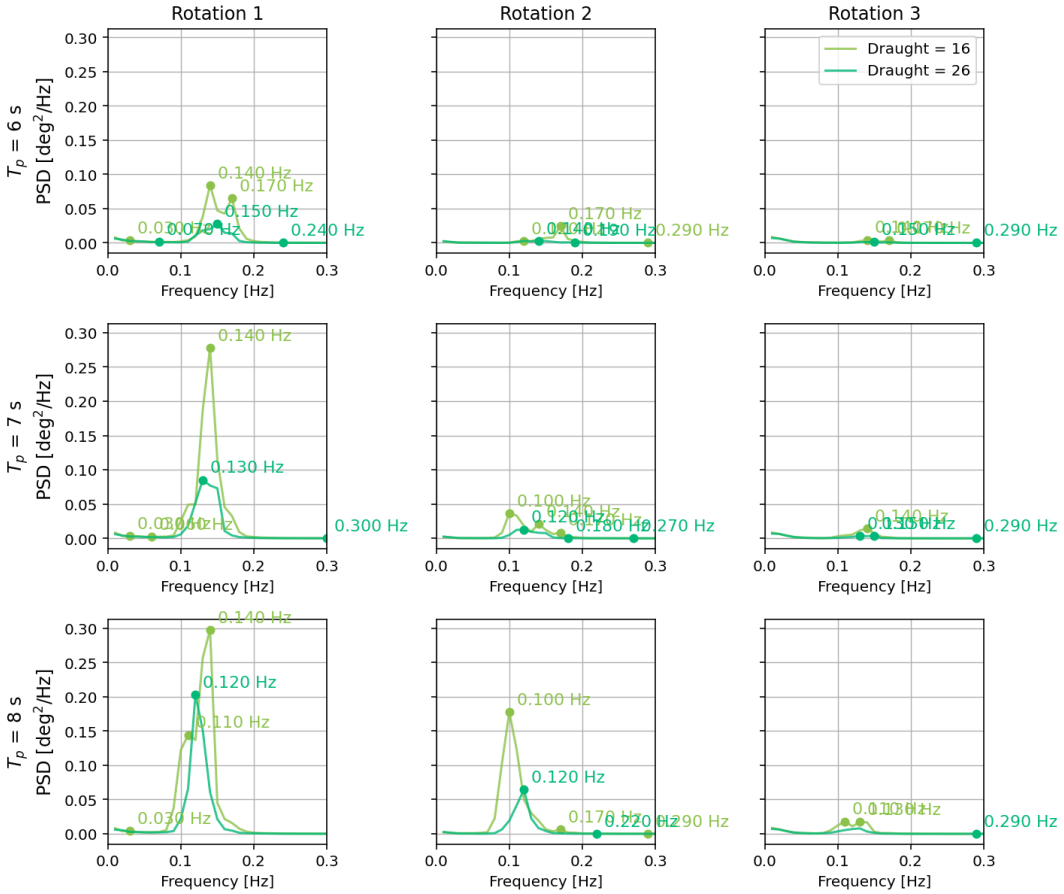

Figure B.4: Spectral density for $T_p = 6$ s, $T_p = 7$ s and $T_p = 8$ s for the rotational response of the BIT at a wave direction of $180°$.

B.2. Lifting Configuration Parameters

B.2.1. BIT Spectral Densities for Various Suspension Length

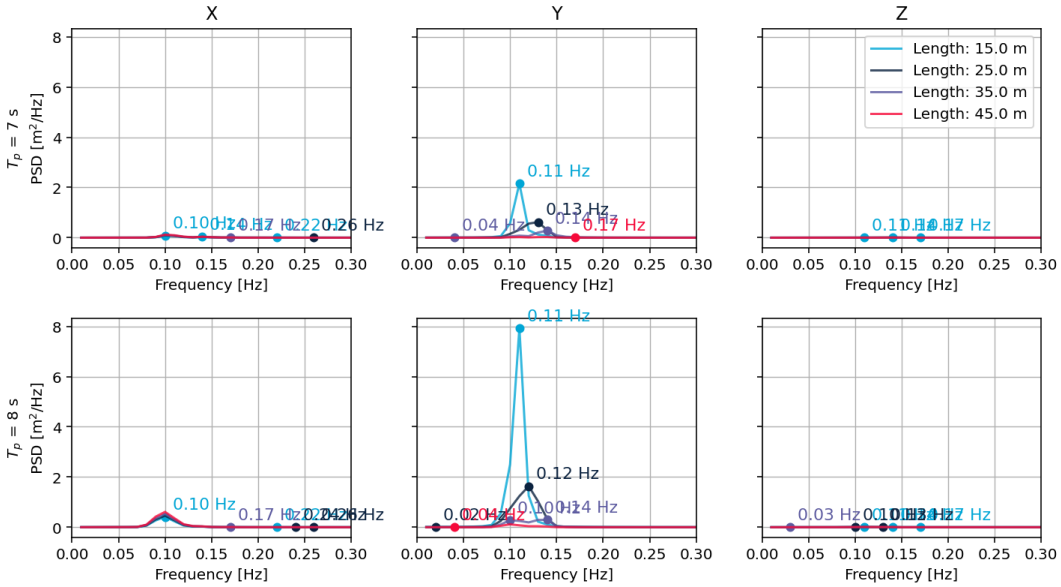

Figure B.5: Spectral density for $T_p = 7\,\text{s}$ and $T_p = 8\,\text{s}$ for the translational response of the BIT at a wave direction of $180°$, for varying suspension lengths.

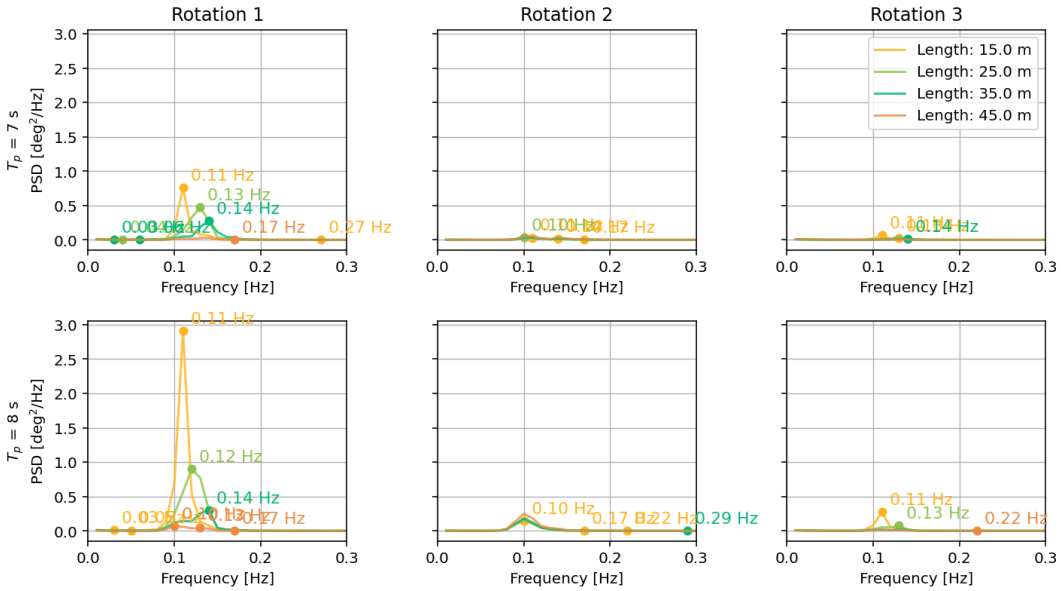

Figure B.6: Spectral density for $T_p = 7\,\text{s}$ and $T_p = 8\,\text{s}$ for the rotational response of the BIT at a wave direction of $180°$, for varying suspension lengths.

B.2.2. BIT Spectral Densities for Various BIT Masses

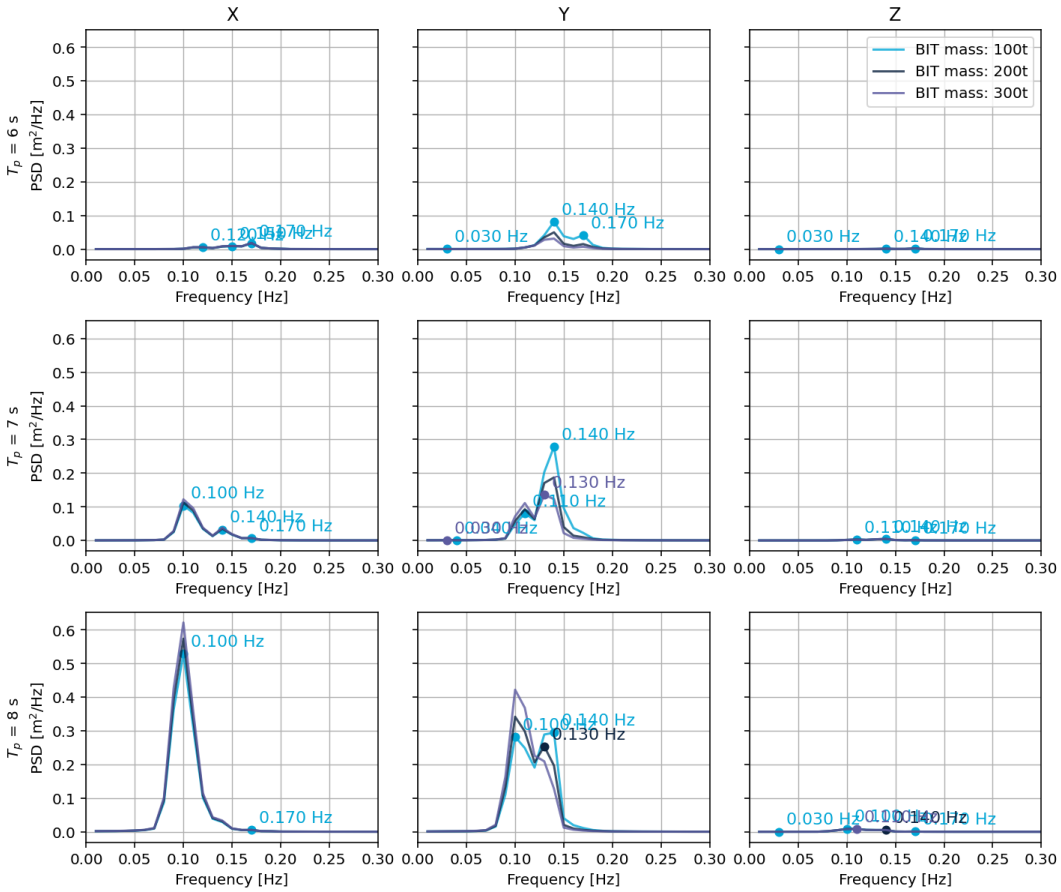

Figure B.7: Spectral density for $T_p = 6$ s, $T_p = 7$ s and $T_p = 8$ s for the translational response of the BIT at a wave direction of $180°$, for varying BIT mass.

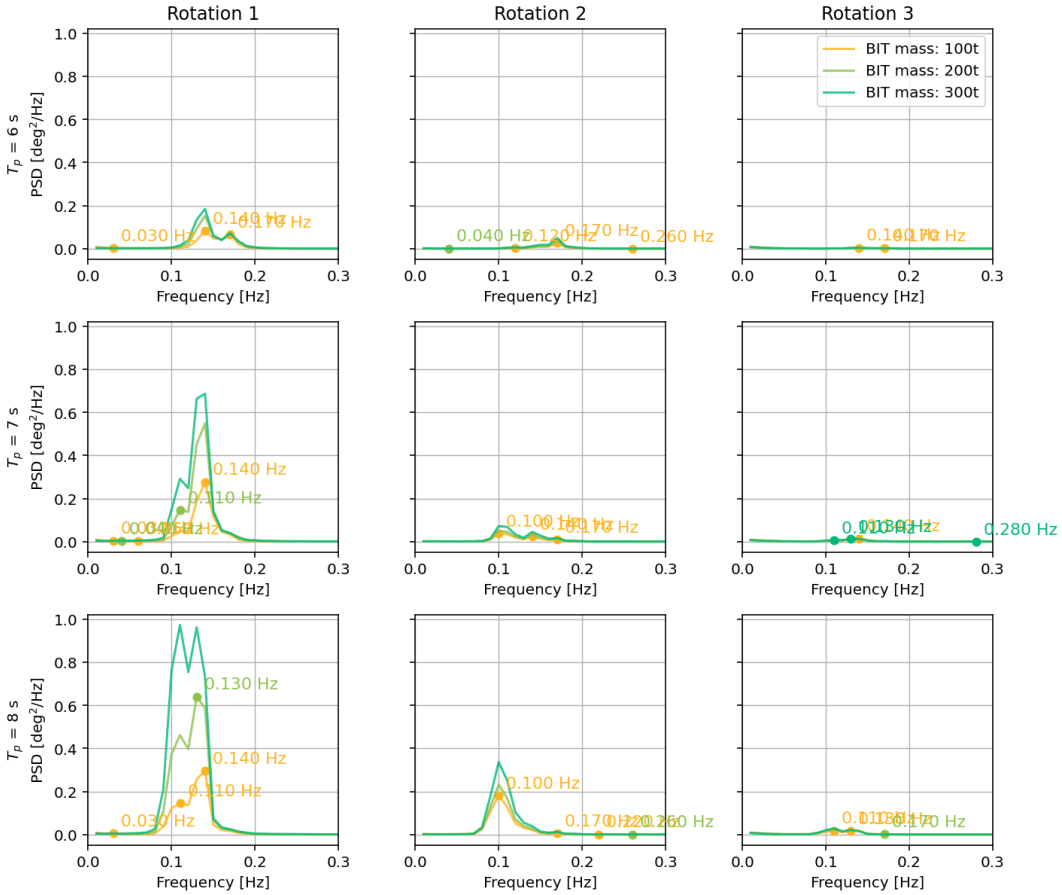

Figure B.8: Spectral density for $T_p = 6$ s, $T_p = 7$ s and $T_p = 8$ s for the rotational response of the BIT at a wave direction of $180°$, for varying BIT mass.

B.3. Tugger Parameters

B.3.1. BIT Spectral Densities for Various Tugger Widths

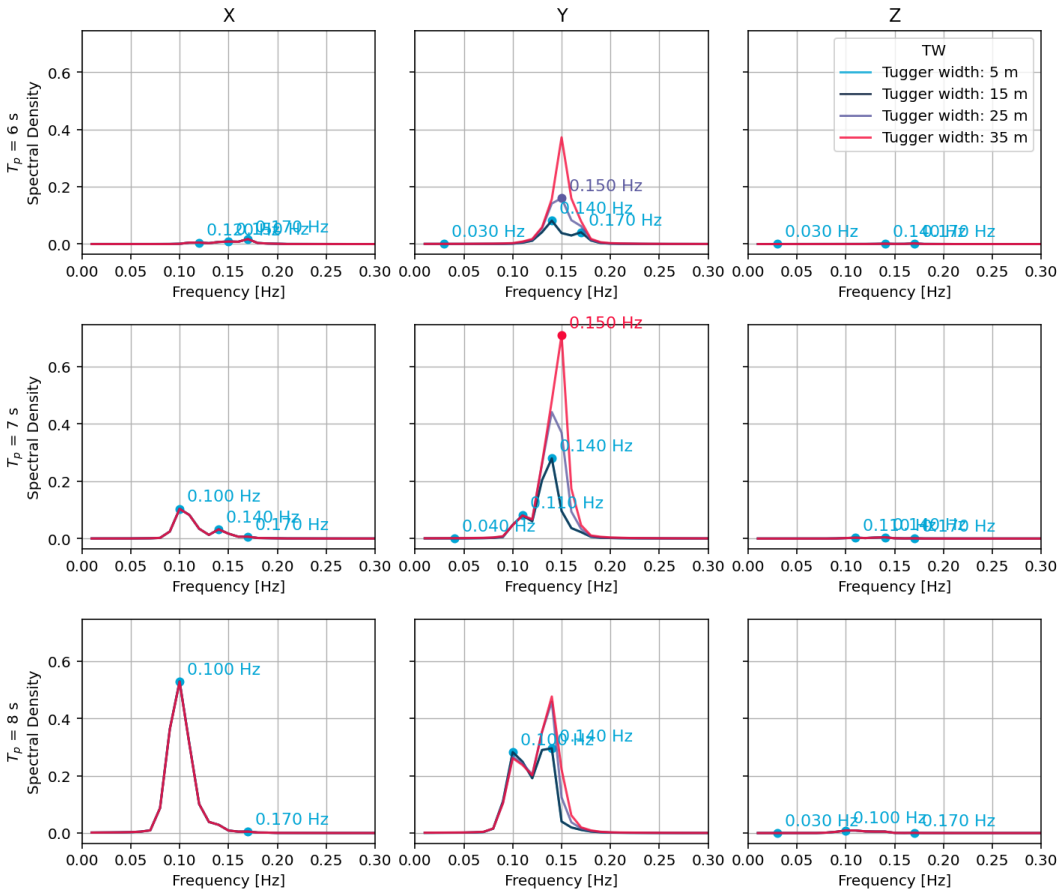

Figure B.9: Spectral density for $T_p = 6$ s, $T_p = 7$ s and $T_p = 8$ s for the translational response of the BIT at a wave direction of $180°$, for varying tugger widths.

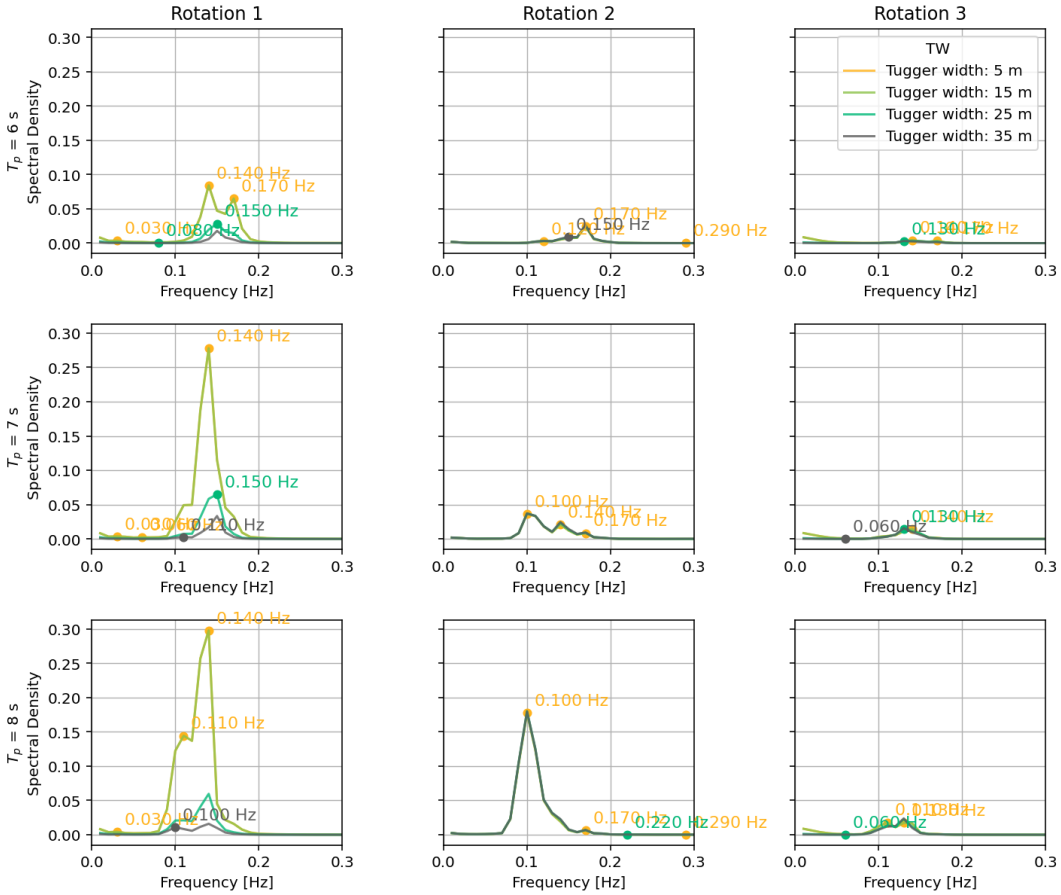

Figure B.10: Spectral density for $T_p = 6\,\text{s}$, $T_p = 7\,\text{s}$ and $T_p = 8\,\text{s}$ for the rotational response of the BIT at a wave direction of $180°$, for varying tugger widths.

B.3.2. BIT Spectral Densities for Various Tugger Stiffnesses

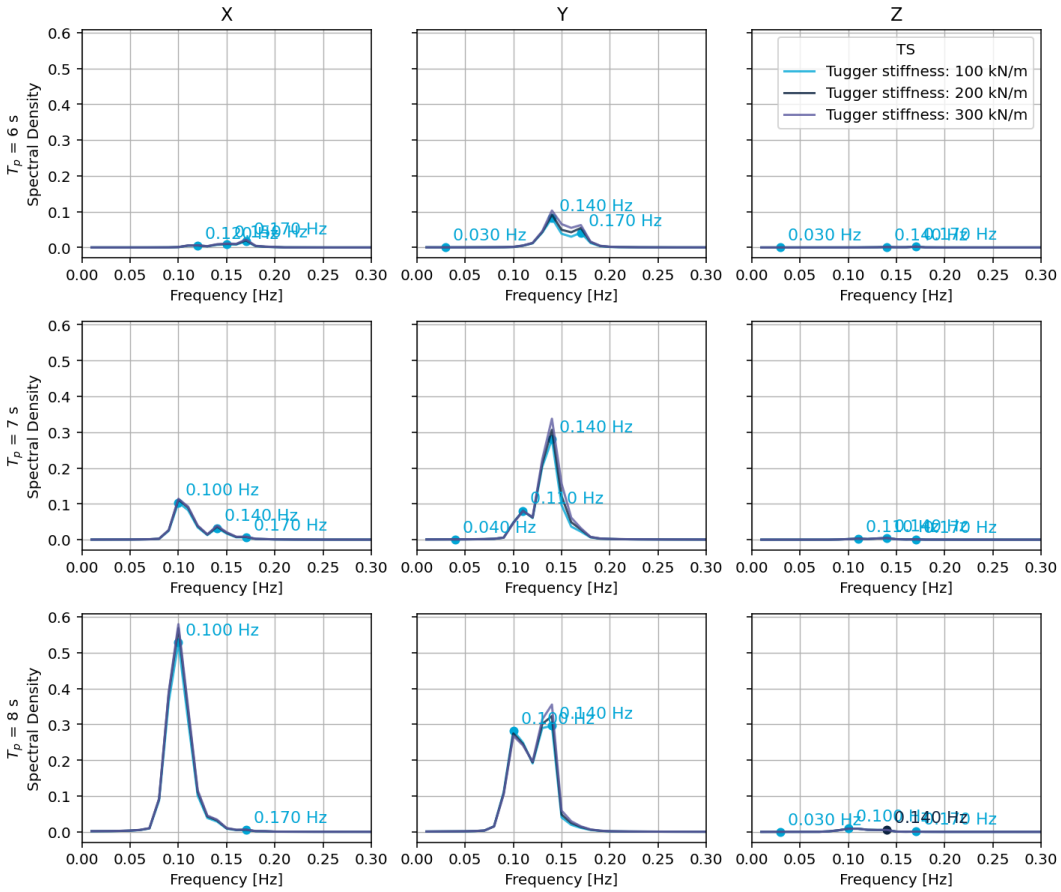

Figure B.11: Spectral density for$T_p = 6\,\text{s}$, $T_p = 7\,\text{s}$ and $T_p = 8\,\text{s}$ for the translational response of the BIT at a wave direction of $180°$, for varying tugger stiffnesses.

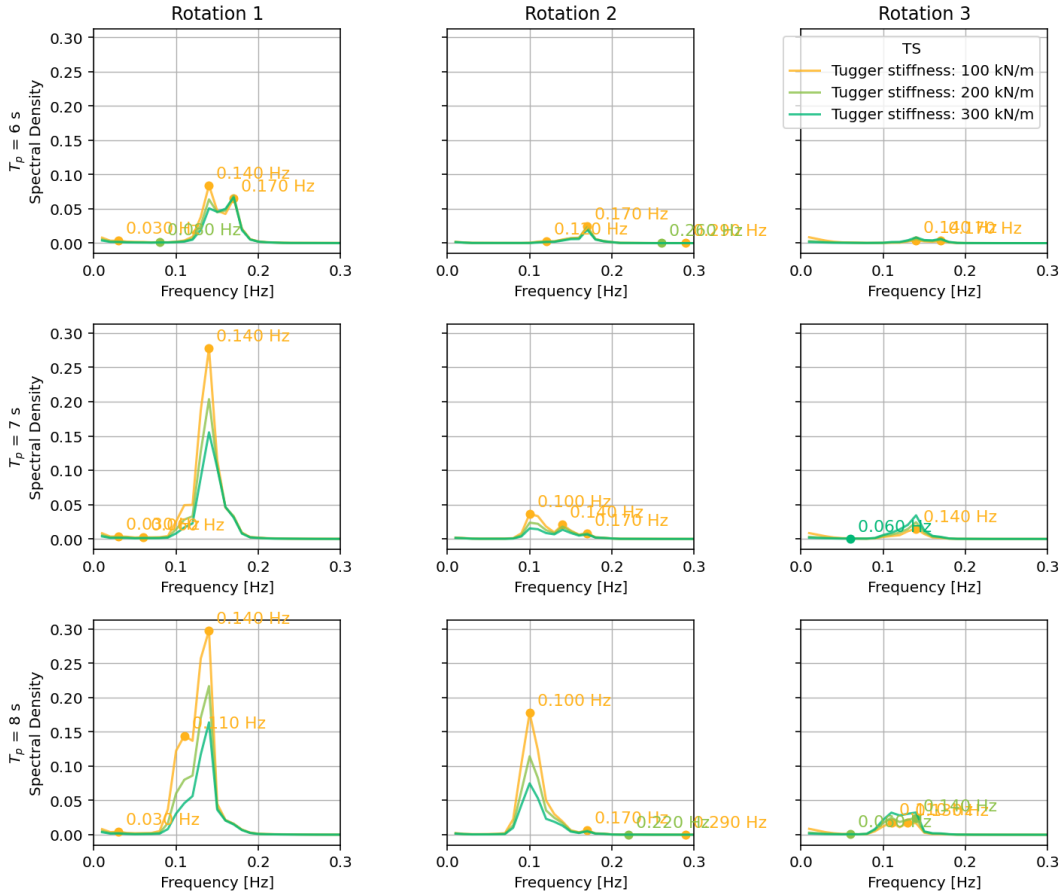

Figure B.12: Spectral density for $T_p = 6\,\text{s}$, $T_p = 7\,\text{s}$ and $T_p = 8\,\text{s}$ for the rotational response of the BIT at a wave direction of $180°$, for varying tugger stiffnesses.

B.3.3. BIT Spectral Densities for Various Tugger Pre-tensions

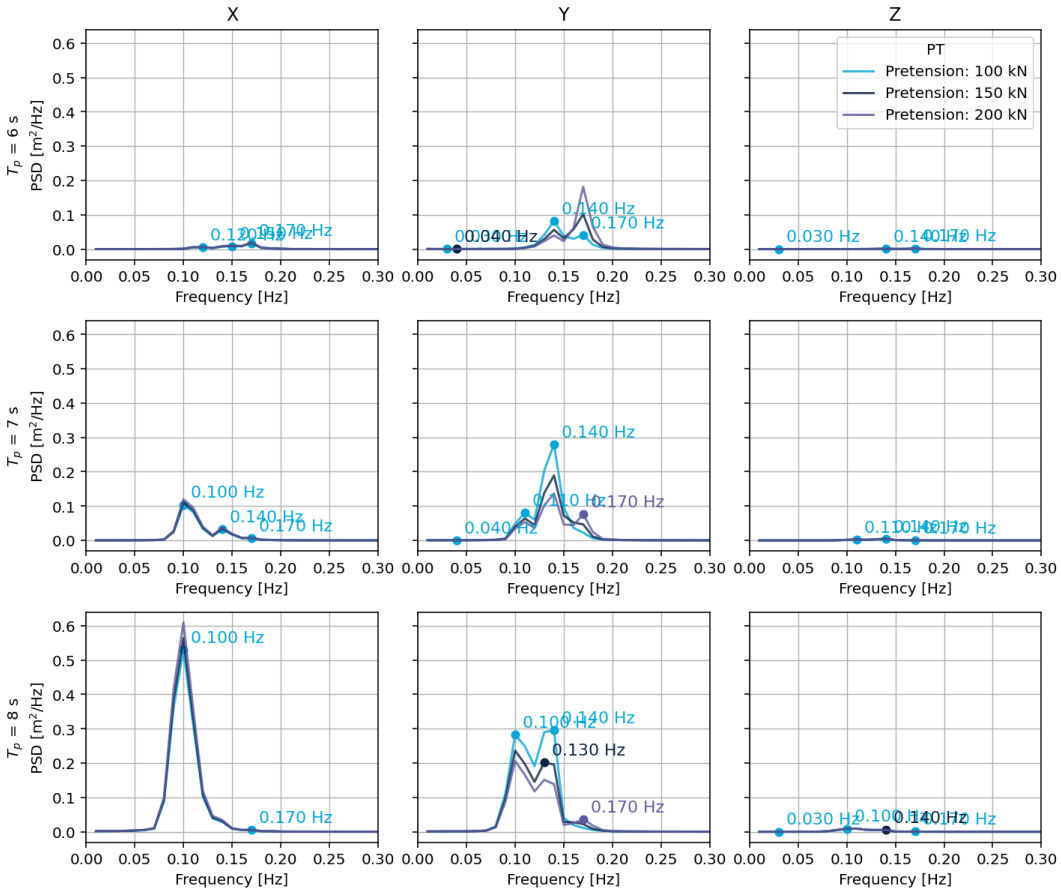

Figure B.13: Spectral density for$T_p = 6$ s, $T_p = 7$ s and $T_p = 8$ s for the translational response of the BIT at a wave direction of $180°$, for varying tugger pre-tensions.

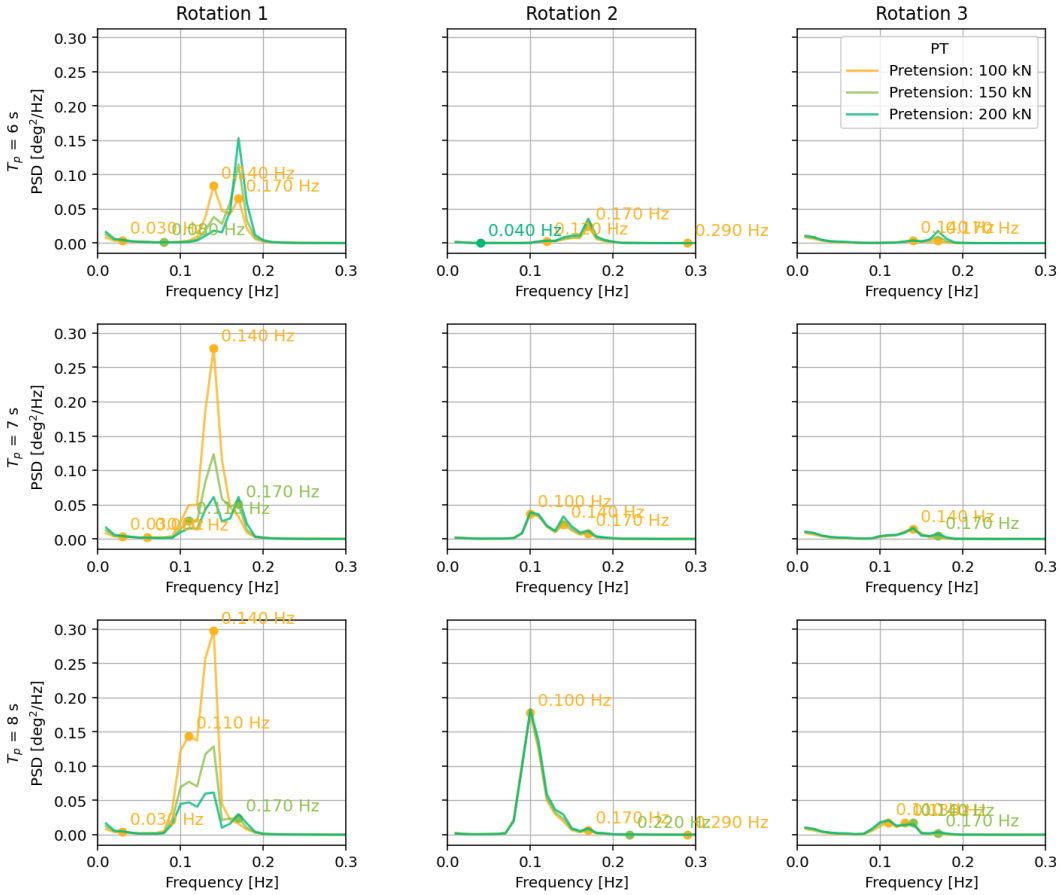

Figure B.14: Spectral density for $T_p = 6\,\text{s}$, $T_p = 7\,\text{s}$ and $T_p = 8\,\text{s}$ for the rotational response of the BIT at a wave direction of $180°$, for varying tugger pre-tensions.